université PARIS-SACLAY

ENSTA ParisTech université PARIS-SACLAY

NNT : 2018SACLY014

Thèse de doctorat

Modélisation de la réponse dynamique d'une paroi solide mise en vibration par un écoulement fluide diphasique

Thèse de doctorat de l'Université Paris-Saclay
préparée à Ecole Nationale Supérieure de Techniques Avancées

Ecole doctorale n°579 Sciences Mécaniques et Energétiques, Matériaux et Géosciences (SMEMAG)
Spécialité de doctorat : Fluides et Energétique

Thèse présentée et soutenue à Chatou, le 8 Novembre 2018, par

WILLIAM BENGUIGUI

Composition du Jury :

Njuki MUREITHI Professeur des Universités, Polytechnique Montréal	Président de jury
Yannick HOARAU Professeur des Universités, Université de Strasbourg (ICUBE)	Rapporteur
Stéphane VINCENT Professeur des Universités, Université de Paris-Est Marne-La-Vallée (LMSME)	Rapporteur
Olivier DOARE Professeur des Universités, ENSTA ParisTech (IMSIA)	Examinateur
Elisabeth LONGATTE Habilitée à Diriger des Recherches, ENSTA ParisTech (IMSIA)	Directeur de thèse
Jérôme LAVIEVILLE Ingénieur chercheur, EDF R&D	Encadrant
Stéphane MIMOUNI Ingénieur chercheur, EDF R&D	Encadrant

À Anaïs,
À mes parents et à ma soeur,
À ma famille,
À la mémoire de mes grands-pères.

Remerciements

Je remercie mon président de jury, *Njuki Mureithi*, d'avoir fait le déplacement depuis Montréal pour évaluer mon travail, ce fut un honneur de l'avoir au sein de mon jury; mes deux rapporteurs, *Yannick Hoarau* et *Stéphane Vincent*, pour avoir relu avec application ce mémoire ; et mon examinateur, *Olivier Doaré*, pour son enthousiasme et ses nombreuses questions. Je suis très heureux d'avoir eu un jury si bienveillant et ouvert lors de ma soutenance.

J'exprime ma gratitude à EDF R&D, en particulier au département MFEE, de m'avoir donné la chance de réaliser mon doctorat CIFRE dans les meilleures conditions. Je remercie ma directrice de thèse, *Elisabeth Longatte-Lacazedieu,* ainsi que les 3 personnes qui ont encadré mon travail au quotidien:

- *Jérôme Laviéville*, je ne pense pas avoir de mots assez forts pour dire à quel point je te suis reconnaissant tant sur le plan technique que humain. Si j'ai fait cette thèse, c'est grâce à toi du premier au dernier jour.
- *Stéphane Mimouni,* qui a toujours fait attention à ce que j'ai le moral et que je ne sois ni trop modeste ni trop confiant par rapport à mes résultats !
- *Enrico Deri,* mon plus grand lecteur, enfin RE-lecteur ☺ ; sans toi la thèse n'aurait pas le même parfum. C'est grâce à toi si j'ai trouvé la motivation et la passion pour aller si loin et me poser autant de questions.

Je voulais aussi exprimer ma gratitude à :

- *Nicolas Mérigoux*, pour son aide depuis le premier jour et son soutien sans faille.
- *André Adobes* et *Mathieu Guingo* pour m'avoir fait confiance durant ces 3 ans. Je ne pense pas que beaucoup de doctorants aient la chance de présenter aussi bien en réunion technique interne qu'à Hawaï en congrès international.
- *Pierre Moussou* pour nos discussions techniques (et administratives☺) qui m'auront été d'une grande aide.
- *Marc Boucker et Anthony Dyan,* pour avoir été des aides et oreilles attentives durant ma thèse.

Je remercie aussi *Céline Caruyer, Chaï Koren, Julien Berland, Sofiane Benhamadouche* et *Martin Ferrand* pour leurs participations à cette thèse et leurs précieux conseils.

Cette expérience m'aura permis de créer des liens d'amitiés forts donnant lieu à des scènes que je ne suis pas prêt d'oublier ; je pense en particulier à des moments passés avec *Jay, Nick, Ché, Gringo, King Congre* et *La Saumur*.

Je n'oublie évidemment pas mes compagnons: *les doctorants* ! Je vous remercie pour ces moments, j'espère que *Gaétan* et *Hamza* vous trouverez un jour plus régulièrement le chemin du but (et plus rapidement), que Riccardo n'aura plus besoin de tricher pour réussir un casse-tête ou que Clément arrivera un jour avant Riccardo. Je souhaite une bonne continuation aux docteurs et futurs docteurs que j'ai pu côtoyer *Cécile, Daria, Lucie, Meissam, Norah, Solène, Li, Thibaut et Vladimir*. *Sophie la blagueuse*, merci pour tout ! *Benjam'* plus communément appelé *CS_PARALL,* je suis déjà pressé d'être à la prochaine soirée Raclette (avec du vrai fromage) pour polémiquer sur l'origine des prénoms ! Notre thèse aura fait naître une belle amitié ☺

Enfin je souhaite remercier « Le Bureau » qui fut un temple pour moi et mes désormais grands amis :

- Ma première co-bureau, *SaraH*, je la remercie pour son « ouverture » et pour sa culture des sciences « annexes ».
- Mon deuxième co-bureau, *Antoine*, mon Dalon de Neuilly, merci pour tout, Sany et toi étaient ma fami parisienne lorsque j'habitais à Tours. Je suis pressé d'aller raler un gazon à La Réunion et en particulier du pwason.

Notre amitié a été durant toute ma thèse un soutien extrêmement important dans des moments parfois compliqués; j'espère qu'elle perdurera le plus longtemps possible.

Je remercie ma famille qui a toujours été derrière moi depuis le début de mes études quelques soient mes choix et qui aujourd'hui encore m'écoute et me conseille. *Babé* « travaille dans les bulles », certains seraient très heureux de le savoir !

Enfin, je tiens à dire « MERCI » à Anaïs, *mon p'tit roc*, de m'avoir toujours soutenu quelques soient les évènements. Sa tendresse, son affection et ses combats ont su me faire sortir de ma bulle quand il le fallait et ont contribué à la réussite de mon doctorat.

Contents

List of Figures ix

List of Tables xvii

Nomenclature xix

Publications xxiii

Introduction 1

1 Interface tracking method dedicated to moving bodies in two-phase flow 9

1.1 Interface tracking method dedicated to fluid-structure interaction 9

1.1.1 Popular interface tracking methods with adaptative grid 9

1.1.2 Immersed Boundary Methods 11

1.2 Time and Space Dependent Porosity method definition 13

1.2.1 Porous mass balance equation and media definition 14

1.2.2 Momentum balance equation 19

1.3 Robustness of the method 23

1.3.1 Test cases with stationary solids 23

1.3.2 Test cases with moving solids 25

1.3.3 Applications of the Time and Space Dependent Porosity method 27

2 Fluid-structure interaction with Time and Space Dependent Posority 37

2.1 Fluid structure coupling with the TSDP 39

2.1.1 Two-phase flow force computation with the Time and Space Dependent Porosity method 39

2.1.2 Newmark algorithm 40

2.1.3 Iterative implicit algorithm 41

2.2 Numerical validation of the fluid-structure coupling 42

2.2.1 Cylinder removed from its equilibrium position in a still fluid 42

2.2.2 Flow-induced vibration of a free cylinder with $Re = 100$ 46

2.2.3 Free fall of a spherical solid on a free surface. 50

3 Numerical investigation on two-phase cross-flow **55**
3.1 Selection of a numerical model to use in tube bundle configuration . . . 59
3.1.1 Experiment . . . 60
3.1.2 Sensitivity to the mesh refinement . . . 61
3.1.3 Numerical Investigation . . . 63
3.2 Investigation on the mixtures used in experiments . . . 73
3.2.1 Two-phase flow around a cylinder, literature review . . . 75
3.2.2 Influence of void fraction on the force around a cylinder for a steam-water flow . 77
3.2.3 Parameters of influence for a dispersed flow around a cylinder . . . 79
3.2.4 Impact of the mixture on the force around a tube . . . 84

4 Industrial application: Simulating vibration induced by two-phase flow in a tube bundle **91**
4.1 Flow characteristics . . . 92
4.1.1 Bubbly flow . . . 93
4.1.2 Churn flow . . . 94
4.2 Fluid-structure interaction in an in-line tube bundle . . . 101
4.2.1 Vibration of a single-tube induced by a single-phase flow across a 7x7 tube-bundle 102
4.2.2 Vibration of a single-tube induced by a two-phase flow across a 7x9 tube-bundle 103

Conclusion and Perspectives **107**

Bibliography **109**

Appendix A Two-phase flow modeling with NEPTUNE_CFD **117**
A.1 Toward two-phase flow numerical modeling . . . 117
A.2 Two-fluid approach . . . 118
A.3 Dispersed approach - Spherical bubbles . . . 119
A.3.1 Drag force . . . 120
A.3.2 Lift force . . . 120
A.3.3 Added mass force . . . 121
A.3.4 Turbulent dispersion . . . 121
A.4 Continuous approach - Large interfaces . . . 121
A.4.1 Large Interface Model . . . 122
A.4.2 Large Bubble Model . . . 123
A.5 Multi-regime approches . . . 124
A.5.1 Generalized Large Interface To Dispersed approach . . . 124
A.5.2 Multi-field approach . . . 125
A.6 Turbulence models . . . 126

List of Figures

1 a) Pressurized Water Reactor sketch (source: World Nuclear Association). b) Cross-sketch of an EPR steam generator. The production of steam is sketched by blue to red arrows. Vibration due to cross flows are located in the red circles. 2

2 Generic idealized response with increasing flow reduced-velocity of a structure, Païdoussis (2006). 3

3 Downstream vortices of a cylinder (Weaver et al., 1993). 4

4 Void fraction influence on the structure response with increasing flow reduced-velocity. 5

5 a) Comparison between the theoretical model of hydrodynamic mass (Rogers et al., 1984) with experimental data. The decrease of the hydrodynamic mass is responsible of the increase of the critical reduced velocity. b) Comparison between the theoretical model from Pettigrew (1995) and experiments for different mixtures and configurations. The variations of two-phase damping with void fraction are responsible for the variation of the slope of fluid-elastic departure. 5

1.1 A kinematically driven propeller spins with a number of attached Chimera grids. The grids move and rotate with the rigid body frame of the propeller. (English et al., 2013) . 11

1.2 Cut-cell approach, sketch of the different steps of the method. Moreover, each flux from faces concerned in the merging is re-defined. 12

1.3 Cell-porosity computation: nodes in the solid domain are in red, others in black. In a cell, if each node is solid (blue), it is a solid-cell; if each node is not solid (white), it is a fluid-cell; otherwise it is a a cut-cell (green). 15

1.4 Fluid-structure interface crossing a face in a two-dimensional configuration. Each cell area is calculated by using triangle and rectangle areas when it is required. 16

1.5 Decomposition of the domain according to the position of each cylinder. In each subdomain, the solid velocity is taken equal to the corresponding solid. 17

1.6 Fluid-structure interface crossing a cell face. Sub-cycles are required in this case to approximate step by step the value of the face-porosity. 18

1.7 Cell crossed by the fluid-structure interface, geometric characteristics re-shaping. . . . 20

1.8 Sketch of the cell center displacements. 20

1.9 Sketch of the face center displacements. 21

1.10 Iterative determination of the cell centers. Initial positions are represented with bullets. . 21

1.11 Geometric points representation for an inclined channel. 23

1.12 Poiseuille flow: L^2 relative error and order conservation graphics. 24

1.13 Sketch (left) of the Taylor-Green vortices around an immersed square solid with slip walls and numerical results for 5 grid refinements (right). 25
1.14 Definition of the characteristic wake dimensions for the steady flow over a stationary circular cylinder (left) and numerical streamlines for $Re = 40$. 26
1.15 Pressure profile after discovering a cell (accelerating solid) after 1s (left) and 2s (right). The solid is in green. 26
1.16 Geometry of cylinder at fluid velocity case (left) and velocity error for a cylinder at fluid velocity in single and two-phase flow (with 2 approaches : dispersed and continuous), (right). 27
1.17 Geometry of the cylinder suddenly stopped case (left) and drag coefficient around the cylinder moving with $Re = 40$ and suddenly stopped. Numerical results are compared with other methods (Koumoutsakos and Leonard, 1995; Bergmann et al., 2012) (right). 28
1.18 Vorticity isolines for 8 different times with numerical simulation (left) and experimental data (right) from Koumoutsakos and Leonard (1995) 29
1.19 Geometry of the bubble impact on a cylinder case. 30
1.20 Contour comparison of a bubble impacting a cylinder between NEPTUNE_CFD with a body-fitted mesh and the Time and Space Dependent Porosity method at $t = 0.01, 0.1, 0.2, 0.3, 0.4, 0.5, 0$
1.21 Snapshots of a bubble impacting a cylinder with the Time and Space Dependent Porosity method at $t = 0.01, 0.1, 0.2, 0.3, 0.4, 0.5, 0.6, 0.7\ s$. 31
1.22 Sketch of the tank (Janosi et al., 2004). 32
1.23 Experiment/Numerical simulation confrontation of a dam-break on wet bed for $d = 18\ mm$. 32
1.24 Geometry of the wave tank case, (Gao, 2003). 33
1.25 Free surface evolution for 2 different positions 0.65 m (left) and 5.45 m (right). Comparison between experiment (Gao, 2003) and numerical results from TSDP. 33
1.26 Two-phase flow in a centrifugal pump. Air and water are injected by the bottom. The mesh is a box with uniform cartesian cells. The porosity defines the blades and the boundaries of the domain. 35

2.1 Fluid-structure interaction with partitioned approach, the explicit or weak coupling. . . 38
2.2 Fluid-structure interaction with partitioned approach, the iterative implicit or strongly coupling. 38
2.3 Sketch of the iterative determination of the structure displacement due to the fluid forces. 41
2.4 Cylinder removed from its equilibrium position in a still fluid, geometry. 43
2.5 Cylinder removed from its equilibrium position in a still fluid after 1 period on the left, after 31 periods on the right, sub-cycles and δ_{max} sensitivity. 44
2.6 Cylinder removed from its equilibrium position in a still fluid, time step sensitivity. . . 45
2.7 Cylinder removed from its equilibrium position in a still fluid, mesh sensitivity. 46
2.8 Flow-induced vibration of a free cylinder with $Re = 100$, geometry. 46

2.9 Mesh utilized for the flow-induced vibration case with $Re = 100$. On the left, the entire mesh is presented. On the right, a zoom is realized in the zone of interest where the cylinder is. This area is large since the refinement must remain the same whatever the cylinder displacement. . . . 47
2.10 Flow-induced vibration at $Re = 100$ for $m^* = 1.25$ and $k^* = 2.48$. Picture of the cylinder displacement and a vortex shedding over time. In this case, the amplitude of displacement is 60% of the diameter. . . . 48
2.11 Response for undamped systems for various cases: A^* amplitude, f^* frequency, C_L max lift coefficient and $C_{D,av}$ averaged drag coefficient. Comparison between numerical results from Shiels et al. (2001), Marcel (2010) and the present method. . . . 49
2.12 Response for undamped systems plotted against effective elasticity. Comparison between numerical results from Shiels et al. (2001) and the present method. . . . 49
2.13 Confined cylinder released in a fluid, geometry. . . . 50
2.14 Free-fall of a sphere on a free-surface: mesh refinement for teflon (on the left). Numerical/experimental displacement along time of a sphere free-falling on a free surface for 4 different materials (on the right). . . . 51
2.15 Polypropylene and nylon spheres falling on a free surface of water. Numerical (bottom) and experimental (top) snapshot of the sphere entry in water. . . . 52
2.16 Teflon and steel spheres falling on a free surface of water. Numerical (bottom) and experimental (top) snapshot of the sphere entry in water. . . . 53

3.1 Pictures (from the top to the bottom) and flow pattern sketches of bubble, dispersed, large bubbles, churn, intermittent and annular air/water flows in a staggered tube bundle Kanizawa and Ribatski (2016) . . . 56
3.2 Picture of a bubbly and churn flow in in-line tube bundle, Murakawa et al. (2016). . . . 57
3.3 Flow regime map comparison for two-phase flow across a staggered tube bundle. Ulbrich and Mewes (1994) (line) and Noghrehkar et al. (1999) (dash). . . . 57
3.4 Influence of the surface tension on the bubble size, Pettigrew and Knowles (1997). For two different inlet void fractions, the bubble diameter is reduced by lowering the surface tension. . . . 59
3.5 Inclined tube bundle experiment (Soussan et al., 2001). In blue and green, North/South and West/East planes are colored. . . . 61
3.6 Snapshot of the mesh of the tube bundle. It is presented in 2D for only a few tubes in order to see the refinement around tubes . . . 62
3.7 Numerical result using the **Generalized Large Interface Model with a R_{ij}-ε SSG turbulence model** for three mesh refinement called Grid 1, Grid 2 and Grid 3. Averaged void fraction and gas velocity along North/South and West/East lines compared with experimental data. . . . 62
3.8 Numerical result using the available numerical models from NEPTUNE_CFD. Averaged void fraction and gas velocity along North/South and West/East lines compared to experimental data. . . . 63

3.9 Numerical result using the **Generalized Large Interface Model with a R_{ij}-ε SSG turbulence model taking into account a surface tension force**. Averaged void fraction and gas velocity along North/South and West/East lines compared to experimental data. 66
3.10 Numerical results using the **dispersed approach with a R_{ij}-ε SSG turbulence model with constant or variable bubble diameters**. Averaged void fraction and gas velocity along North/South and West/East lines compared to experimental data. 67
3.11 Numerical result using the **Generalized Large Interface Model with different turbulent models**. Averaged void fraction and gas velocity along North/South and West/East lines compared to experimental data. 68
3.12 Numerical result using the **Generalized Large Interface Model with a R_{ij}-ε SSG turbulence model**. From left to right: instantaneous void fraction distribution on NS plane, averaged void fraction distribution on NS plane, instantaneous void fraction distribution on OE plane and averaged void fraction distribution on OE plane. 70
3.13 Numerical result using the **Multi-Fields approach with a R_{ij}-ε SSG turbulence model**. From left to right: instantaneous void fraction distribution on NS plane, averaged void fraction distribution on NS plane, instantaneous void fraction distribution on OE plane and averaged void fraction distribution on OE plane. 70
3.14 Numerical result using the **Generalized Large Interface Model taking into account the surface tension force with a R_{ij}-ε turbulent model**. From left to right: instantaneous void fraction distribution on NS plane, averaged void fraction distribution on NS plane, instantaneous void fraction distribution on OE plane and averaged void fraction distribution on OE plane. 71
3.15 Numerical result using the **Generalized Large Interface Model without any turbulent model**. From left to right: instantaneous void fraction distribution on NS plane, averaged void fraction distribution on NS plane, instantaneous void fraction distribution on OE plane and averaged void fraction distribution on OE plane. 71
3.16 Numerical result using the **Generalized Large Interface Model with a k-ε turbulent model**. From left to right: instantaneous void fraction distribution on NS plane, averaged void fraction distribution on NS plane, instantaneous void fraction distribution on OE plane and averaged void fraction distribution on OE plane. 72
3.17 Numerical result using the **dispersed approach with a R_{ij}-ε SSG turbulence model**. From left to right: instantaneous void fraction distribution on NS plane, averaged void fraction distribution on NS plane, instantaneous void fraction distribution on OE plane and averaged void fraction distribution on OE plane. 72
3.18 Numerical experiment for the inclined tube-bundle experiment with **freon/freon (top view)** and **air/water (bottom view)**. Instantaneous and time-averaged void fraction are present in the NS and WE plane. 74
3.19 Picture of bubbly flow around a cylinder for $D_{cylinder} = 40\ mm$, $\alpha_0 = 8\ \%$, and $U_0 = 0.45,\ 0.9,\ 1.9\ m/s$ from left to right, Inoue et al. (1985). 75
3.20 Evolution of the reference equivalent spectra versus frequency for different inlet void fraction, (Pascal-Ribot and Blanchet, 2007). 76

3.21 77
3.22 Drag and lift force spectrum for four different inlet void fraction (respectively left and right). 78
3.23 Drag (left) and lift (right) force records along time for 0-5% (top) and 10-20% (bottom) of void fraction. 79
3.24 Drag (left) and lift (right) force records along time for 50-80% (top) and 90-100% (bottom) of void fraction. 80
3.25 Averaged void fraction distribution around a cylinder with $\alpha_{inlet} = 8\%, U_{inlet} = 0.9m/s$ and $D = 40\ mm$. From left to right, there are experimental data, mesh 1, mesh 2 and mesh 3. 81
3.26 Averaged void fraction distribution around a cylinder with $\alpha_{inlet} = 4\%, 15\%, U_{inlet} = 0.9\ m/s$ and $D = 40\ mm$. From left to right, there are experimental data for $\alpha_{inlet} = 4\%$ and its simulation, $\alpha_{inlet} = 15\%$ and its simulation. 81
3.27 Averaged void fraction distribution around a cylinder with $\alpha_{inlet} = 8\%$, $U_{inlet} = 0.45,\ 1.9\ m/s$ and $D = 40\ mm$. From left to right, there are experimental data for $U_{inlet} = 0.45\ m/s$ and its simulation, $U_{inlet} = 1.9\ m/s$ and its simulation. 82
3.28 Averaged liquid (left) and gas (right) velocity distribution around a cylinder with $\alpha_{inlet} = 8\%, U_{inlet} = 0.45$ (top), 1.9 (bottom) m/s and $D = 40\ mm$. 83
3.29 Averaged void fraction distribution around a cylinder with $\alpha_{inlet} = 8\%, U_{inlet} = 0.9\ m/s$ and $D = 40\ mm$. From left to right, $\sigma = 0.017,\ 0.035,\ 0.075\ N/m^2$. 84
3.30 Pictures of the final bubble shape for case B and D from BHAGA 85
3.31 Geometry of the bubble rise (left) and the bubble impact on a cylinder (right) cases. . . 85
3.32 Bubble velocity from numerical simulation along the time for case B and D. 86
3.33 Bubble shape comparison between experiment and numerical result for case B. The bubble is in 3D with an opacity of 50%. 86
3.34 Bubble impact on a cylinder with two mesh refinements. 87
3.35 Snapshots of the impact of the bubble from case B on a cylinder at 4 different times. . . 88
3.36 Snapshots of bubble from case B (left) and D (right) before impact. 88
3.37 Forces on the cylinder for case B (left) and D (right). Drag and lift forces are respectively in red and blue. For the case B, the forces computed with the two meshes are in agreement. 89

4.1 VISCACHE tube bundle geometry for single-phase flow (left) and two-phase flow (right). Rigid tubes are filled in white and flexible tubes in black. 92
4.2 Void fraction distribution across the tube bundle for water/freon (left) and water/steam (right) for equivalent inlet volume flow rates with a 10% inlet void fraction. The half left of each tube bundle is presented with a volume distribution and the half right with a surface distribution on a slice. 93
4.3 Void fraction distribution across the tube bundle for water/freon (left) and water/steam (right) for equivalent inlet mass flow rates with a 10% inlet void fraction. The half left of each tube bundle is presented with a volume distribution and the half right with a surface distribution on a slice. 94

4.4 Void fraction distribution across the tube bundle for water/freon (left) and water/steam (right) for equivalent inlet volume flow rates with a 50% inlet void fraction. The half left of each tube bundle is presented with a volume distribution and the half right with a surface distribution on a slice. 95
4.5 Void fraction distribution across the tube bundle for water/freon (left) and water/steam (right) for equivalent inlet mass flow rates with a 50% inlet void fraction. The half left of each tube bundle is presented with a volume distribution and the half right with a surface distribution on a slice. 96
4.6 Comparison of (from top to bottom) time-averaged void fraction, time-averaged streamwise liquid velocity, time-averaged transverse liquid velocity and instantaneous bubble diameter along the different rows of the tube bundle. Results are respectively on the left and right for water/freon and water/steam for a 10% inlet void fraction with equivalent volume flow rates. 97
4.7 Comparison of (from top to bottom) time-averaged void fraction, time-averaged streamwise liquid velocity, time-averaged transverse liquid velocity and instantaneous bubble diameter along the different rows of the tube bundle. Results are respectively on the left and right for water/freon and water/steam for a 10% inlet void fraction with equivalent mass flow rates. 98
4.8 Comparison of (from top to bottom) time-averaged void fraction, time-averaged streamwise liquid velocity, time-averaged transverse liquid velocity and instantaneous bubble diameter along the different rows of the tube bundle. Results are respectively on the left and right for water/freon and water/steam for a 50% inlet void fraction with equivalent volume flow rates. 99
4.9 Comparison of (from top to bottom) time-averaged void fraction, time-averaged streamwise liquid velocity, time-averaged transverse liquid velocity and instantaneous bubble diameter along the different rows of the tube bundle. Results are respectively on the left and right for water/freon and water/steam for a 50% inlet void fraction with equivalent mass flow rates. 100
4.10 Root-mean-square amplitude of cylinder motion (left) and dominant Strouhal number $St = fd/U_g$ (right) as functions of the gap velocity U_g for lift direction only. Comparison of the results from the present study, Granger et al. (1993) and Berland et al. (2014) . . 102
4.11 Tube frequency (left) and root-mean-square amplitude of cylinder motion (right) as functions of the homogeneous velocity U_g for a **bubbly flow**. Comparison for lift direction only of the results from the present study, and Delenne et al. (1997). 103
4.12 Tube frequency (left) and root-mean-square amplitude of cylinder motion (right) as functions of the homogeneous velocity U_g for a **churn flow**. Comparison for lift direction only of the results from the present study, and Delenne et al. (1997). 103
4.13 a) VISCACHE tube bundle geometry for single-phase flow (left). Rigid tubes are filled in white and flexible tubes in black. b) Displacement of the center tube for a unique mobile tube and mobile flexible cell of 9 tubes. 104

A.1 Sketch of a dispersed approach. 119
A.2 Large interface approach. 121
A.3 Three cell stencil. 122
A.4 Sketch of the multi-regime approach. 124
A.5 Turbulent scale, different methods. 126

List of Tables

1.1 Comparison between experimental results (with an "*"), other simulations and the present study for a cylinder at $Re = 40$. 26

2.1 Cylinder removed from its equilibrium position in a still fluid, numerical and experimental prediction of frequency and reduced damping comparison. 45
2.2 Force coefficients and Strouhal prediction for a single-phase flow around a cylinder with $Re = 100$. Comparison between results from Pomarede et al. (2010) and the present study. 47
2.3 Numerical cases from Shiels et al. (2001) computed in the present study. 48
2.4 Numerical and experimental pinch-off time comparison. 51

3.1 Comparison of mixtures used in experiment in terms of physical properties. 58
3.2 Hierarchy of mesh refinement used for the sensitivity study. 61
3.3 Sensitivity to the time of computation depending on the two-phase numerical model. The cluster that was used is an Atos-bull cluster equipped with Intel@Xeon CPU E5 2680 v4 @ 2.40 GHz (Broadwell) nodes with 28 cores. 66
3.4 Physical properties of a bubble rise for case B and D from Bhaga and Weber (1981). . 85

4.1 Physical properties of water (1 bar), freon-water (7 bar) and steam generator operating condition: steam-water (70 bar). 92

Nomenclature

Roman characters

$a_{0...7}$	Newmark coefficients	$(-)$
C	Damping	$N.s/m$
C_d, C_k	Coupling coefficient	$(-)$
C_D, C_L	Drag and lift coefficient	$(-)$
D or d	Diameter	m
$dt, \Delta t$	Time step	s
Eo	Eotvos number	$(-)$
F	Force	N
f	Frequency	Hz
g	Gravity	m/s^2
I^*	Displaced cell center	$(-)$
k	Phase indicator	$(-)$
K	Stiffness	$N.m$
L	Length	m
l, g	Liquid or gas	$(-)$
M	Mass	kg
$\mathbf{M}$	Momentum transfer	N
Mo	Morton number	$(-)$
$\underline{n}$	face unit normal vector	$(-)$
P	Pressure	Pa
R	Radius	m
Re	Reynolds number	$(-)$
S_I	Surface of cell I	m^2
St	Strouhal number	$(-)$

t	Time	s
T	Temperature	K
U or u	Velocity	m/s
We	Weber number	$(-)$
x, y, z	Space coordinates	m

Greek characters

α	Phase fraction	$(-)$
β	Solid fraction during sub-iteration	$(-)$
δ	Convergence parameter	$(-)$
ε	Porosity	$(-)$
γ or β	Newmark stability coefficient	$(-)$
μ	Viscosity	$Pa.s$
Ω	Volume	m^3
ω	Pulsation	rad/s
ϕ	Flux	m/s
ρ	Density	kg/m^3
σ	Surface tension	$N.m^2$
τ	Reynolds-stress tensor	N
θ	Value between 0 and 1	$(-)$
ξ	Reduced damping	$(-)$

Acronyms

CEA	Commissariat à l'Energie Atomique
CFD	Computational Fluid Dynamics
DNS	Direct Numerical Simulation
EBRSM	Elliptic Blending Reynolds Stress Model

EDF	Électricité de France
FEI	Fluid Elastic Instability
FSI	Fluid-Structure Interaction
GLIM	Generalized Large Interface Model
IBM	Immersed Boundary Method
IRSN	Institut de Radioprotection et de Sureté Nucléaire
LBM	Large Bubble Model
LES	Large Eddy Simualtion
LIM	Large Interface Model
NS	North South
PWR	Pressurized Water Reactor
RANS	Reynolds-Averaged Navier-Stokes
RMS	Root Mean Square
SG	Steam Generator
TSDP	Time and Space Dependent Porosity
VIV	Vortex Induced Vibration
WE	West East

Publications

1. W. Benguigui, J. Laviéville, S.Mimouni, N. Mérigoux, E. Longatte, *First steps in the development of an eulerian fixed grid postulation for two-phase flow-induced vibration numerical modeling*, Flow Induced Vibration, La Haye, Pays-Bas, 2016.

2. W. Benguigui, J. Laviéville, S.Mimouni, E. Longatte, *Suivi d'une interface solide mobile au sein d'un écoulement diphasique par une méthode de frontière immergée*, CSMA, Gien, 2017.

3. W. Benguigui, E. Deri, J. Laviéville, S.Mimouni, E. Longatte, *Numerical experiment on two-phase flow behaviors in tube bundle geometry for different mixtures*, Pressure Vessels and Piping, Waikoloa Village, Hawai USA, 2017.

4. W. Benguigui, E. Deri, J. Laviéville, S.Mimouni, E. Longatte, *Numerical investigation and analysis of a dispersed two-phase flow across a single rigid cylinder*, Flow Induced Vibration, Toronto, Canada, 2018.

5. W. Benguigui, E. Deri, J. Laviéville, S.Mimouni, E. Longatte, *Numerical investigation of a single bubble impacting a cylinder, fist steps towards the up-scaling*, Flow Induced Vibration, Toronto, Canada, 2018.

6. W. Benguigui, A. Doradoux, J. Laviéville, S. Mimouni, E. Longatte, *A discrete forcing method dedicated to moving bodies in two-phase flows*, International Journal for Numerical Methods in Fluids, 2018 .

Introduction

In thermal power stations, the generated heat is used to boil water in order to drive a steam turbine connected to an electric generator. In nuclear pressurized water reactors (Pressurized Water Reactor), the heat is generated in the core and carried out by a primary liquid water circuit. Then, via a tubular heat exchanger, called steam generator, power is transferred to a boiling secondary water circuit (see Figure 1 a)). This hence produced steam is dried before entering the turbine.

There are three or four steam generators per reactor in France. They can measure up to 20 m and weigh as much as 800 tons. They can contain from 3000 to 16 000 U-tubes with a diameter of approximately 20 mm. A sketch of the EPR steam generator is proposed in Figure 1 b) : this type of power plan will start soon to produce power in France. In typical PWR recirculating steam generators, the primary system coolant flows through U tubes with a tube sheet at the bottom of the generator and U bends at the top of the tube bundle. Primary coolant enters the steam generator usually at 315 - 330^{o}C on the hot leg side and leaves at about 288^{o}C on the cold leg side. The secondary system water is fed through a feedwater nozzle, to a feedwater distribution ring, into the downcomer, where it mixes with recirculating water draining from the moisture separators. This downcomer water flows to the bottom of the steam generator, across the top of the tube sheet, and then up-wards through the tube bundle, where steam is generated. About 25% of the secondary bulk water is converted to steam as it passes through the tube bundle up-wards, the remainder is recirculated.

As steam generators degrade over time, their integrity is extremely important both for economic and safety reasons. Consequently, during scheduled maintenance outages or shutdowns, steam generator tubes are inspected. If necessary a tube might be plugged to remove it from operation. The French regulatory agency requires a baseline inspection of all tubing full length before operation, periodic inspections at least every two years, and complete inspections (presumably 100% of the tubes full length) every ten years. The tube support plate and sludge pile inspections might also be realized.

Steam generator problems may constrain the plants to perform unscheduled or extended maintenance operations. Unfortunately, steam generator maintenance and replacement are expensive and the origins of the degradations are multiple. The present work is motivated by one of the main ones: flow induced vibration of heat exchanger tubes. This phenomenon might be seen in two different locations of the steam generator (Pettigrew and Taylor, 2003) where there is a cross-flow : at the bottom of the bundle under single-phase flow and at the top under two-phase flow with high void fractions (see Figure 1 b)). At the bottom of the bundle, it is a single phase flow. Two kinds of degradation mechanisms may be generated by flow induced vibration: fretting wear and high cycle fatigue. Anti-vibration bars, tube support plates or tubes might be affected by these mechanisms. In general, before having leakage or rupture problems, tubes are plugged in order to put them out of service. However, few nuclear power

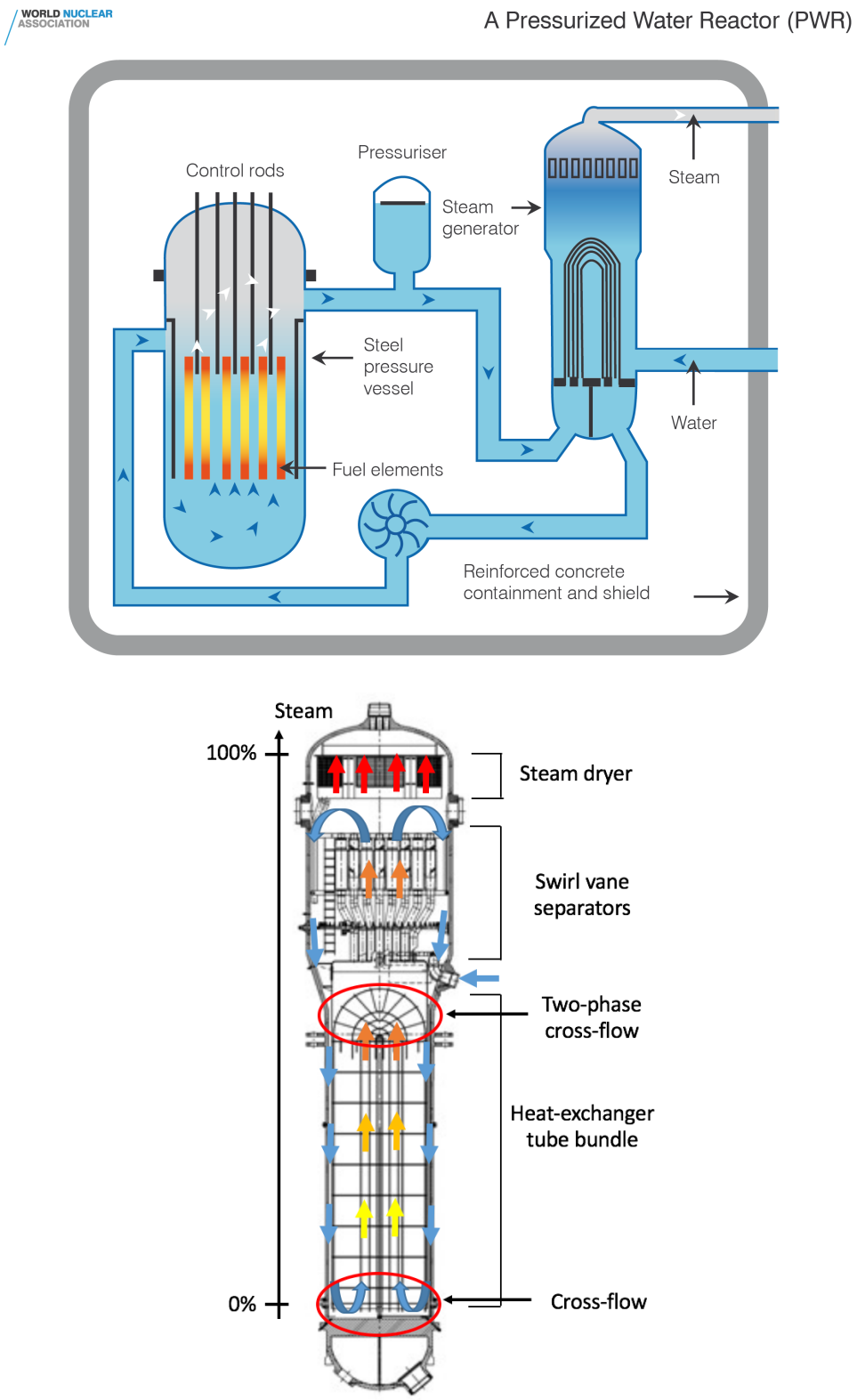

Figure 1 a) Pressurized Water Reactor sketch (source: World Nuclear Association). b) Cross-sketch of an EPR steam generator. The production of steam is sketched by blue to red arrows. Vibration due to cross flows are located in the red circles.

plants abroad reported tube ruptures. Consequently, flow induced vibration, being a major concern for the correct steam generator behavior, has been studied in order to understand and prevent this phenomenon.

According to Price (1995), cross-flow induced vibration mechanisms are indexed in three main categories: Tubulence-Induced-Vibrations (TIV); Vortex-Induced-Vibrations (VIV); Fluid-Elastic Instability (FEI) or Motion-Induced-Vibrations (MIV). Experimental data from literature illustrating vibration regimes according to the flow velocity highlight distinctly three different ranges of vibrations.

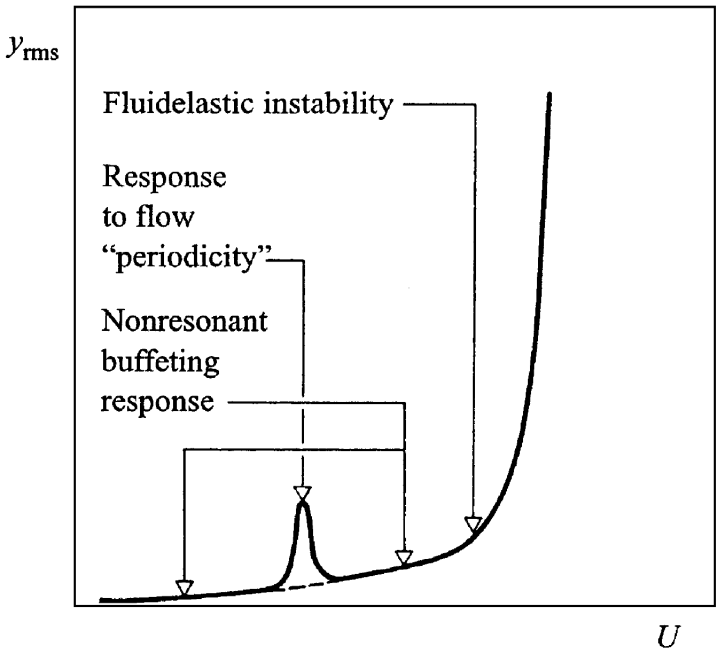

Figure 2 Generic idealized response with increasing flow reduced-velocity of a structure, Païdoussis (2006).

A solid body immersed in a fluid flow is subjected to random turbulent forces given by the pressure fluctuation at the wall: this results in TIV vibration. It is possible to model the object as a filter taking energy from the fluid. In fact, the solid begins to vibrate with a slight amplitude. These vibrations are more or less large depending on the Reynolds number. For a steam generator, turbulence is essential to stimulate heat transfer. Even if this phenomenon leads to low vibration magnitudes, it is vital to take it into account because of its influence on the tube duration.

The wake downstream of the cylinder produces periodic vortices on both tube sides (see Figure 3). The structure is not impacted by the shedding as long as the vortex shedding frequency is different from the natural frequency of the tube. When these frequencies are close, a peak is observed in response amplitude (see Figure.2). VIV is stable thanks to the non-linearities of the system .

Fluid-elastic instability is the most violent phenomenon for the structure as it might cause damages. In fact, it is the result of hydrodynamic forces which originate as a result of the vibration itself. The larger the amplitude of vibration, the larger the force, consequently vibration amplitude increases with velocity. This self-amplified phenomenon appears above a critical velocity and most of the time leads to tube failure. Therefore, fluid-elastic instability is of major concern for industry especially nuclear power plants. Many studies have been performed in order to predict FEI critical velocity for decades (Langre, 2002).

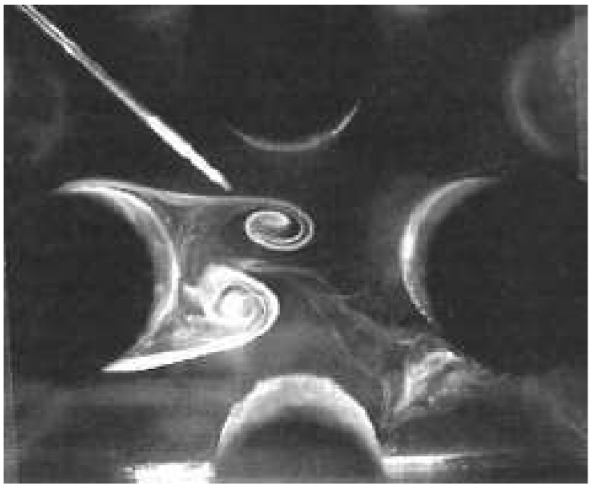

Figure 3 Downstream vortices of a cylinder (Weaver et al., 1993).

In reality, two-phase cross flows appear in more than half of the heat exchangers utilized in industry (Green and Hestroni, 1995; Noghrehkar et al., 1999). Consequently, the phenomenon is even more challenging since void fraction and two-phase flow regime affect the dynamic parameters of the tube. The two-phase character of the problem is therefore of primary interest. For bubbly flows, under 20% of void fraction, the response of the tube is similar to the one in single phase flow. By increasing the void fraction, the critical reduced velocity is increased according to Deri (2018). The higher the void fraction, the lower the VIV intensity. Between the bubbly and the intermittent flow, the regime transition is characterized by the decrease of the fluid-elastic departure (see green arrow in Figure.4). During the intermittent flow, between 30% and 70% of void fraction, the fluid-elastic slopes are low (see the response for $\alpha = 60\%$ in Figure.4), probably because of the mix of small and large gas structures. Then, for more than 70% of void fraction, the slope increases with void fraction (green arrow in Figure.4). Beyond 85%, the curve of the RMS depending on the velocity is unchanged. These phenomena are observed on different experiments with different mixtures and mass flow rates. Based on the influent parameters such as the array orientation for example, different authors tried to explain the reason why the vibration are highly different depending on the flow pattern.

In a heat exchanger, the dynamic response of a tube is characterized by its inertia, stiffness and damping. Illustrated in different experimental studies, these two-phase dynamic parameters (added mass and damping only) are different from single-phase flow ones which is consistent since damping and hydrodynamic mass in single phase flows depend on fluid properties.

Added mass is defined as the equivalent mass of external fluid vibrating with the structure (Pettigrew and Taylor, 1994). In two-phase flow across a tube, hydrodynamic mass decreases linearly with void fraction increment as seen in Figure 5 a). This is relevant since it would explain the increase of critical reduced velocity when void fraction increases.

Damping is responsible of the energy dissipation of the system. In two-phase flow, there is a strong dependency on void fraction as seen in Figure 5 b). For intermediate void fraction, consequently intermittent regime, the damping reaches a maximum. The relationship between local void fraction fluctuations and damping ratio makes sense, since there are large temporal fluctuations in the momentum

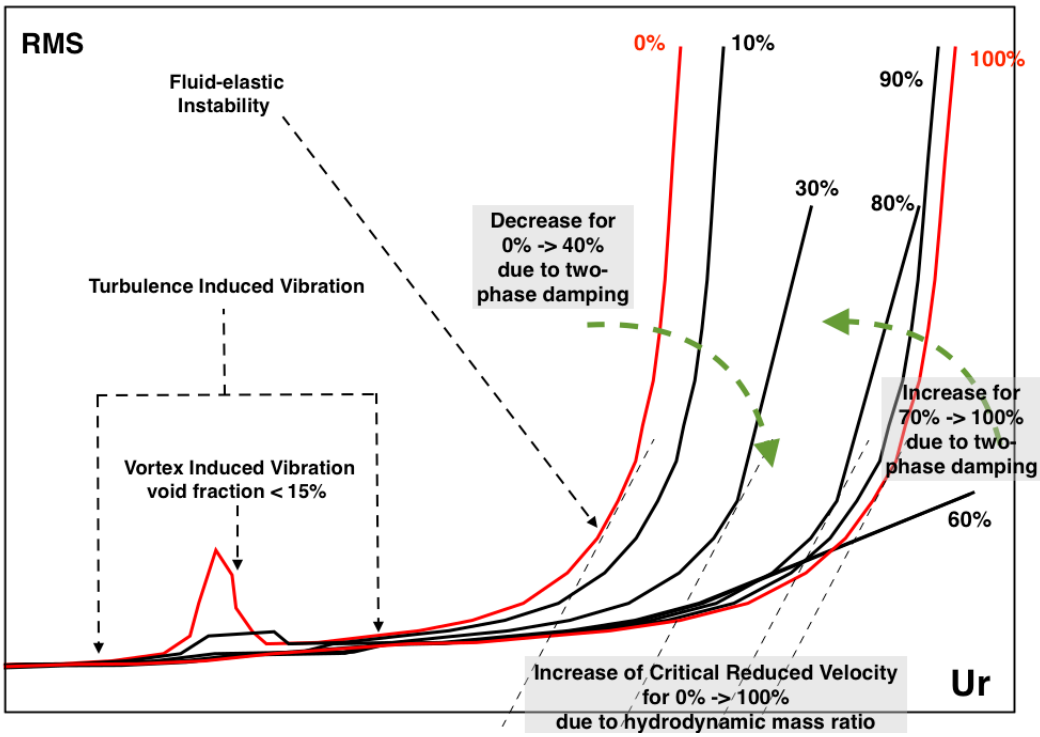

Figure 4 Void fraction influence on the structure response with increasing flow reduced-velocity.

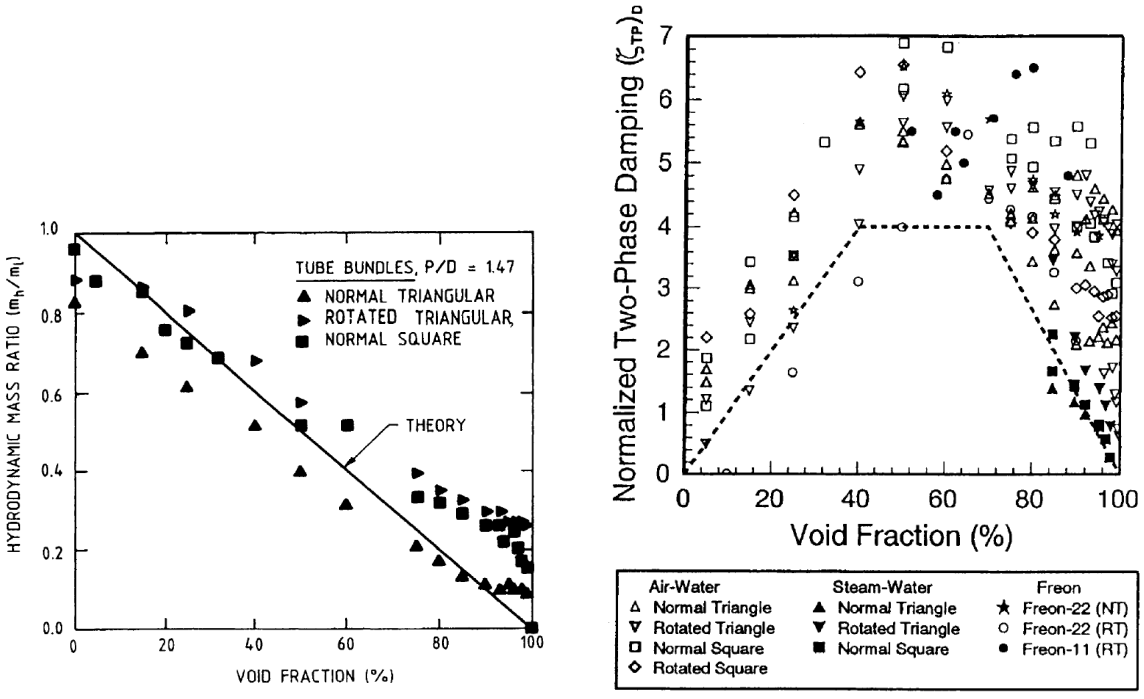

Figure 5 a) Comparison between the theoretical model of hydrodynamic mass (Rogers et al., 1984) with experimental data. The decrease of the hydrodynamic mass is responsible of the increase of the critical reduced velocity. b) Comparison between the theoretical model from Pettigrew (1995) and experiments for different mixtures and configurations. The variations of two-phase damping with void fraction are responsible for the variation of the slope of fluid-elastic departure.

whenever gas and liquid slugs alternatively impinge on the vibrating tube in intermittent flow. Damping is responsible for the variation of the fluid-elastic instability departure proposed in Figure 4.

Since a major knowledge has been shared from experiments, the numerical prediction of fluid-elastic instability has been investigated. It requires a fluid-structure interface tracking method to follow the motion, high resolution of the turbulence in order to predict correctly hydrodynamic forces at the wall and a robust coupling algorithm to avoid numerical issues. When the motion is computed based on fluid forces acting on the cylinder, the method is called "Direct Numerical Flow-Structure coupled CFD". Tubes are allowed to move freely according to the load at wall. Each tube is considered by a mass/damping/stiffness system. Using Large Eddy Simulation to correctly model turbulence and Arbitrary Lagrangian Eulerian method (described in other sections) to displace tubes, the direct approach might be time-consuming but representative of experiments. Pedro et al. (2016); Shinde et al. (2014) are examples that successfully utilized this approach in simulating flow in tube-bundles. An other method consists in imposing the displacement of a single tube, recording the fluid forces on this tube and the surroundings to predict the instability based on theoretical models (Hassan et al., 2010; Bouzidi et al., 2014). A major knowledge has been shared for years on vibrations induced by single-phase flows. Influent parameters have been studied in details. Nowadays, the objective of the present work is to address vibrations induced by two-phase flows.

Two-phase flow induced vibration phenomenon is more complex. Reduced-scale experiments were performed to characterize the flow patterns and the vibrations. Most of the time, modeling mixtures are used since an experiment with steam and water is expensive. However, an effort is made to use fluids having similar fluid properties. In contrast to single-phase flow, this phenomenon has not really been investigated with numerical simulation. Only few studies based on strong assumptions (using 2D simulation, with fixed bubble diameter, with a RANS turbulence model) were performed (Sadek et al., 2018). By imposing motion, results are in correct agreement with the experiment, however to predict the motion results are not accurate between 10% and 90% of void fraction, consequently in two-phase flow. Since the maturity of two-phase flow numerical simulation allows to perform multi-regime flows, it is now time to deal with two-phase flows in order to complete and enforce the knowledge coming from experiments.

Organization of the present manuscript

Simulating gas-liquid flows involving a wide range of spatial and temporal scales and multiple topological changes remains a major challenge nowadays. Computational cost associated with direct numerical simulation still being unaffordable, the two-fluid Euler-Euler approach is a proper way to compute such kind of flow. The present work is dedicated to the simulation of two-phase flow induced vibration with the code NEPTUNE_CFD detailed in appendix A. Organized in four parts presented below, the manuscript begins by describing the required developments to perform fluid structure interaction in the code before going through two-phase flow across tube bundle and the prediction of the fluid-elastic instability threshold on the VISCACHE experiment.

1. **Time and Space Dependent Porosity method:** the numerical simulation of interactions between immersed structures and two-phase flows requires an accurate fluid-structure interface tracking method. In the present work, a discrete forcing method based on a porous medium approach is

proposed to follow non-deformable rigid body with an imposed velocity by using a finite-volume Navier-Stokes solver dedicated to multi-phase flows and based on a two-fluid approach. To deal with the action reaction principle at the solid wall interfaces in a conservative way, a porosity is introduced allowing to locate the solid and insuring no diffusion of the fluid-structure interface. The volumetric fraction equilibrium is adapted to this novelty. Mass and momentum balance equations are formulated on a fixed cartesian grid. Interface tracking is addressed in detail going from the definition of the porosity to the changes in the discretization of the momentum balance equation. This so-called Time and Space Dependent Porosity (TSDP) method is then validated by using analytical and elementary test cases. Finally, a feasibility study is performed to predict the flow patterns in a centrifugal pump.

2. **Fluid Structure Interaction with the Time and Space Dependent Porosity method** The fluid-structure coupling is a tough numerical challenge. Depending on the chosen scheme, the prediction of displacement differs since accuracy might require computational time. Even if it is more time-consuming, an iterative algorithm is chosen and detailed. The force computation with the Time and Space Dependent Porosity is detailed since no body-fitted mesh is used. In order to predict the displacement after each iteration, a Newmark algorithm is implemented. The validation of the present fluid-structure coupling is performed on three cases: a cylinder release in a fluid at rest, a single-phase cross-flow around a free-cylinder at $Re = 100$, and the free-fall of a sphere on a free surface. Finally, the method is applied on an industrial application: the hydraulic dashpot.

3. **Numerical investigation on two-phase cross-flow** Two-phase flow across tube bundle knowledge comes from experimental and theoretical feedbacks only. In the present section, a fine study is carried out to enhance this knowledge since simulations give access to many informations. First, the numerical models are evaluated to determine the most competitive one. The influence of different numerical and physical parameters is checked. Based on two different mixtures, two-phase flows across tube bundles are numerically explored. Then, in order to have access to fine information, two-phase flow across a single cylinder and the impact of a single bubble on a cylinder are computed. Finally, using the results from each numerical investigation, depending on the mixture physical properties, two-phase cross-flow are described and possible perspectives are given.

4. **Industrial application: Simulating vibration induced by two-phase flow in a tube bundle** The numerical experiment of changing mixture is performed in order to quantify the error when freon/water is used instead of steam/water. Being able to follow an immersed structure motion induced by a two-phase flow and having determine the required numerical model to use in previous sections, the direct numerical prediction of vibration induced by two-phase flow in an in-line tube bundle is performed. A description of the simulated experiment is realized and numerically studied for rigid cylinder and then for free-cylinders.

Conclusions and outlooks are discussed at the end of the document.

Chapter 1

Interface tracking method dedicated to moving bodies in two-phase flow

1.1 Interface tracking method dedicated to fluid-structure interaction

To follow numerically the motion of a structure on a mesh, it is necessary to have a dedicated method. Different kinds of fluid-structure interface tracking methods are found in the literature such as Arbitrary Lagrangian Eulerian, Chimera, Immersed Boundary and others. In order to highlight the discrepancies between each one, some are presented in the present section.

Depending on the geometry, amplitude of motion or the required accuracy, one interface tracking method may appear more appropriated than an other. Two kinds of interface-tracking method are distinguished:

- Adaptative grid method (deformation or motion) where the grid is updated along time depending on the motion. It might be adapted to the motion like the (Arbitrary Lagrangian Eulerian (Noh, 1964)), or the mesh dedicated to the solid is moved like in the Chimera (Benek et al., 1983).
- Fixed grid method where the grid is not used to follow the motion. Two ways are consequently possible: having moving boundaries on a body-fitted mesh (Lighthill, 1958), or have a dedicated function to follow the solid: Immersed Boundary Method (Peskin, 1972; Mittal and Iaccarino, 2005).

1.1.1 Popular interface tracking methods with adaptative grid

A) Arbitrary Lagrangian Eulerian

The Arbitrary Lagrangian Eulerian formalism defines structures and near-wall fluid areas with Lagrangian coordinates, fluid with Eulerian coordinates, and between this two areas with arbitrary coordinates. Here, the grid is body fitted depending on the geometry of the structure. Based on the solid velocity, the grid is deformed or distorted to follow its motion. Consequently, the grid velocity is

dependent from the solid velocity and introduced in fluid dynamic equations. However, far from the structure, in the Eulerian coordinate area, the grid velocity is null; only the near-structure zone is distorted. In the arbitrary area (between Eulerian and Lagrangian areas), an arbitrary velocity is given in order to fit the grid displacements.

Introduced by Noh (1964), the method is fully described in Donea et al. (2004) and different applications are highlighted. In the Arbitrary Lagrangian Eulerian method, computational mesh inside the domains can move arbitrarily to optimize the shapes of elements or to follow the motion of a rigid structure.

The grid update is the key point in this method given that it is required for each time step. Consequently, it has to be :

- robust and accurate in order to prevent from having large modification of the mesh topology;
- low time-consuming as it is called at each time step.

Unfortunately, there is no algorithm satisfying fully both conditions. In fact, this method is dedicated to slight vibration such as cylinder vibrations in tube bundles since the grid distortion is not important. For example, it is impossible to follow a rotating propeller with an ALE interface tracking method.

However, for flow induced vibration, especially for cylinder or tube bundle, the method has been popular for many years.

B) Chimera/Overset grid

Grid generation is often the limiting factor for industrial simulations. To overcome this problem, some solutions are proposed like the Immersed Boundary Method (IBM) or Chimera method. The last one, chimera method (or also called overset grid method) appears increasingly used for complex research applications and more and more for huge industrial applications.

Initiated by Benek et al. (1983), the principle is to decompose the complex full domain into simple subdomains independently meshed by curvilinear grids. The only constraint is a superposition of grids to allow the link of the flow description. A first step of the process is to detect overlapped cells and to determine if it is an interpolated cell (it means that its flow data are coming from an other grid), a calculated cell (it means that flow data are coming from its own grid), or a cell with no interest for the flow (not interpolated nor calculated). Donor cells and the associated weights that compose the interpolation are evaluated for each valid overlapped cell in order to compute interpolation values. Consequently, two grids that are allowed to communicate by their cells are overlapped. There is no limitation in the number of grids.

Beyond simplifying the mesh generation, this technique offers a powerful solution to deal with moving bodies given. Moreover, a complex geometry is meshed thanks to an assembly of simple grids. This is illustrated in the study of English et al. (2013).

Figures 1.1 demonstrates the efficiency of this method for a complex problem. However, its implementation in an existing code is time-consuming and difficult: interpolations, overlapped cell detection, many grids... In the present work, as the geometry may be consider simple (tube bundles), this method appears to not be the most adapted.

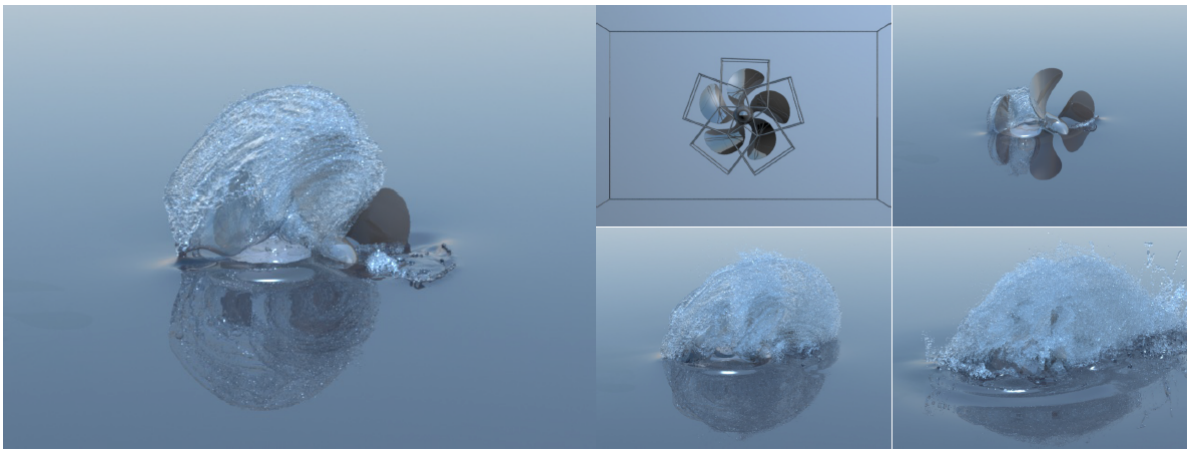

Figure 1.1 A kinematically driven propeller spins with a number of attached Chimera grids. The grids move and rotate with the rigid body frame of the propeller. (English et al., 2013)

1.1.2 Immersed Boundary Methods

The term immersed boundary methods is a class of methods devoted to describe accurately moving immersed bodies (such as two-phase flow, or fluid-structure interaction) in a fixed Cartesian grid. Immersed Boundary Method (IBM) consists in representing fluid in an Eulerian framework and solid in a Lagrangian one on a unique mesh. This procedure is less time-consuming and eliminates issues from re-meshing or deforming-mesh, such as the mesh distortions and the mesh interpolation errors in the body-fitted mesh methods (ALE for example). Two categories are identified :

- **Continuous forcing**: operator discretization is unchanged, however a source term is added in the momentum balance equation in order to take into account the immersed boundary. Penalty method and Peskin approach are continuous forcing methods.
- **Discrete-forcing**: operator discretization is different close to the fluid-structure interface in order to take into account the boundary. Cut-cell and Ghost-cell are discrete-forcing methods.

A) Continuous forcing methods

Peskin approach This kind of method was first introduced by Peskin (1972) for the simulation of blood flow in human heart. At the beginning, the method was only dedicated to flexible boundaries in motion. By adding a source term in the momentum equation, the boundaries of the immersed body are taken into account. One grid is dedicated to follow the structure with a Lagrangian framework and the other one for the fluid with an Eulerian framework. As the structure grid does not follow the Eulerian one, the interface force is imposed at the nodes.

Penalty methods Arquis and Caltagirone (1984); Caltagirone and Arquis (1986) introduced penalty methods dedicated to fluids mechanics. The concept is to consider a unique equation on the whole domain. A penalty source term, describing the constraint from a subdomain, is added in the momentum balance equation. This term is then multiplied by a penalty parameter dependent on the concerned subdomain. This parameter is here a kind of local permeability: a value of 0 meaning that the subdomain

is the solid, a value of 1 the fluid. For solid in displacement, it serves to impose the solid velocity in its subdomain. Different studies improves the order of the method in the recent years by interpolation of the velocity at the interface from the nodes (Carbou and Fabrie, 2003; Sarthou, 2009).

B) Discrete-forcing methods

The concept of these methods, in mirror of continuous forcing ones, is to keep unchanged the conservation laws at the wall by modifying the operator discretizations in order to have the right condition at the fluid-structure interface. These methods are robust and used for different situations from bubbly flow to fluid-structure interaction. Bai et al. (2010) used Cartesian cut cell approach to simulate waves for example.

Cut-cell method (Clarke et al., 1986; Ye et al., 1999) This approach modifies the shape of the control volumes near the interface by cutting and merging them. Mass, convective, diffusive fluxes and gradients have to be computed on each face of these new cells. Figure 1.2 shows how to conform the immersed fluid-structure interface by cutting and merging the concerned cells.

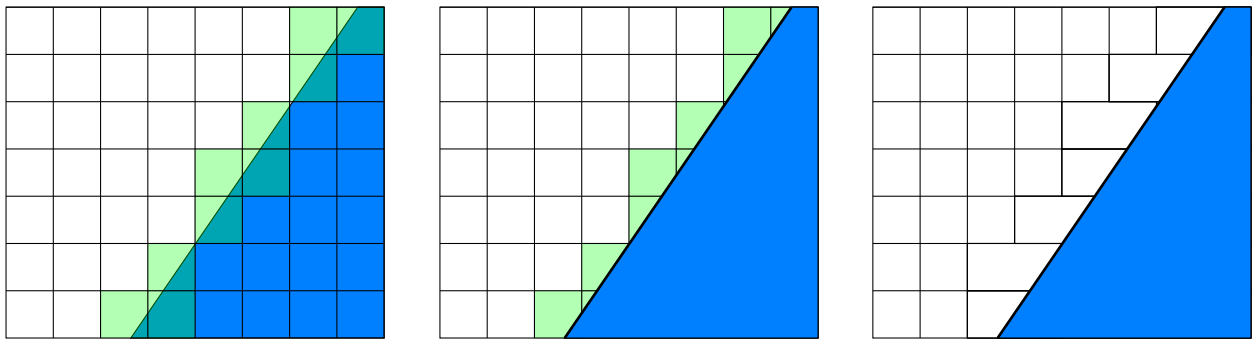

a) Interface-cell recognition *b) Cell cutting step* *c) Cell merging step*

Figure 1.2 Cut-cell approach, sketch of the different steps of the method. Moreover, each flux from faces concerned in the merging is re-defined.

Embedded Boundary Method Developed by Johansen and Colella (1998), this approach is similar to the cut-cell method since interface-cells are cut. However, the solution is still calculated at the center of the cell even if it is not in the fluid domain. Fluxes are like in the cut-cell method computed at corrected faces.

Ghost-cell Method Developed by Tseng and Ferziger (2003), this approach consists in the introduction of a force in the Navier-Stokes equation in order to impose the exact boundary condition at the fluid-structure interface. For each cell crossed by the interface, a ghost zone is introduced in the non-fluid area where the boundary condition has to be enforced. When the interface is on a node, the velocity at the node is the solid one. For the other situations, the velocity is extrapolated in each ghost-cell in order to get the accurate velocity at the interface.

The major disadvantage of this method is the numerical instability when the interface is close from a node. The extrapolation coefficients are consequently very large and may cause convergence trouble. Two solutions are proposed:

- displace locally the interface position to be accurately on the node,
- use the symmetric of the concerned node as the interpolation point.

This method is robust and used for different situations like bubbly flow or fluid-structure interaction.

In the following section, a Discrete Forcing method dedicated to moving bodies in two-phase flow is proposed. This is not the first time a work is dedicated to this kind of flow with a discrete-forcing method. For example, Hu et al. (2006) investigated breaking waves, he used the cut-cell method to reproduce the reef. However, most of the time these methods are implemented in multi-phase flow code based on a one-fluid approach. The novelty of the present work is to implement a discrete forcing method in a code based on a two-fluid approach and to adapt the volumetric fraction equilibrium and the momentum balance equation to it.

1.2 Time and Space Dependent Porosity method definition

The present developments are implemented within a finite-volume CFD code dedicated to multiphase flows and based on the two-fluid (extended to n) approach. Using a pressure correction approach (Ishii, 1975), it is able to simulate multiphase flows by solving a set of three balance equations for each field (2 in adiabatic cases):

$$\begin{aligned} \frac{\partial(\alpha_k\rho_k)}{\partial t} + \underline{\nabla}\cdot(\alpha_k\rho_k\underline{U}_k) &= 0 \\ \frac{\partial(\alpha_k\rho_k\underline{U}_k)}{\partial t} + \underline{\nabla}\cdot(\alpha_k\rho_k\underline{U}_k\underline{U}_k) &= -\alpha_k\underline{\nabla}P + \alpha_k\rho_k\underline{g} + \underline{\nabla}\cdot\overline{\overline{\tau}}_k + \sum_{p=1}^{N}\sum_{p\neq k}\underline{M}_{p\to k} \end{aligned} \tag{1.1}$$

where α, ρ, $\underline{U}$, P, τ, $\underline{g}$ and $\underline{M}$ are respectively the volume fraction, the density, the velocity, the pressure, the Reynolds-stress tensor, the gravity and the momentum transfer to the phase k. The k-phase volumetric fraction is written α_k. In multiphase flow, one property of the k-phase volumetric fractions is:

$$\sum_{k=1}^{N}\alpha_k = 1 \tag{1.2}$$

with N the number of fluid phases included into the fluid domain.

The aim of discrete forcing methods is to strictly ensure the conservation laws at the close vicinity of the interface. The idea is to reshape the cells crossed by the interface and to build specific schemes inside them. The interface is approximated as a plane in each cut-cell. The domain contains the structure, which is considered as a real part of the calculation domain. A tag function is therefore required to determine the solid location on the cells. The main advantage of these methods lies in the non-explicit

representation of the structure, meaning that it is possible to perform calculations on complex geometries using Cartesian grids. The major challenge of these methods is to reconstruct the interface properties.

In order to locate the solid, cells are identified as a solid, fluid, or interface cells. In the present method, the whole domain is considered in the framework of a porous media approach where a time and space dependent fraction called porosity is 0 in the solid, and 1 in the fluid. The fluid-structure interface is consequently represented with a porosity between 0 and 1. Here, the porosity is as follows:

$$\varepsilon(\underline{x},t) = 1 - \alpha_s(\underline{x},t) \tag{1.3}$$

with α_s the volumetric fraction of the solid phase, and $\varepsilon(\underline{x},t)$ the porosity (in $\underline{x}$ at time t) being between $[0,1]$. Therefore, the previous relation (1.2) describing the volumetric fraction balance becomes:

$$\sum_k \alpha_k(\underline{x},t) = \varepsilon(\underline{x},t) \tag{1.4}$$

This method involves a non-moving Cartesian grid where the body is meshed and defined with a porosity equal to 0 insuring no mass transfer between solid and fluids. In a finite-volume framework, the porosity is computed for a cell I by using the following relation:

$$\varepsilon_I = \frac{\text{fluid volume of the cell } I}{\text{total volume of the cell } I}. \tag{1.5}$$

Here, the solid motion is tracked thanks to the porosity evolution in a Lagrangian framework. To take into account the solid motion and the presence of an interface in cut-cells, the porosity has to be convected and the momentum balance equations are formulated differently.

1.2.1 Porous mass balance equation and media definition

The time and space dependent porosity definition is the key element in the method. The total volume of the solid domain should be constant whether the object is moving or not. Acting like volumetric fraction, a porosity is computed for each cell and for each face of the domain in order to convect the structure.

A) Cell-porosity computation

Three kinds of cells are possible and defined thanks to the porosity:

1. if the cell is solid, porosity value is 0 ;
2. if the cell is fluid, porosity value is 1 ;
3. in other cases, the cell contains an interface.

At each time step, the porosity is computed by using a Volume of Fluid Initialization (VOFI) method (Bnà et al., 2015b,a) as follows. An implicit function f is introduced. This function is defined as follows : $f(x,y,z) = 0$ with x, y,and z defining a point located on the interface between the fluid domain and the

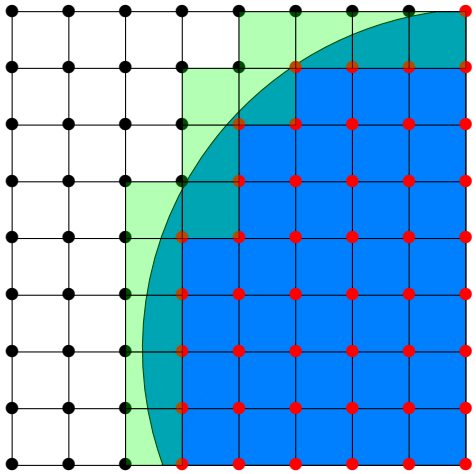

Figure 1.3 Cell-porosity computation: nodes in the solid domain are in red, others in black. In a cell, if each node is solid (blue), it is a solid-cell; if each node is not solid (white), it is a fluid-cell; otherwise it is a a cut-cell (green).

solid domain. Then, this function is used in order to evaluate in each cell the porosity. Examples of cells with porosity of 0, 1 and intermediate values are displayed on Figure 1.3.

B) Geometric face-porosity determination

If a face is cut by the fluid-structure interface, the two Cartesian neighboring cells sharing this face are required to compute geometrically the face porosity. Based on the node coordinates and the porosity of each cell, it is determined geometrically by assuming the interface to be locally straight (linear function) instead of curved. Several configurations are possible and illustrated in two dimensions in Figure 1.4 for $\varepsilon_I > \varepsilon_J$.

The interface is defined by: $y = Ax + B$ where A and B are two real coefficients. In each cell, the blue surface is computed based on node coordinates, A, B. Consequently, for a given case :

$$\begin{cases} S_I = 1 - \alpha_I = s_1(A,B,x) \\ S_J = 1 - \alpha_J = s_2(A,B,x) \end{cases} \tag{1.6}$$

where S_I and S_J designate respectively the blue areas of both cells, s_1 and s_2 are two functions computing the area based on A, B and x. The computation of this system leads to an evaluation of A and B, and then ε_{IJ}. For example, node coordinates are given in Figure.1.4 for case (A). Based on them, the blue surface is computed in each cell such as:

$$\begin{cases} S_I = 1 - \alpha_I = BL + AL^2/2 \\ S_J = 1 - \alpha_J = (AL + B)L + AL^2/2 \end{cases} \tag{1.7}$$

Then, by solving the present system, A and B are computed. Finally, $\varepsilon_{IJ} = 1 - (AL + B)$. For three-dimensional cases, the mesh is assumed enough refined to use exactly the same method.

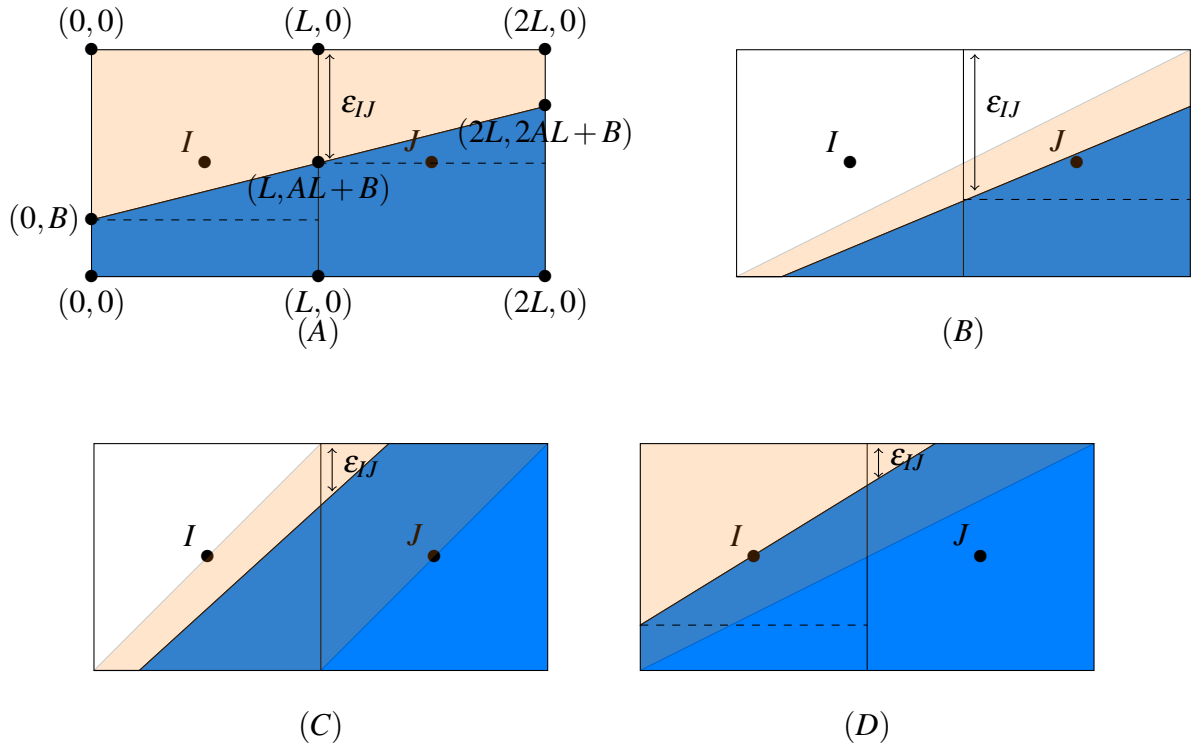

Figure 1.4 Fluid-structure interface crossing a face in a two-dimensional configuration. Each cell area is calculated by using triangle and rectangle areas when it is required.

C) Convected porosity computation

As described in (1.4): the porosity has to be treated like k-phase volumetric fractions, hence convecting the porosity is necessary. There are no mass transfer between a solid and other phases, therefore:

$$\frac{\partial \varepsilon}{\partial t} + \nabla \cdot (\varepsilon \underline{U_s}) = 0 \tag{1.8}$$

with $\varepsilon = \sum_k \alpha_k$. In a finite-volume framework, the discretization at each time step is given by:

$$\frac{\varepsilon_I^{n+1} - \varepsilon_I^n}{\Delta t} \Omega_I + \sum_{J \in N_I} \varepsilon_{IJ}^n \phi_{IJ} = 0 \tag{1.9}$$

with $\phi_{IJ} = \underline{U_s} \cdot \underline{n_{IJ}}$, where $\underline{n_{IJ}}$ is the face unit normal vector between cells I and J, and N_I neighboring cells around I. For multiple solids, the domain is decomposed in subdomains depending on the position of each structure in order to differentiate their own velocities like in Figure 1.5. In order to allow the independent motion of different structures with several velocities, the solid volumetric phase fraction $\alpha_s = 1 - \varepsilon$ is convected since it is null outside each structure. The convection equation becomes:

$$\frac{{\alpha_s}_I^{n+1} - {\alpha_s}_I^n}{\Delta t} \Omega_I + \sum_{J \in N_I} ({\alpha_s}_{IJ}^n - 1) \phi_{IJ} = 0. \tag{1.10}$$

Outside structures, one gets $\sum_{J\in N_I}\phi_{IJ}=0$. Given that α_s is also null outside solid sub-domains, the convection equation is thus formulated in an equivalent way in order to keep the minimum and the maximum principles true:

$$\frac{\alpha_{s_I}^{n+1}-\alpha_{s_I}^{n}}{\Delta t}\Omega_I+\sum_{J\in N_I}(\alpha_{s_{IJ}}^{n}-\alpha_{s_I}^{n})\phi_{IJ}=0. \tag{1.11}$$

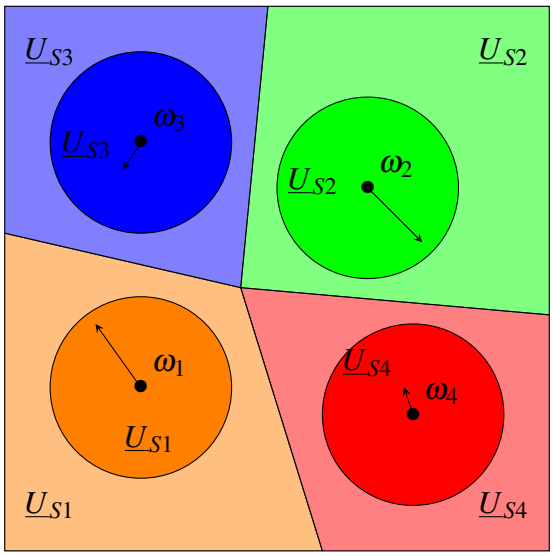

Figure 1.5 Decomposition of the domain according to the position of each cylinder. In each subdomain, the solid velocity is taken equal to the corresponding solid.

To minimize the numerical diffusion and keep positivity and maximum principles for porosity, a θ-scheme is used to define the face porosity fraction, and each time step is subdivided into sub-time step to approximate accurately the face porosity. An example of 2D configuration is given in Figure 3.34. Using a θ-scheme, the porosity is expressed in terms of the current face function α_{sGEOM} and a decentered value $\alpha_{sUPWIND}$ as follows :

$$\alpha_{sIJ}=\theta_{IJ}\alpha_{s_{IJ}}^{GEOM}+(1-\theta_{IJ})\alpha_{s_{IJ}}^{UPWIND} \tag{1.12}$$

with $\theta_{IJ}\in[0,1]$. Using an upwind decentered scheme yields : $\alpha_{s_{IJ}}^{UPWIND}=\alpha_{sI}$ for $\phi_{IJ}>0$ and $\alpha_{s_{IJ}}^{UPWIND}=\alpha_{sJ}$ for $\phi_{IJ}<0$. $\alpha_{s_{IJ}}^{UPWIND}\in[0,1]$. As far as possible, θ_{IJ} is close to 1 in order to preserve the highest geometric contribution. The UPWIND and geometric face porosity computation are satisfied thanks to a Courant condition on the time step. Introducing the time step subdivision, let i be an integer $i\in[0,i_{max}]$ and β the solid fraction during a sub-iteration such that $\beta_I^0=\alpha_{s_I}^n$ and $\beta_I^{i_{max}}=\alpha_{s_I}^{n+1}$. The sub-cycling time step becomes: $dt=\dfrac{\Delta t}{i_{max}}$. Therefore, the θ-scheme is used to define β_{IJ}^i and leads to the $\alpha_{s_{IJ}}^n$ thanks to the relation:

$$\alpha_{s_{IJ}}^{n}=\frac{\sum_{i\in[0,i_{max}]}\beta_{IJ}^{i}}{i_{max}}. \tag{1.13}$$

This relation is used to solve iteratively the mass balance equation (1.11). The derivation of the iterative θ-scheme is presented below. For a cell I, lets assume $0\leq\beta_I^i\leq 1$ and derive $0\leq\beta_I^{i+1}\leq 1$:

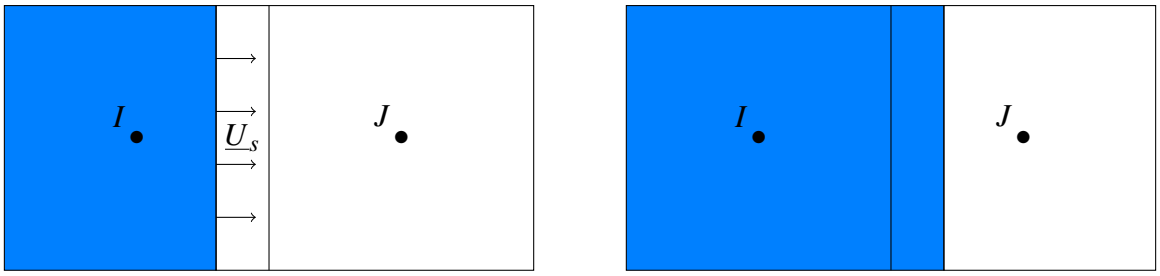

Figure 1.6 Fluid-structure interface crossing a cell face. Sub-cycles are required in this case to approximate step by step the value of the face-porosity.

1. **Positivity**

$$\frac{\beta_I^{i+1}-\beta_I^i}{dt}\Omega_I+\sum_{J\in N_I}(\beta_{IJ}^i-\beta_I^i)\phi_{IJ}=0$$

It is possible to formulate the expression by highlighting decentered terms according to the flux sign:

$$\frac{\beta_I^{i+1}-\beta_I^i}{dt}\Omega_I+\sum_{J\in N_I,\phi_{IJ}\geq 0}(\theta_{IJ}\beta_{IJ}^{i,GEOM}+(1-\theta_{IJ})\beta_I^i-\beta_I^i)\phi_{IJ})$$

$$+\sum_{J\in N_I,\phi_{IJ}<0}(\theta_{IJ}\beta_{IJ}^{i,GEOM}+(1-\theta_{IJ})\beta_J^i-\beta_I^i)\phi_{IJ})=0$$

One defines $A=-\sum_{J\in N_I,\phi_{IJ}<0}(\theta_{IJ}\beta_{IJ}^{i,GEOM}+(1-\theta_{IJ})\beta_J^i)\phi_{IJ})$ which is positive.

$$\frac{\beta_I^{i+1}}{dt}\Omega_I=\frac{\beta_I^i}{dt}\Omega_I+A+\sum_{J\in N_I,\phi_{IJ}<0}\beta_I\phi_{IJ}-\sum_{J\in N_I,\phi_{IJ}\geq 0}\theta_{IJ}(\beta_{IJ}^{i,GEOM}-\beta_I^i)\phi_{IJ}$$

To ensure the positivity of β_I^{i+1}, the condition is:

$$\sum_{J\in N_I,\phi_{IJ}\geq 0}\theta_{IJ}(\beta_{IJ}^{i,GEOM}-\beta_I^i)\phi_{IJ}\leq\frac{\beta_I^i}{dt}\Omega_I+A+\sum_{J\in N_I,\phi_{IJ}<0}\beta_I\phi_{IJ} \tag{1.14}$$

2. **Maximum:** Let assume $\beta_I^{i+1}=1-\varepsilon_I^{i+1}$. To ensure the positivity of ε_I^{i+1} (consequently $\beta_I^{i+1}\leq 1$), the condition is similarly:

$$\sum_{J\in N_I,\phi_{IJ}\geq 0}\theta_{IJ}(\varepsilon_{IJ}^{i,GEOM}-\varepsilon_I^i)\phi_{IJ}\leq\frac{\varepsilon_I^i}{dt}\Omega_I+A+\sum_{J\in N_I,\phi_{IJ}<0}\varepsilon_I\phi_{IJ} \tag{1.15}$$

Therefore, θ_{IJ} has to ensure both conditions. θ_{IJ} is defined per cell (not per face) as a θ_I. Thus, the conditions become for a cell I:

$$\begin{cases} \theta_{I,1} \leq \dfrac{\frac{\beta_I^i}{dt}\Omega_I + A + \sum_{J\in N_I,\phi_{IJ}<0}\beta_I\phi_{IJ}}{\sum_{J\in N_I,\phi_{IJ}\geq 0}(\beta_{IJ}^{i,GEOM} - \beta_I^i)\phi_{IJ}} \\ \theta_{I,2} \leq \dfrac{\frac{\varepsilon_I^i}{dt}\Omega_I + A + \sum_{J\in N_I,\phi_{IJ}<0}\varepsilon_I\phi_{IJ}}{\sum_{J\in N_I,\phi_{IJ}\geq 0}(\varepsilon_{IJ}^{i,GEOM} - \varepsilon_I^i)\phi_{IJ}} \end{cases} \tag{1.16}$$

First, as the priority is the geometric part of β_{IJ}, θ_I has to be maximum:

$$\begin{cases} \theta_{I,1} = \dfrac{\frac{\beta_I^i}{dt}\Omega_I + A + \sum_{J\in N_I,\phi_{IJ}<0}\beta_I\phi_{IJ}}{\sum_{J\in N_I,\phi_{IJ}\geq 0}(\beta_{IJ}^{i,GEOM} - \beta_I^i)\phi_{IJ}} \\ \theta_{I,2} = \dfrac{\frac{\varepsilon_I^i}{dt}\Omega_I + A + \sum_{J\in N_I,\phi_{IJ}<0}\varepsilon_I\phi_{IJ}}{\sum_{J\in N_I,\phi_{IJ}\geq 0}(\varepsilon_{IJ}^{i,GEOM} - \varepsilon_I^i)\phi_{IJ}} \end{cases} \tag{1.17}$$

To satisfy both conditions with one value of θ_I, the minimum has to be taken between $\theta_{I,1}$ and $\theta_{I,2}$. As these conditions have to be true for all cell around, consequently the θ_I has to satisfy conditions from all cells around, therefore:

$$\theta_I = MIN(\theta_k, \theta_I) = MIN(\theta_k, MIN(\theta_{I,1}, \theta_{I,2})) \tag{1.18}$$

with $k \in N_I$. To determine A in each cell, its minimum is taken in order to not overestimate the maximum value of θ_I. Consequently:

$$A = \sum_{J\in N_I,\phi_{IJ}<0} MIN(\beta_{IJ}^{GEOM}, \beta_J)\phi_{IJ} \tag{1.19}$$

1.2.2 Momentum balance equation

A) Geometric parameter definitions

To express the presence of a fluid-structure interface in a cell, one requirement is to define structure geometric parameters: structure unit normal vector and interface center of gravity. The interface is consequently considered as a new face in each cell.

Figure 1.7 represents a crossed-cell in 2D, where G is the interface center of gravity, and $\underline{n_p}$ the structure unit normal vector. For a fully fluid cell, the following relation is satisfied:

$$\sum_{J\in N_I} \underline{n_{IJ}} = 0 \tag{1.20}$$

Consequently, for the interface cell presented in Figure 1.7, based on the different face porosities, the relation becomes:

$$\sum_{J\in N_I} \varepsilon_{IJ}\underline{n_{IJ}} + \underline{n_p} = 0 \tag{1.21}$$

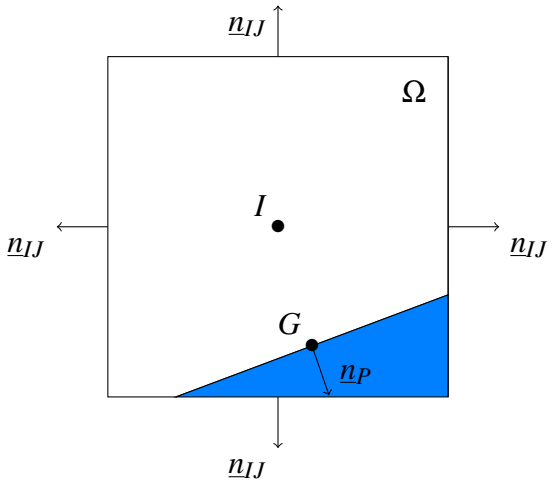

Figure 1.7 Cell crossed by the fluid-structure interface, geometric characteristics re-shaping.

Then, G is defined as the solid face center of gravity. According to the finite volume discretization, it can be expressed as :

$$\varepsilon_I \Omega = \sum_{J \in N_I} \varepsilon_{IJ} \underline{x}_{G_{IJ,k}} . \underline{n}_{IJ,k} + \underline{x}_{G_P,k} . \underline{n}_{P,k} \tag{1.22}$$

with x_G the face centers of gravity and $k = x,\ y$ or z. From (1.22), G coordinates are obtained.

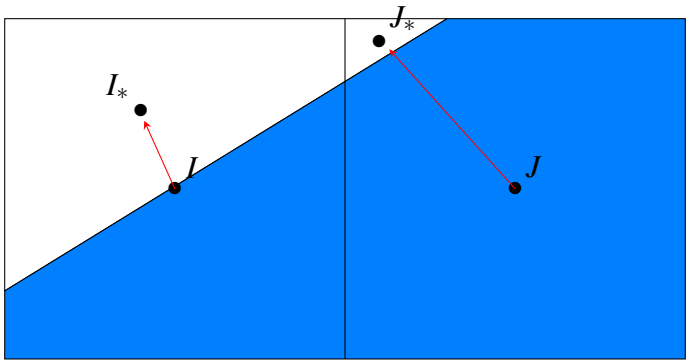

Figure 1.8 Sketch of the cell center displacements.

When the volume of the cell is reduced because of the structure, cell centers of gravity are recomputed depending on the solid face (like in cut-cell methods (Clarke et al., 1986; Ye et al., 1999)). For a fully solid cell, the velocity is $\underline{U_s}$. But, for a cut-cell, the velocity is the fluid one taking into account the presence of the solid and its motion. According to the diffusion theorem, the center of gravity of a fully fluid cell is written:

$$i_G = \frac{1}{\Omega} \sum_{J \in N_I} \frac{i_{IJ}^2}{2} S_{IJ,i} \tag{1.23}$$

with $i = x,\ y,\ z$. Therefore, for a cut-cell like in Figure 1.8, the porosity ε_I is taken into account:

$$i_G = \frac{1}{\varepsilon_I \Omega} \sum_{J \in N_I} \frac{i_{IJ}^2}{2} S_{IJ,i} \tag{1.24}$$

However, given that the face centers of gravity are not necessary in the fluid domain, an error is introduced. In order to avoid approximation, based on these new cells centers, face centers are determined as shown in Figure 1.9.

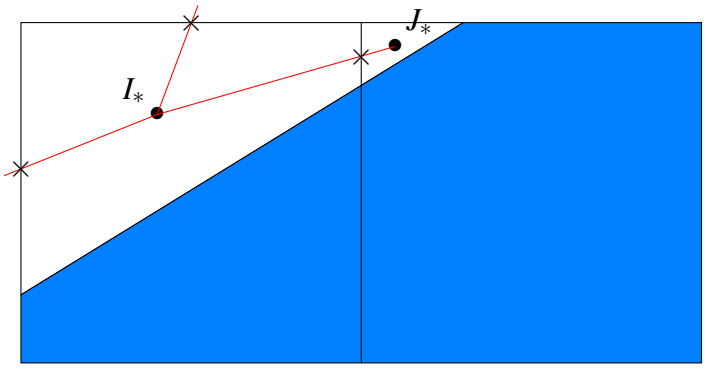

Figure 1.9 Sketch of the face center displacements.

Then, based on these displaced face centers, cell centers are re-computed with (1.24). Finally, these two steps are repeated until convergence. In Figure. 1.10, the convergence of the sub-cycles to determine the cell centers is shown. It is possible to highlight that a single prediction is not enough. Here, 10 sub-cycles are presented but only 5 are necessary.

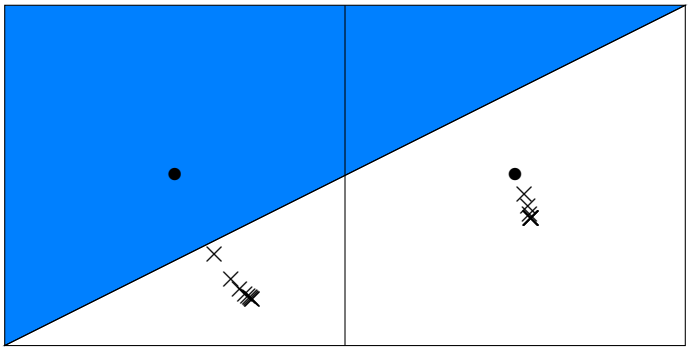

Figure 1.10 Iterative determination of the cell centers. Initial positions are represented with bullets.

B) Pressure field

A diffusion equation is solved inside the solid by taking into account the dual of a Dirichlet boundary condition as:

$$\nabla^2 P = 0 \text{ with } P = P_{fluid} \text{ at the fluid-structure interface.} \tag{1.25}$$

Initially, for a regular Cartesian grid, for two cells I and J, the pressure at the face joining them is given by:

$$P_{IJ} = \frac{1}{2}(P_I + P_J). \tag{1.26}$$

Based on displaced cell centers of gravity (Figure 1.7), the face pressure is computed with a geometric ponderation between P_I and P_J at the intersection between the face and IJ. Consequently, the approximation of pressure computed at the face is improved since it depends on the position of each cell center of

gravity around.

The pressure gradient reconstruction is required at the fluid-structure interface in order to not disturb the flow around the structure. Based on the displaced cell center of gravity computed previously, it is possible to write for an intersected cell I:

$$P_G = P_I + \underline{IG}.\underline{\nabla P_I}. \tag{1.27}$$

Using finite-volume method, the pressure gradient is written:

$$\int_{\Omega_I} \nabla P_I d\Omega = \sum_{J \in N_I} \varepsilon_{IJ} P_{IJ} \underline{n}_{IJ} + P_G \underline{n}_p. \tag{1.28}$$

As,

$$\sum_{J \in N_I} \varepsilon_{IJ} \underline{n}_{IJ} + \underline{n}_p = 0 \tag{1.29}$$

this yields to the implicit formula:

$$\underline{\nabla P_I} \varepsilon_I \Omega = \sum_{J \in N_I} \varepsilon_{IJ} (P_{IJ} - P_I) \underline{n}_{IJ} - \sum_{J \in V_I} \varepsilon_{IJ} (\underline{IG_P}.\underline{\nabla P_I}) \underline{n}_{IJ}. \tag{1.30}$$

Moreover, in order to reduce numerical approximation, a correction is applied to the pressure gradient. We called it "correction by the gradient of the linear" in such way that for a linear profile, the pressure gradient is correct. The pressure gradient coming from (1.30) is written $\underline{\nabla P_I^{(1)}}$. For a cell I, the correction is applied as followed:

$$\underline{\nabla P_I^{corr}} = \overline{\overline{M}}_{corr}^{-1}.\underline{\nabla P_I^{(1)}} \tag{1.31}$$

with $\overline{\overline{M}}_{corr} = \frac{1}{\varepsilon\Omega} \sum_{J \in N_I} \varepsilon_{IJ} x_{IJ} \underline{n}_{IJ} + x_p \underline{n}_p$.

C) Diffusive terms

According to the finite-volume discretization, for a cell I, the diffusion term without the wall contribution is written as:

$$\sum_{J \in N_I} \alpha_{IJ} \mu_{IJ} \frac{\underline{U_J} - \underline{U_I}}{IJ} \mid\mid \underline{n}_{IJ} \mid\mid . \tag{1.32}$$

with α_{IJ} the phase face volumetric fraction between I and J.

To take into account the additional face, the diffusion term in I is projected on the fluid-structure interface characterized by $\underline{n_P}$.

$$\alpha_I \mu_I \frac{\underline{U_P} - \underline{U_I}}{IP} \mid\mid \underline{n}_P \mid\mid . \tag{1.33}$$

Here, $\underline{U_P}$ is defined as the cell velocity projected on the wall, and according to the solid velocity with a non-slip condition:

$$\underline{U_P} = (\underline{U_{solid}}.\underline{n_P}).\underline{n_P} + \underline{U_I} - (\underline{U_I}.\underline{n_P}).\underline{n_P}. \tag{1.34}$$

Finally, the diffusion term for a cut-cell I is written as:

$$\sum_{J\in V_I} \alpha_{IJ}\mu_{IJ}\frac{\underline{U_J}-\underline{U_I}}{IJ} \mid\mid \underline{n_{IJ}} \mid\mid + \alpha_I\mu_I\frac{\underline{U_P}-\underline{U_I}}{IP} \mid\mid \underline{n_P} \mid\mid . \tag{1.35}$$

D) Gradient computation

Excluding pressure gradient, each gradient is computed like:

$$\underline{\nabla X_I^{(1)}}\varepsilon_I\Omega = \sum_{J\in N_I} \varepsilon_{IJ}X_{IJ}\underline{n_{IJ}} + X_p\underline{n_p} \tag{1.36}$$

with X a given variable. Then, the gradient is corrected by the gradient of the linear.

$$\underline{\nabla X_I^{corr}} = \overline{\overline{M}}_{corr}^{-1}.\underline{\nabla X_I^{(1)}} \tag{1.37}$$

with $\overline{\overline{M}}_{corr} = \frac{1}{\varepsilon\Omega}\sum_{J\in N_I} \varepsilon_{IJ}x_{IJ}\underline{n_{IJ}} + x_p\underline{n_p}$.

1.3 Robustness of the method

In order to evaluate the previously-mentioned Time and Space Dependent Porosity method, it is necessary to validate it. Some of the configurations used to assess its consistency are given below.

1.3.1 Test cases with stationary solids

A) Single-phase flow in an inclined channel

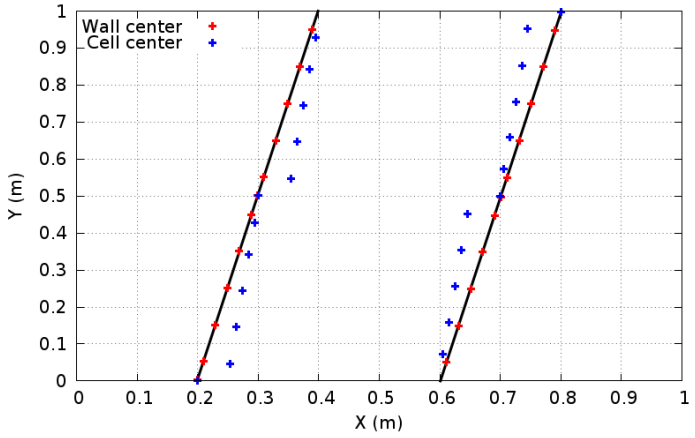

Figure 1.11 Geometric points representation for an inclined channel.

The configuration involves a square domain representing a channel conveying a single-phase flow. In the context of the TSDP method, the channel walls are described by the porosity. The flow enters into the channel with a given inclination. Several inclinations are tested. This elementary configuration is chosen because an analytical formulation of the solution is available for comparison with numerical results. The square dimensions are 1mx1m. Several two-dimensional grid refinements are considered.

First, with a 10x10x1 mesh, the center of gravity from the solid faces and the new cell centers of gravity are computed for an inclined channel in Figure 1.11. The grid is represented in black dash and the walls in black. Their computation has been validated for different cases such as a cylinder for example. Then, several channel inclinations are computed to check the validity of the proposed novelties defined previously and the interface reconstruction for a Poiseuille flow with wall crossing cells (geometric parameters are fully used). Thanks to the different stated changes, results are in agreement with analytical solutions for different inclinations. The L^2 relative error is computed for pressure, and velocity. Based

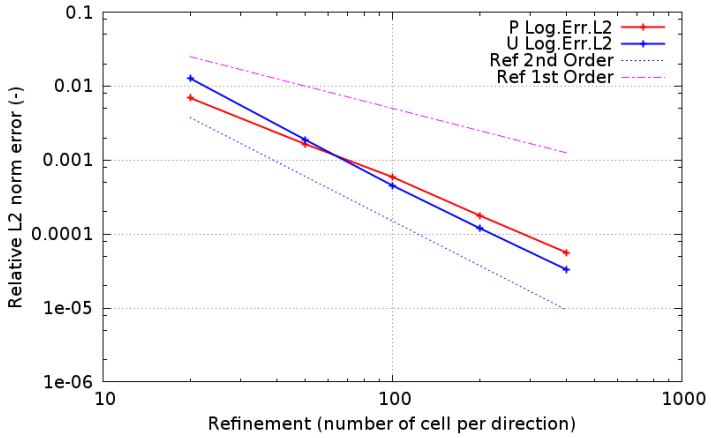

Figure 1.12 Poiseuille flow: L^2 relative error and order conservation graphics.

on five mesh refinements, it attests the order conservation despite the time and space porosity method implementation: 1.60 for pressure and 1.95 for velocity.

B) Taylor-Green vortices around an immersed body

The configuration involves a square domain containing Taylor-Green vortices with an immersed square solid in the center where a slip condition is ensured at its walls. Therefore as shown in Figure 9 the vortices are not disturbed in this area. Domain borders have periodic conditions. The theoretical flow is characterized by flow velocity components u_x and u_y in both space directions x and y of the form :

$$\begin{cases} u_x(x,y,t) = -cos(\pi x)sin(\pi y)e^{-2\pi^2\mu t} \\ u_y(x,y,t) = sin(\pi x)cos(\pi y)e^{-2\pi^2\mu t} \end{cases} \tag{1.38}$$

The single-phase fluid flow is assumed to be incompressible. 5 grid refinements are considered in this case. The fluid-structure interface does not cross any cells, consequently porosity in the domain is 1 or 0. This choice reduces the approximation done when the structure has an angle in one cell. This case highlights the correct reconstruction of a wall with slip condition, and the correct implementation of the method which does not affect the order conservation. In Figure 1.13, the L^2 relative error for velocity is plotted depending on the grid refinement. It is possible to see that the coarse mesh is too coarse to follow the vortices (only 3 cells per vortex). Then, for the others, depending on the chosen algorithm, the order conservation is ensured.

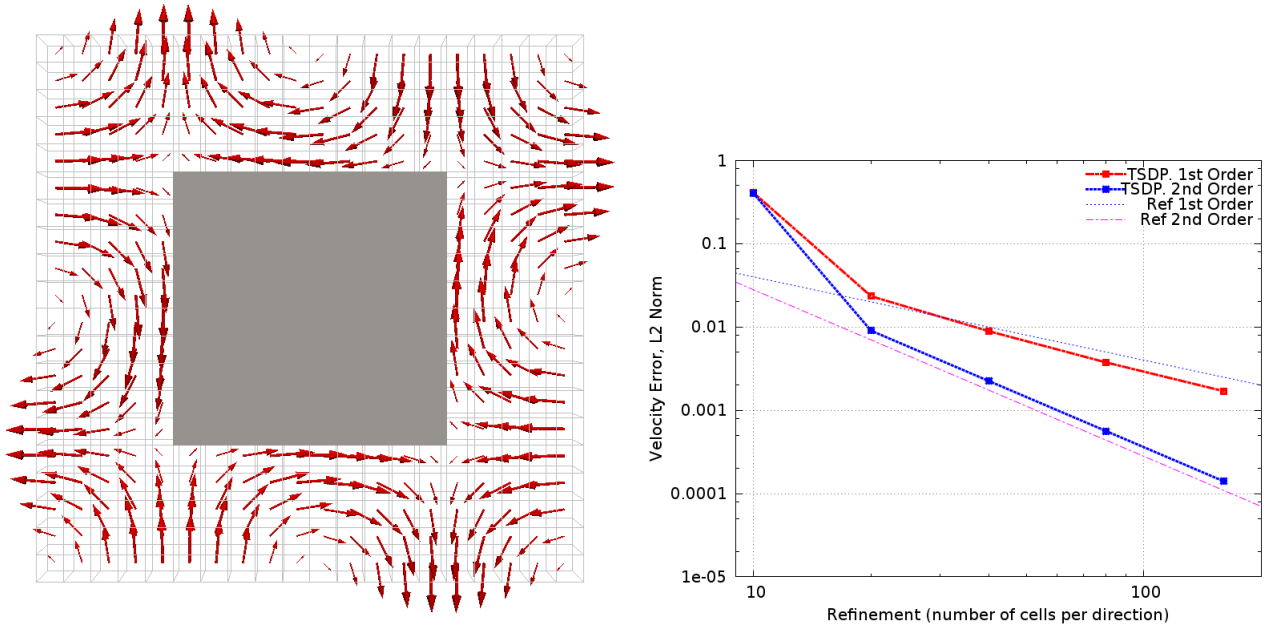

Figure 1.13 Sketch (left) of the Taylor-Green vortices around an immersed square solid with slip walls and numerical results for 5 grid refinements (right).

C) Laminar wake of a cylinder, $Re = 40$

A non-moving cylinder is considered immersed in a flow with a Reynolds number of 40. In this case, the flow at the wake of the cylinder is stable and creates two symmetric recirculation zones as displayed in Figure 1.14.

A cylinder having a diameter $D = 1\ m$ and a center $(4, 7.5)$ is immersed in a domain $[0, 15m][0, 15m]$ discretized such as $\Delta x = \Delta y = 0.05\ m$. The inlet velocity of the fluid is $1\ m/s$. The Reynolds number is 40.

The force acting on the cylinder is computed with cells having a porosity between 0 and 1 (cut cells) by using the pressure and velocity gradient at wall :

$$\mathbf{F} = \oint \mathbf{n}(-P\bar{\bar{I}} + \mu(\overline{\overline{\nabla \mathbf{U}}} + \overline{\overline{\nabla^T \mathbf{U}}}))dS \tag{1.39}$$

Then, the drag and lift coefficients are defined by:

$$C_D = \frac{F_x}{\frac{1}{2}\rho U_0^2 D} \qquad C_L = \frac{F_y}{\frac{1}{2}\rho U_0^2 D} \tag{1.40}$$

In Table 3.1, the present method is in agreement with different other referenced works for each characteristics variables. The correct wall reconstruction is therefore assessed.

1.3.2 Test cases with moving solids

A) One dimensional moving body

The case of an incompressible flow and a solid animated by a constant acceleration in a one dimensional channel of length $10m$ using 4 grid refinements is considered. In the fluid, the momentum balance

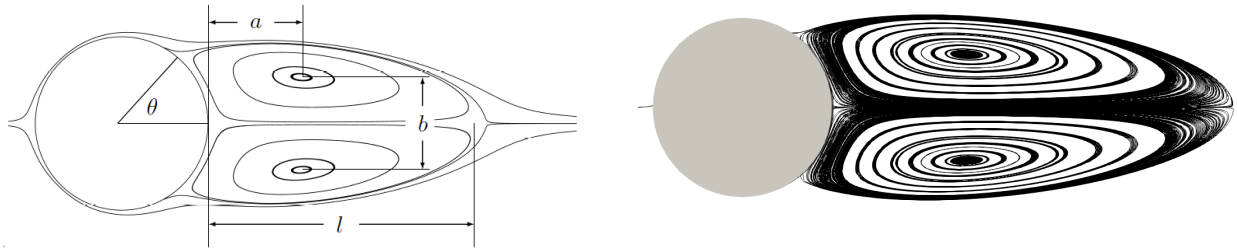

Figure 1.14 Definition of the characteristic wake dimensions for the steady flow over a stationary circular cylinder (left) and numerical streamlines for $Re = 40$.

	l/D	a/D	b/D	θ	C_D
Re = 40					
Tritton (1959) *	-	-	-	-	1.59
Coutanceau and Brouard (1977)*	2.13	0.76	0.59	53.8	-
Taira and Colonius (2007)	2.30	0.73	0.60	53.7	1.54
Wang and Zhang (2011)	2.36	0.72	0.6	53.8	1.54
Present study	2.25	0.746	0.597	53.7	1.56

Table 1.1 Comparison between experimental results (with an "*"), other simulations and the present study for a cylinder at $Re = 40$.

equation gives $\frac{\partial u}{\partial t} = -\nabla p$, consequently this case allows to assess the validity of the pressure gradient computation when cell are recovered or discovered by the solid, since it is given by the solid acceleration. Moreover, it demonstrates the capacity of the θ-scheme to provide the correct face porosity.

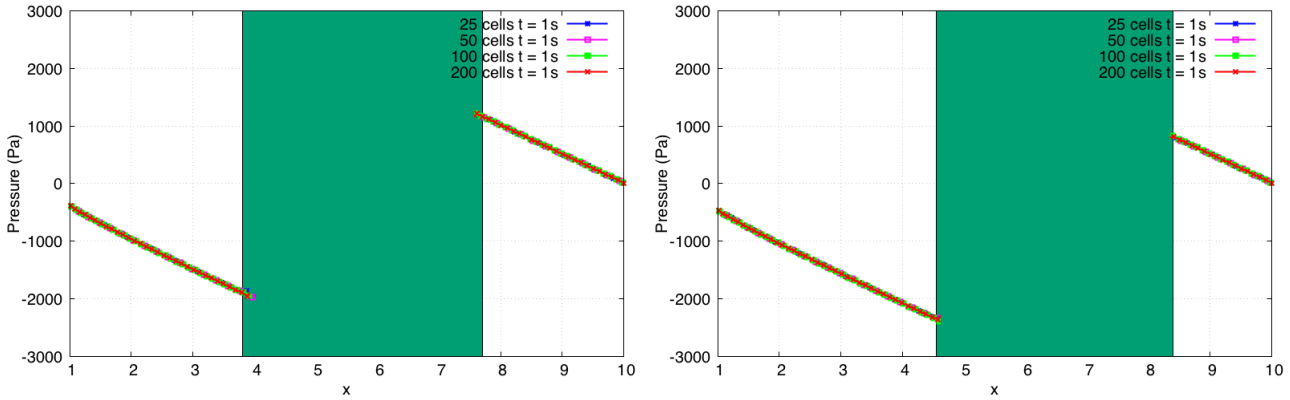

Figure 1.15 Pressure profile after discovering a cell (accelerating solid) after 1s (left) and 2s (right). The solid is in green.

On Figure 1.15, for an acceleration of $0.5 m/s^2$, after 1s and 2s, with 4 mesh refinements, the Time and Space Dependent Porosity method predicts the correct pressure since the slope is 0.5.

B) Fluid and solid moving at the same velocity

In a square domain 2mx2m, cylinder and fluid(s) have the same velocity $u_x = 0.1m/s$ and $u_y = 0.1m/s$ such as: For an incompressible flow, the pressure must remain at its initial value. In the present study, the

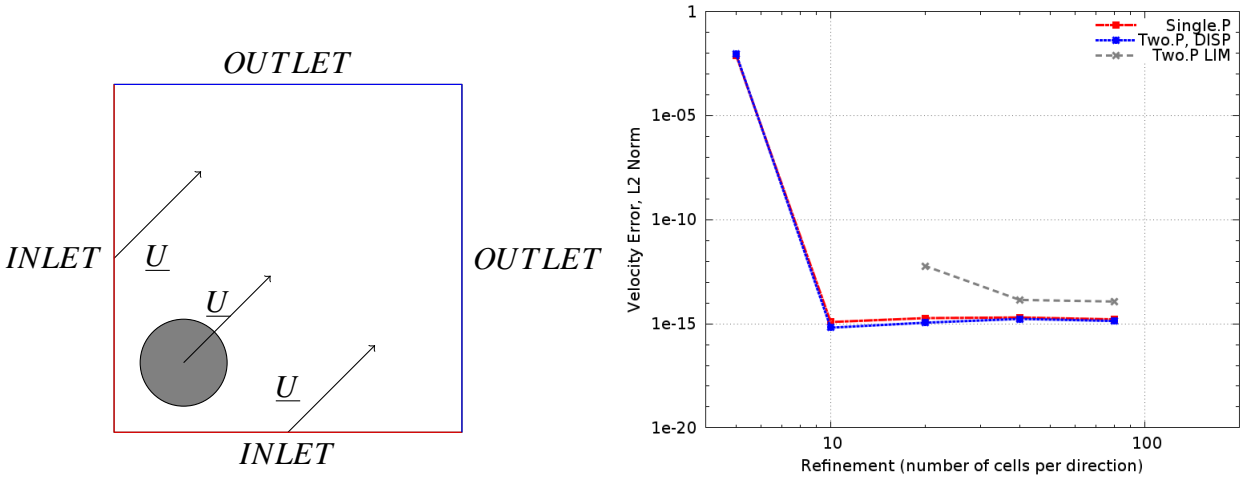

Figure 1.16 Geometry of cylinder at fluid velocity case (left) and velocity error for a cylinder at fluid velocity in single and two-phase flow (with 2 approaches : dispersed and continuous), (right).

initial condition is $P_{domain} = 0\ Pa$. Moreover, the velocity must remain unchanged. The aim is to validate the convection of the porosity using single then two-phase flow. In fact, this case does not work if the porosity is not convected.

In Figure 1.16, with 5 mesh refinements, results are presented in terms of L^2-norm error for velocity in single phase-flow, dispersed-flow ($\alpha = 10\%$) and Large Interface model (liquid-gas interface between (0,0) and (2,2)). Only 3 mesh refinements are presented with the Large Interface model since the interface recognition function needs a minimum of 5 cells.

The first mesh, having only 5 cells in each direction, is obviously too coarse. For the other, with any approach, it is possible to see that the error is extremely low. From the second refinement, the mean pressure in the domain is always under $10^{-12}\ Pa$.

1.3.3 Applications of the Time and Space Dependent Porosity method

Some applications of the method are here presented:

1. a cylinder moving in a fluid at rest at $Re = 40$ and suddenly stopped,
2. bubble impact on a cylinder,
3. a dam break on a wet bed,
4. a paddle oscillating on a free surface.

Numerical simulations are here performed in single or two-phase flow with moving body. The displacement is still imposed by the user.

A) Suddenly stopped cylinder

Based on Koumoutsakos and Leonard (1995), 2D numerical simulation of cylinder instantaneously moving and stopped for a laminar Reynolds number of 40 is performed. The cylinder is moving with a constant velocity during 5 seconds in a fluid at rest, and stopped at $t = 5\ s$. During 10 seconds, drag coefficients around the cylinder are recorded. The geometry of the case is reported in Figure 1.17.

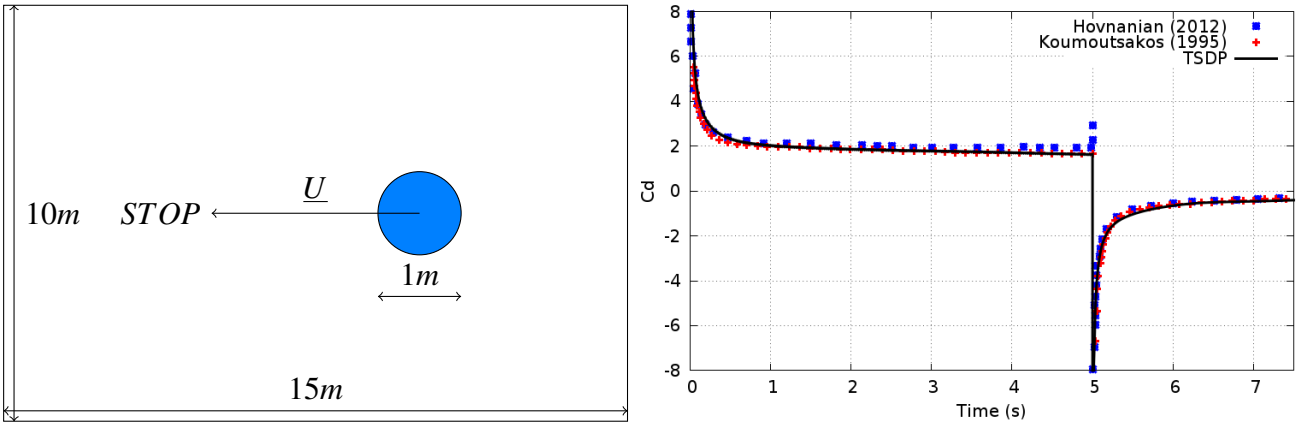

Figure 1.17 Geometry of the cylinder suddenly stopped case (left) and drag coefficient around the cylinder moving with $Re = 40$ and suddenly stopped. Numerical results are compared with other methods (Koumoutsakos and Leonard, 1995; Bergmann et al., 2012) (right).

As the Reynolds number is low, only the laminar part of the velocity gradient is relevant. The wall pressure is detected thanks to the pressure gradient with a first order development. Consequently, the global drag coefficients are in agreement over time. In Figure 1.17, at $t = 5s$, it is possible to see on the drag coefficient tendency a strong change which is the results of the cylinder velocity becoming 0. A slight discrepancy may be seen at $t = 5s$ with other results, otherwise they are in a reasonable agreement. In Figure 1.18, isolines of vorticity at 8 different instants are presented from the numerical simulation (left) and from the experiment (right). First column is dedicated to instant before the stop and the second to after. Obviously, the isolines represented are in excellent agreement with experimental data.

B) Bubble impact on a cylinder

The present 3D-application is a comparison between a computation utilizing a body-fitted mesh and another one utilizing the Time and Space Dependent Porosity. In Figure.3.31, the fluid is at rest. The large cylinder represents a solid obstacle and the small one a bubble. The bubble goes up thanks to gravity.

The fully-developed regime gives a bubble Reynolds number of 3.57, an Eötvos number of 116 and a Morton number of 266. The gas is air and the liquid has the following properties: $\rho = 1350\ kg/m^3$, $\mu = 2.02\ Pa.s$, and $\sigma = 0.0785\ N.m$. The liquid is at rest and the gravity is $9.81\ m/s^2$. A fully cartesian mesh is used with $\Delta x = \Delta y = \Delta z = 0.6mm$. To body-fit the cylinder, cells crossed by the cylinder or inside it are removed, then border nodes are extrapolated on the cylinder. Hence, for both cases a cartesian grid is used. However, for the standard case, the cells are not strictly cartesian since their node are moved to fit the cylinder.

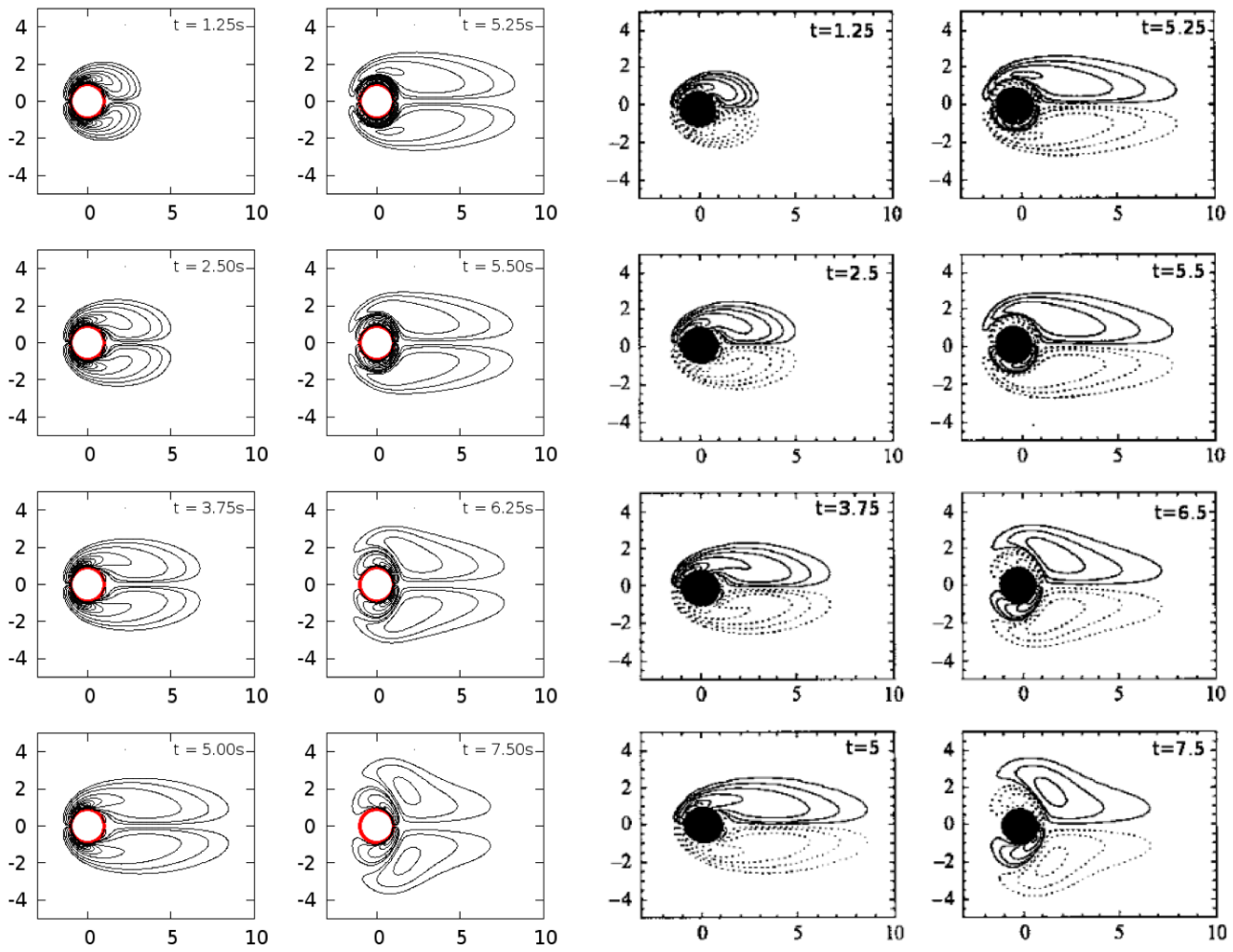

Figure 1.18 Vorticity isolines for 8 different times with numerical simulation (left) and experimental data (right) from Koumoutsakos and Leonard (1995)

The present study is realized with the Large Interface model to follow the bubble. Drag and surface tension forces from Fleau (2017) are applied to the gas phase. Moreover, an interface sharpening equation is required for this kind of simulation.

According to Figure 1.20, both methods are in correct agreement in terms of bubble break-up. However, slight discrepancies might be seen before the cylinder. As it is an unsteady numerical simulation using 15 millions of cells, results are convincing and attest the correct reconstruction of the wall. To clarify discrepancies, in one hand the wall is fully reconstructed, on the other a mesh is generated by extrapolation of its nodes; in both cases some errors are introduced which might explain the discrepancies on the figure. It is relevant to specify that interface sharpening and surface tension models which are used in the present study, are developed for cartesian cells only. Consequently, discrete forcing methods are useful for this kind of simulation.

C) Dam-break on wet bed

The schematic arrangement of the experimental tank (Janosi et al., 2004) is shown in Figure 1.22. The bottom and side walls are made of optically smooth glass, the lock gate is made of plexiglas. The

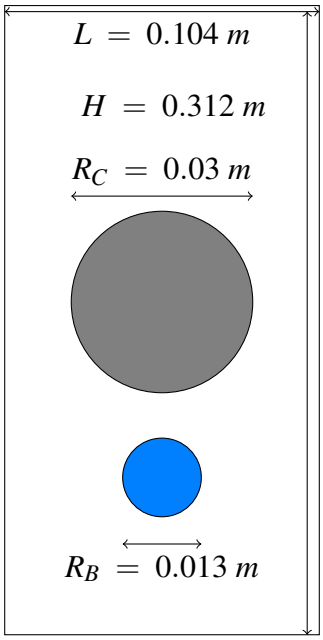

Figure 1.19 Geometry of the bubble impact on a cylinder case.

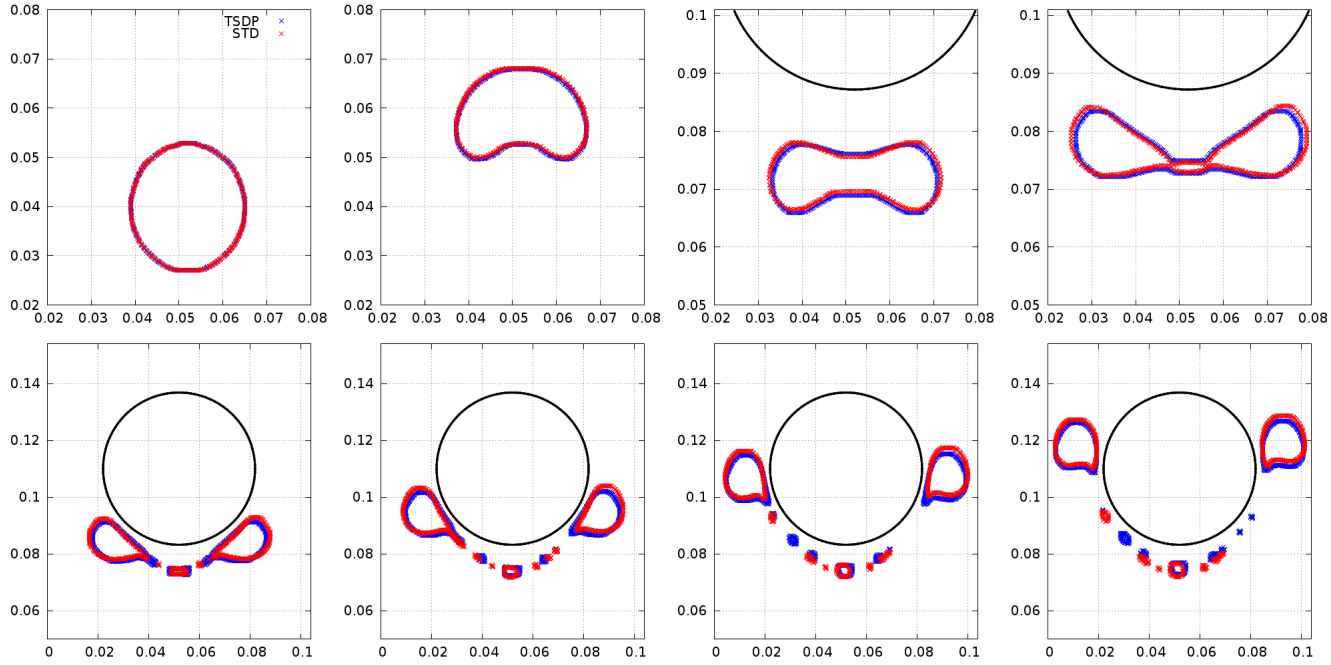

Figure 1.20 Contour comparison of a bubble impacting a cylinder between NEPTUNE_CFD with a body-fitted mesh and the Time and Space Dependent Porosity method at $t = 0.01,\ 0.1,\ 0.2,\ 0.3,\ 0.4,\ 0.5,\ 0.6,\ 0.7\ s$.

distance of the lock gate is $x_0 = 38\ cm$ in the experiments presented here, the initial water height in the lock is 15 cm. Another key parameter is the ambient fluid depth d in the channel before the dam-break: 18 mm and 38 mm. The lock gate is opened with a velocity: $v_0 = 1.5\ m/s$.

In this experiment, the water height is measured during 1 s and snap shots are taken. Water coming from the locked tank produces waves because of the progressive opening of the lock.

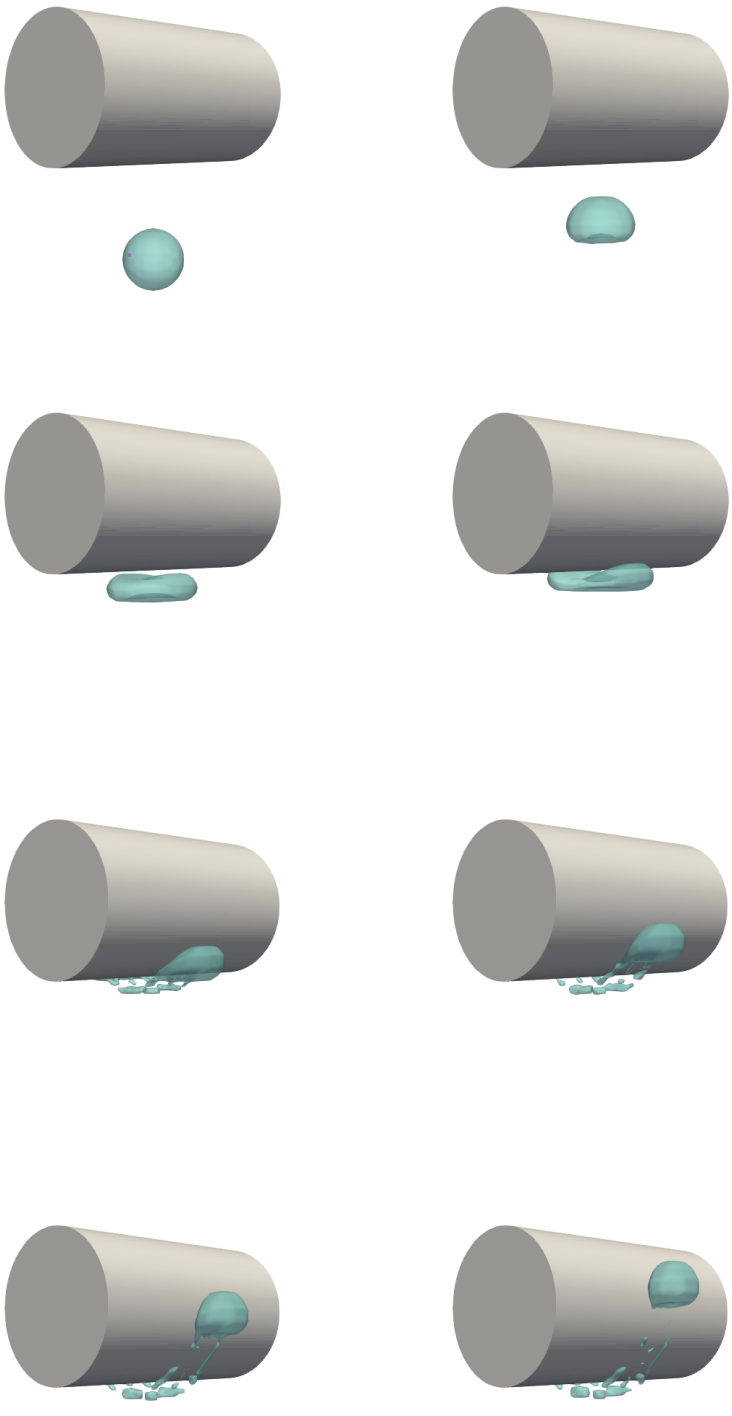

Figure 1.21 Snapshots of a bubble impacting a cylinder with the Time and Space Dependent Porosity method at $t = 0.01,\ 0.1,\ 0.2,\ 0.3,\ 0.4,\ 0.5,\ 0.6,\ 0.7\ s$.

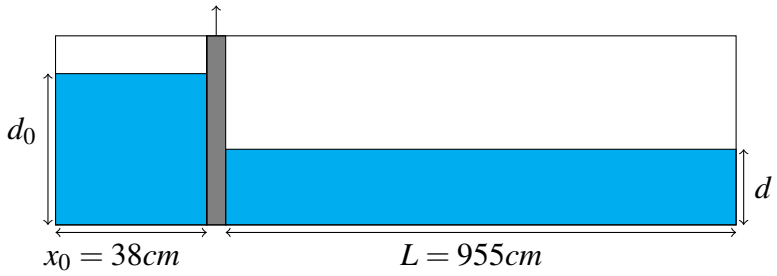

Figure 1.22 Sketch of the tank (Janosi et al., 2004).

In the following 2D-simulation, the lock gate is considered as the structure with a velocity v_0. Lock gate and walls are simulated with a slip condition. Results are compared with experimental pictures for $d = 18\ mm$ and with the water height along x for $d = 38\ mm$.

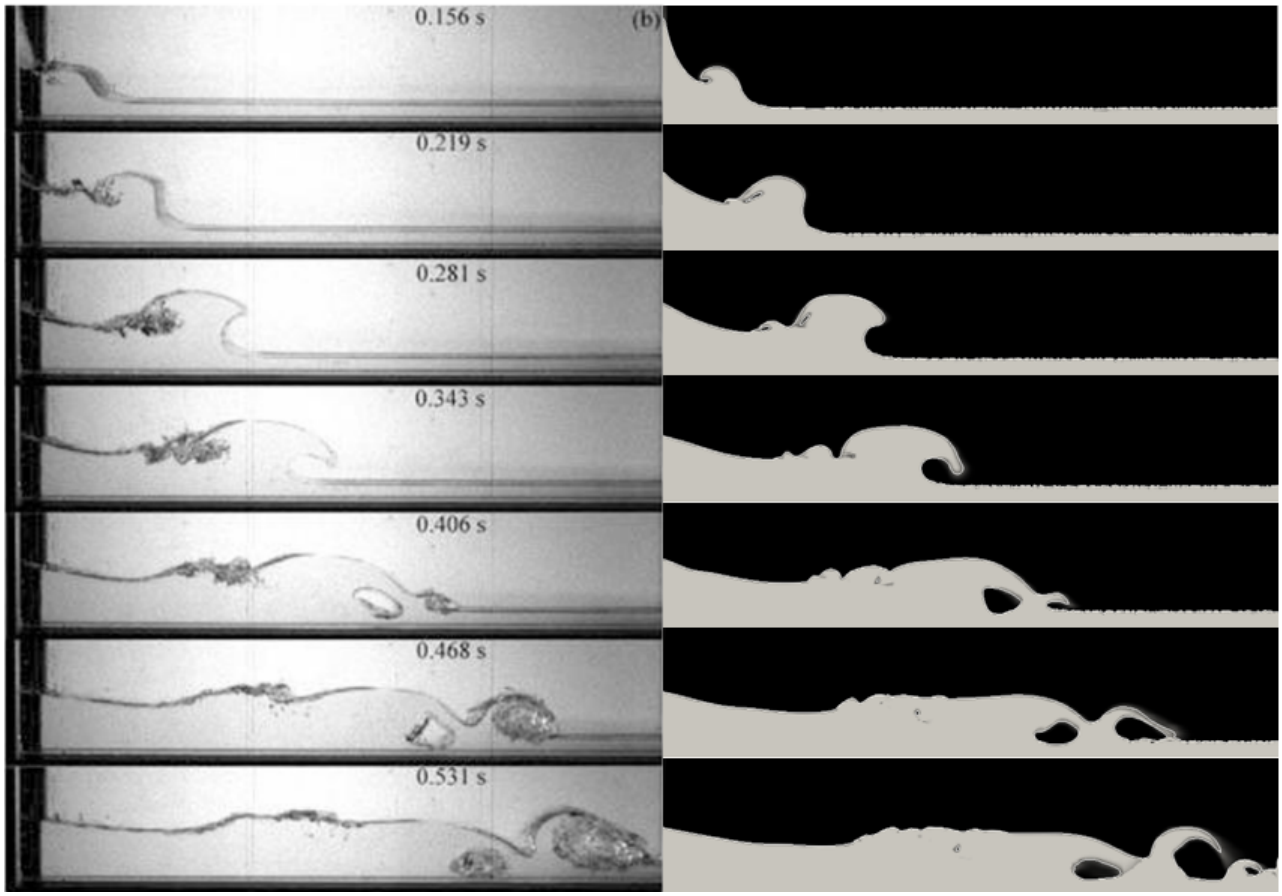

Figure 1.23 Experiment/Numerical simulation confrontation of a dam-break on wet bed for $d = 18\ mm$.

In Figure 1.23, 7 snap-shots are presented according to the experiment (left) and numerical simulation (right). The position of the free surface can be tracked on experimental records, it is simple to compare with numerical simulation. For different times, results are in agreement with experimental data. Waves are well predicted by the method which allows the conclusion that the Time and Space Dependent Porosity method is a satisfying method in this case.

D) Paddle

A 2D-paddle (presented in Figure 1.24) is animated by a sinusoidal motion with a velocity:

$$v(t) = 0.15 \min(1,t)\ cos\left(2\pi t - \frac{3\pi}{2}\right).$$

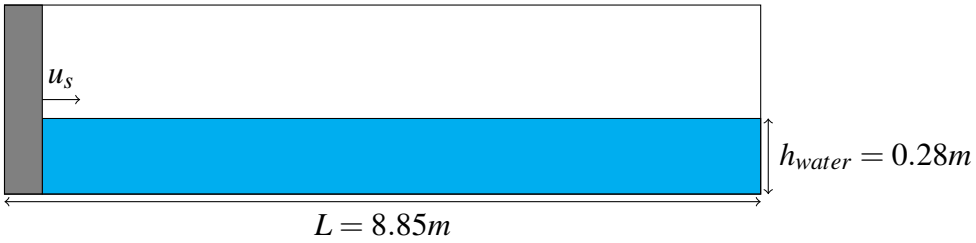

Figure 1.24 Geometry of the wave tank case, (Gao, 2003).

In the wave tank, the initial water depth is $h_{water} = 0.28m$ and its length $L = 8.85m$. As the paddle vibrates, waves appear, the free surface consequently moves, its time-fluctuations are recorded in 3 different positions: $x = 0.65\,m$, $x = 3.55\,m$ and $x = 5.45\,m$.

On Figure 1.25, water height simulation results are compared with experimental data Gao (2003) on 2 mesh refinements for 2 positions. First, in front of the paddle, the beginning of the paddle motion is

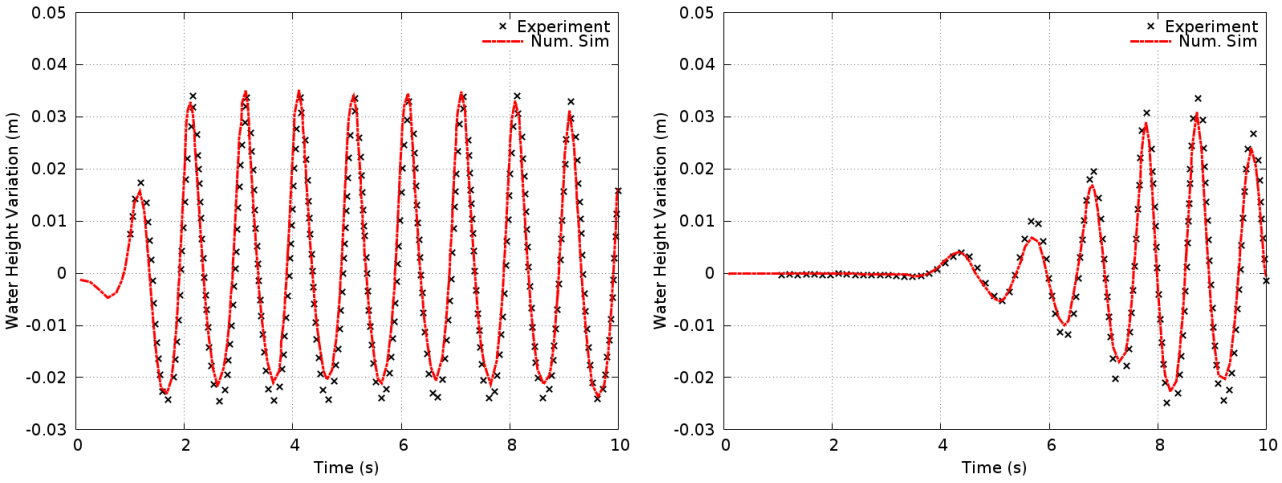

Figure 1.25 Free surface evolution for 2 different positions 0.65 m (left) and 5.45 m (right). Comparison between experiment (Gao, 2003) and numerical results from TSDP.

well captured by the simulation, there is no phase lag and the height amplitude is correct. For the two others, the wave lag is well predicted, there is also no phase lag but slight differences are present for the height amplitude.

Summary and remarks

In steam generators, two-phase flows are responsible of the vibration of the tube bundle. The knowledge in the simulation of two-phase flow is now mature enough to handle this kind of flow. However, an interface tracking method is required to simulate directly the motion of the structure.

In the present part, different methods to track fluid-structure interfaces were presented in order to show an overview. Since the objective is to have no limitation in the motion, an immersed boundary method has been chosen. However, the inconvenient of this kind of method is its accuracy at fluid-solid boundary. The requirement was therefore to be as accurate as mobile-mesh methods for example.

The key point in the development of the Time and Space Dependent Porosity method is its adaptation in the code utilized to compute two-phase cross-flows in tube bundles (which is based on a two-fluid approach). Instead of having the sum of volume fractions equal to one in the domain, it is equal to a time and space dependent porosity defining the location of the solid. Consequently, where the domain is fully fluid or solid, there is no change. The unique change is located at the interface between the structure and the fluid. In this area, the wall is accurately reconstructed based on geometric re-definitions and extrapolations. Moreover, a mass-balance equation is solved for this porosity, like for another volume fraction, avoiding numerical diffusion of the interface. Two-phase flow and turbulent models are then adapted by taking into account the porosity in the different conditioning steps and by accommodating the wall distance function to porous solids.

The method has been validated over a wide range of cases from simple single-phase flow without any structural motion to two-phase flow with moving bodies. The main case in the validation has been the solid moving at the fluid velocity. Being *a priori* very simple, this case highlights the least mistake in numerical schemes. Since the validation is going from separated effects to application cases, it is now possible to compute complex two-phase flows involving structure with motion. In order to illustrate functionalities of the method, a 3D-industrial feasibility test case is shown in Figure 1.26.

In terms of perspectives, two points are not really discussed in this section:

- the time of computation of the volumetric porosity: VOFI offers an accurate and quick resolution of the volumetric porosity, however its use in an industrial code with complex geometries, where uniform cartesian meshes are unfortunately not possible, is sometimes not possible. Consequently, we have to use a splitting method to determine the porosity which is more time-consuming. Given the performance in terms of time and accuracy of VOFI, it would be interesting to generalize it to non-uniform meshes.

- the required refinement at wall for turbulent cases: The wall distance function takes into account porous solids like with body-fitted meshes. Consequently, the turbulence is correctly generated around porous solids but refinement at wall is complicated to generate since only cartesian meshes were used up to now. Different solutions are possible such as to generalize to any kind of cells or to develop a virtual refinement in concerned cells. This second solution is probably the most interesting since we still do not have to mesh complicated geometry.

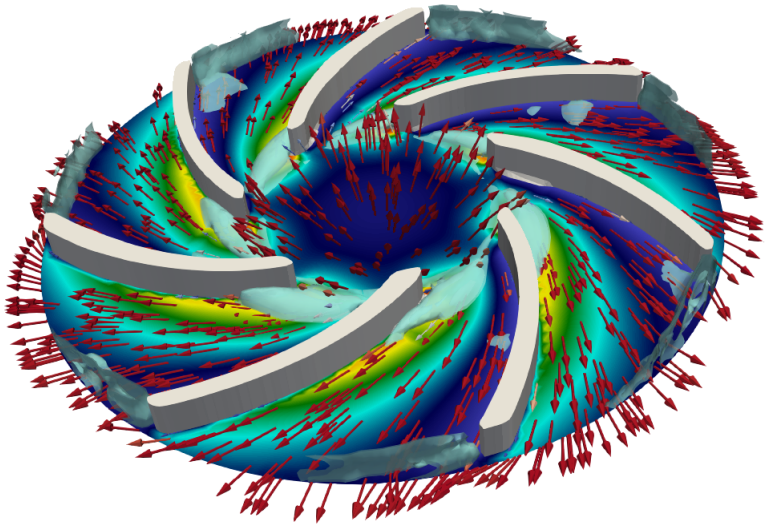

Figure 1.26 Two-phase flow in a centrifugal pump. Air and water are injected by the bottom. The mesh is a box with uniform cartesian cells. The porosity defines the blades and the boundaries of the domain.

Even if some improvements are necessary for an engineering use, considering it is now possible to have solid motion in two-phase flow, a fluid-structure coupling algorithm is now required to simulate the targeted application.

Chapter 2

Fluid-structure interaction with Time and Space Dependent Posority

In the context of strongly coupled physics like fluid-elastic instability, the coupling between fluid and structure solvers is a complex topic. Methods to solve fluid-structure interaction problems are classified into two groups: the monolithic method and the partitioned method. The coupling between a fluid and a structure is located at the interface between each domain. Interfaces have to remain in contact, this is illustrated by two conditions :

- fluid and structure interfaces are displaced with the same velocity:
- interface loads from structure and fluid are equal.

In order to ensure these conditions, monolithic and partitioned methods are suitable.

With the monolithic approach, fluid and solid subdomains do not have distinction in their space and time discretizations (Étienne and Pelletier, 2005; Hübner et al., 2004). Based on a joint algorithm, subdomains are computed simultaneously. Despite the good behavior of these algorithm, it requires the development of a code since fluid and solid solvers are often different and difficult to combine. Consequently, the use of partitioned algorithm is more frequent.

In mirror, the partitioned method solves distinctly fluid and solid systems. Physical domains are often different but exchange data through the fluid-structure interface. This flexibility in the choice of the discretization of each subdomain is the main advantage. Complex solvers developed at first for each subproblem might be utilized with the partitioned approach. Partitioned approach is classified into two groups (Matthies and Steindorf, 2002, 2003; Huvelin et al., 2006; Matthies et al., 2006; Hou et al., 2012):

- Explicit coupling (weakly coupled): subproblems are solved only once, consequently it is low time-consuming coupling. In Figure 2.1, the fluid domain is first solved; then, based on the updated fluid load, solid equations are solved. However, the interface displacement is approximated which generate energy at the interface leading to unstable solutions. The density ratio between solid and fluid is a key point in this instability called added mass effect.
- Iterative implicit coupling (strongly coupled): by utilizing sub-iterations to solve solid and fluid systems, interface conditions are respected. In fact, the explicit coupling is used at each sub-iteration, step by step the wall force and the displacement are computed. In Figure 2.2 Once

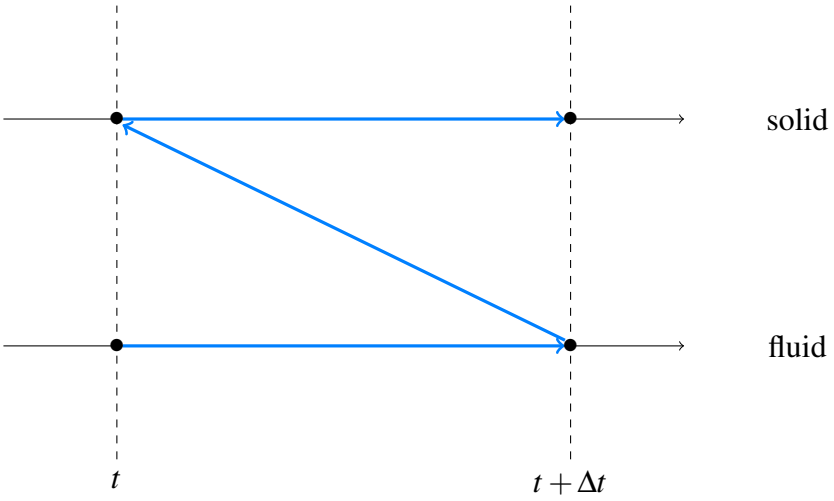

Figure 2.1 Fluid-structure interaction with partitioned approach, the explicit or weak coupling.

convergence is reached, it goes to the next iteration. This approach looks like the monolithic approach. These methods have the inconvenient to be slow. Different methods have been developed for years to accelerate this procedure but are not detailed in the present work (Küttler and Wall, 2008; Song et al., 2013).

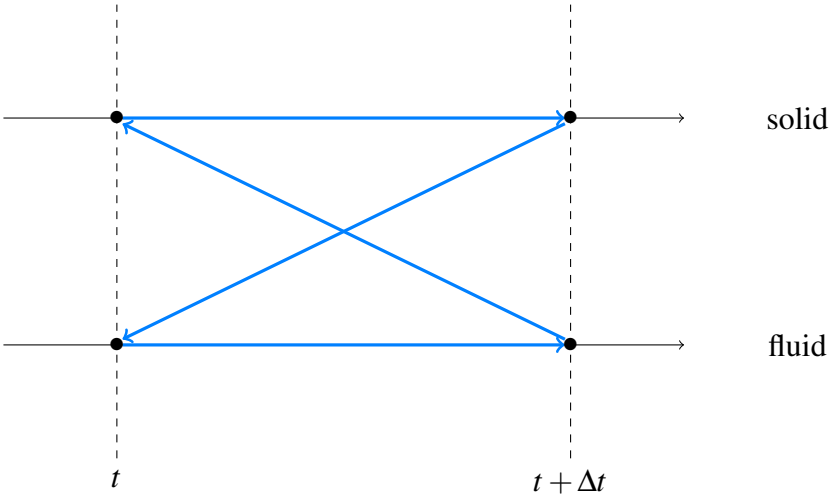

Figure 2.2 Fluid-structure interaction with partitioned approach, the iterative implicit or strongly coupling.

There are consequently multiple ways to perform fluid-structure coupling. In our case, the partitioned approach is required since we already have a fluid solver. Having strongly coupled problem of tube vibration induced by flow, the choice has been made to use an iterative implicit coupling which is presented in the following section. Because of the specific character of the interface tracking method presented previously, the force computation is detailed. Then, the displacement prediction algorithm is presented. Finally, the iterative fluid-structure coupling using the TSDP is detailed. The coupling is then validated over 3 application cases.

2.1 Fluid structure coupling with the TSDP

2.1.1 Two-phase flow force computation with the Time and Space Dependent Porosity method

As presented previously, with the Time and Space Dependent Porosity method, the fluid-structure interface is not represented by the mesh. However, the wall is reconstructed in the concerned cells (cells cut by the interface). In order to compute the whole force at the wall, each force contribution (pressure, friction and gravity) is adapted to the method and presented below.

Pressure contribution For each cell having a porosity in $]0,1[$ (a cell cut by the fluid-structure interface), the pressure at wall is computed. Pressure and pressure gradient are known in each cell. Consequently, for a cell I, the wall pressure is given by:

$$P_{wall} = P_I + \underline{IG}.\underline{\nabla P_I} \tag{2.1}$$

with P_{wall} the pressure at wall, and $\underline{IG}$ the vector between the corrected cell center of gravity and the solid face center of gravity.

Then, the pressure force acting on a solid is computed with:

$$\underline{F}_{pressure} = \int_{\Omega} P_{wall}\, \underline{dS} \tag{2.2}$$

As the assumption of two-fluid approach is to have a single pressure, the computation of the pressure force is unchanged in multi-phase flows.

Friction contribution For each cell having a porosity in $]0,1[$, the friction contribution is computed at the wall. The velocity gradient is known in each cell. Consequently, the whole friction force is computed with:

$$\underline{F}_{friction} = \int_{\Omega} \mu(\overline{\overline{\nabla U_{wall}}} +^{T} \overline{\overline{\nabla U_{wall}}})\, \underline{dS} \tag{2.3}$$

In multi-phase flows, friction contribution from each phase k is required. Therefore, for a cell I:

$$\underline{F}_{I,\ friction} = \sum_{k=1}^{N} \frac{\alpha_{I,k}}{\varepsilon_I} \mu_k(\overline{\overline{\nabla U_{Ik\ wall}}} +^{T} \overline{\overline{\nabla U_{Ik\ wall}}})\, \underline{S_I} \tag{2.4}$$

with N the number of phase. The sum of these contributions leads to the whole multi-phase friction force.

Gravity contribution The mass of the structure is computed as:

$$M_S = \sum_{I=1}^{N_{cell}} \rho_{solid}\, V_I\, (1-\varepsilon_I) \tag{2.5}$$

with N_{cell} the number of cell in the domain, ρ_{solid} the volumetric mass and V_I the volume of the cell I. Then, the gravity force applied on a structure S is written:

$$\underline{F}_{gravity} = M_S \, \underline{g} \tag{2.6}$$

with $\underline{g}$ the gravity.

Finally, the force acting on the structure is written:

$$\underline{F}_{fluid} = \underline{F}_{pressure} + \underline{F}_{friction} + \underline{F}_{gravity} \tag{2.7}$$

Based on it, it is possible to predict the displacement of the structure.

2.1.2 Newmark algorithm

In order to compute the displacement of the structure due to the acting fluid forces, the Newmark algorithm is used to solve the following system (Newmark, 1959):

$$[M].\ddot{X} + [C].\dot{X} + [K].X = F \tag{2.8}$$

with X a 3D displacement vector; M, C, K are the (3,3) mass, damping, and stiffness matrices. The resolution of this second order linear differential equation of the structure is carried out in space by the Newmark method.

In order to compute the displacement and velocity discretization, γ and β are defined such as:

$$\dot{X}_{t+\Delta t} = \dot{X}_t + \Delta t.[(1-\gamma).\ddot{X}_t + \gamma.\ddot{X}_{t+\Delta t}] \tag{2.9}$$

$$X_{t+\Delta t} = X_t + \Delta t.\dot{X}_t + \frac{\Delta t^2}{2}.[(1-2\beta).\ddot{X}_t + 2\beta.\ddot{X}_{t+\Delta t}] \tag{2.10}$$

Then, the linear differential equation of the structure is written:

$$M.\ddot{X}_{t+\Delta t} + C.\dot{X}_{t+\Delta t} + K.X_{t+\Delta t} = F_{t+\Delta t} \tag{2.11}$$

which might be reduced to:

$$\begin{gathered} \widetilde{F} = X_{t+\Delta t}.\widetilde{K} \\ \widetilde{K} = K + \frac{1}{\beta.\Delta t^2}.M + \frac{\gamma}{\beta.\Delta t}.C \\ \widetilde{F} = F_{t+\Delta t} + C.(\frac{\gamma}{\beta.\Delta t}.X_t + (\frac{\gamma}{\beta} - 1).\dot{X}_t + \frac{\Delta t}{2}(\frac{\gamma}{\beta} - 2).\ddot{X}_t) + M.(\frac{1}{\beta.\Delta t^2}.X_t + \frac{1}{\beta.\Delta t}.\dot{X}_t + (\frac{1}{2\beta} - 1).\ddot{X}_t) \end{gathered} \tag{2.12}$$

Coefficients a_k are defined: $a_0 = \frac{1}{\beta.\Delta t^2}, a_1 = \frac{\gamma}{\beta.\Delta t}, a_2 = \frac{1}{\beta.\Delta t}, a_3 = \frac{1}{2\beta} - 1, a_4 = \frac{\gamma}{\beta} - 1, a_5 = \frac{\Delta t}{2}(\frac{\gamma}{\beta} - 2)$, $a_6 = \Delta t.(1-\gamma)$, et $a_7 = \gamma.\Delta t$. Consequently:

$$\begin{aligned} \widetilde{F} &= X_{t+\Delta t}.\widetilde{K} \\ \widetilde{K} &= K + a_0 M + a_1 .C \\ \widetilde{F} &= F_{t+\Delta t} + C.(a_1.X_t + a_4\dot{X}_t + a_5\ddot{X}_t) + M.(a_0.X_t + a_2\dot{X}_t + a_3\ddot{X}_t) \end{aligned} \tag{2.13}$$

Once the system is solved, the displacement appears. Velocity and acceleration are computed such as:

$$\begin{aligned} \ddot{X}_{t+\Delta t} &= a_0.(X_{t+\Delta t} - X_t) - a_2.\dot{X}_t - a_3.\ddot{X}_t \\ \dot{X}_{t+\Delta t} &= \dot{X}_t + a_6.\ddot{X}_t + a_7.\ddot{X}_{t+\Delta t} \end{aligned} \tag{2.14}$$

This approach is frequently used in mechanic since it allows to choose the order of integration, to introduce or not numerical damping, and is accurate. It is unconditionally stable for:

$$\begin{aligned} \gamma &> 0.5 \\ 2\beta &> \gamma \end{aligned} \tag{2.15}$$

A positive numerical damping is introduced for $\delta > 0.5$ and a negative for $\delta < 0.5$. The most frequently combination used is $\delta = 0.5$, $\beta = 0.25$ given that there is no numerical damping introduced, it is unconditionally stable, and is a 2nd order scheme. This combination is used in the present work.

2.1.3 Iterative implicit algorithm

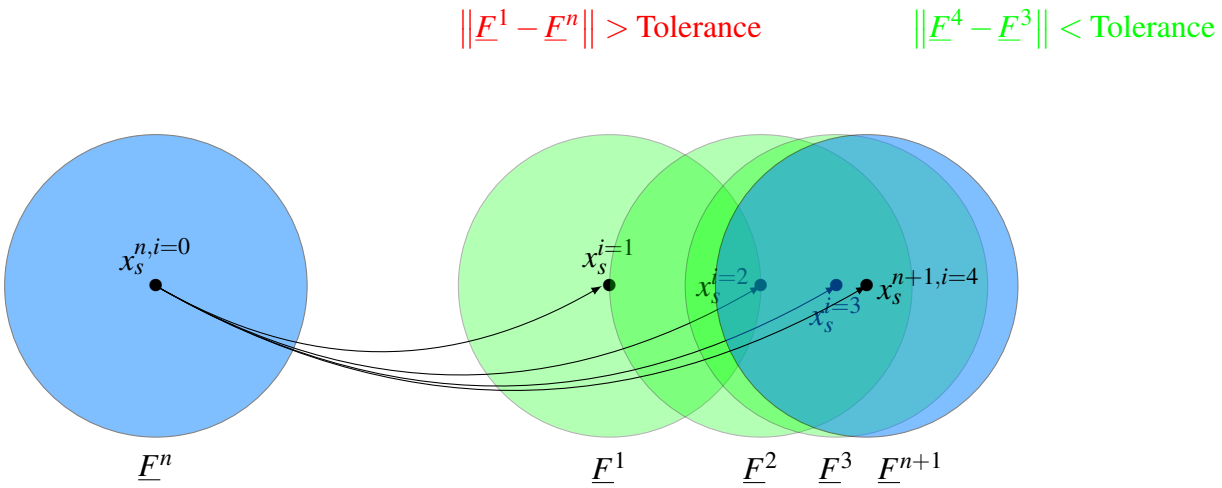

Figure 2.3 Sketch of the iterative determination of the structure displacement due to the fluid forces.

The computation of a force at the wall is sensitive since the solid is moving. In order to reduce this error, this force and the displacement are determined iteratively (see Figure 2.3). Step by step the solid is moved until convergence. The iterative implicit fluid-structure coupling scheme used with the Time and Space Dependent Porosity method is presented here:

Algorithm 1 Implicit Fluid-structure coupling scheme, computation of the displacement x_s^{n+1}

Given $\underline{x}_s^n$, $\underline{\dot{x}}_s^n$, $\underline{u}_f^n$, P^n
while $\left\|\underline{F}^{i+1} - \underline{F}^i\right\| <$ Tolerance **do**
  if Sub-cycle 1 **then**
    Computation of $\underline{F}^i$ with $\underline{u}_f^n$ and P^n
  else
    $\underline{F}^i = \underline{F}^{i+1}$
    $i = i+1$
    Restore time step to $\underline{x}_s^n$, $\underline{\dot{x}}_s^n$, $\underline{u}_f^n$, P^n
  end if
  Newmark algorithm gives $\underline{x}_s^{i+1}$ and $\underline{\dot{x}}_s^{i+1}$
  Porosity calculation
  Computation of $\underline{u}_f^{i+1}$, P^{i+1}
  Computation of $\underline{F}^{i+1}$ with $\underline{u}_f^{i+1}$ and P^{i+1}
end while
$\underline{F}^{n+1} = \underline{F}^{i+1}$, $\underline{x}_s^{n+1} = \underline{x}_s^{i+1}$, $\underline{\dot{x}}_s^{n+1} = \underline{\dot{x}}_s^{i+1}$, $\underline{u}_f^{n+1} = \underline{u}_f^{i+1}$, $P^{n+1} = P^{i+1}$

Based on the fluid flow properties of the previous iteration, the forces are computed. Then, thanks to the Newmark algorithm, the displacement and the velocity of the solid are calculated and the fluid domain is solved depending on the new position of the solid. Based on the updated fluid domain, the fluid forces at the wall is computed and compared to the previous one. The fluid domain is then restarted to its state at the beginning of the present iteration. When the comparison of the forces is under a certain tolerance, the flow is updated and the next iteration starts. The determination of the convergence is described in the first validation case.

2.2 Numerical validation of the fluid-structure coupling

In order to evaluate the fluid-structure coupling with the Time and Space Dependent Porosity method, three test cases are chosen:

- the cylinder removed from its equilibrium position in a still fluid,
- flow-induced vibration of a free cylinder with $Re = 100$,
- free fall of a spherical solid on a free surface.

A sensitivity to the time step and to the number of cycles is performed on the first test case. Then, for the second case, a wide range of reduced velocity is computed in order to validate the correct prediction of the amplitude. Finally, based on two experiments, the two-phase character of the force is challenged.

2.2.1 Cylinder removed from its equilibrium position in a still fluid

In order to get the added-mass and the damping coefficient in a fluid domain, a manner consists in removing a tube from its equilibrium position with a given amplitude and recording its response. Based on its response, added-mass and damping coefficient are deducted.

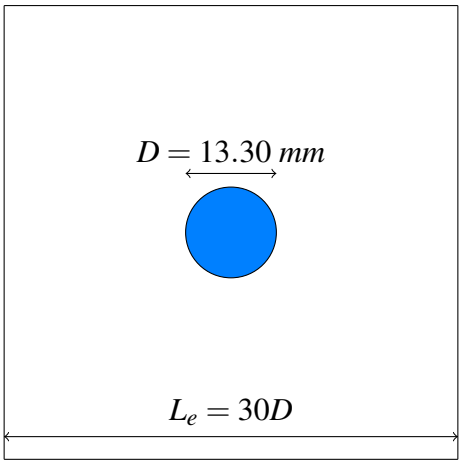

Figure 2.4 Cylinder removed from its equilibrium position in a still fluid, geometry.

A cylinder with a diameter D is immersed in an incompressible fluid domain where the confinement coefficient is $L_e/D = 30$ (with L_e the characteristic length of the domain). The fluid is water with a density $\rho = 1000\ kg/m^3$ and a kinematic viscosity $\nu = 10^{-6}\ m^2/s$. The tube is released without any velocity with an amplitude $S_0 = 0.001D$.

The tube is represented with a mass-spring system with damping:

$$\ddot{X}_s + 2\xi_s\omega_s\dot{X}_s + \omega_s^2 X_s = 0 \tag{2.16}$$

with $\omega_s^2 = K_s/M_s$ and $\xi_s = \dfrac{C_s}{2\omega_s M_s}$. The characteristics of the tube are $D = 13.30\ mm$, $\omega_s = 2\pi\ 15.90 = 99.90\ rad/s$, $\xi_s = 0.36\%$, and $M_s = 0.298\ kg/m$.

When the tube is immersed in a fluid at rest, the fluid action is represented by an added mass M_a and a damping C_a:

$$M_s(\ddot{X}_s + 2\xi_s\omega_s\dot{X}_s + \omega_s^2 X_s) = -M_a\ddot{X}_s - C_a\dot{X}_s \tag{2.17}$$

Consequently,

$$(M_s + M_a)\ddot{X}_s + (C_a + C_s)\dot{X}_s + K_s X_s = 0 \tag{2.18}$$

The objective is to numerically deduced the pulsation and the reduced damping of the system:

$$\omega_{fs}^2 = \frac{K_s}{(M_s + M_a)} \text{ and } \xi_{fs} = \frac{C_s + C_a}{2\omega_{fs}(M_s + M_a)} \tag{2.19}$$

According to AMOVI experiment (Baj, 1998), for low Reynolds number, the frequency of the system is $f_{fs,exp} = 12.866\ Hz$ and reduced damping $\xi_{fs,exp} = 1.00\%$.

The geometry of the simulation is presented in Figure 2.4. The time step is constant and the maximum Courant number is under 1.

A) Sensitivity to the number of cycles

In the present study, a particular attention is paid to the tolerance in the fluid-structure coupling algorithm since it defines when the displacement is correctly predicted. Consequently, in order to determine it, we define δ like:

$$\delta = (\frac{F^{k+1} - F^k}{F^k})^2 \tag{2.20}$$

with F^{k+1} and F^k forces computed respectively after $k+1$ and k sub-cycles. The objective of this case is to show the importance in the choice of a value for δ_{max} to predict the displacement with a reasonable computational time.

Therefore, the displacement is computed with few constant numbers of sub-cycles from 2 to 15. Then, different runs are carried out with a fixed δ_{max} from 1.0 10^{-3} to 1.0 10^{-8}.

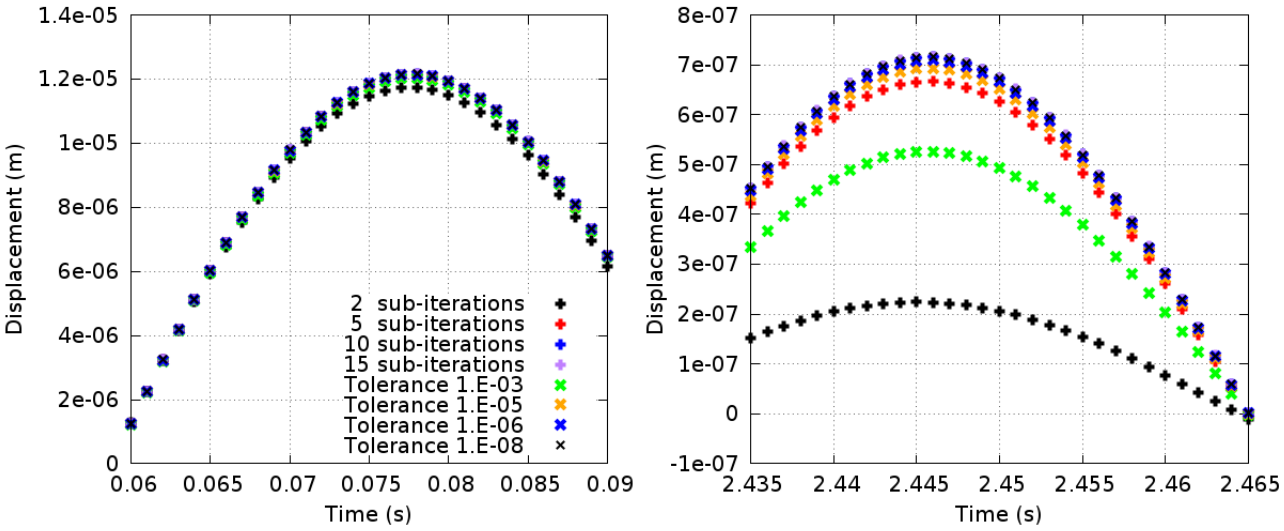

Figure 2.5 Cylinder removed from its equilibrium position in a still fluid after 1 period on the left, after 31 periods on the right, sub-cycles and δ_{max} sensitivity.

In Figure 2.5, the displacement of the cylinder is presented after 1 and 31 periods of oscillation for different convergence criterion. According to the results, it appears that 2 and 5 sub-iterations are not enough. However, with 10 and 15 sub-cycles, the predictions of displacement are close. For $\delta_{max} = 1.0\ 10^{-3}$, the criterion is distinctly not relevant to predict accurately the displacement. In contrast, 1.0 10^{-6} and 1.0 10^{-8} are in agreement with the prediction of displacement with 10 and 15 sub-cycles. 1.0 10^{-5} slightly under-estimates the displacement. This convergence might be time-consuming consequently a δ_{max} is chosen in order to avoid unnecessary sub-cycles. Since we are working with strongly coupled problems, the choice for the following studies has been $\delta_{max} = 1.0\ 10^{-6}$ as a tolerance (between 2 and 10 sub-cycles are necessary at each iteration for the present case).

B) Sensitivity to the time step

In Figure 2.6, a time step sensitivity is presented based on the intermediate refinement. The frequency and the reduced damping are computed for different time step going from 2.00 10^{-3} to 6.25 10^{-5} s. According to the results, the frequency is converging faster than the reduced damping. Results are

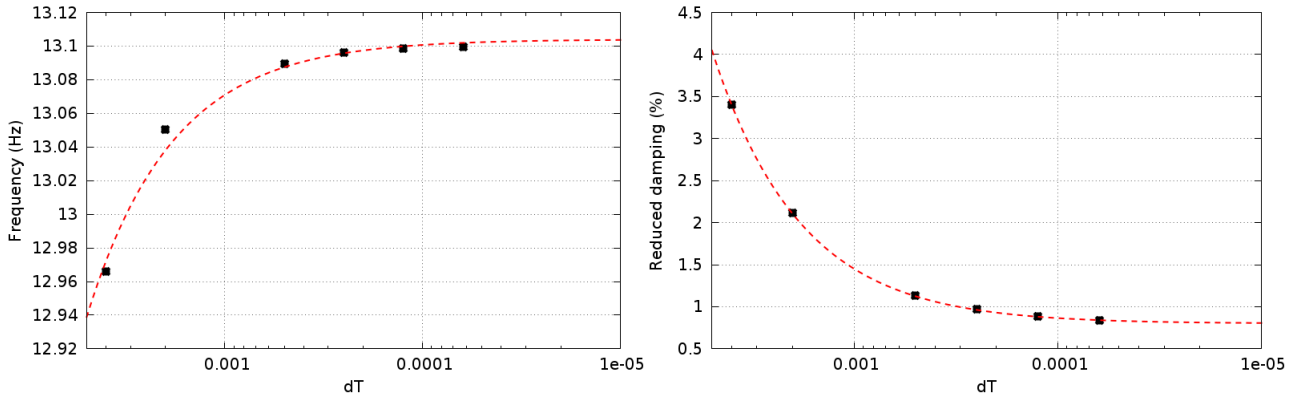

Figure 2.6 Cylinder removed from its equilibrium position in a still fluid, time step sensitivity.

compared with the experimental results in Table. 2.1. There is a correct agreement between them for frequency only. For damping, the error is probably due to the mesh refinement which is slightly too coarse to get the exact solutions.

	Frequency (Hz)	Reduced damping (%)
Experimental	12.866	1.000
Present Simulation, time step sensitivity	13.11	0.8
Error	1.89%	20%
Present Simulation, mesh sensitivity	13.07	1.01
Error	1.58%	1.0%

Table 2.1 Cylinder removed from its equilibrium position in a still fluid, numerical and experimental prediction of frequency and reduced damping comparison.

C) Mesh sensitivity

In Figure 2.7, a mesh sensitivity is presented for four meshes. Frequency and reduced damping are compared with experimental results in Table. 2.1 where it is possible to see how accurate is the numerical prediction. The present results show the correct choice of δ.

Based on the present case, the tolerance required by the iterative algorithm is chosen. A time and space sensitivity studies are performed leading to accurate predictions of the displacement in terms of frequency and amplitude. Consequently, it is considered that the fluid-structure coupling algorithm is now ready to be used with the Time and Space Dependent Porosity method for application cases.

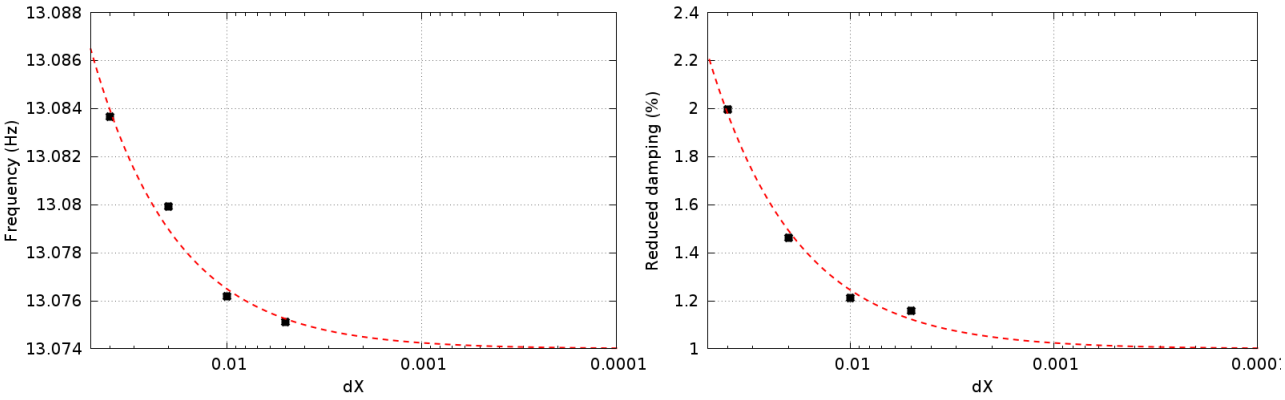

Figure 2.7 Cylinder removed from its equilibrium position in a still fluid, mesh sensitivity.

2.2.2 Flow-induced vibration of a free cylinder with $Re = 100$

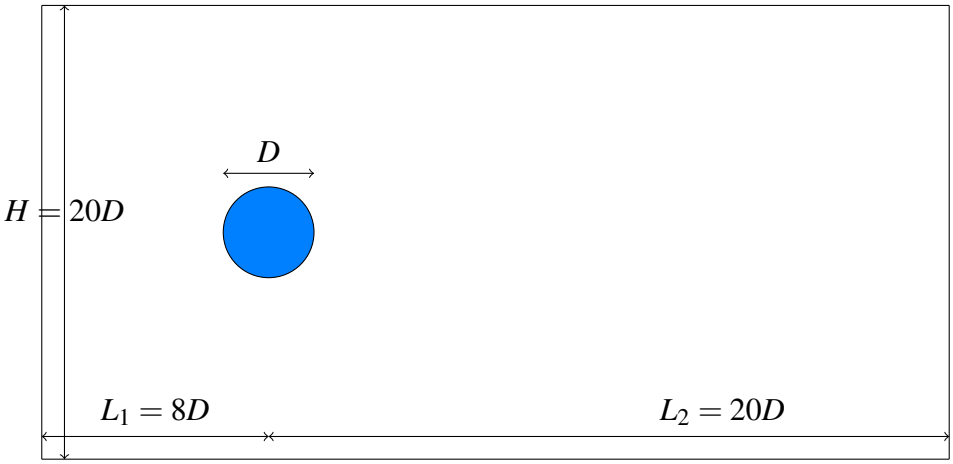

Figure 2.8 Flow-induced vibration of a free cylinder with $Re = 100$, geometry.

In the present case, we are interested in flow-induced vibration of a free-cylinder with $Re = 100$. In order to avoid boundary effects, the domain is considered infinite, that is why the size of the domain is large. In Figure 2.8, the domain used in the current work is presented. In order to insure a Reynolds number of 100, the flow characteristics are the diameter $D = 0.025\ m$, the inlet velocity $U_0 = 4.0\ 10^{-3}\ m/s$, the density $\rho = 1000\ kg/m^3$ and the dynamic viscosity $\mu = 1.0\ 10^{-3}\ Pa.s$.

Moreover, the prediction of the fluid force around the cylinder requires a fine mesh. The thickness of the smallest cells is $1.0\ 10^{-4}\ m$. The mesh is presented in Figure 2.9. For this Reynolds number, it is allowed to work with a 2 dimensional domain (one cell in the third direction). The left side is defined as the inlet, the right as the outlet. The cylinder wall is considered with a non-slip condition. Other surface are considered with a slip condition.

Fluid forces at wall are computed on the cylinder surface. Since the domain is 2 dimensional, they are divided by the length L of the cylinder which was chosen as $L = 2.0\ 10^{-4}\ m$. The drag and lift coefficient are then computed as:

$$C_i = \frac{F_i}{\frac{1}{2}\rho U_0^2 DL} \tag{2.21}$$

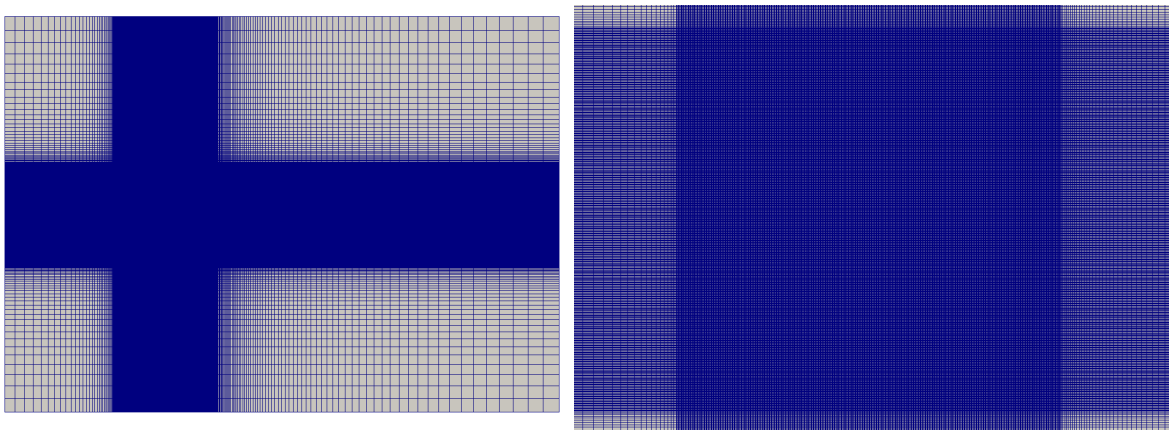

Figure 2.9 Mesh utilized for the flow-induced vibration case with $Re = 100$. On the left, the entire mesh is presented. On the right, a zoom is realized in the zone of interest where the cylinder is. This area is large since the refinement must remain the same whatever the cylinder displacement.

with $i = x$ or y. The fluid flow is unsteady and the maximum Courant number is taken under 1. In order to predict the correct vibration, the forces have to be correctly predicted. First, with a fixed cylinder, numerical results are compared to the result of Pomarede et al. (2010) in Table 2.2.

	$C_{x,averaged}$	$C_{y,maximum}$	Strouhal
Pomarede et al. (2010)	1.389	0.328	0.166
Present Simulation	1.391	0.335	0.166
Error	0.1%	2.13%	0.005%

Table 2.2 Force coefficients and Strouhal prediction for a single-phase flow around a cylinder with $Re = 100$. Comparison between results from Pomarede et al. (2010) and the present study.

Numerical results are in correct agreement with Pomarede et al. (2010). The forces are consequently well predicted. The flow being fully developed, it is now possible to allow the cylinder to vibrate depending on the fluid forces in the lift direction only (y).

First, we respectively define the reduced mass and the reduced stiffness:

$$m^* = \frac{m}{\frac{1}{2}\rho D^2 L} = \frac{\pi}{2}\frac{\rho_{solid}}{\rho} \tag{2.22}$$

with m the mass of the cylinder, and ρ_{solid} the volumetric mass of the cylinder.

$$k^* = \frac{k}{\frac{1}{2}\rho U_0^2} \tag{2.23}$$

The present cases are based on the work of Shiels et al. (2001) who explores a large range of reduced mass and stiffness with zero damping. In Figure 2.10, an example of velocity field around the free-cylinder is proposed for $m^* = 1.25$ and $k^* = 2.48$. The amplitude of displacement is here 60% of the diameter. It is possible to see the vortex shedding by looking at the different snapshots.

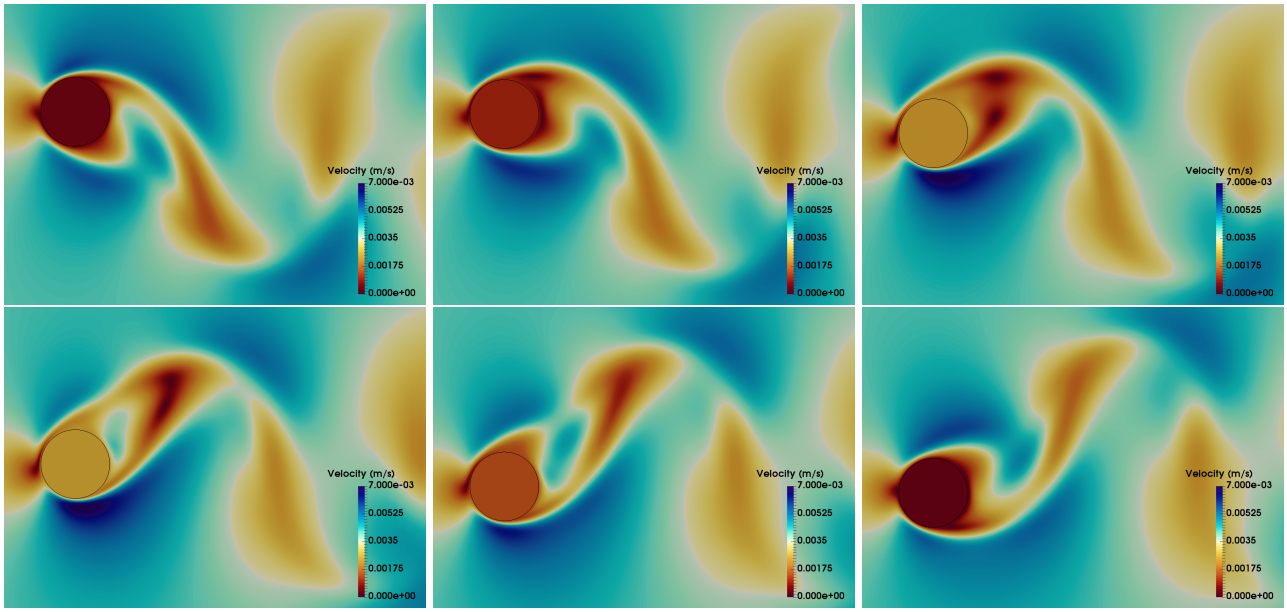

Figure 2.10 Flow-induced vibration at $Re = 100$ for $m^* = 1.25$ and $k^* = 2.48$. Picture of the cylinder displacement and a vortex shedding over time. In this case, the amplitude of displacement is 60% of the diameter.

In Table 2.3, we present the characteristics of the cases computed in the present study. Since the application of the thesis is a cross-flow in a tube-bundle where $m^* > 1$, we only consider cases with $m^* > 1$. Cases with $m^* < 1$ would be more difficult to simulate and would require a different coupling method which is not of primary interest here.

Case	A	B	C	D	E	F	G	H	I	J
m^*	4.00	2.50	1.50	5.00	5.00	10.0	15.0	1.25	2.50	5.00
k^*	0.0	0.0	0.0	4.74	9.88	19.78	29.68	2.48	4.96	8.74

Table 2.3 Numerical cases from Shiels et al. (2001) computed in the present study.

In Figure 2.11, numerical results from Shiels et al. (2001), Marcel (2010) and the present method are compared for a wide range of reduced-mass and damping. Amplitude, frequency, maximum lift coefficient and time-averaged drag coefficients are presented in the four different graphics.

The amplitude of vibration predicted by the present method is in a correct agreement with the others. The major discrepancy seems to be for case D and F where the characteristic shedding frequency is going

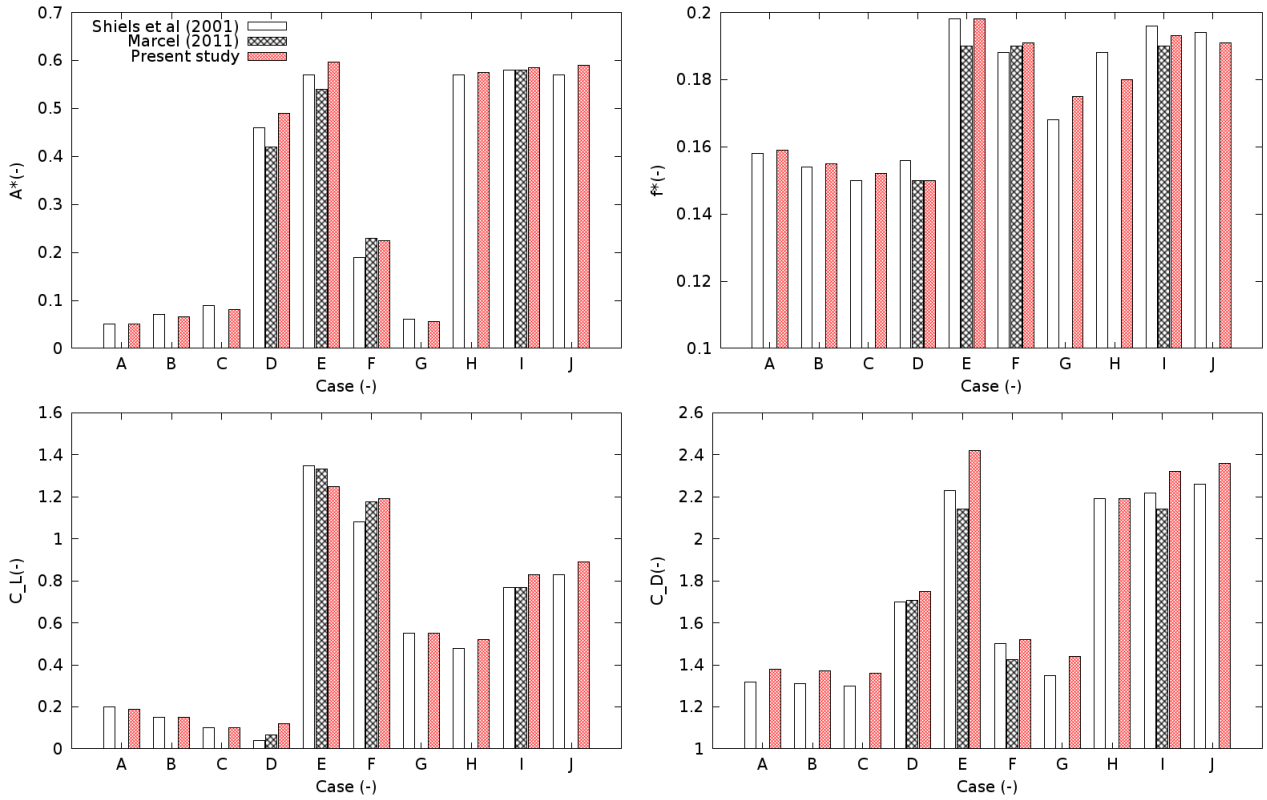

Figure 2.11 Response for undamped systems for various cases: A^* amplitude, f^* frequency, C_L max lift coefficient and $C_{D,av}$ averaged drag coefficient. Comparison between numerical results from Shiels et al. (2001), Marcel (2010) and the present method.

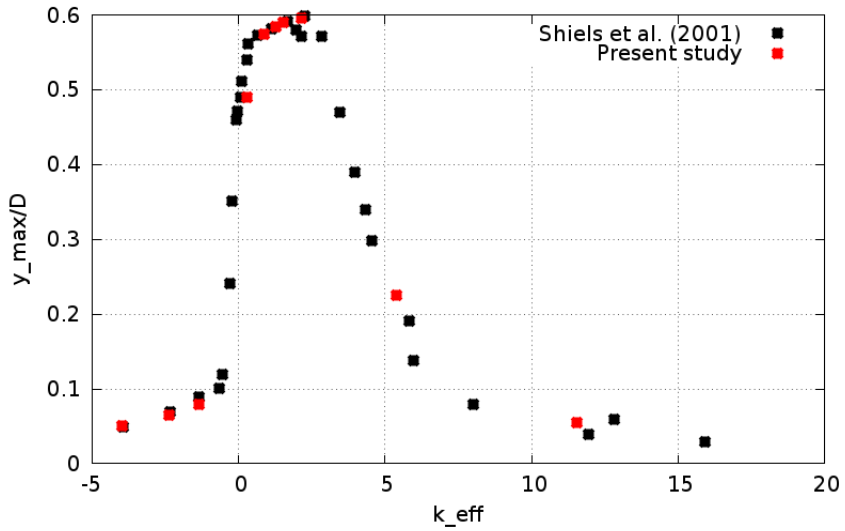

Figure 2.12 Response for undamped systems plotted against effective elasticity. Comparison between numerical results from Shiels et al. (2001) and the present method.

to coincide with the natural structural frequency. The other parameters are also correctly predicted by the present method.

In Figure 2.12, the response for undamped cases presented previously is plotted against effective elasticity (defined in Shiels et al. (2001)). It appears that the maximum amplitude is the same with both

methods. Moreover, the variation of amplitude with effective elasticity (which is dependent on k^*, m^* and f^*) are approximatively the same.

These results are very encouraging since the fluid-structure method based on an immersed approach leads to predictions in agreement with the ones based on ALE approach. It is consequently a concrete validation in single-phase flow of our method. In the following section, an application case is performed with two-phase flow.

2.2.3 Free fall of a spherical solid on a free surface.

The present case deals with free-fall of spheres from air to water performed experimentally by Aristoff et al. (2010). A sphere is held at height H above a water tank. The tank has dimensions of 30x50x60 cm^3. The sphere is released from rest and falls toward the water, reaching it with approximate speed $U_0 = \sqrt{2gH_0}$, with H_0 the initial altitude of the sphere. The geometry is presented in Figure 2.13. The impact sequence is recorded with high speed camera. The trajectory of the sphere and its impact speed are determined based on records. Spheres are made of different materials: polypropylene, nylon, teflon and steel. Their densities are respectively 0.86, 1.14, 2.30, and 7.86 kg/cm^3.

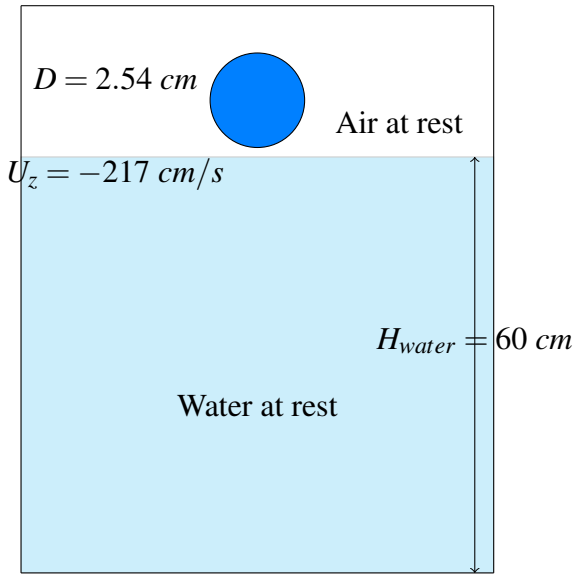

Figure 2.13 Confined cylinder released in a fluid, geometry.

The impact of a sphere on water creates subsurface air cavity which are different depending on the material. As the sphere falls, it transfers momentum to the water by forcing it radially outward. This inertial expansion of the fluid is resisted by hydrostatic pressure which eventually reverses the direction of the radial flow, thereby initiating cavity collapse. The collapse accelerates until the moment of pinch-off, at which the cavity is divided into two separate cavities. The most obvious differences between the four impact sequences are the trajectories of the spheres. As the sphere density decreases, several trends are readily apparent:

- the depth of pinch-off decreases
- the depth of the sphere at pinch-off decreases

- the pinch off depth approaches the sphere depth at pinch-off.

The diameter of the sphere is $D = 2.54\ cm$, the impact velocity is $U_z = -217\ cm/s$. The air and water are at rest at the initial state. The air influence from the fall before impact is consequently neglected.

In order to simulate the phenomenon, a 3D-mesh is used since it is a sphere. The dimension of the tank are respected to avoid pressure field discrepancies. The free surface is computed thanks to the Large Interface Model presented in appendix. There is no turbulence model. The time step is adaptive and the maximum Courant number remains under 1.

First, a mesh refinement study is performed. The chosen material is the teflon. The simulation is performed on 3 refinements of 100 000, 500 000 and 2 500 000 cells. These different meshes are refined along the sphere trajectories. In Figure 2.14, trajectories of a teflon sphere are plotted along time for the 3 refinements. The coarse mesh seems to slightly underestimate the depth along time. However, mesh 2 and 3 are in correct agreement along time with the experimental data.

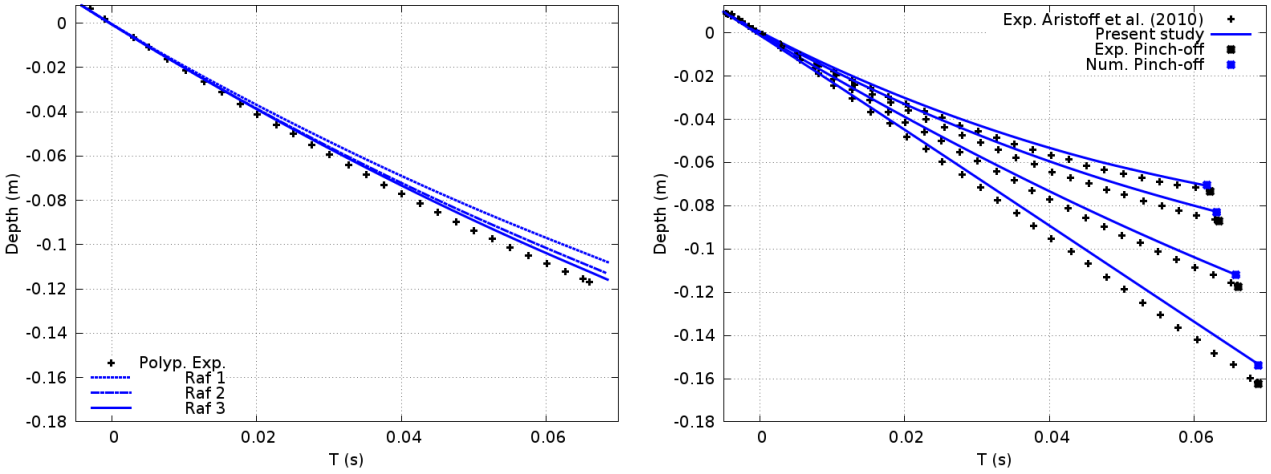

Figure 2.14 Free-fall of a sphere on a free-surface: mesh refinement for teflon (on the left). Numerical/-experimental displacement along time of a sphere free-falling on a free surface for 4 different materials (on the right).

According to the previous result, the numerical simulation are performed with the mesh 3. With three other materials (polypropylene, nylon and steel), the same test case is computed. In Figure 2.14, numerical and experimental trajectories are compared. There is a correct agreement between them. Consequently, the effort of the water entry coming from water and air are correctly reproduced with our numerical model.

	Polypropylene	Nylon	Teflon	Steel
Experiment	62.2	63.5	66.1	68.9
Simulation	61.5	63.1	65.8	68.7
Error	1.11%	0.62%	0.46%	0.2%

Table 2.4 Numerical and experimental pinch-off time comparison.

Based on the snapshots of the free-fall (see Figure 2.15 and 2.16), it is possible to find the pinch-off time. Another method is to use the velocity where a radical change happens exactly at the pinch-off.

Since the experimental pinch-off time are available, a confrontation with numerical results is performed in Table.2.4. There is an excellent agreement between simulation and experiment for the pinch-off time prediction. Moreover, Figure 2.14 highlights the correct prediction of the pinch-off depth and time since there is a maximum of 5% of error.

In Figure 2.15 and 2.16 based on the snapshots given in the experimental study, the numerical simulations are compared along time. For the different materials, the air-water interface is correctly reproduced by the simulation. This case is consequently the first two-phase flow application using the Time and Space Dependent Porosity method with a fluid-structure coupling.

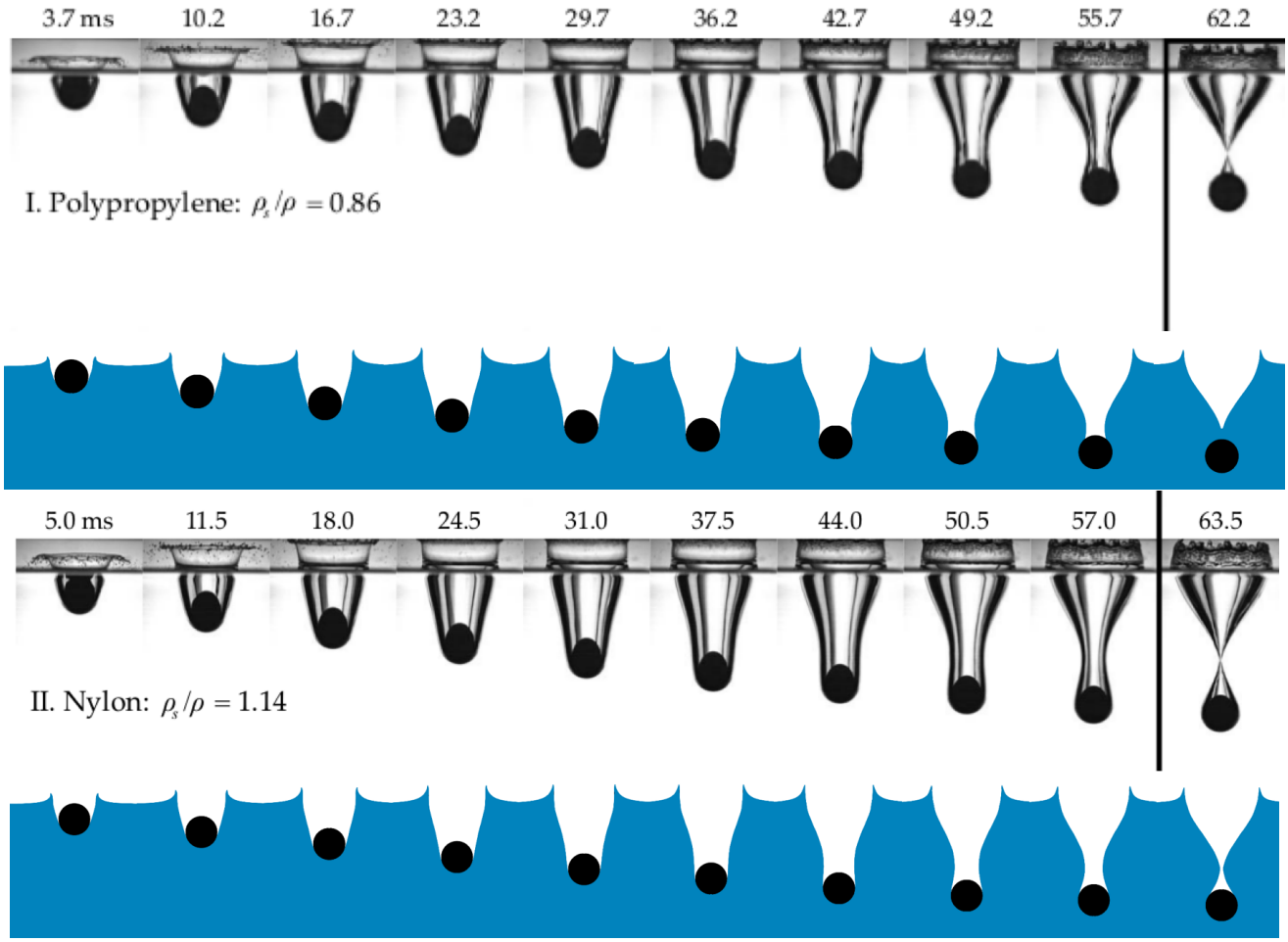

Figure 2.15 Polypropylene and nylon spheres falling on a free surface of water. Numerical (bottom) and experimental (top) snapshot of the sphere entry in water.

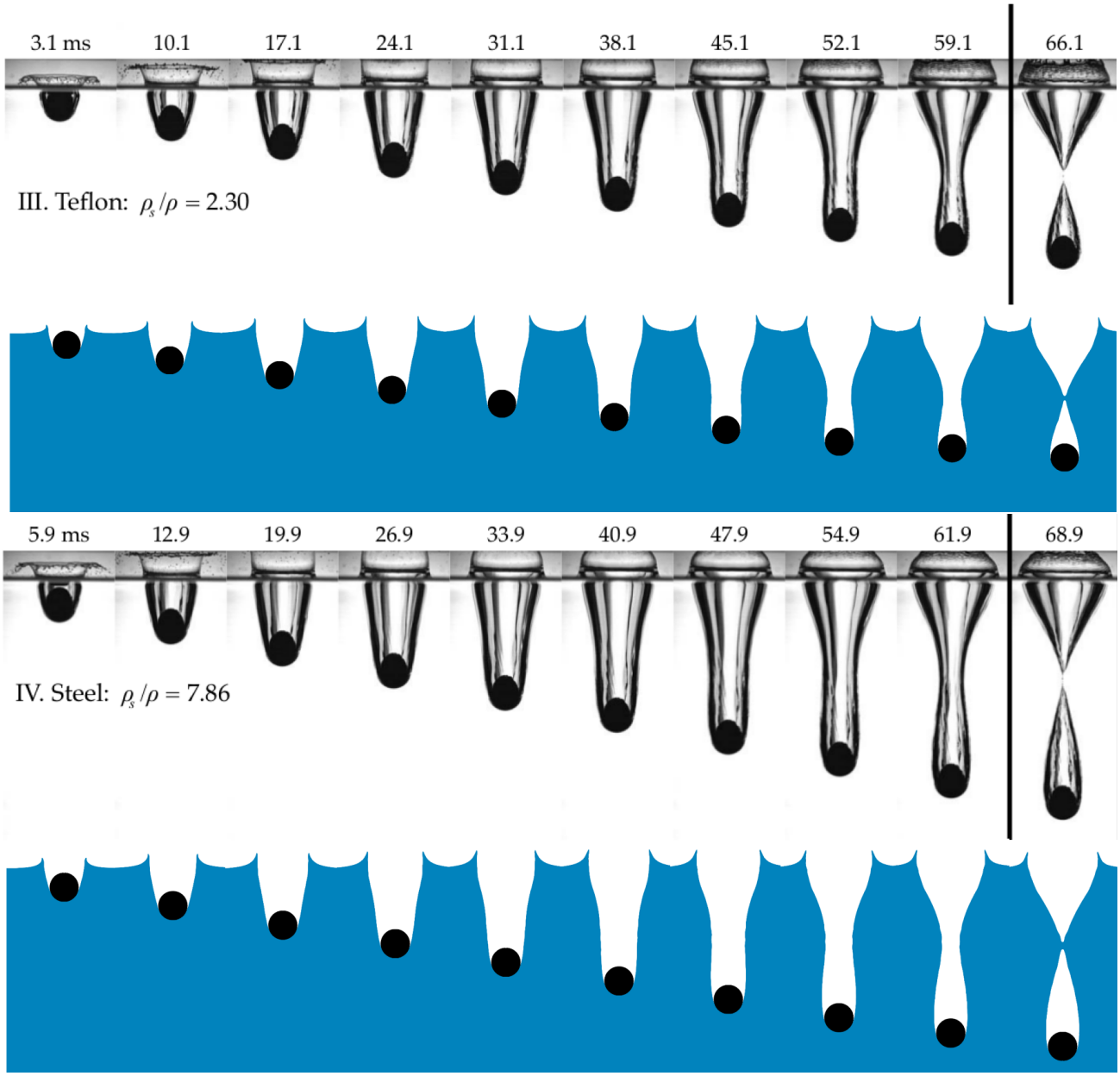

Figure 2.16 Teflon and steel spheres falling on a free surface of water. Numerical (bottom) and experimental (top) snapshot of the sphere entry in water.

Summary and Remarks

After a short description of existing fluid-structure coupling algorithm, the present algorithm has been presented. The computation of the force at wall with the Time and Space Dependent Porosity method is highlighted since it is not conventional. In order to predict the displacement of the structure, a Newmark algorithm is used. Finally, the iterative implicit fluid-structure coupling is described.

Based on three different cases, the coupling is validated before going through the targeted application. First, with the cylinder removed from its equilibrium position in a still fluid, the tolerance parameter to stop iterations is determined. Then, flow-induced vibrations of a cylinder at $Re = 100$ are predicted for different values of mass and stiffness. This has been the first case of flow-induced vibration using

the Time and Space Dependent Porosity method with its fluid-structure interaction module. Finally, a fluid-structure interaction case in two-phase flow is realized. Here, the free-fall of a sphere on a free-surface is studied and compared with experimental results.

Because of the computation time, we did not perform the free-fall of sphere on a liquid-liquid free-surface with high viscosities and densities from Pierson and Magnaudet (2018a,b). A perspective is to perform these case since the two-phase character of the force is highly challenged. These cases are of primary interest since they validate fluid-structure interaction with two-phase flow.

The use of an immersed boundary method to perform fluid-structure interaction is comfortable since it allows large or slight displacement without any dependency on the mesh and consequently to work on complex industrial applications such as hydraulic dashpots for example. In hydraulic dashpots, the free-falling structures slow down because of the reduced distance between the structure and the wall. Therefore, there is large displacement with a very slight thickness between the structure and the wall. The prediction of the structure displacement in this configuration is possible with the FSI module developed in the present work.

A perspective of development is to implement the coupling for rotation since there is only translation for now. Applications like wind turbines or water wheels would be possible to study with the present method.

After these two parts, it is now possible to predict the motion of structure induced by a two-phase flow. A concrete development and validation step has been carried out. Consequently, all the technical tools are gathered to simulate two-phase flows induce vibration in tube bundle. However, before going through the simulation of the phenomenon encountered in steam generators, two-phase cross flows are investigated through different cases.

Chapter 3

Numerical investigation on two-phase cross-flow

In the present chapter, the objective is to physically characterize two-phase cross flows across tube bundles. Based on a numerical approach, the present study tries to illustrate the most influential physical parameters when switching from a two-phase flow mixture to another. Since the high pressure and temperature in operating steam generators limit the instrumentation options, experiments are often performed with other mixtures which are supposed to preserve some features of the original one and allow easier instrumentation. Based on these experiments, using unsteady or semi-analytical models, the stability of a steam generator tube bundle is deduced. The vibrations induced by two-phase flow phenomena are strongly dependent on the flow pattern, and consequently on the mixtures and their physical properties. Cross-flow may induce more vibration to steam generator tubes than internal or axial two-phase flow; that is why this flow is of primary interest since it is responsible for tube fatigue and failure in the U-bends.

In two-phase flow, the flow pattern is dependent on physical properties and mass flow rates from both phases. Recently, Kanizawa and Ribatski (2016) proposed a classification of flow pattern for tube arrays. Based on visual observation such as in Figure 3.1, two-phase flow regimes are distinguished as follows:

- **Bubbly flow** : spherical bubbles smaller than tube spacing dispersed in the continuum liquid phase. This flow pattern is observed for low j_g and for the entire j_l range. There is no significant bubbles coalescence. In this case, the void fraction is low ($< 30\%$). However, for very low j_l, dispersed bubbly flow are possible with an important density of bubbles. In Figure 3.2, the picture of a bubbly flow in an in-line tube-bundle is presented.

- **Churn:** chaotic repartition of gas and liquid in similar proportions. Gas structure equivalent diameter may be higher than the tube diameter. Turbulence induced by bubbles is important. Here the void fraction is between 30% and 90%. In Figure 3.2, the picture of a churn flow in an in-line tube-bundle is presented. Sometimes for high j_g and j_l, a specific churn flow is observed and characterized by intermittent passage of liquid slugs and large gas portions, both at high velocity.

- **Annular flow:** characterized by liquid films around cylinders and droplet flow. It appears for very high void fraction with low j_l and high j_g.

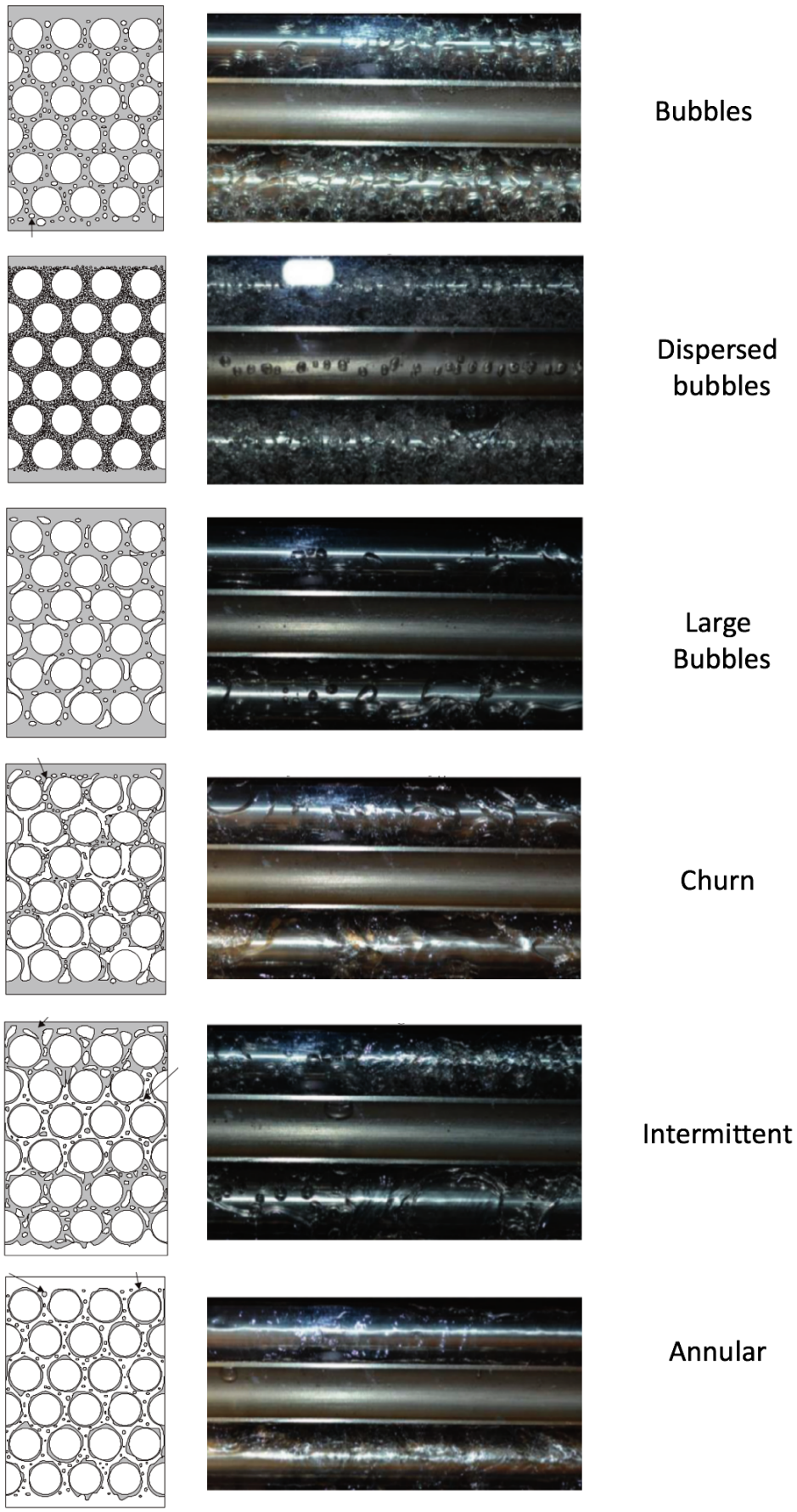

Figure 3.1 Pictures (from the top to the bottom) and flow pattern sketches of bubble, dispersed, large bubbles, churn, intermittent and annular air/water flows in a staggered tube bundle Kanizawa and Ribatski (2016)

Recently, based on literature survey, Mao and Hibiki (2017) classified the different regime depending on the observations from many sources. Many details on the flow pattern from different experiments are presented in their work.

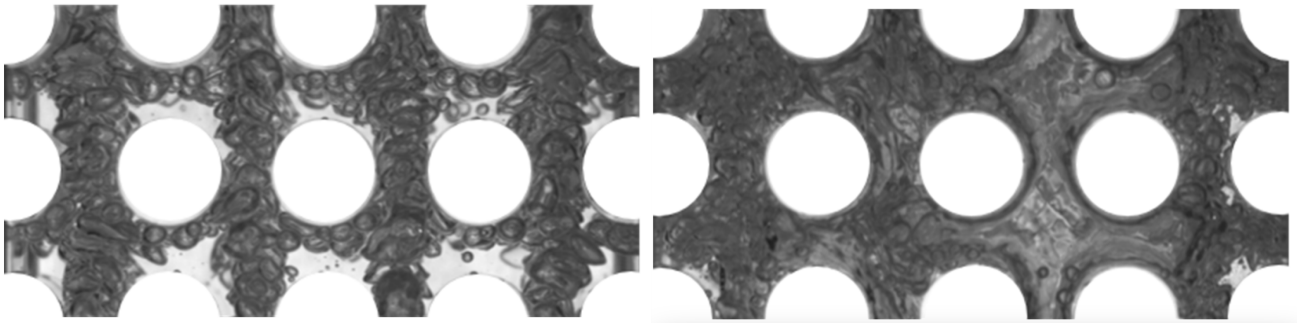

Figure 3.2 Picture of a bubbly and churn flow in in-line tube bundle, Murakawa et al. (2016).

Based on these regime definitions, different experimental studies proposed flow regime maps. One of the first flow regime map is from Grant and Chisholm (1977). Nevertheless, most popular ones are from Ulbrich and Mewes (1994) and Noghrehkar et al. (1999) established respectively by means of visual analysis of flow photographs and by automatic analysis of void probe PDF. Map axis depend on superficial velocities. On Figure 3.3, both maps are compared for a staggered tube-bundle. Many flow regime maps

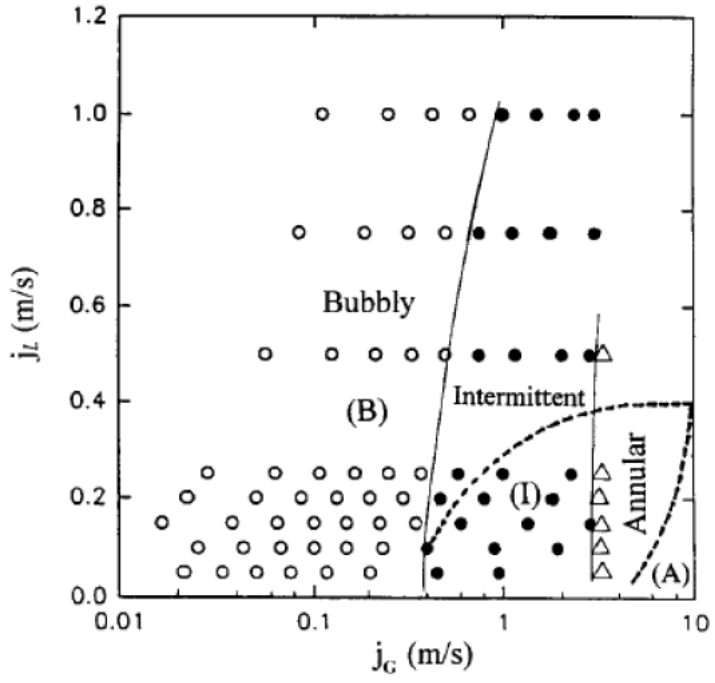

Figure 3.3 Flow regime map comparison for two-phase flow across a staggered tube bundle. Ulbrich and Mewes (1994) (line) and Noghrehkar et al. (1999) (dash).

have been computed for different geometries and mixtures. The considered industrial application being steam generator, the mixture of interest is steam/water at $P = 70\ bar$. As an experiment with similar pressure is expensive, most experiments are performed with air-water at low pressure. However, some experiments are realized with freon/freon, freon/water and others. The choice of the working-fluid is

important in order to be physically similar to the steam water. It is therefore a key point in the use of modeling fluids.

Mixture	Constituant	Pressure	Temperature	$\frac{\rho_L}{\rho_g}$	$\frac{\mu_L}{\mu_g}$	σ
Steam/Water	1	50-70 *bar*	Saturation	25 - 20	47	0.020
Air/Water	2	1 *bar*	293 *K*	833	55.6	0.075
Freon/Water	2	7 *bar*	293 *K*	25 - 20	11.1	0.072
Freon/Freon	1	7 *bar*	Saturation	20.2	14.9	0.006

Table 3.1 Comparison of mixtures used in experiment in terms of physical properties.

Experimental investigations have used steam/water (Axisa et al., 1985; Nakamura et al., 1995b; Mureithi et al., 2002; Mitra et al., 2009), refrigerants (Feenstra and Weaver, 2000; Soussan et al., 2001; Deri, 2018), or air/water mixture (Pettigrew, 1989; Kanizawa and Ribatski, 2016; Benito and Mureithi, 2017).While the experiments using the steam/water mixtures closely resemble the actual steam generators such experiments are very expensive and difficult to perform. Experiments using refrigerants such as Freon-11 are easier to perform since the mass ratio is similar to the targeted one but at low pressure. It is argued that the density ratio of the two phases will affect the difference in flow velocity between the phases.

The previous Table 3.1 compares the different physical properties of each mixture where it is possible to notice some discrepancies. Three relevant quantities are compared:

- **Viscosity ratio**: ratios are respectively from 20 to 100. Here, liquid phases are strongly different in terms of viscosity. However, for such high Reynolds numbers in this kind of geometry, viscous effects seem to be at the second order to influence the two-phase flow regime.
- **Volumetric mass ratio**: ratios are respectively from 20 to 850. When gas is heavier, it may affect the upward velocity of the gas and its ability to follow the liquid. The lighter is a bubble, the more it will follow the liquid stream.
- **Surface tension**: surface tensions are respectively from 0.006 to 0.075 N/m. The effect is on the size and shape of the gas structure. The lower is the surface tension, the weaker is the interface, and the smaller are the gas structures. It plays an important role in controlling the bubble size which is highlighted in Figure 3.4.

These discrepancies are responsible for gas structure size, gas velocity or turbulence; consequently to the fluid forces acting on a cylinder. More recently, Azuma et al. (2018) used a mixture of SF6-ethanol at 6.8 bar having the same physical properties of steam/water at 70 bar. The last assumption made is that there is only one constituent in reality, consequently condensation and vaporization are not taken into account. As such, the use of refrigerants represents a practical alternative where the density ratio and surface tension are closer to those of the steam/water mixture than air/water (Mohany et al., 2012). However, it has been shown that for tube bundle experiments, the impact of vaporization at the wall due to heated tube on the flow was low.

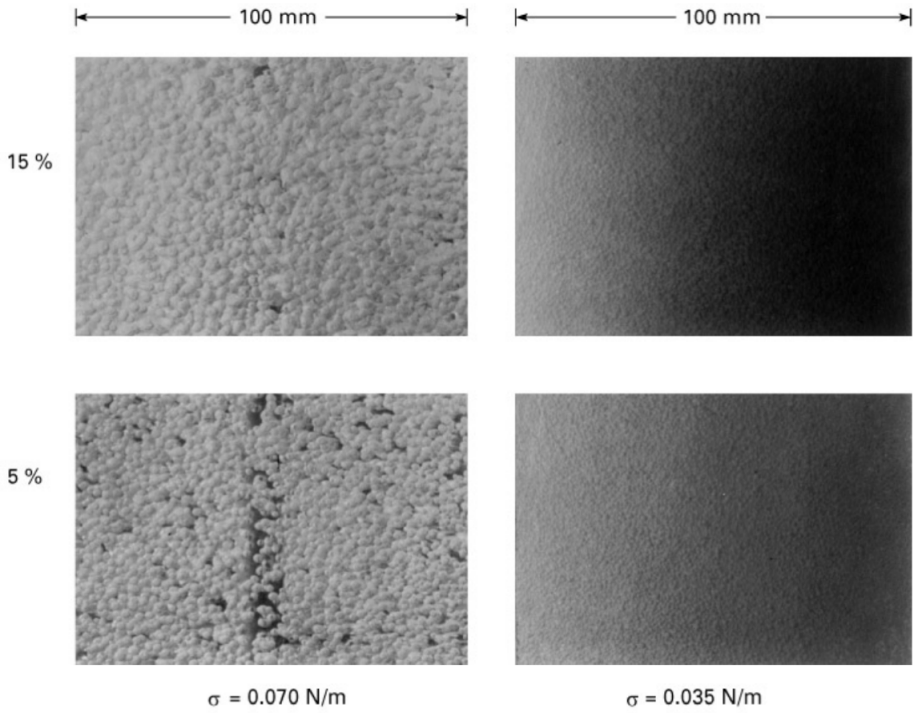

Figure 3.4 Influence of the surface tension on the bubble size, Pettigrew and Knowles (1997). For two different inlet void fractions, the bubble diameter is reduced by lowering the surface tension.

Due to the complexity of the two-phase flow-induced vibrations, the majority of the investigations were directed towards experimental studies. However, the maturity of two-phase flow numerical solvers now allow to perform representative simulations and consequently to study the flow pattern. A numerical model is consequently qualified on a tube bundle configuration to determine the most efficient one to use. Then, on the same geometry, we switch from the previous mixture to another in order to notice discrepancies in the flow able to affect the fluid forces at the wall. Assumptions are there required on the inlet parameters. Moreover with a complex geometry such as the tube bundle, it is extremely difficult to determine parameters of influence. Unfortunately, only a general comment on the void, velocity and size distribution is possible. Therefore, physical properties have been studied on a more simple geometry: the single cylinder. With 3 different mock-up, the influence of parameters are investigated. Finally, the gas structure to cylinder size ratio is highlighted as the most important parameter of influence. Few possible future investigations to complete this study are given at the end of the chapter.

3.1 Selection of a numerical model to use in tube bundle configuration

As presented in the introduction, the flow patterns are of primary interest in these kinds of study. We know that the two-phase flow is characterized by the huge diversity of gas structure sizes. Consequently, a multi-regime model able to track large interfaces as well as dispersed bubbles is required. The present work will show that it is not possible to get the right void distribution by using a spherical bubble assumption and therefore to get the right force at wall. In the present section, different available two-

phase numerical models and closure laws are investigated in order to determine the most competitive to use in tube bundle configurations:

- Generalized Large Interface Model, using a single field for the gas. Depending on the void fraction distribution, the gas field is dispersed or continuous. It allows to simulate a wide range of flow patterns.
- Multi-field approach, using two fields for the gas. Similar to the previous one, the present model uses a dispersed field and a continuous field for the gas depending on local flow parameters. This approach uses the Large Bubble Model (instead of the Large Interface Model in the Generalized Large Interface Model) as a continuous field.
- Dispersed approach, using a dispersed field for the gas. Here, bubbles are considered spherical with a diameter which might be constant or computed based on Ruyer et al. (2007).

Further details can be found in the appendix.

3.1.1 Experiment

The void fraction and gas velocity measurements, coming from an experiment using a freon/freon mixture flowing in an inclined tube bundle, are compared with numerical results. This experiment was performed by the French Atomic Energy Commission (CEA) (Soussan et al., 2001). The experimental device is a tight square channel holding a tube bundle of 40 rows of 5 inclined cylinders (4 tubes and 2 half-tubes) with an angle of inclination $a = 30^o$. These adiabatic tubes have an external diameter of 13.5 mm. For the present study, in order to reduce the computational time, only 11 rows are considered based on the conclusion from Bouillet et al. (2007). Indeed, previous computations on this configuration have already shown that 11 rows of tubes are enough to correctly study the flow properties and pattern. The geometry used for the following numerical simulations is illustrated in Figure 3.5.

The experiment involves a saturated freon (R114) liquid-vapor flow. We often indicate this mixture as *freon/freon*. The physical properties are respectively for liquid and vapor:

- Density: $\rho_l = 1273.974\ kg/m^3$, $\rho_g = 63.2\ kg/m^3$;
- Viscosity: $\mu_l = 2.066.10^{-4}\ Pa.s$, $\mu_g = 1.382.10^{-5}\ Pa.s$;
- Surface tension: $\sigma = 6.005.10^{-3}\ N/m$;
- Temperature and pressure: $T = 350.4\ K$, $P = 8.7.10^5\ Pa$.

Initially, the channel is filled with liquid freon only. At the inlet, the liquid and gas superficial velocities are respectively 0.183 m/s and 0.319 m/s . The constant pressure in the domain is $8.7.10^5\ Pa$. The fluid properties are taken at saturation, consequently no mass transfer occurs.

Void fraction and gas velocity are measured along the line $North - South$ (NS) defined by $x = 48.75mm$ and $z = 276.36mm$, and the line $West - East$ (WE) defined by $y = 48.75mm$ and $z = 276.36mm$.

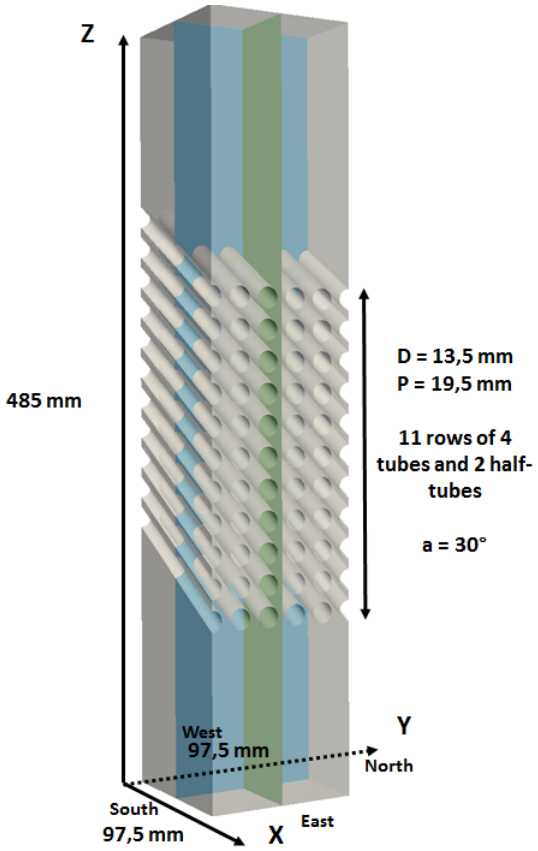

Figure 3.5 Inclined tube bundle experiment (Soussan et al., 2001). In blue and green, North/South and West/East planes are colored.

3.1.2 Sensitivity to the mesh refinement

The mesh has been generated with a particular attention paid to the mesh quality. The resulting grids are fully hexahedral without any non-conformity respectively called Grid 1, Grid 2 and Grid 3 presented in Table 3.2 and Figure 3.6. The cells characteristic size continuity has also been taken into account to build as much as possible a uniform mesh. A sensitivity study has been done with three different refinements for each case. For the present case, the physical time duration is 15 s and the averaging starts from 6 s. All the simulations presented in this section are unsteady with a Courant number under 1.

Mesh refinement	Overall number of cells	Number of cells in between two consecutive tubes
Grid 1	540 960	4
Grid 2	6 480 540	14
Grid 3	59 703 980	32

Table 3.2 Hierarchy of mesh refinement used for the sensitivity study.

In Figure.3.7, averaged void fraction and gas velocity along North/South and West/East lines predicted by the Generalized Large Interface Model with a R_{ij}-ε SSG turbulence model for three mesh refinements are presented. Grid Level 1 appears to be much too coarse to catch the flow dynamics around the tubes, while Grid Level 2 is considered to be satisfying for future use in this kind of applications. Overall, the predicted results are in the correct range of void fraction and gas velocity.

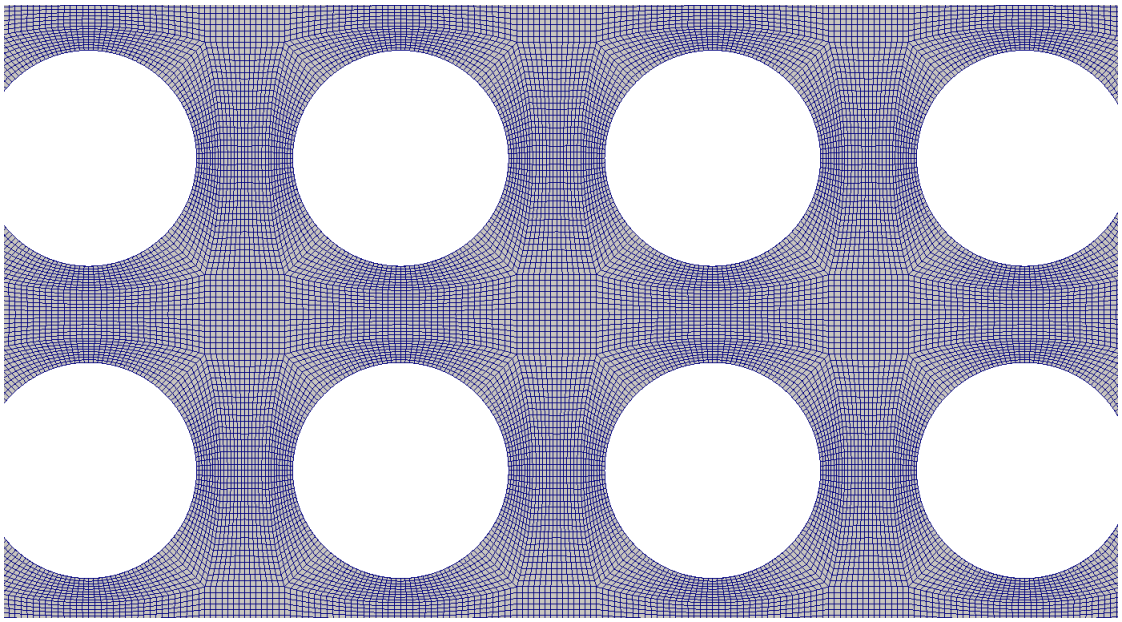

Figure 3.6 Snapshot of the mesh of the tube bundle. It is presented in 2D for only a few tubes in order to see the refinement around tubes

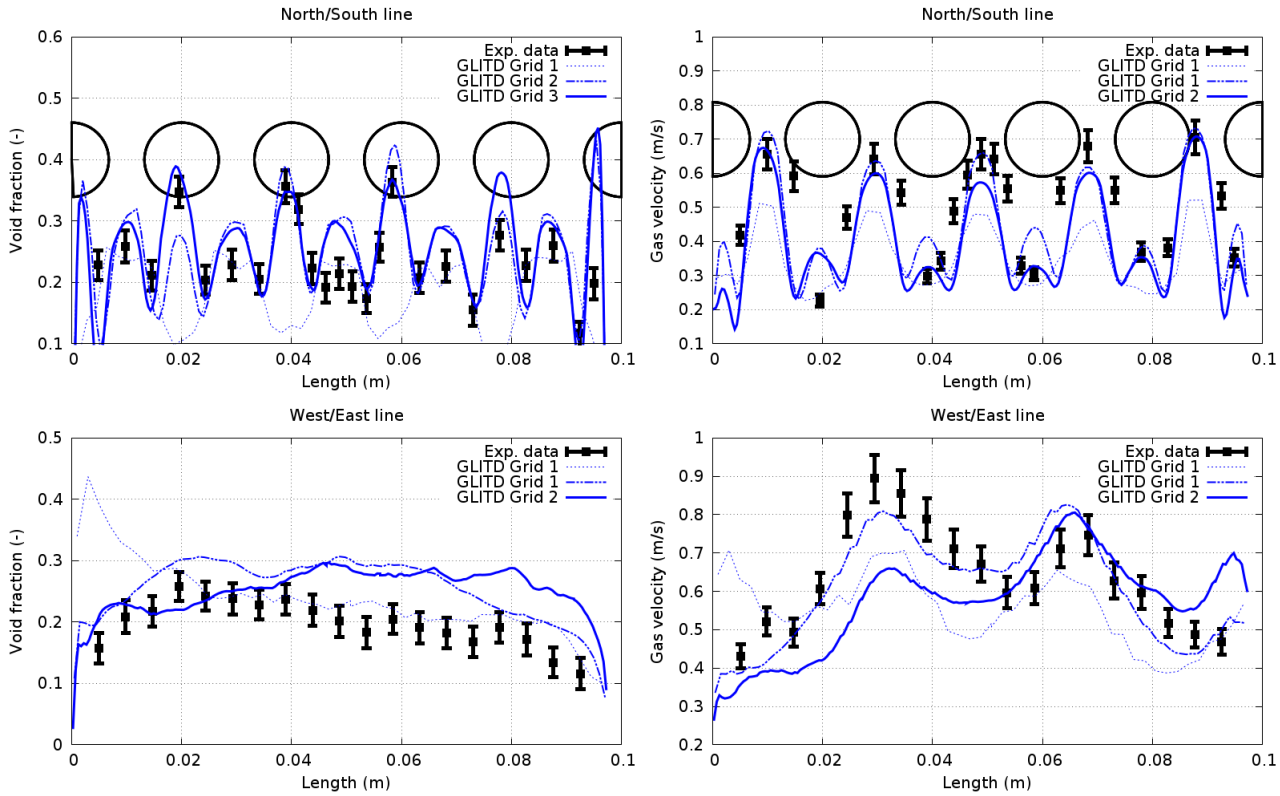

Figure 3.7 Numerical result using the **Generalized Large Interface Model with a R_{ij}-ε SSG turbulence model** for three mesh refinement called Grid 1, Grid 2 and Grid 3. Averaged void fraction and gas velocity along North/South and West/East lines compared with experimental data.

Along NS line, there is a correct agreement between Grid 2 and 3 with the experimental data. However, for Grid 1, it appears that between 2 rows of cylinder (here between the 7th and 8th) the void fraction is under-estimated in front of the cylinders (represented in black on the graphic). This is probably due

to the low number of cells. In contrast, the other grids are in correct agreement in each area. The gas velocity profiles are in agreement with the previous comments.

Along WE line, the void fraction distribution is correctly predicted for each refinement in terms of profile shape, however amplitudes are slightly different from the experiment. With Grid 1, the void is over-estimated in the upper-part of the tube. For the two-others, there is a kind of plateau around 30% of void fraction along tube which is partly over-estimated compared to experimental data. According to Figure. 3.12 (NS and WE slices of the domain are presented at the end of the present section), the gas is slightly going to the upper part of the tube. Consequently, our overestimation is probably due to the reduction of the number of tube rows (40 in the experiment, 11 in the present numerical study). It would also explain the profile of velocity which is slightly under-estimated in the upper part of the tube. Gas structures being larger in the upper part of the tubes, their velocity is higher due to the buoyancy effect. Since the number of rows is reduced with respect to the experiment, the void fraction is low in the upper part and the concentration of large gas structures is consequently lower so the gas velocity.

For the following study, the Grid 2 is used since the time of computation is lower than for grid 3 and the mesh is refined enough to correctly predict the void and velocity distribution.

3.1.3 Numerical Investigation

A) Two-phase flow model sensitivity study

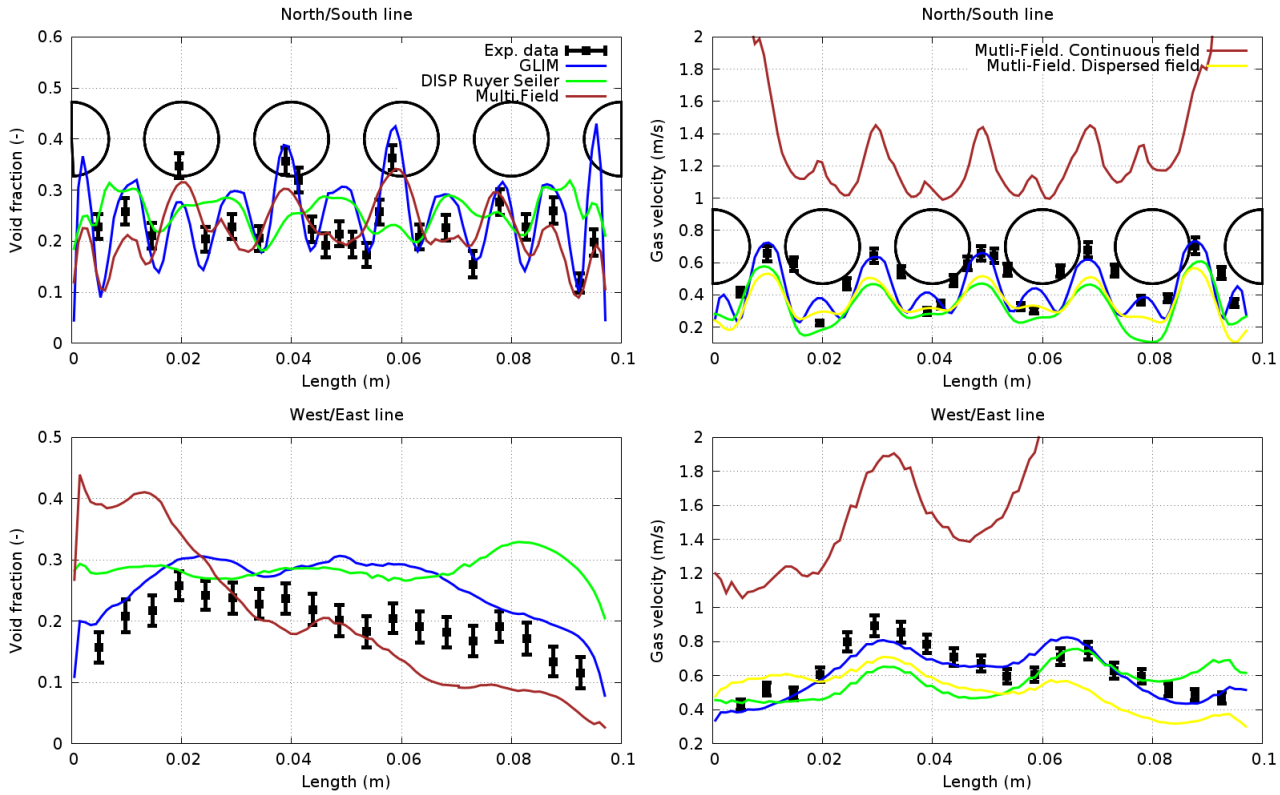

Figure 3.8 Numerical result using the available numerical models from NEPTUNE_CFD. Averaged void fraction and gas velocity along North/South and West/East lines compared to experimental data.

In the present subsection, a two-phase flow model sensitivity study is performed over three two-phase numerical models. The present discussion is based on Figures 3.8, 3.12, 3.13 and 3.17 representing respectively:

- the averaged void fraction and averaged gas velocity from the three models along NS and WE lines compared to experimental data,
- NS and WE instantaneous and time-averaged void fraction distribution slices computed with the Generalized Large Interface Model with R_{ij}-ε SSG turbulence model,
- NS and WE instantaneous and time-averaged void fraction distribution slices computed with the Multi-field model with R_{ij}-ε SSG turbulence model,
- NS and WE instantaneous and time-averaged void fraction distribution slices computed with the dispersed model with R_{ij}-ε SSG turbulence model and a variable bubble diameter.

According to Figure 3.8, along NS line, the void peaks in front of cylinders (black circle on the figure) are correctly reproduced by multi-regime approaches. However, it seems that the dispersed approach is not able or sufficient to predict the void distribution in front of cylinders. Multi-regime approach profiles are very similar but the Multi-field model appears to be the most predictive in terms of void fraction distribution along the NS line.

Along NS line, the gas velocity is well predicted by the Generalized Large Interface model (GLIM). It is possible to illustrate the role of the balance between dispersed and continuous approach for the gas field by looking at the dispersed profile which is close to the GLIM one but slightly underestimated. Moreover, with the Multi-field approach, gas velocity profiles from the dispersed field and from the continuous field are presented and reinforce this remark since the continuous field velocity is really higher than the dispersed field velocity (which is close to the dispersed approach prediction). Here, the continuous field is higher since the large gas structures has a larger buoyancy force because of their volume.

Along WE line, the void fraction distribution from the three models are different. The dispersed approach predicts a quasi-constant void fraction of 30%. Consequently, the tube inclination does not seem to have a real influence with this approach. Bubbles are drained by the liquid since they are too small. At the opposite, for both multi-regime models, the prediction shows an influence of the tube inclination. In the upper part of the tube, GLIM approach fits the experimental data by predicting a low void fraction. In contrast, the multi-field approach predicts a high concentration of gas in this area. This is probably due to larger gas structures rising along tubes and very dependent on the inclination. The rest of the profiles is consequently under-estimated by the multi-field approach where the GLIM appear more in agreement with the experimental data.

Along WE line, the gas velocity distribution is well predicted by the GLIM. Dispersed approach and dispersed field from the multi-field are underestimating it along the whole line. In contrast, it is possible to highlight the high velocities coming from the continuous gas field of the multi-field approach. Once again, this is due to the buoyancy effect.

Finally, from the Figure 3.8, the dispersed approach is not fitted for this kind of flow since it does not reproduce the influence of the tube inclination, neither the void fraction peaks in front of cylinder. The Multi-field approach appears to have a better prediction of the NS void fraction profile but it produces a

higher concentration of void in the upper parts of the tube bundle probably due to larger gas structure predictions. It is difficult to conclude on the gas velocity profiles coming from the Multi-field approach. Therefore, the GLIM is probably the most competitive model regarding these profiles.

According to Figure 3.12, 3.13 and 3.17, void fraction distributions from the three approaches are strictly different even if the profiles along NS and WE lines were similar. The conclusion for the dispersed approach is illustrated on Figure 3.17 given that there is no strong discrepancy between the void fraction between two horizontal tubes and in front of cylinders, and the inclination has no real influence on the bubble distributions. The NS time-averaged void fraction distribution from the dispersed approach is similar to the one from the GLIM (aside from the front of the cylinders). In Figure 3.12, the instantaneous profiles illustrate an important dispersed contribution ponctuated by larger continuous gas structure flows which appears to be more concentrated higher in the tube bundle. It would explain the WE time-averaged void fraction distribution which predicts slightly more and more gas in the upper parts of tube when we are higher in the tube bundle. Consequently, the higher we are in the tube bundle, the larger gas structures we have, the higher concentration of void in the upper parts of the tube since large gas structure are rising along the tube depending on the inclination. In Figure 3.13, each slice is strongly different from the GLIM ones. First, instantaneous profiles reveal a low dispersed gas contribution and a high continuous gas field contribution in mirror with the GLIM. Then, regarding the NS time-averaged slice, the higher we are in the tube bundle, the lower is the void fraction. This is explained by the WE time-averaged slice which shows a high concentration of void in the upper parts of tube, thus an important influence of the inclination and possibly large gas structures. Since the continuous gas is used when bubble are considered too large to be modeled by the dispersed approach, the transition criterion from dispersed to continuous is probably too low compared to the transition criterion from the GLIM. In the present case, the two main differences between them is the use of a surface tension force in the continuous gas field of the multi field approach and the transition criterion (discrepancies between both approaches are detailed in appendix).

Therefore, a simulation is performed with the Generalized Large Interface Model taking into account the surface tension force with R_{ij}-ε SSG turbulence model is presented in Figure 3.9 and 3.14. In the present case, the surface tension is low since $\sigma = 6.0\ 10^{-3}\ N/m$. The results using the surface tension force or not are very similar. It highlights the low influence of the surface tension force in this case. Consequently, the main discrepancy between the GLIM and the Multi-field approach is probably the transition criterion.

As we are looking for the most competitive model, computational times are also recorded and presented in the following Table 3.3. Each numerical simulation is performed with 420 processes over 15 s of physical time. Once again, there are important discrepancies between the models. The Multi-field approach is the most expensive since there is a third field which is also coupled with the others. It is known that the resolution of a continuous field is more expensive than a dispersed field which explains that the GLIM is more expensive than the dispersed approach.

Regarding the overall discussion, a multi-regime approach is required. Moreover, in the present study, the Generalized Large Interface Model appears to be the most competitive model to use in tube bundle configurations. In the literature, numerical simulation using a single-fluid model are carried out based on

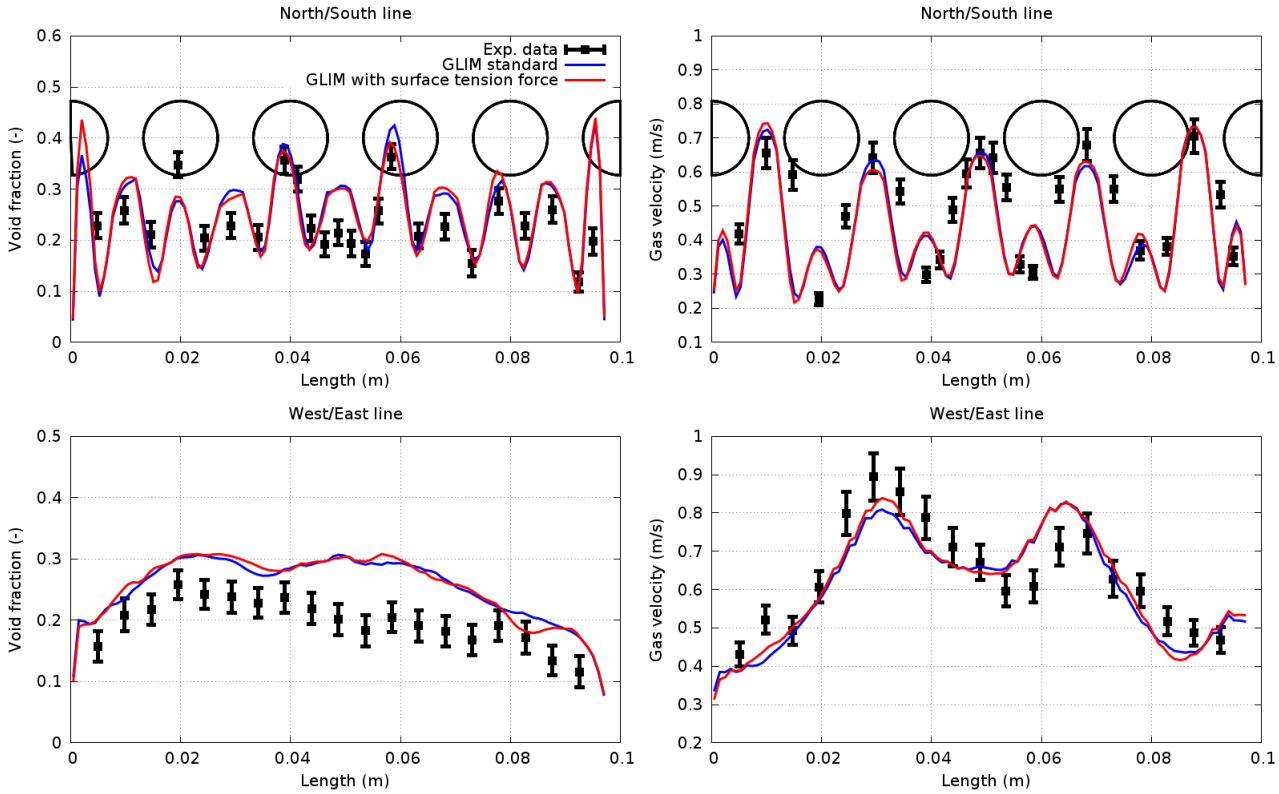

Figure 3.9 Numerical result using the **Generalized Large Interface Model with a R_{ij}-ε SSG turbulence model taking into account a surface tension force**. Averaged void fraction and gas velocity along North/South and West/East lines compared to experimental data.

Numerical model	Time of Computation with 420 processes	Total CPU Time
Generalized Large Interface	27 hours	11 340 hours
Multi-field	84 hours	35 280 hours
Dispersed	11 hours	4 620 hours

Table 3.3 Sensitivity to the time of computation depending on the two-phase numerical model. The cluster that was used is an Atos-bull cluster equipped with Intel@Xeon CPU E5 2680 v4 @ 2.40 GHz (Broadwell) nodes with 28 cores.

the following assumption: bubbles are spherical and having a constant diameter. Most of the time, the two-phase flow behavior is not of primary interest since vibration due to the two-phase flow is the main studied phenomenon. In the following subsection, this assumption is debated.

B) Dispersed-approach with a constant and variable bubble diameters

Since some studies are addressing the topic of vibration induced by two-phase flow in tube arrays with an assumption of spherical bubble with sometimes a constant diameter, we tried to reproduce the two-phase distribution in a tube bundle with the same kind of assumption. In the present subsection, a bubble diameter sensitivity study is performed using a dispersed approach. The present discussion is based on Figure 3.10.

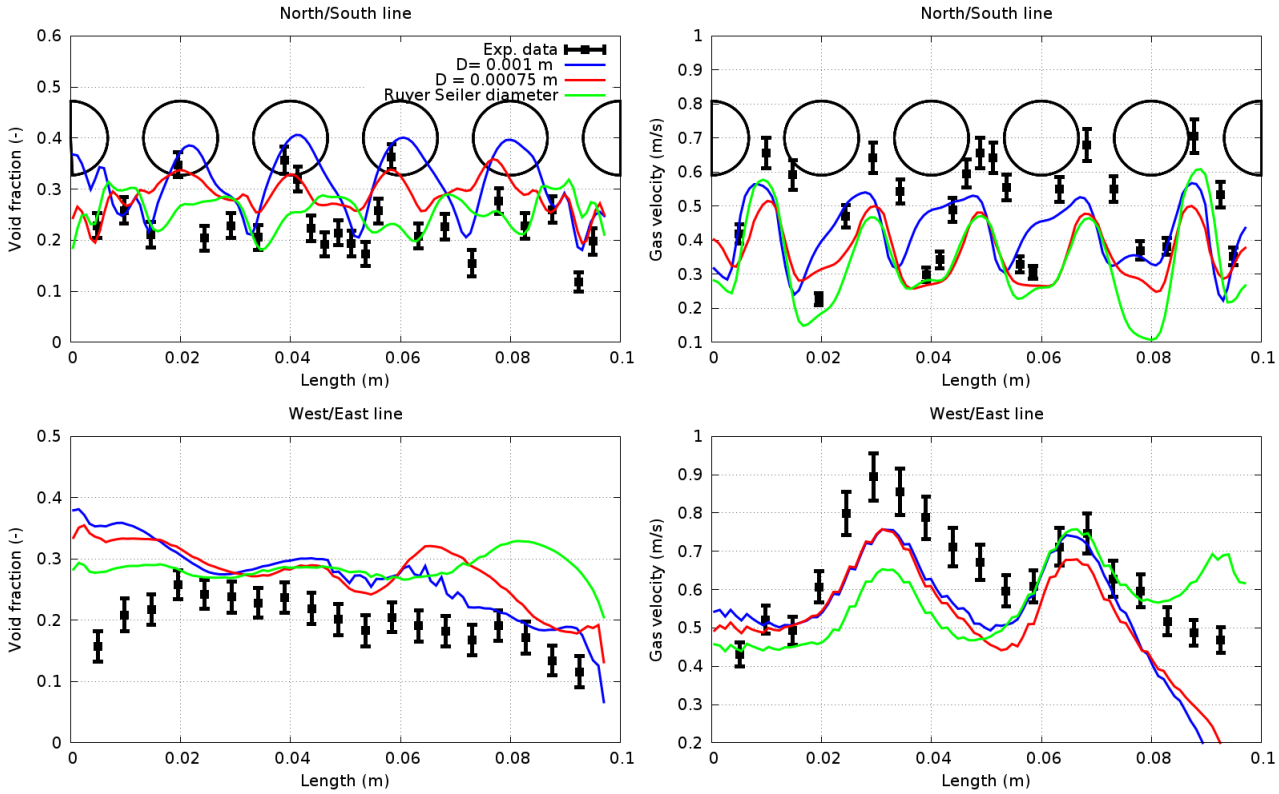

Figure 3.10 Numerical results using the **dispersed approach with a R_{ij}-ε SSG turbulence model with constant or variable bubble diameters**. Averaged void fraction and gas velocity along North/South and West/East lines compared to experimental data.

- the averaged void fraction and averaged gas velocity with three different diameters (variable or constant with $D = 1.0\ 10^{-3}$ or $7.5\ 10^{-4}\ m$ along NS and WE lines compared to experimental data,
- NS and WE instantaneous and time-averaged void fraction distribution slices computed with the dispersed approach with R_{ij}-ε SSG turbulence model and a variable diameter,
- NS and WE instantaneous and time-averaged void fraction distribution slices computed with the dispersed approach with R_{ij}-ε SSG turbulence model and a constant diameter of $1.0\ 10^{-3}\ m$,
- NS and WE instantaneous and time-averaged void fraction distribution slices computed with the dispersed approach with R_{ij}-ε SSG turbulence model and a variable diameter of $7.5\ 10^{-4}\ m$.

According to Figure 3.10, each model is in the correct range of void fraction but with strong discrepancies in their variations along NS and WE lines and planes.

Along NS line, the approach using a variable diameter remains nearly constant with a void fraction of 25%. In contrast, using constant diameters, the higher is the diameter, the more important are the variations with an amplitude of 20% for $D = 1.0\ 10^{-3}\ m$. With this diameter, the prediction of void distribution along this line is the most predictive. The variable diameter leads to low diameters explaining the low variation of amplitude. In contrast, gas velocity profiles are not in good agreement with the experimental data. In fact, the maximum velocity is too low. This is due to the assumption of small spherical bubbles. These peaks are due to intermittent gas slug going up in the tube bundle which can not be predicted by this kind of approach.

Along WE line, the choice of a constant diameter appears to be the worst solution to simulate this kind of flow. Since the size of gas structure is larger and larger along tubes due to inclination, a constant size leads to a correct agreement where bubble diameter is correctly chosen only. But around this location, the diameter being too small (lower in the tube) or high (in the upper part) the void and the gas velocity are not well predicted. Consequently, for constant diameter, it appears that the void fraction and velocity is well predicted at the middle of the tubes. However, in the lower part, the gas velocity prediction is strongly underestimated, and in the upper part the void fraction is over-estimated. Nevertheless, even by using a variable diameter, the dispersed approach is still not able to predict the flow. It highlights the necessity to use a multi-regime approach.

C) Turbulent model sensitivity

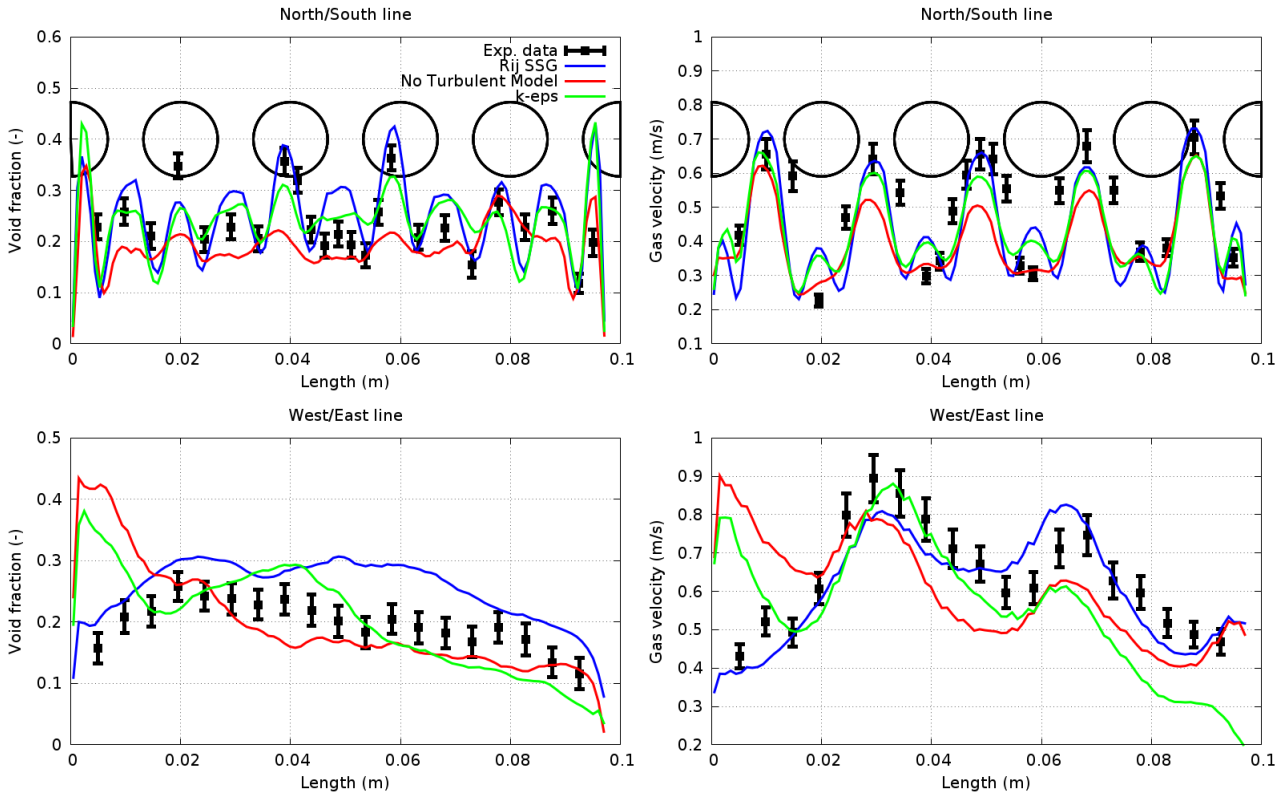

Figure 3.11 Numerical result using the **Generalized Large Interface Model with different turbulent models**. Averaged void fraction and gas velocity along North/South and West/East lines compared to experimental data.

In the present subsection, a turbulence model sensitivity study is performed on the available models in NEPTUNE_CFD. The present discussion is based on Figures 3.11, 3.12, 3.16 and 3.15 representing respectively:

- the averaged void fraction and averaged gas velocity predicted with three different turbulent models along NS and WE lines compared to experimental data,
- NS and WE instantaneous and time-averaged void fraction distribution slices computed with the GLIM with R_{ij}-ε SSG turbulence model,

- NS and WE instantaneous and time-averaged void fraction distribution slices computed with the GLIM with k-ε turbulence model,
- NS and WE instantaneous and time-averaged void fraction distribution slices computed with the GLIM without any turbulent model.

The influence of the turbulence model plays a role :

- on the liquid velocity profiles since the turbulent viscosity is not the same,
- on the break-up or coalescence prediction consequently on the size of bubbles.

According to Figure 3.15, the turbulent model has an important influence on the void distribution. It appears that for the present refinement, the use of a turbulent model is required since the profiles without turbulent model are the worst.

Along NS line, numerical results using R_{ij}-ε SSG and k-ε are in correct agreement with the experimental data. The void amplitude is higher with the R_{ij}-ε. In contrast, there is mostly no variation of void fraction without turbulent model.

Along WE line, discrepancies between R_{ij}-ε SSG and k-ε are more noticeable. In fact, it occurs that the turbulence model has an important influence in the upper part of the tube. Overall, R_{ij}-ε SSG turbulence model is the most predictive. Regarding the evolution along the z-axis, with the overestimation of the void (so the velocity) in the upper part of the tube, the predictions on the real geometry containing 40 rows of tubes would be in a better agreement with the R_{ij}-ε SSG than using k-ε turbulence model (see Figure 3.16).

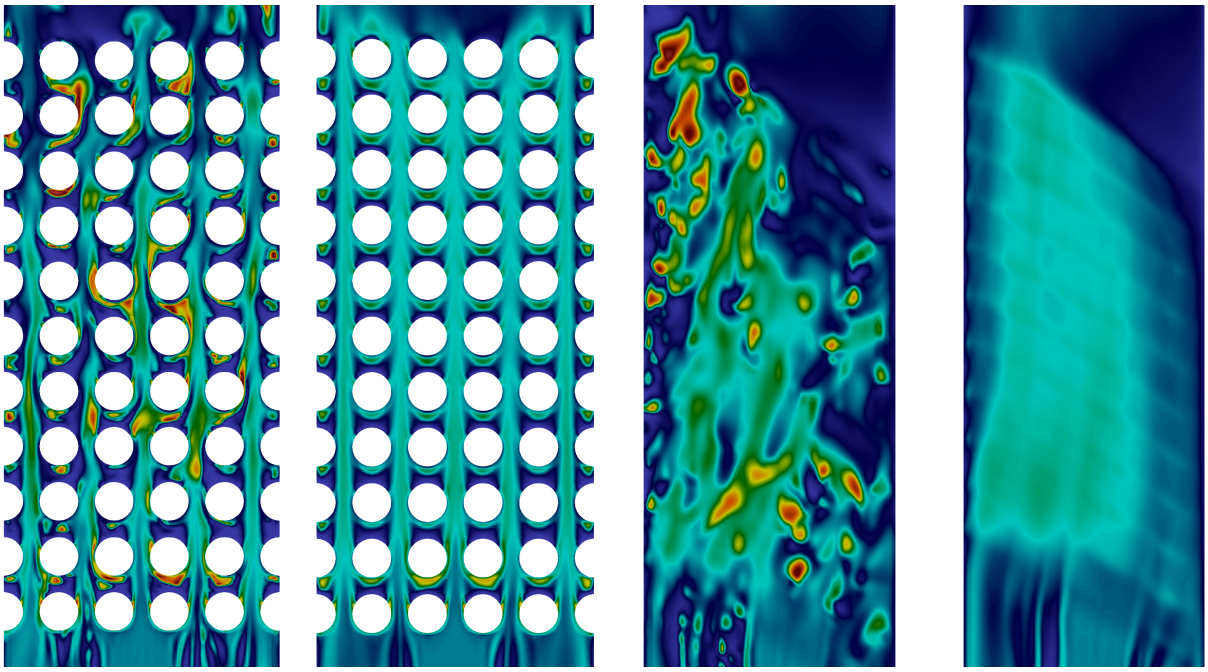

Figure 3.12 Numerical result using the **Generalized Large Interface Model with a R_{ij}-ε SSG turbulence model**. From left to right: instantaneous void fraction distribution on NS plane, averaged void fraction distribution on NS plane, instantaneous void fraction distribution on OE plane and averaged void fraction distribution on OE plane.

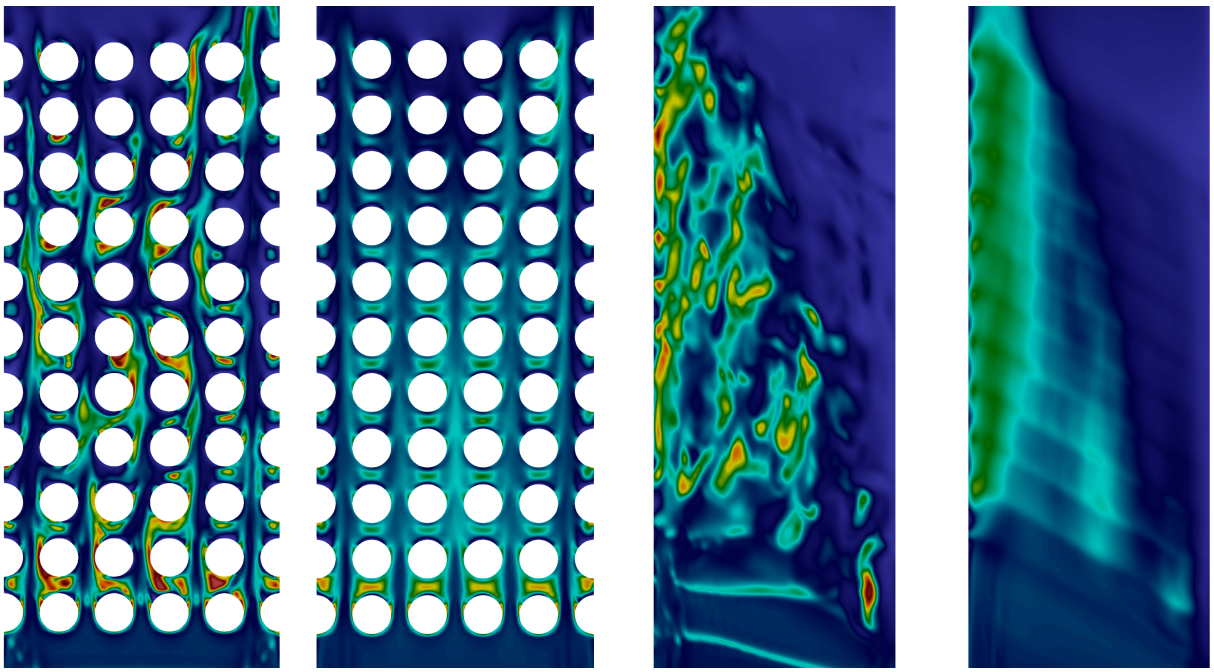

Figure 3.13 Numerical result using the **Multi-Fields approach with a R_{ij}-ε SSG turbulence model**. From left to right: instantaneous void fraction distribution on NS plane, averaged void fraction distribution on NS plane, instantaneous void fraction distribution on OE plane and averaged void fraction distribution on OE plane.

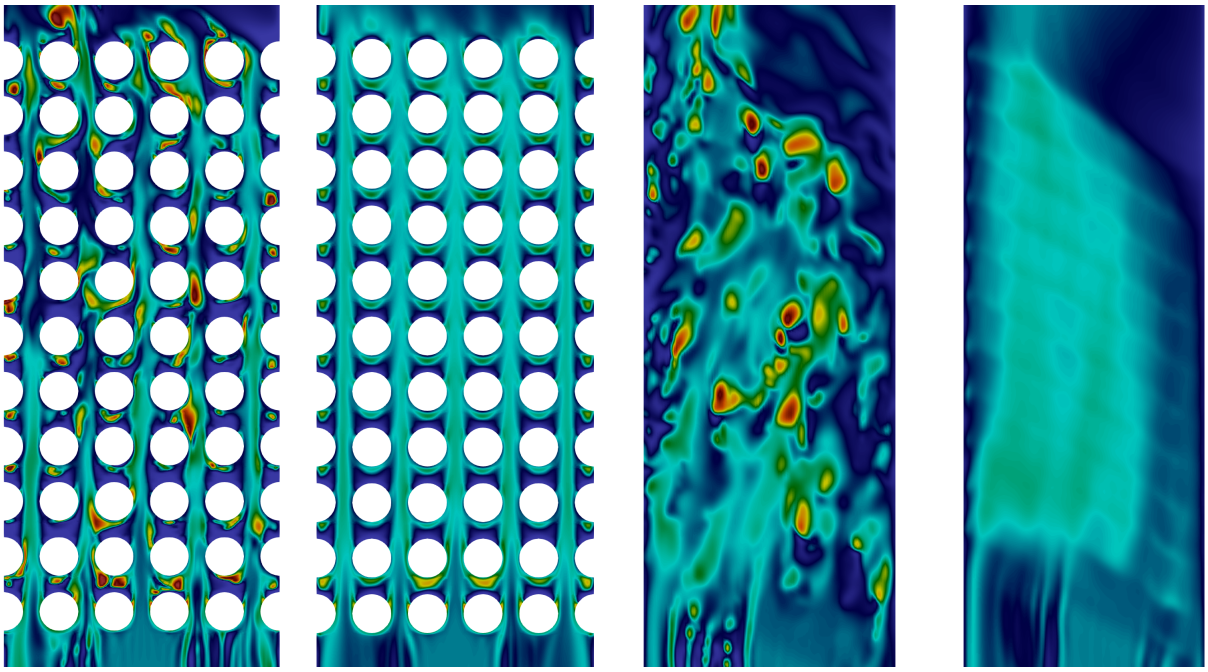

Figure 3.14 Numerical result using the **Generalized Large Interface Model taking into account the surface tension force with a R_{ij}-ε turbulent model**. From left to right: instantaneous void fraction distribution on NS plane, averaged void fraction distribution on NS plane, instantaneous void fraction distribution on OE plane and averaged void fraction distribution on OE plane.

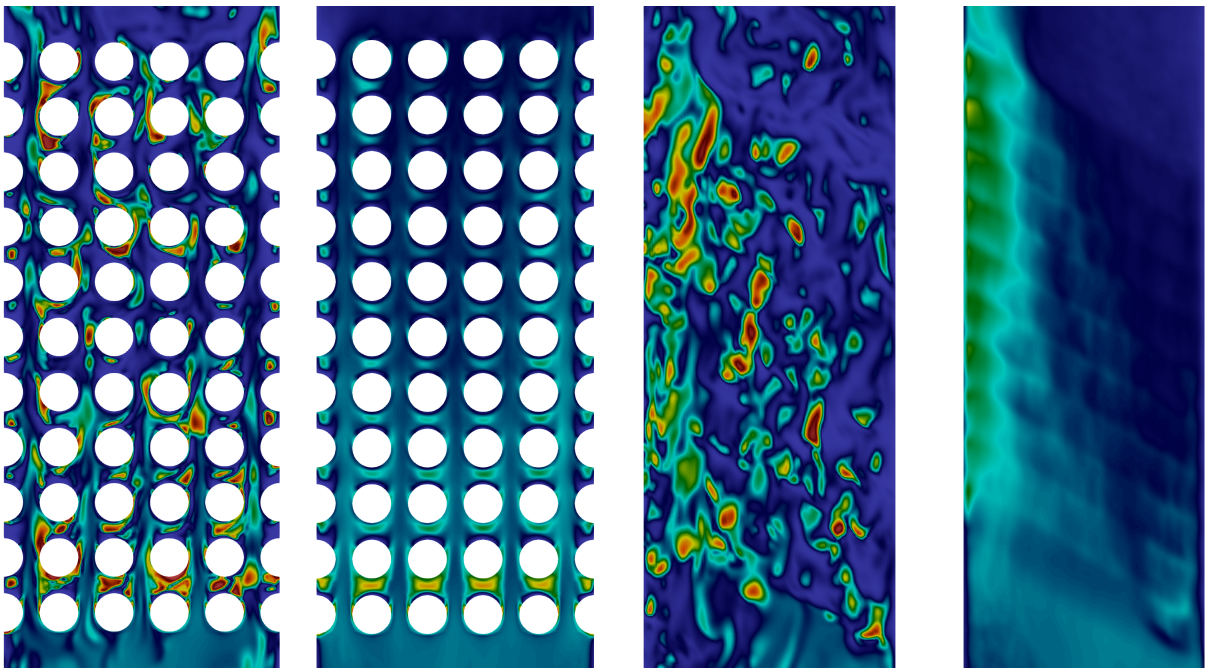

Figure 3.15 Numerical result using the **Generalized Large Interface Model without any turbulent model**. From left to right: instantaneous void fraction distribution on NS plane, averaged void fraction distribution on NS plane, instantaneous void fraction distribution on OE plane and averaged void fraction distribution on OE plane.

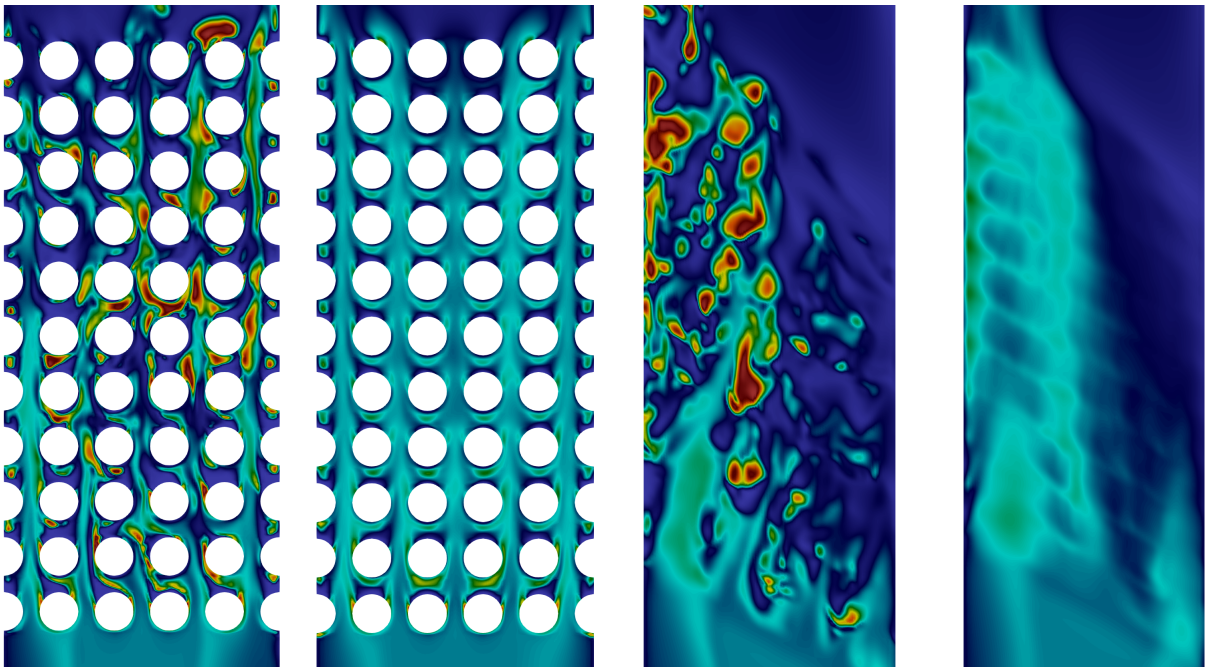

Figure 3.16 Numerical result using the **Generalized Large Interface Model with a k-ε turbulent model**. From left to right: instantaneous void fraction distribution on NS plane, averaged void fraction distribution on NS plane, instantaneous void fraction distribution on OE plane and averaged void fraction distribution on OE plane.

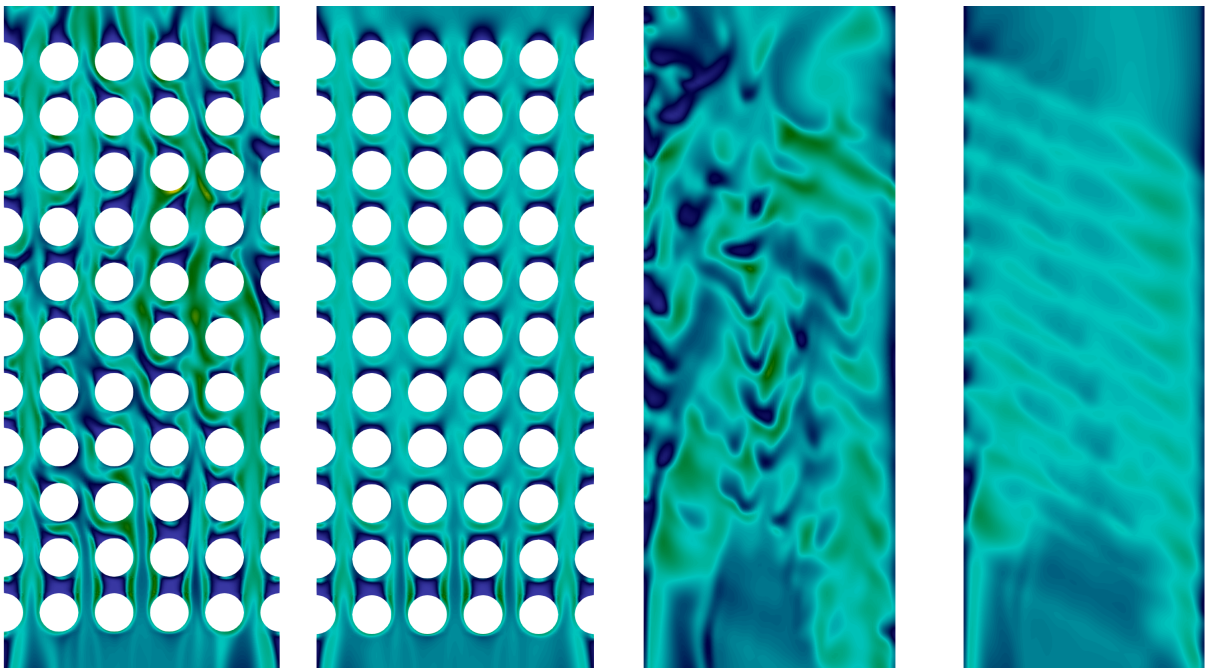

Figure 3.17 Numerical result using the **dispersed approach with a R_{ij}-ε SSG turbulence model**. From left to right: instantaneous void fraction distribution on NS plane, averaged void fraction distribution on NS plane, instantaneous void fraction distribution on OE plane and averaged void fraction distribution on OE plane.

3.2 Investigation on the mixtures used in experiments

Flow-induced vibrations of tubes in two-phase flow heat exchangers are a concern for the nuclear industry. When operating conditions are too severe to allow convenient measurement procedures, relevant phenomena are investigated by means of small-scale experiments using modeling fluids which are different from the real ones. Similarity has then to be taken into account. Some experiments tried to address this topics in the past. Gay et al. (1988) compared air/water with freon/water mixtures in a triangular pitch bundle. Axisa et al. (1985) and Nakamura et al. (1995a) compared steam/water with air/water. All these experiments involved large facilities and took several years to perform.

Relying on numerical simulations, we start to set-up a methodology to compare two different mixtures which may be used as modeling fluids in experiments. As we considered flow regime prediction to be a key point at this stage, an horizontal pipe where a two-phase flow regime map was experimentally obtained in air/water Bottin et al. (2014) has been used to validate the multi-regime approach previously mentioned in air/water flow (Benguigui et al., 2017). A numerical experiment is performed by exchanging the two working fluids of the test cases. The aim of this study is to see if for the same inlet superficial velocities (consequently the same volumetric flow rates), two mixtures exhibit the same behavior or not. Then, air/water is used in the inclined tube bundle. The main assumption of this model is the fixed critical void fraction range where the model chooses a dispersed or a continuous approach for the gas field which can be different depending on the two-phase flow mixture.

We simulate the tube bundle experiment by using an air/water mixture instead of freon/freon. Results with both mixtures are compared in terms of instantaneous and time-averaged void fraction distributions in Figure 3.18. Air/water and freon/freon do not have the same void fraction distributions. Void fraction is lower in front of most of the cylinders for air/water and higher for freon/freon. While in two-phase freon gas structures accumulate behind the cylinders (Figure 3.18, top) in air/water they don't (Figure 3.18, bottom). This kind of behavior, i.e. no gas behind cylinders in air/water, were also observed in a previous experiment of air/water in tube bundles Remy (1982) for different inlet void fractions and superficial velocities. Moreover, in freon/freon, North/South void fraction profile has globally a smoother aspect compared to air/water where the gas phase concentrates mainly in the flow channels between the cylinders. In freon/freon in West/East plane (along the cylinder span), void fraction profile is higher in the lower part of each tube compared with air/water where void fraction is higher in the top part. Gas structures seems consequently to be larger with air than with freon, probably due to the surface tension discrepancy. These void fraction distributions show the possible discrepancies in terms of fluid forces around cylinders depending on the choice of the mixture. The variation in terms of void fraction profile in front of cylinder is of primary interest for fluid forces on the cylinders due to the two-phase flow. The load depending on the void fraction around the cylinder comes consequently mainly from the liquid in air/water and from both phases in freon/freon. This may probably lead to different vibration amplitudes. The tube inclination dependence appears to be more significant with air/water, this may be due to the higher mass ratio between the fluid phases and the larger gas structures.

The two-phase flow behaviors are consequently strongly different between the two selected mixtures of the present study. However, it does not show explicitly that the forces (so the vibrations) around cylinders are also strongly different. Moreover, the assumption made on inlet parameters are questionable.

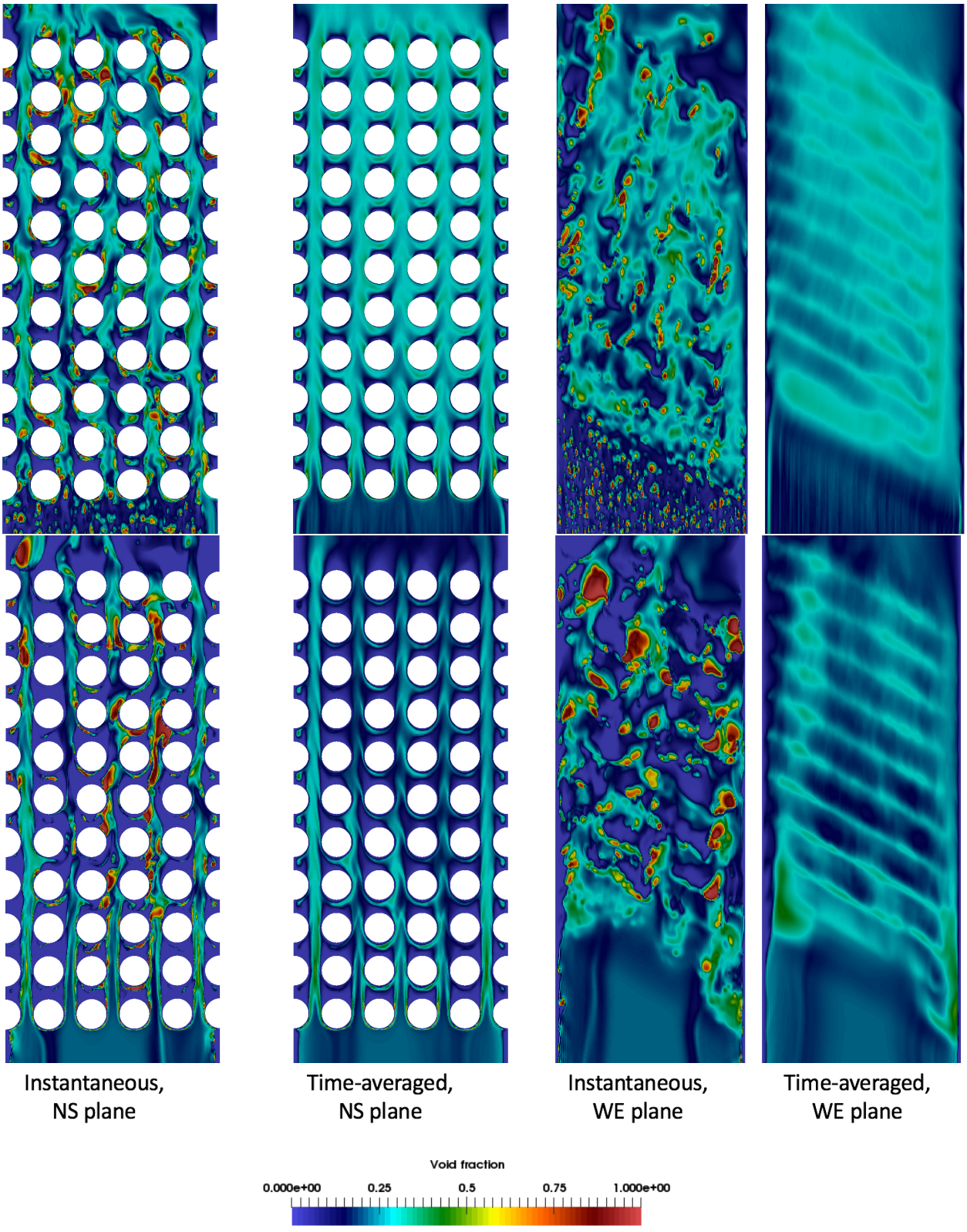

Figure 3.18 Numerical experiment for the inclined tube-bundle experiment with **freon/freon (top view)** and **air/water (bottom view)**. Instantaneous and time-averaged void fraction are present in the NS and WE plane.

Consequently, in order to study two-phase cross flow and the influence of mixture physical properties we choose to work with only one cylinder.

3.2.1 Two-phase flow around a cylinder, literature review

To understand the impact of two-phase flow on tube-bundle, it is important to see how bubbles may affect turbulence in the wake of a cylinder. Moreover, depending on the two-phase flow regime, a cylinder may have a different response. For two-phase cross-flow around a single cylinder, Karman vortices (like in single-phase flow) are formed for void fractions below 15% only, according to Hara and Ohtani (1982). This critical void fraction for vortex shedding depends on the ratio of the averaged bubble diameter to the cylinder diameter, and increases with decreasing bubble diameter. Moreover, Hara (1982) measurements of the fluctuating lift and drag forces for various void fraction highlight that beyond a certain void fraction these forces increase dramatically.

In 1985, Inoue et al. (1985) published a sensitivity study to void fraction, velocity, bubble to cylinder diameter ratio where the changes due to two-phase flow in terms of pressure or velocity profiles are also compared. These air/water experimental data are an interesting starting point to numerically study two-phase flow across a single cylinder. In their study, they addressed a particular interest to bubble

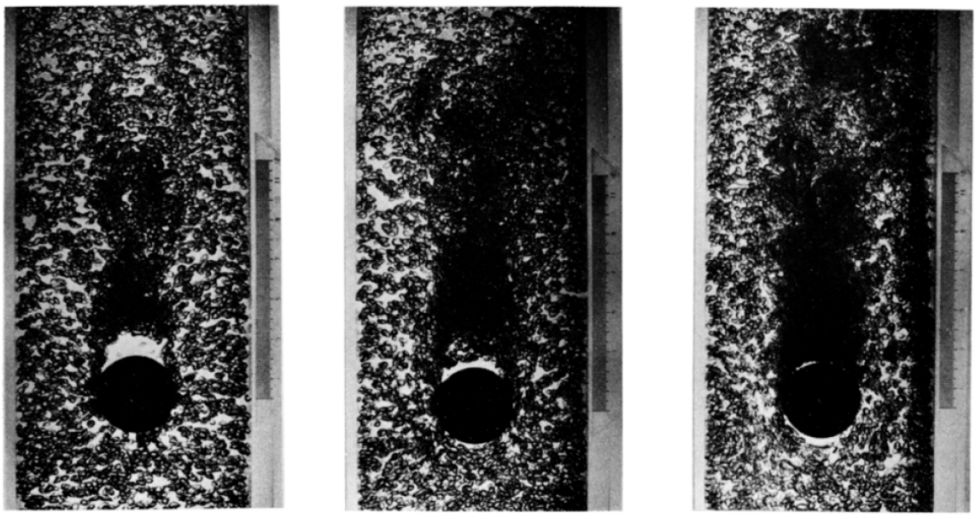

Figure 3.19 Picture of bubbly flow around a cylinder for $D_{cylinder} = 40\ mm$, $\alpha_0 = 8\ \%$, and $U_0 = 0.45,\ 0.9,\ 1.9\ m/s$ from left to right, Inoue et al. (1985).

densification and to the turbulence changes because of the bubbles. In the wake of the cylinder, at the separation point, there is a densification of bubbles which is bigger and closer to the wall when the velocity increases. Due to the static pressure gradient, there is no bubble close to the cylinder. The liquid layer thickness in the rear of the cylinder is thicker when the velocity is lower. In contrast, at the front, the layer is thicker for higher velocities. By increasing the cylinder diameter, the densification of bubble is bigger. Then, when the inlet void fraction is increased, the peak position of bubble may go downstream but the void distribution is not disturbed.

Then, in 1993, Meng (1993) performed two different experiments on dispersed two-phase flows around obstacles. The first one is in air/water at atmospheric pressure, and the second is at high pressure

(60 bar) with only one component, water. He studied the void fraction distribution, Reynolds number and bubble to cylinder size ratio influence. Main observations are similar to the ones from Inoue et al. (1985) for the atmospheric pressure experiment. Once again, among the three characteristic parameters, $d_{bubble}/D_{cylinder}$ is found to be the most important parameter to determine void fraction distribution patterns of a bubbly flow past a cylinder.

The experiments under the atmospheric pressure and high pressure conditions show differences on two points, mainly because of the small ratio of bubble size to cylinder size in the second case:

- In the wake, small bubbles are more dispersed (by turbulence) than big ones. As a result of the peak void fraction region for small size bubbles not only is farther away from the cylinder but also has a lower α/α_0 value than that for big size ones at the same Re.
- Elongation of the peak void region is observed as Re increases under higher pressure condition. Such a process is not so readily discerned at atmospheric pressure since it involves large bubbles. The suppression effect of bubbles on turbulence in the wake is much stronger than the one with the smaller bubbles. Mixing effect (or cross flow-axis effect) is to a large extent suppressed by the presence of big bubbles.

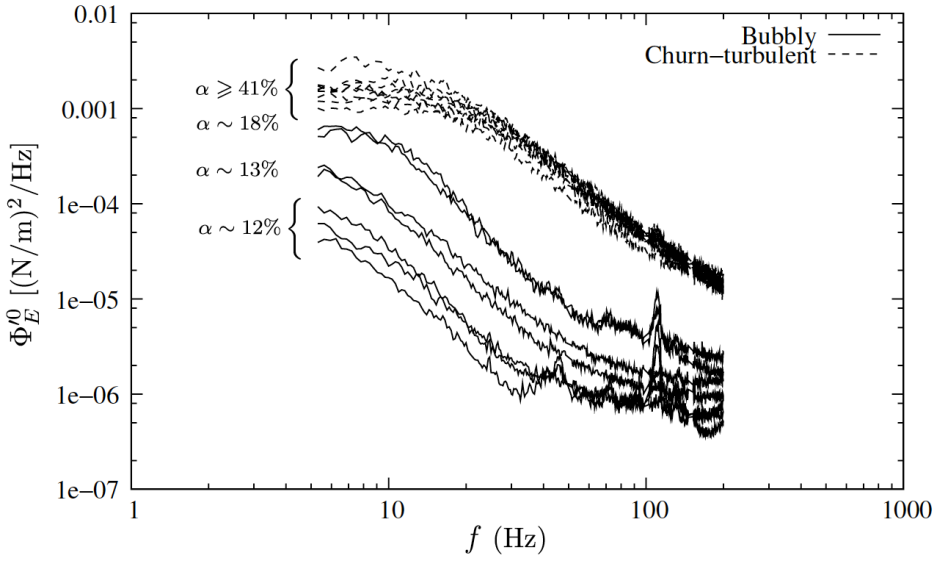

Figure 3.20 Evolution of the reference equivalent spectra versus frequency for different inlet void fraction, (Pascal-Ribot and Blanchet, 2007).

Pascal-Ribot and Blanchet (2007) studied forces around a single cylinder for different inlet void fraction inlet and velocities with an air/water mixture. They assessed the buffeting lift forces exerted on a rigid cylinder in air/water cross-flow. An interesting result is presented in Figure 3.20 which reveals the role of two-phase flow regimes. Two different zones are observed :

- over 41% of void fraction, a cluster of the force spectra is observed. The void fraction influence seems to be very low after this key critical value of void.

- under 41% of void fraction, the spectra is increased with the void fraction. Consequently, even if the void distribution is not disturbed by inlet void increase, it has an influence on the force spectra.

Their experiment highlights that bubble size affects the fluctuation intensity in terms of fluid force at the wall. In the wake of the cylinder, velocity profiles are strongly dependent on the size of bubbles.

Finally, thanks to few experiments with a single cylinder, the high influence of bubble to cylinder size ratio (mainly), velocity and inlet void fraction is highlighted. In the present thesis, a numerical study is dedicated to learn more about this kind of flow which is a source of behavior understanding for flow across tube arrays.

3.2.2 Influence of void fraction on the force around a cylinder for a steam-water flow

In the present work, the objective is to show the role of void fraction on fluid forces. Based on a single cylinder experiment, it is possible to observe similar behaviors with a tube bundle (Pascal-Ribot and Blanchet, 2007). Relying on the validation of the numerical model to predict correctly two-phase flow regimes (Merigoux et al., 2016; Benguigui et al., 2017); we tried to numerically identify flow pattern, based on the fluid force records.

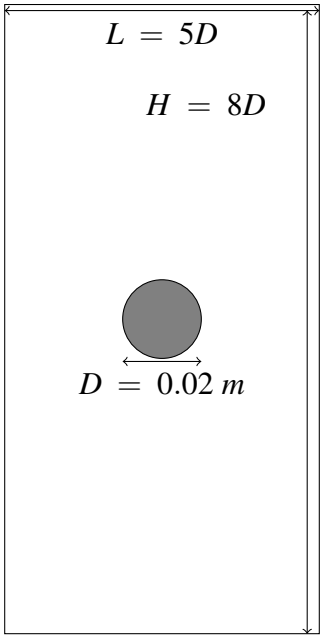

Figure 3.21

A cylinder is considered with a diameter $D = 20\ mm$, a length $L = 2D$. The 3D-domain is 5Dx8Dx2D. A steam-water flow under 70 bar is considered and modeled with the Generalized Large Interface Model (detailed in appendix) since a wide range of void fraction is explored from 0% to 100%. Performing a simulation of flow around a cylinder for such Reynolds number is tough. Consequently, a R_{ij}-ε EB-RSM (Elliptic Blending Reynolds Stress Model) turbulence model is used. This model does not use any wall law, therefore the mesh has to be fine enough at the wall.

Steam and water are injected with the exact same velocity $u = 1\ m/s$. 9 steam-injectors are on the inlet surface. The rest of the surface injects only dispersed flow. Symmetry conditions are used for the surfaces around. The fluid-forces are recorded.

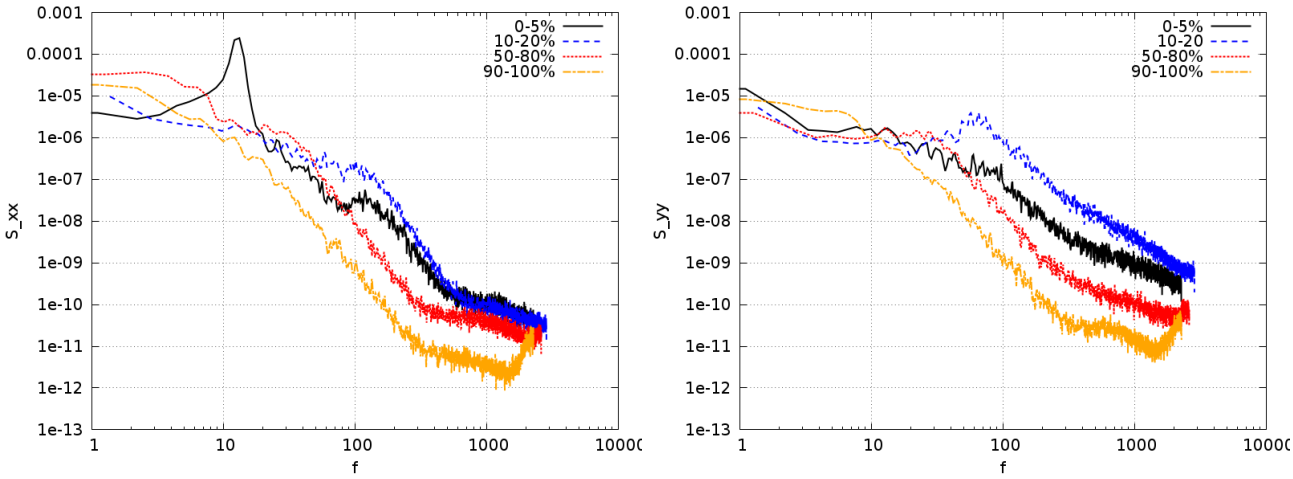

Figure 3.22 Drag and lift force spectrum for four different inlet void fraction (respectively left and right).

In Figure 3.22, four force spectrums are presented in drag and lift for different inlet void fractions. It is possible to see that they are different depending on the void fraction and consequently the flow pattern. Below 20% of void fraction, spectrums are very similar, the main difference being around 80 Hz. This is due to the injectors of steam which periodically produce large bubbles, consequently the bubble release frequency. However, the peak of frequency (characteristic in single phase flow) decreases with void. Then, for higher void fractions, the force spectrum is lower and lower for mid and high frequencies and similar for low frequencies.

In order to better understand the impact of void fraction, the force records are presented in Figure 3.23 and 3.24. From 0-5% to 10-20%, the force amplitude is reduced for the drag and increased for the lift. Moreover, the periodic behavior of the force is less noticeable by increasing the void. In fact, the passage of bubbles around the cylinder and their impact are respectively responsible for the decrease of the drag and the peak in the lift (see subsection “Impact of the mixture on the force around a tube”). It would also explains the reduction of the periodic behavior of the signal. Then, the density and the viscosity of the steam are lower than the liquid which reduce the amplitude of the force. From 10-20% to 50-80%, the lift amplitude is reduced and drag signals are radically different. For the lift amplitude, this is probably due to the reduction of the homogeneous density. For the drag, the impact of large structure of gas and liquids and their passage leads to this intermittent signal with large and small periods of more or less large amplitude. From 50-80% to 90-100%, for both signals, it appears that the two-phase character plays an important role in the noise of each signal since the 90-100% is not as noisy as the 50-80% one. The last signals are consequently low in drag and lift amplitude with very few noise coming from the remaining liquid structures. Based on this quick study of the influence of void fraction on the forces around a cylinder, it is possible to highlight the great influence of the different flow patterns. Thanks to other runs, it has been highlighted that the variation of void fraction is not responsible of the discrepancies between these 4 signals, but the variation of flow pattern is. Therefore, the role of flow pattern is of primary interest for the understanding of two-phase flow induced vibrations in tube bundles.

Consequently, since the flow pattern depends on the mixture, the reproduction of a steam-water flow at 70 bar with another mixture should consider the capability of having the same flow pattern.

In order to study the parameter of influence at the inlet, we choose to consider only the bubbly flow regime.

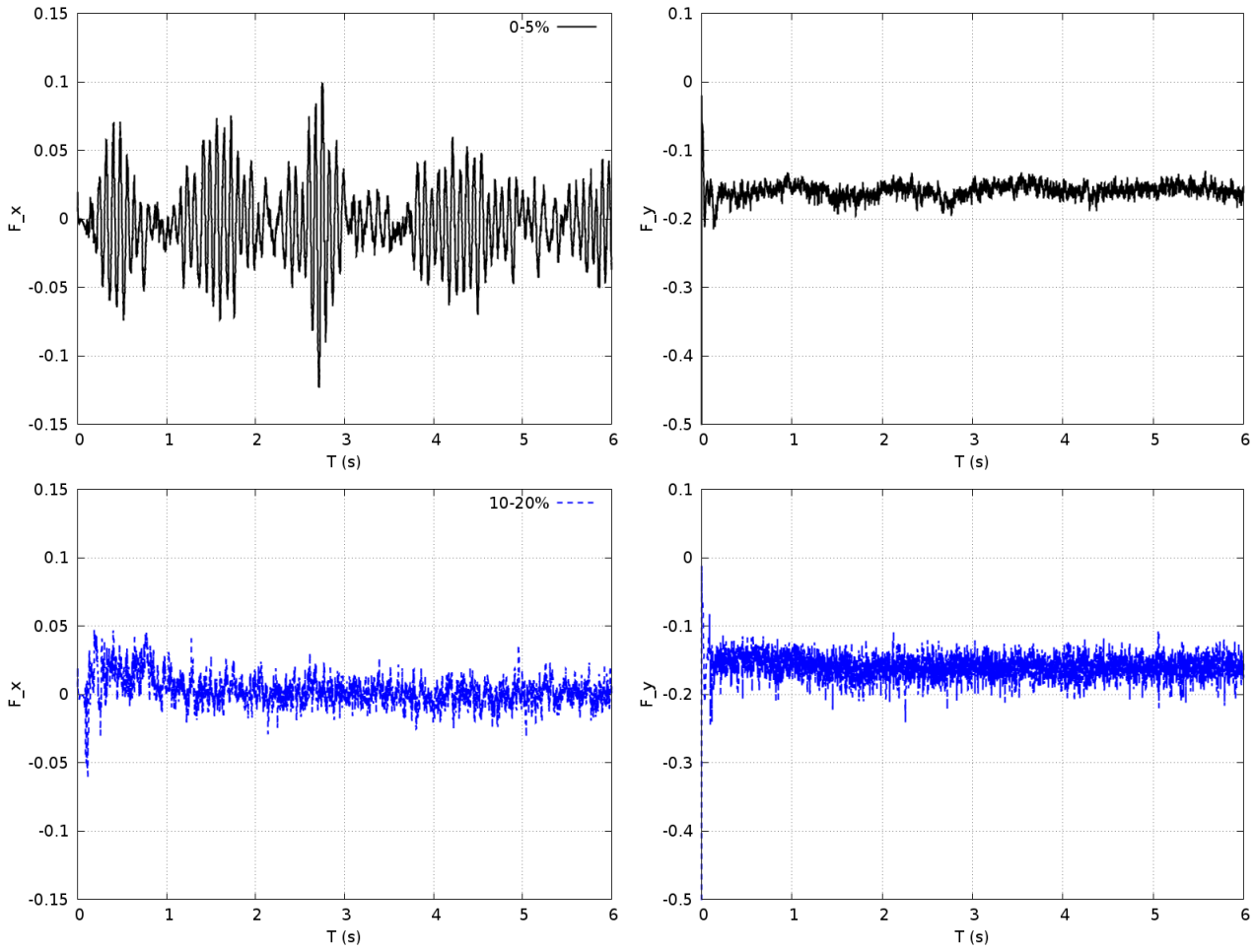

Figure 3.23 Drag (left) and lift (right) force records along time for 0-5% (top) and 10-20% (bottom) of void fraction.

3.2.3 Parameters of influence for a dispersed flow around a cylinder

The experiment from Inoue et al. (1985) deals with two-phase flow around a confined single rigid cylinder. It is a vertical upward air/water flow. Air is injected into water in order to have a uniform bubbly two-phase flow. The cross section is a rectangle of 120x60 mm.The total length of the channel is 1900 mm and the cylinder is located at 1300 mm from the inlet. The length of the cylinder is 58 mm and its diameter is between 10 and 40 mm. The flow characteristics are investigated for different bubble to cylinder diameter ratios, inlet velocities and inlet void fractions. The main parameters measured are the averaged void fraction, liquid velocity and static pressure.

Since the CFD code is able to generate a uniform inlet bubble distribution, the height of the domain is reduced from 1900 mm to 1000 mm with a cylinder located at 400 mm. The case with $\alpha_{inlet} = 8\%$, $U_{inlet} = 0.9\ m/s$ and $D = 40\ mm$ is used for the presented validation. A dispersed approach is used to

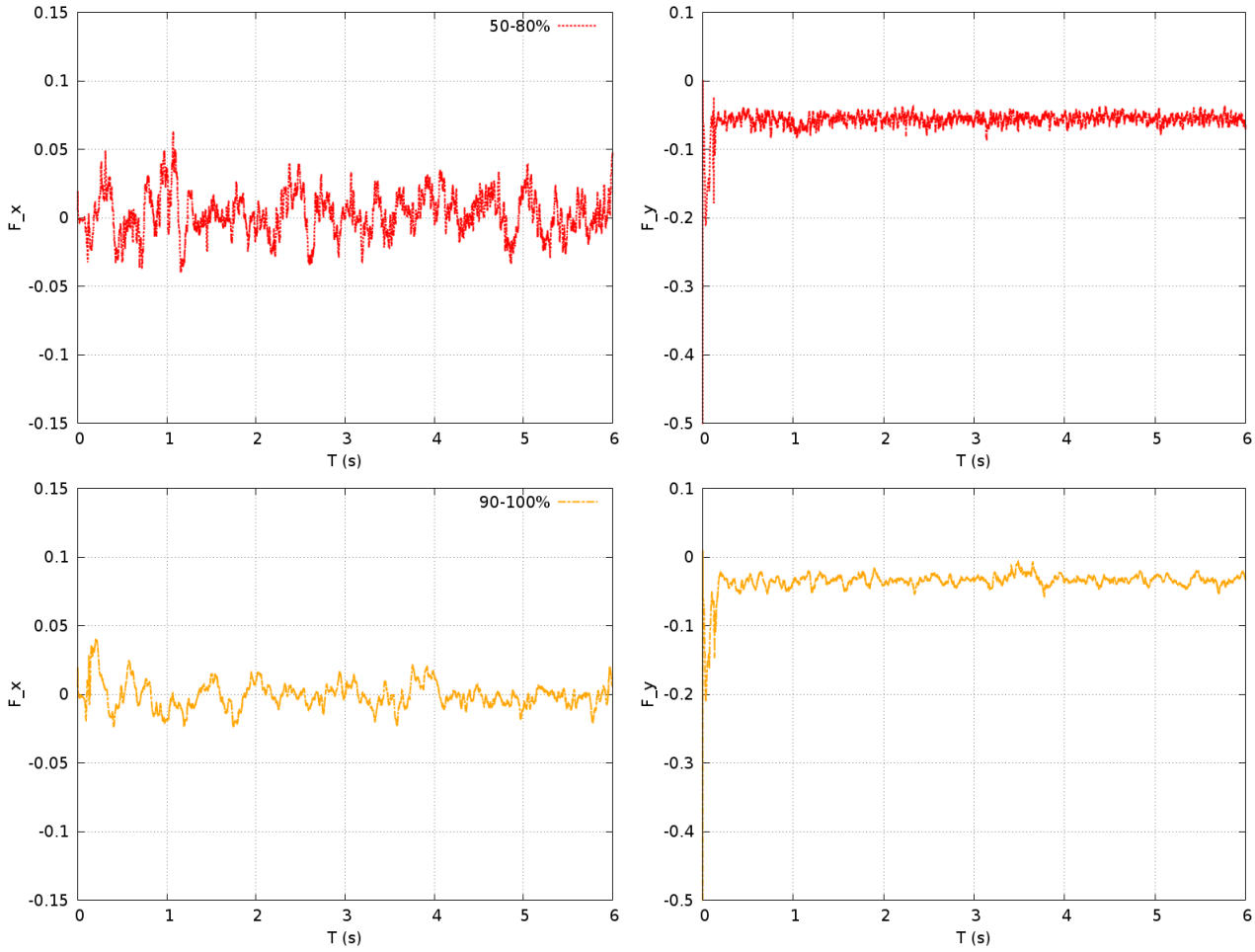

Figure 3.24 Drag (left) and lift (right) force records along time for 50-80% (top) and 90-100% (bottom) of void fraction.

model bubbly flows, its description is proposed in appendix. Top and bottom surfaces are respectively identified as inlet and outlet. The other walls have a non-slip condition. The simulation is unsteady and performed during 5 seconds. A mesh refinement study is performed and compared to experimental results. In the present case, the Reynolds number is 36 000 which is really high. The mesh has thereafter to be very fine close to the cylinder wall to correctly capture the vortex shedding. The result obtained with 3 mesh refinements is presented in Figure 3.25. In comparison with the experiment, the more the mesh is refined, the closer we are from the experiment. The numerical prediction is not accurate where the vortices are created. In this area, the bubbles are captured by the vortices which explains the densification of bubble. But in the simulation, the vortices are not accurately reproduced given that the Reynolds number is extremely high. Consequently, at this location, the simulation is not accurate even if the behavior is correctly reproduced. For the rest of the study, the most refined mesh available at this time is used to enrich the experimental conclusions.

According to Figure 3.26, the inlet void fraction influences the location of the vortices. In fact, the lower is the void fraction, the closer the vortices are from the cylinder. By increasing the void fraction, the distribution is similar but larger. If the two cases with 4% and 8% have similar profiles, the last one is different. This is due to the bubbles affecting the liquid flow. This observation was also made by Pascal-Ribot and Blanchet (2007) in another way. They showed that under 11% of void, the forces were

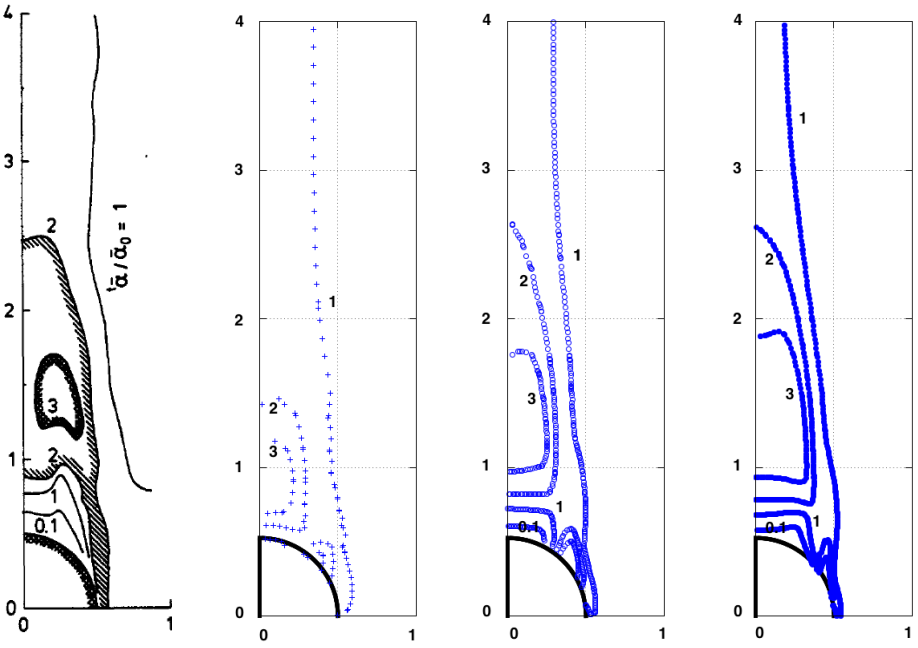

Figure 3.25 Averaged void fraction distribution around a cylinder with $\alpha_{inlet} = 8\%$, $U_{inlet} = 0.9m/s$ and $D = 40\ mm$. From left to right, there are experimental data, mesh 1, mesh 2 and mesh 3.

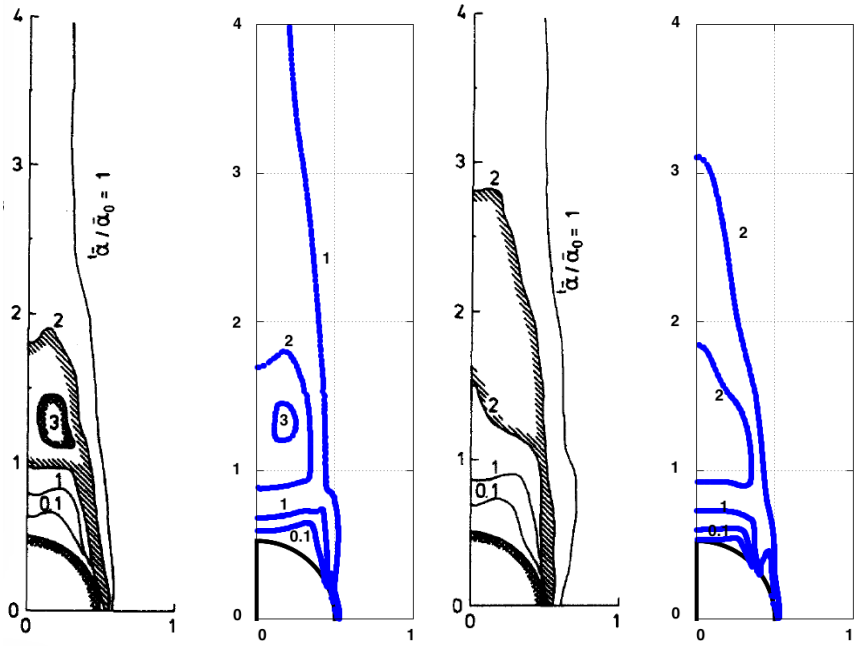

Figure 3.26 Averaged void fraction distribution around a cylinder with $\alpha_{inlet} = 4\%,\ 15\%$, $U_{inlet} = 0.9\ m/s$ and $D = 40\ mm$. From left to right, there are experimental data for $\alpha_{inlet} = 4\%$ and its simulation, $\alpha_{inlet} = 15\%$ and its simulation.

similar. However between 11% and 20%, the force spectra exhibits a clear dependence on void fraction: it increases with the void.

According to Figure 3.25-3.27, the averaged void fraction profiles depend on the inlet velocity. For $U_{inlet} = 0.9,\ 1.9\ m/s$, bubbles are captured by the vortices created by the liquid flow around the cylinder. The higher is the velocity, the more concentrated and less dissipated is the void fraction distribution.

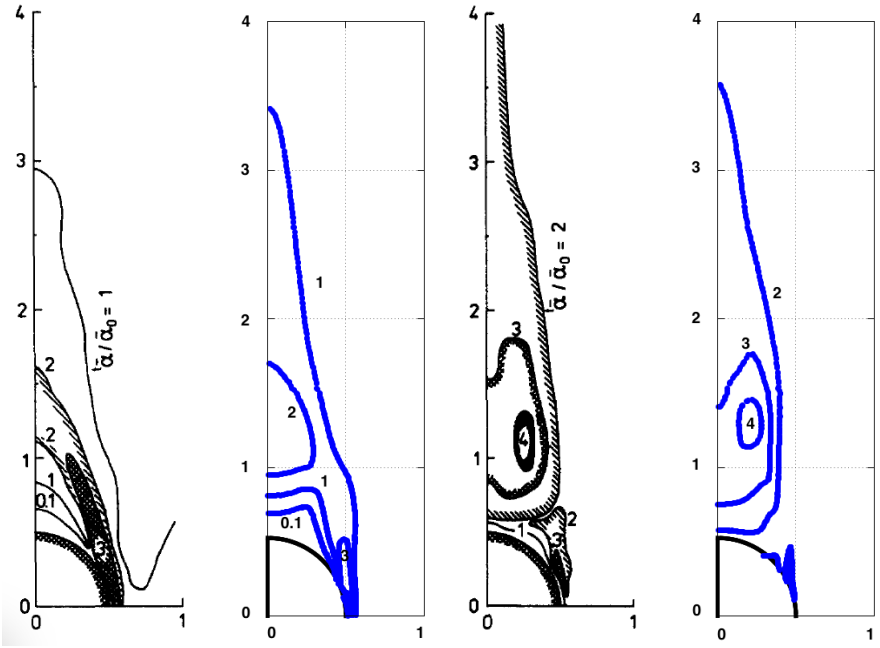

Figure 3.27 Averaged void fraction distribution around a cylinder with $\alpha_{inlet} = 8\%$, $U_{inlet} = 0.45,\ 1.9\ m/s$ and $D = 40\ mm$. From left to right, there are experimental data for $U_{inlet} = 0.45\ m/s$ and its simulation, $U_{inlet} = 1.9\ m/s$ and its simulation.

However, for lower velocity, the profile is strongly different. Thanks to numerical simulation, other quantities are available such as the diameter or the gas and liquid velocities. Since the velocity is too high, the bubble coalescence is low and the diameter remains constant. However, for low velocity, the bubble velocity is driven by the buoyancy, consequently the coalescence is more present and the bubble diameter is higher in the rear of the cylinder. This explains the discrepancies between liquid and gas velocity profiles in Figure 3.28. Inlet void fraction and velocity (or size ratio) are presented in Inoue's article and in the present work. Numerical simulations are important to investigate this kind of flow, since once it is validated, many variables are available such as velocity, diameters or turbulence fields. However, the objective of the present work is to characterize the fluid force at the wall with a steam-water mixture. Having different physical properties, bubbles are smaller in steam-water flow for example. Instead of lowering the cylinder diameter, we chose to lower the surface tension so the bubble diameter to change the bubble to cylinder size ratio. In previous cases, only flow characteristics are changed, e.g the Reynolds number. In order to show the important influence of the mixture, we changed the surface tension of the mixture to see how it might modify the flow. In fact, surface tension is an important parameter which is present in bubble characteristic non-dimensional numbers like Eotvos, Morton or Weber:

$$Eo = \frac{\Delta\rho g D^2}{\sigma},\quad Mo = \frac{g\mu_L^4\Delta\rho}{\rho_L^2\sigma^3},\quad We = \frac{\rho U D}{\sigma} \tag{3.1}$$

Moreover, the surface tension is related to the bubble diameter given that it is the liquid-gas interface strength. Consequently, the lower is the surface tension, the lower is the bubble diameter. Based on the same initial case, we only changed the surface tension to study its impact on void fraction distribution. According to the void fraction profiles on Figure 3.29, by lowering the surface tension, the vortex

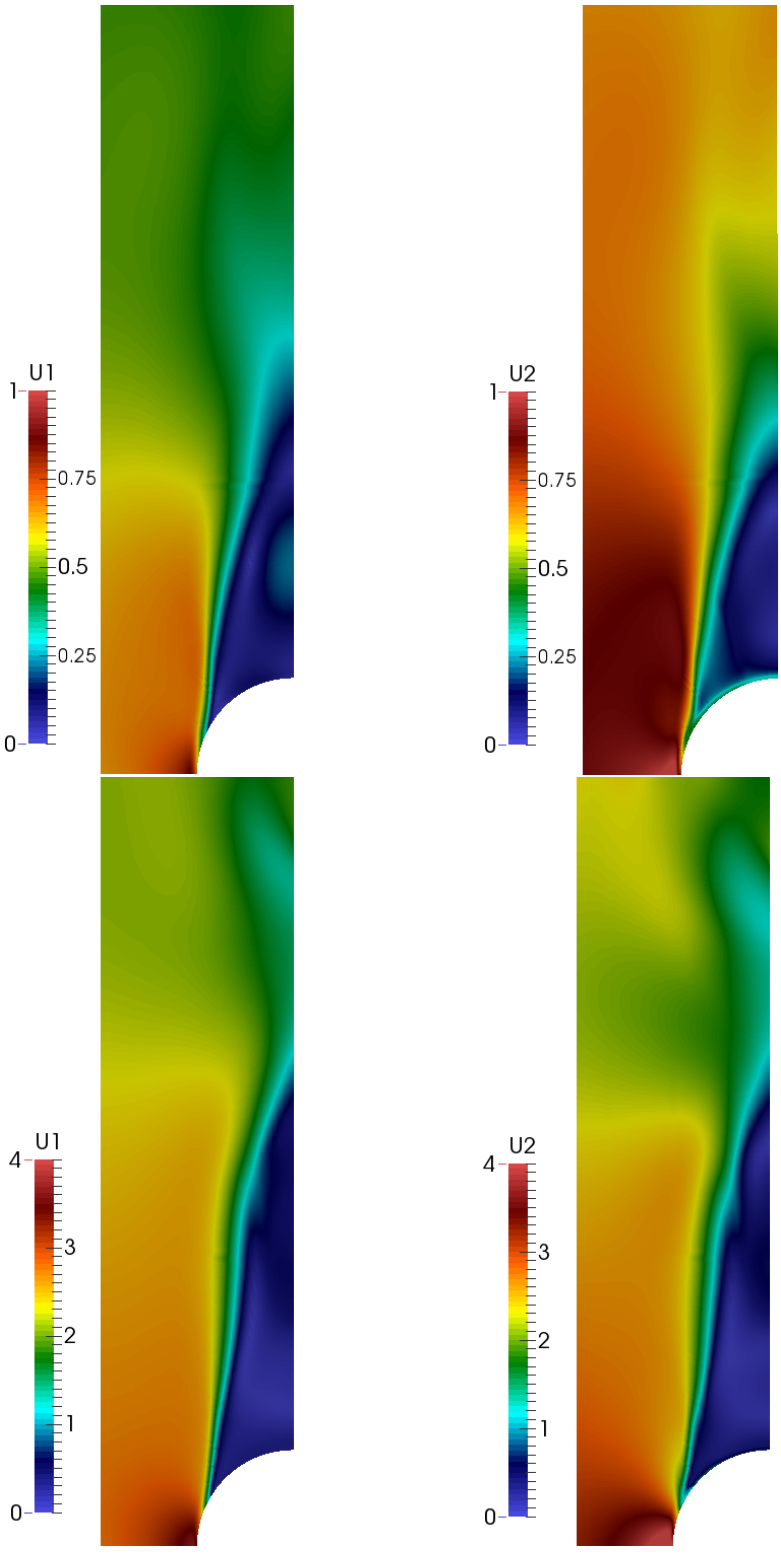

Figure 3.28 Averaged liquid (left) and gas (right) velocity distribution around a cylinder with $\alpha_{inlet} = 8\%$, $U_{inlet} = 0.45$ (top), 1.9 (bottom) m/s and $D = 40\ mm$.

shedding is less disturbed and close to the single-phase flow case since bubbles are smaller. The surface tension has consequently an important influence on turbulent energy which is of primary interest in two-phase cross flow given that it is responsible of vibrations. It appears here that the size ratio is the most important parameter of influence which agrees with the different author's conclusions cited in the

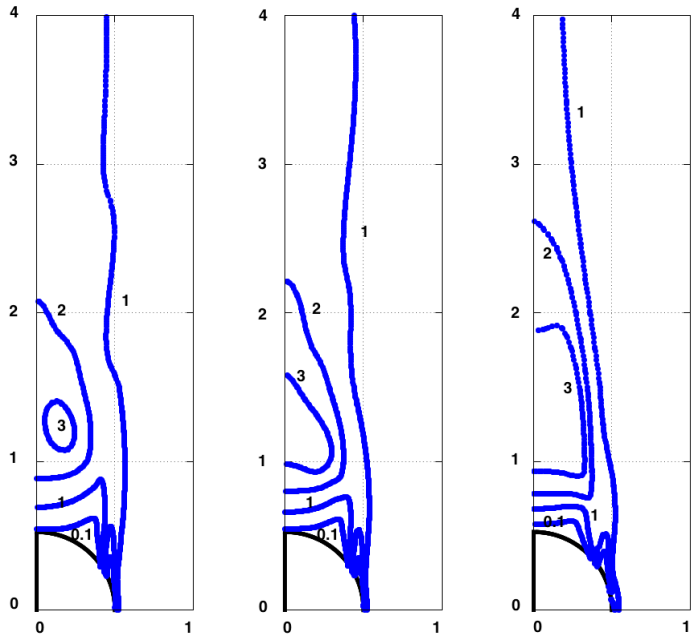

Figure 3.29 Averaged void fraction distribution around a cylinder with $\alpha_{inlet} = 8\%$, $U_{inlet} = 0.9\ m/s$ and $D = 40\ mm$. From left to right, $\sigma = 0.017,\ 0.035,\ 0.075\ N/m^2$.

literature review. In reduced-scale experiment, most of the time, the tube diameter is around 20 *mm*. For a given Eotvos number of 0.1 (spherical bubble), diameter are respectively 0.875 *mm* and 0.22 *mm* for air/water and freon/freon mixtures. However, based on operating conditions, we would have 0.52 *mm*. Consequently, the discrepancy in terms of size ratio between these three mixtures is large and leads automatically to strong discrepancies in terms of flow patterns at least in bubbly flow.

Therefore, in order to better understand the influence of a mixture, we investigate, for a given size ratio, the impact of a single bubble on a cylinder for different liquid viscosity.

3.2.4 Impact of the mixture on the force around a tube

Bhaga and Weber (1981) experiment consists in analyzing bubble rises in a quiescent fluid for different Reynolds and Morton numbers ($Re = \frac{\rho_L U_b D_b}{\mu_L}$ and $Mo = \frac{g\mu_L^4 \Delta\rho}{\rho_L^2 \sigma^3}$ with σ the surface tension). The objective of the present subsection is to add a cylinder in front of the rising bubbles once the final state (shape and velocity) is reached in order to study the impact of a single bubble on a cylinder.

The square vertical channel is 183 cm high and 29.2 cm large. For each case, only the liquid viscosity may vary significantly. However, the Eotvos number ($Eo = \frac{\Delta\rho g D^2}{\sigma}$) remains equal to 116. Pictures of the bubble final shapes and final velocity are available. 2 cases are presented below in Figure 1 and Tab.1. Each bubble is injected with a volume 9.3 cm^3 and a diameter 26.09 *mm*. Initially, the bubble is assumed spherical. As the only property that may vary is the liquid viscosity, volumetric mass and surface tension are averaged respectively to 1350 kg/m^3 and 0.0785 N/m. Consequently, based on Morton and Reynolds numbers, viscosity and final bubble velocity are deduced and presented in the following Table 3.4.

The geometry is described in Figure 3.31. A 3D Cartesian mesh 0.104x0.104x0.312 m is used with a cell size of $5.10^{-4} m$. Initially, the bubble is spherical with a diameter of 0.013 *m*. Side- and bottom-boundaries are defined as symmetries. The top is defined as an outlet with an atmospheric

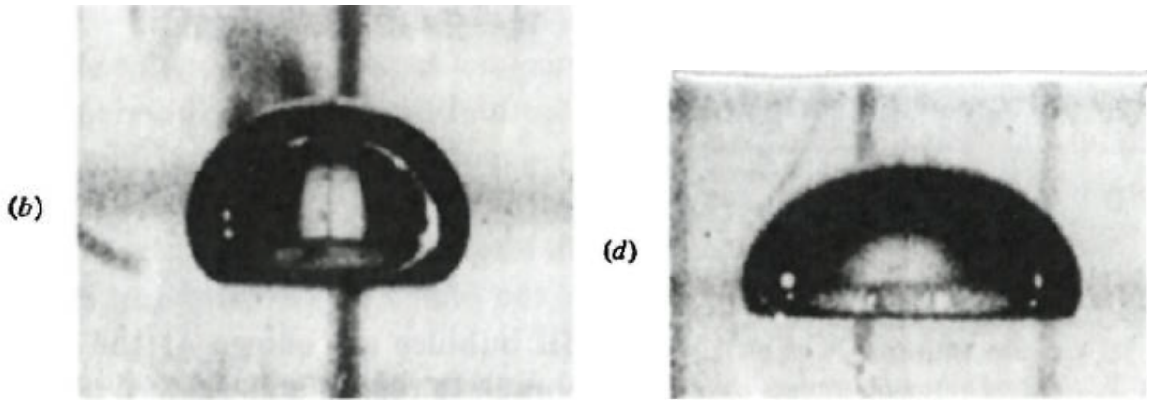

Figure 3.30 Pictures of the final bubble shape for case B and D from BHAGA

Experiment	B	D
Reynolds (-)	3.57	13.33
Morton (-)	266	5.51
Terminal velocity (cm/s)	20.5	29.0
Viscosity (Pa.s)	2.02	0.77

Table 3.4 Physical properties of a bubble rise for case B and D from Bhaga and Weber (1981).

pressure condition. The gravity is 9.81 m/s. The Large Interface Model is used to track the bubble. Drag, surface tension and gravity are the forces acting on the bubble. The time step is adaptive with a Courant number under 1. The physical time duration is 0.6 s. The gas velocity is recorded during the whole simulation.

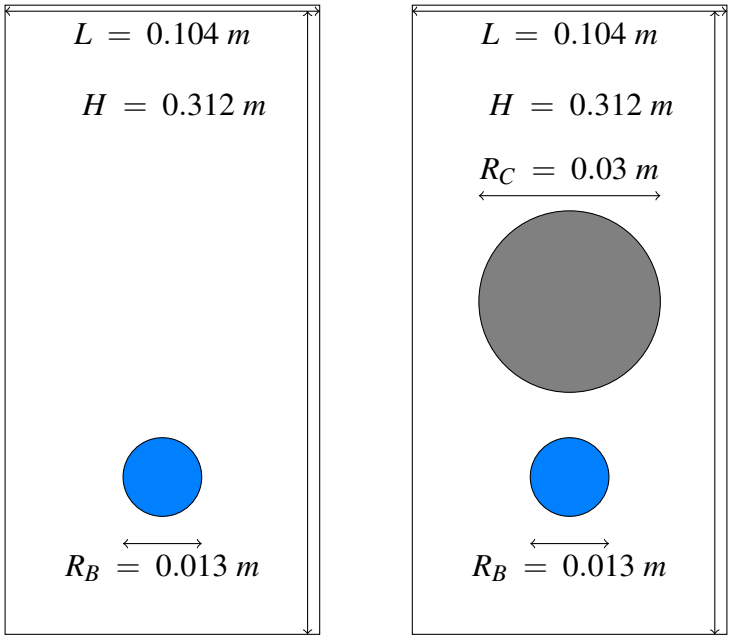

Figure 3.31 Geometry of the bubble rise (left) and the bubble impact on a cylinder (right) cases.

For the two cases presented before, the bubble velocity is presented in Figure 3.32. After 0.2 s, in each case, the velocity is constant and in a correct agreement with the terminal velocity, measured in the experiment. Moreover, the shape of each bubble is reproduced by the simulation in Figure 3.33. The

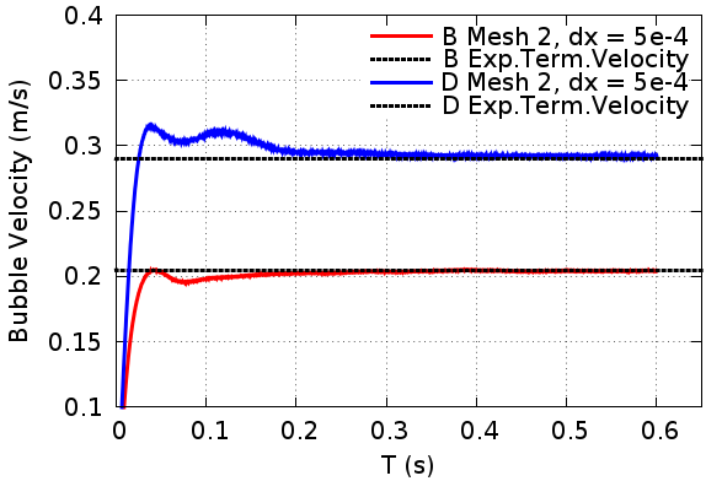

Figure 3.32 Bubble velocity from numerical simulation along the time for case B and D.

numerical model is then considered suitable to simulate bubble rise in quiescent fluid for different values of the Morton and Reynolds numbers. The idea of this work is to use this ability to study under the same conditions the bubble impact on a cylinder.

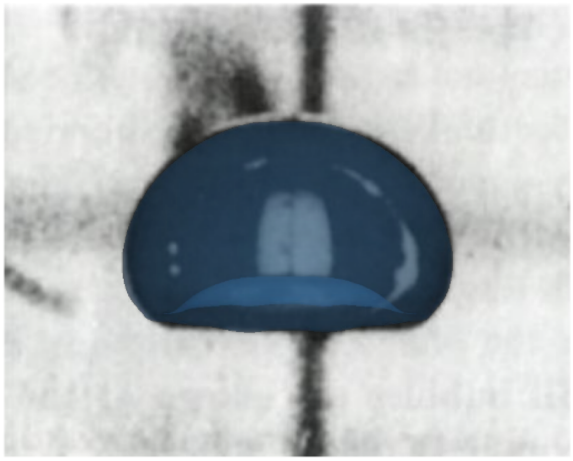

Figure 3.33 Bubble shape comparison between experiment and numerical result for case B. The bubble is in 3D with an opacity of 50%.

The geometry is sketched in Figure 3.31. A 3D Cartesian mesh 0.104x0.104x0.312m is used with a step of $5.10^{-4}m$. Initially, the bubble is spherical with a diameter of 0.013 m in (0.052,0.052). Side- and bottom-boundaries are defined as symmetries. The top is defined as an outlet with a constant pressure condition. The gravity is 9.81 m^2/s. A cylinder is immersed in (0.052,0.156) with a diameter of 0.03 m by using a Discrete Forcing Method described previously. There is a non-slip condition at cylinder wall. The Large Interface Modeled is used to track the bubble. Drag, surface tension and gravity are the forces acting on the bubble as previously. The time step is adaptive with a Courant number under 1. The time duration is 1.0 s. The gas velocity is recorded during the whole simulation.

The simulation is carried out on 2 mesh refinements for case B, see Figure 3.34. Most of the time, both refinements are in reasonable agreement. However, because of the break-up, small gas structures are

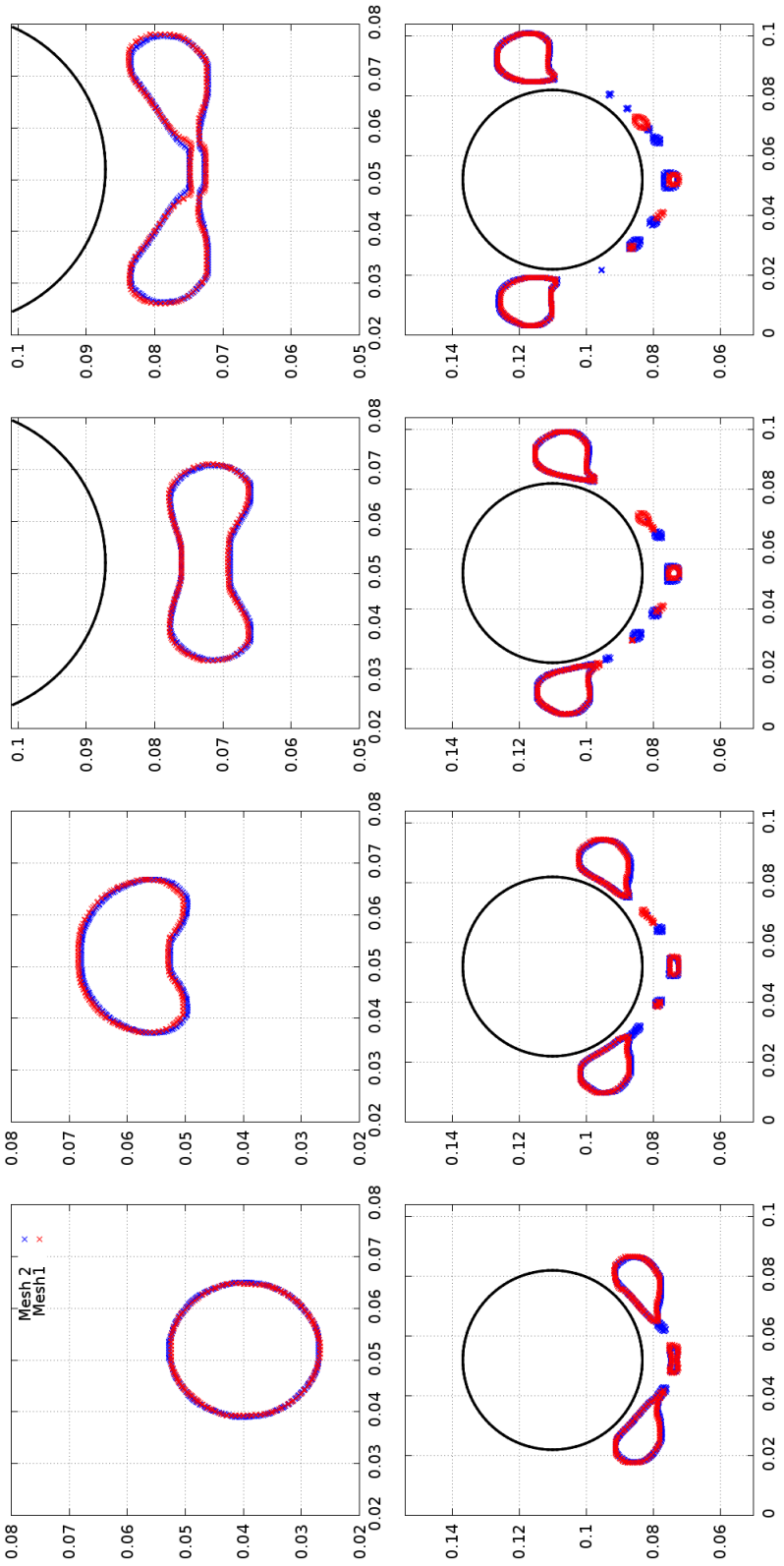

Figure 3.34 Bubble impact on a cylinder with two mesh refinements.

released and remain under the cylinder. They are different depending on the refinement. In the present study, they are considered meaningless since the two main bubbles govern the efforts at wall.

In Figure 3.35, the bubbles from case B and D have different terminal velocities and shapes (snapshot a). By reaching the near-wall region, bubbles are more and more flattened (snapshot b). Because pressure

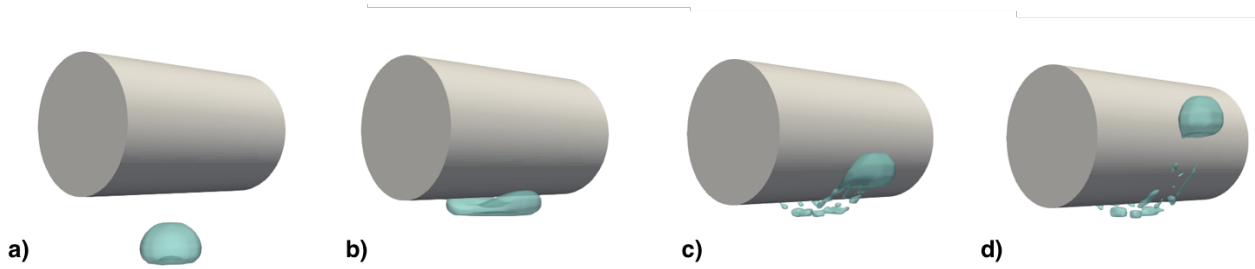

Figure 3.35 Snapshots of the impact of the bubble from case B on a cylinder at 4 different times.

effects, bubble is thinner and thinner at its center. Therefore, on each side of the cylinder, a bubble is growing and is released when the center becomes too thin. This is the break up (snapshot c). Then, each bubble rises around the cylinder (snapshot d).

According to Figure 3.36, since the fully developed bubble D is larger, the flattening step is more important in space. Then, according to Figure 3.35, the shape of main bubbles after break-up is also different which is in agreement with the Clift et al. (1978) diagram since the Reynolds and Eotvos numbers are lower (bubble diameter is about 13 mm). Because of the lower liquid viscosity, the velocity of the gas structures is higher in the second cases like in the simple rise of a bubble.

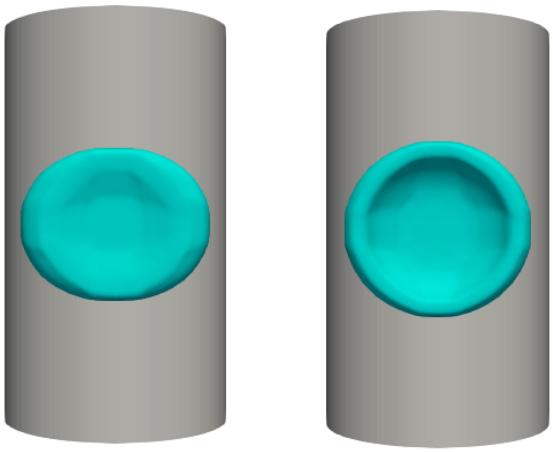

Figure 3.36 Snapshots of bubble from case B (left) and D (right) before impact.

During the rise of the bubble around the cylinder, there is always a liquid film between the gas and the cylinder. Consequently, there is no real impact. The thinner is the liquid film between the gas and the cylinder, the higher is the pressure, and the easier is the bubble break-up. Even after the break-up, bubbles are sliding close to the wall with a liquid layer between them. This property of having a liquid layer at the bottom of the cylinder was also observed for dispersed flow around a cylinder in Inoue et al. (1985) or in tube bundle in Murakawa et al. (2016) for example.

In Figure 3.37, the drag and lift forces from case B (left) and D (right) are given. In each case, a peak appears at the bubble break-up. This peak is more sizable in lift given that the bubbles are released in the lift direction. In case D, the peak is earlier and higher since the bubble comes faster. During the rise of two-bubbles around the cylinder, the drag is disturbed; it decreases after the impact. Then, the drag comes

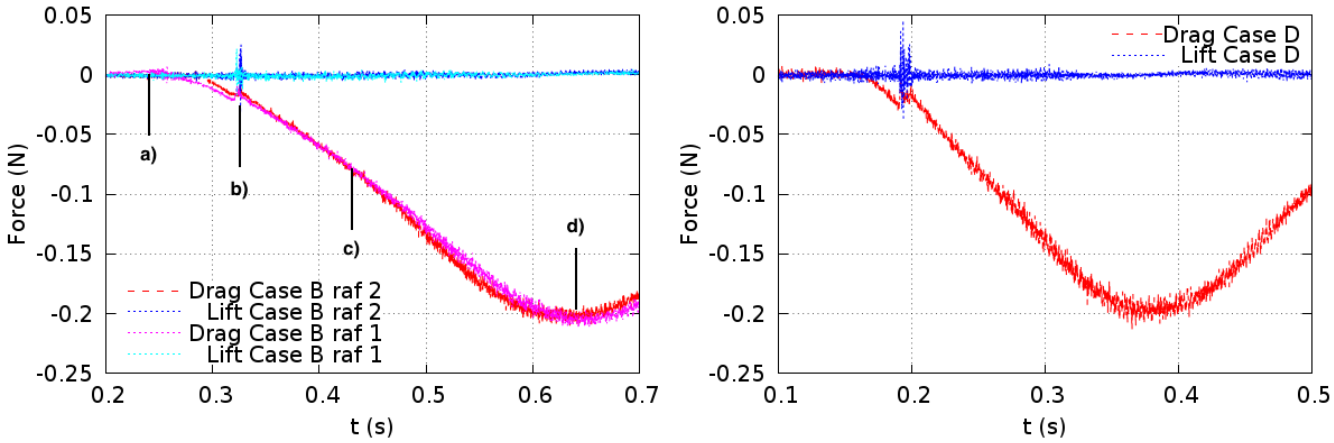

Figure 3.37 Forces on the cylinder for case B (left) and D (right). Drag and lift forces are respectively in red and blue. For the case B, the forces computed with the two meshes are in agreement.

back to its initial value when bubbles are leaving the cylinder. The phenomenon is quicker in case D but the variations are the same in both cases. Having the same volume with the same mass, the amplitude variation of the drag is consequently very similar despite the discrepancy in velocity at the impact. The terminal velocity is of influence on the lift since faster is the bubble higher is the amplitude. Moreover, as the bubble from case D is more spread (see Figure 3.36) on the cylinder surface, the break-up is longer according to the lift records where the peak is larger in case D than B.

Summary and remarks

The numerical simulation of two-phase cross-flows is a tough challenge. Having a numerical model able to simulate a wide range of void fraction and consequently flow patterns is not trivial. A sensitivity study to numerical models available in NEPTUNE_CFD has been performed in order to identify the most efficient one for the flows of interest. Accuracy and time of computation has been taken into account to choose the model to simulate two-phase cross-flow in tube bundles: the Generalized Large Interface Model. Our study was only performed with two(multi)-fluid approach. It would be interesting to compare to the mixture model since most of the other authors of the field are using this approach. In this section, we chose to work on a complex geometry with an inclined tube bundle in order to be able to trust our numerical model on the simpler target geometry: an in-line tube bundle without inclination.

As the quantification of the mixture effect on vibration is an objective of the present thesis, we compared on the exact same geometry two different mixtures: freon/freon and air/water. After having validated the numerical model on both mixtures, we compared an air/water and a freon/freon flow across the inclined tube bundle previously discussed. For inlet parameters, we considered like in experiments the same volumetric flow rate at the inlet consequently the same superficial velocity. However, it was not possible to obtain the same void distribution or even the same regime. There were consequently two explanations to this: the inlet assumption made were wrong or it was not possible to get approximately the same flow with another mixture if it does not respect some rules. In fact, if we look at the mass ratio, the viscosity ratio or the surface tension in these mixtures, they have no common point. Consequently,

we tried to characterize two-phase cross flow and the impact of the mixture physical properties by doing 3 numerical sensitivity studies on a single cylinder under cross-flows:

- Impact of the inlet void fraction on the force spectrum: inlet void fraction is not responsible for the discrepancies in the force spectrum, nevertheless the flow pattern is. Numerical simulations allow to explain why force signals are different depending on the flow pattern. From single-phase flow to bubbly flow, the force spectrums are similar but the force records are not. In fact, the passage of bubbles lower the drag amplitude and leads to noise. For intermittent and churn flow, the signals are very noisy due to the chaotic mixture. However, the overall spectrum is lower since the overall density is lower. Finally, for very high void fraction, the noise is reduced since we have mainly gas.

- Parameters of influence on the void fraction distribution for a bubbly flow: inlet void fraction and velocity are changed to see their influence on the void distribution. Variation of void fraction (remaining in the bubbly regime) does not have a huge influence. However, the bubble to cylinder size ratio appears to be the most influential parameters. Instead of lowering the cylinder diameter, we lowered the surface tension which plays an important role on the size of gas structures. We found the same conclusion as Inoue et al. (1985) when they lowered the cylinder diameter. Consequently, it shows for a given flow pattern that the most important parameter to respect for a single cylinder is the bubble to cylinder size ratio. The geometric parameter is consequently of primary interest; in tube bundle, it has been shown by Deri (2018) that the gap also plays a role in the flow pattern.

- Characterization of a bubble impact on a cylinder for different physical properties: based on the previous case, we choose to work with a given cylinder size ratio. Here, the rise of a bubble around a single cylinder in a liquid at rest is investigated for two different liquid viscosity. By reducing the liquid velocity, the only change is the terminal velocity of the bubble and its shape at the break-up. If we look at the force records, the shape is strictly the same since the change in the drag amplitude is strictly the same. However, due probably to the velocity of the bubble, the lift peak at break up is larger.

Based on these 3 investigations, it is possible to say that the surface tension plays an important role in the characteristic size of the gas structures whereas the mass ratio and the viscosity ratio are more important for the gas velocity distribution. For bubbly flow at least, the bubble to cylinder size ratio seems to be the most influent parameter. The respect of geometric similarities are consequently of primary interest when switching mixtures.

A new eye is given thanks to these investigations, however the link with the tube bundle has not been done yet. An important perspective would be to link the variations of amplitude in the force records to the size of the gas or liquid structures based on the study of single bubbles of different size impacting a cylinder.

Chapter 4

Industrial application: Simulating vibration induced by two-phase flow in a tube bundle

Flow-induced vibration damage is a major concern for designers and operators of nuclear power plant steam generators. Problems may typically arise either at the secondary fluid entrance at the bottom of the steam generators or in their U bend region, where single phase or two-phase cross-flows are respectively observed. Those flow conditions may lead to fluid-elastic instability phenomena associated with large amplitude tube displacements and consequent damage for one or several tubes in arrays.

Many efforts have been made to determine the threshold critical flow velocity to instability, both for single phase or two-phase mixtures Chen (1987); Weaver and Fitzpatrick (1987); Pettigrew and Taylor (1991). Nowadays methodologies to estimate that velocity (Chen, 1983; Granger, 1991) are based on unsteady semi-analytical models for fluid dynamic forces, generally associated with dimensionless fluid force coefficients obtained from experiments.

In this last chapter, we analyze two expriments which have been performed on a square inline tube bundle configuration, the first experiment under single-phase water cross-flow and the second one under two-phase freon/water cross-flow. All the tubes in the bundle are fixed except the central one which is let free to vibrate both in lift and drag directions. For those experiments frequency, damping ratio and tube motion amplitude evolution versus flow velocity and void fraction are available.

The diameter of the tubes is 22 mm and their length is 0.25 m. The pitch ratio is 1.44. In the single phase experiment, the tube bundle is composed of 7x7 tubes. It is composed of 7x9 tubes in the two-phase experiment. (see Figure 4.1). The physical properties of the experiments are presented in Table 4.1. In both directions the vibration mode has a natural frequency $f = 40\ Hz$, and the logarithmic decrement in water is $\delta = 0.095$. The mass ratio $m/\rho d^2$ is 4, where m is the mass of the tube per unit length, and ρ the fluid density. More details about the experiment in single phase and two-phase flow can be respectively found in Granger et al. (1993) and Delenne et al. (1997).

The aim of this final chapter is to numerically obtain dimensionless fluid force coefficient in two-phase flow with the previously developed method and to investigate on a same configuration a freon/water flow and a steam/water flow under operating conditions to quantify the error due to the mixture.

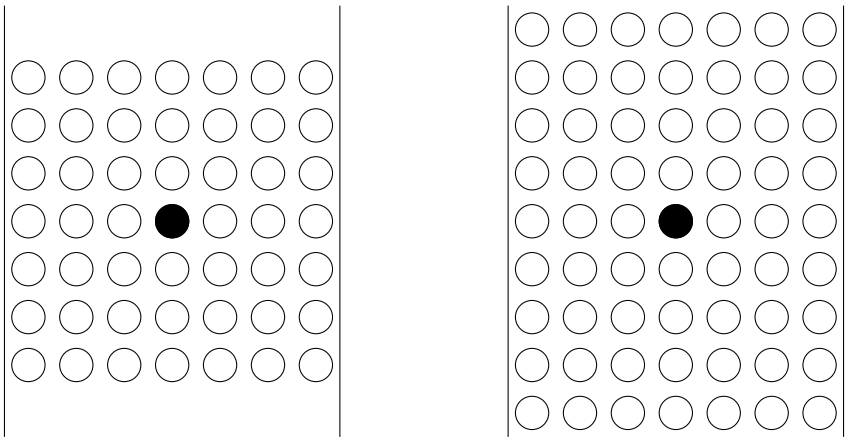

Figure 4.1 VISCACHE tube bundle geometry for single-phase flow (left) and two-phase flow (right). Rigid tubes are filled in white and flexible tubes in black.

		ρ (kg/m^3)	μ $(Pa.s)$	σ (N/m)
Single-phase flow				
	Water (1 bar)	1000	$1.0\ 10^{-3}$	-
Two-phase flow				
	Water (7 bar)	990	$9.0\ 10^{-4}$	0.072
	Freon (7 bar)	50	$1.6\ 10^{-5}$	
	Water (70 bar)	740	$9.4\ 10^{-5}$	0.017
	Steam (70 bar)	37	$1.9\ 10^{-5}$	

Table 4.1 Physical properties of water (1 bar), freon-water (7 bar) and steam generator operating condition: steam-water (70 bar).

4.1 Flow characteristics

In the present study, a comparison is performed between a freon/water and a steam/water (under operating conditions) flow across the tube bundle presented before without any motion. Based on what we have seen in the previous chapter, we chose to work with realistic inlet boundary conditions. In fact, when it comes to experimentally reproduce the real two-phase flow with another mixture to investigate tube vibration, there are alternative possibilities:

- same volume flow rates (and consequently same superficial velocities);
- same mass flow rates (and consequently same same quality).

In order to avoid any doubt in the reproduction of a similar flow, we choose to try both solutions. Two cases are considered: 10% and 50% of void fraction in order to compare the mixtures for different flow patterns. The Generalized Large Interface Model is used in this chapter given the conclusion of the previous one.

4.1.1 Bubbly flow

In the present case, the inlet condition for freon/water are the following: $\dot{m}_g = 0.11\ kg/s$ and $\dot{m}_l = 27.71\ kg/s$. The pressure and the temperature are respectively $P_{domain} = 5.07\ bar$ and $T = 282.08\ K$.

Equivalent volume flow rates

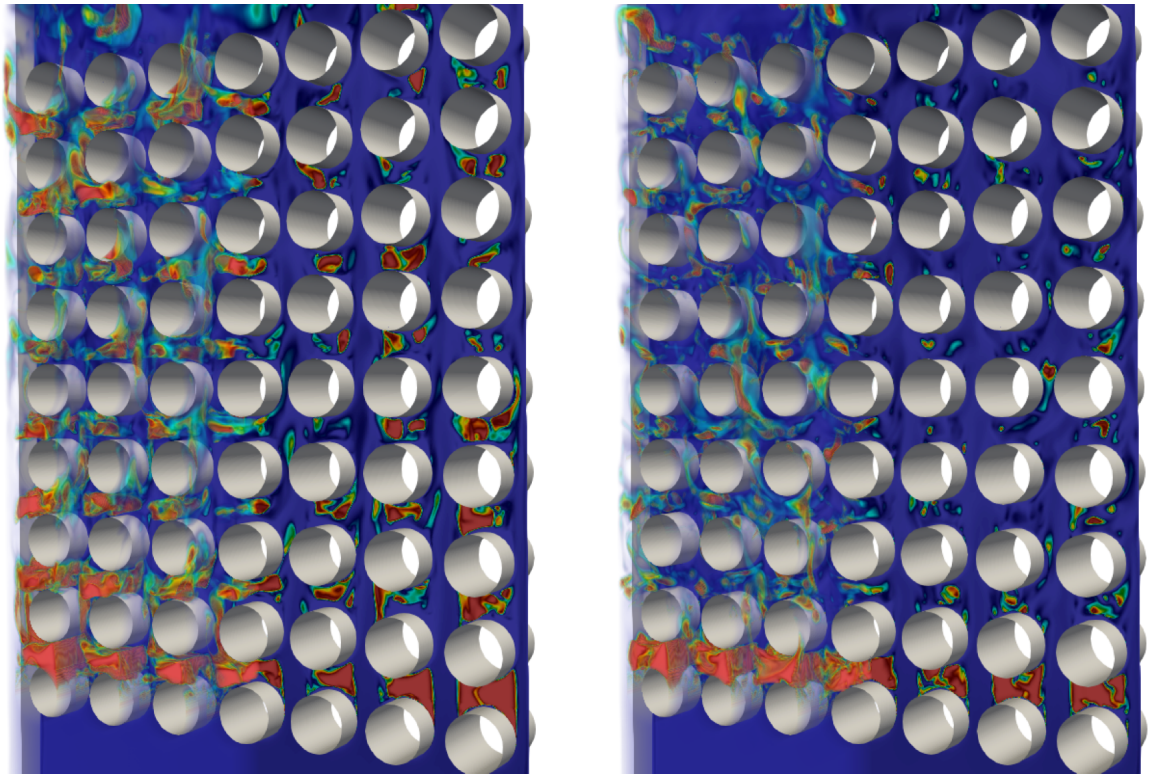

Figure 4.2 Void fraction distribution across the tube bundle for water/freon (left) and water/steam (right) for equivalent inlet volume flow rates with a 10% inlet void fraction. The half left of each tube bundle is presented with a volume distribution and the half right with a surface distribution on a slice.

According to Figures 4.2 and 4.6, for a bubbly flow regime with 10% inlet void fraction, based on equivalent inlet volume flow rates, the void fraction distributions are different. Even if the mass ratios are very similar between each mixture, there is a large discrepancy of void fraction distributions in-between the rows. In fact, the void is higher in-between 2 rows of cylinders in water/freon than with water/steam. The stream-wise liquid velocities are similar, however with water/freon, peaks of velocity are higher. This is probably due to the liquid density disparity (water density is higher in water/freon). Transverse velocities are very different. The profiles are similar between each row in steam/water. In comparison, there are many different amplitudes depending on the rows with water/freon. This is clearly a consequence of the gas properties. Bubbles are larger in water/freon since the surface tension is higher. Larger bubbles disturb the liquid turbulence and consequently the transverse velocity profiles. Finally, with larger bubbles, we have larger peaks in void fraction distribution between two cylinders. In this first case, it appears that because of the difference of surface tension, the bubble to cylinder size ratios are different, and consequently with larger bubbles the disturbance of the liquid stream is higher in water/freon than in steam/water under operating conditions.

Equivalent mass flow rates

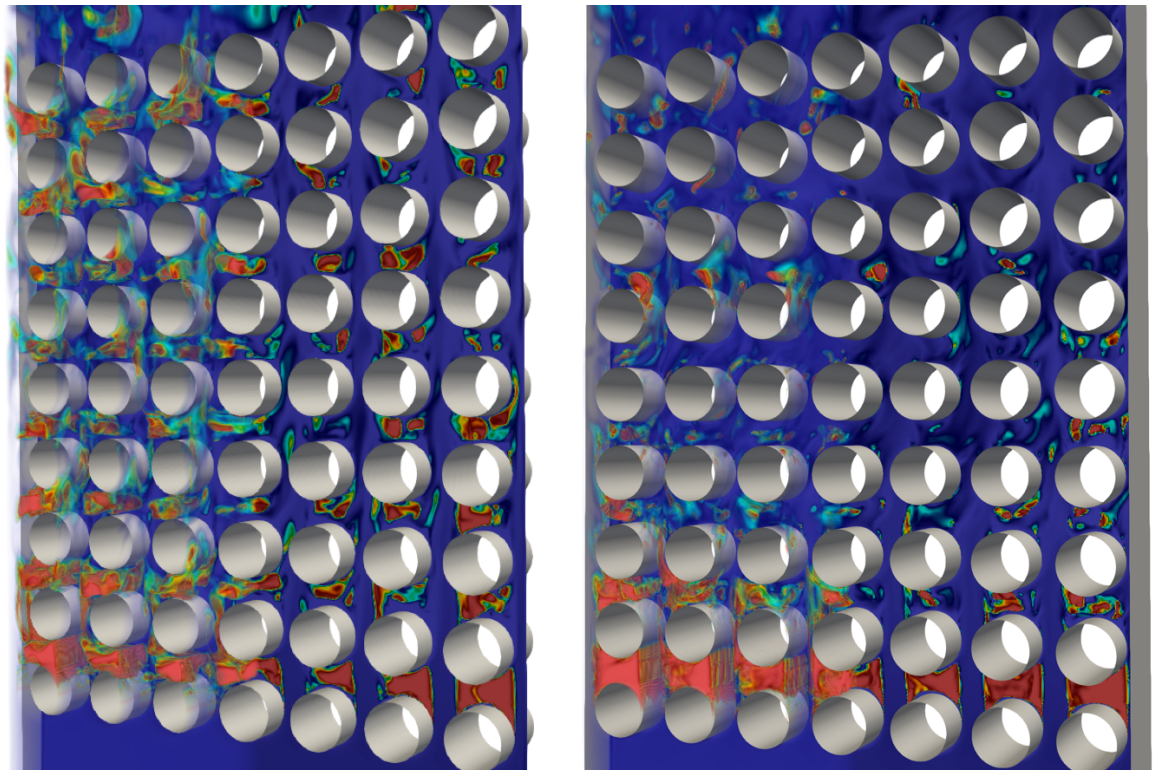

Figure 4.3 Void fraction distribution across the tube bundle for water/freon (left) and water/steam (right) for equivalent inlet mass flow rates with a 10% inlet void fraction. The half left of each tube bundle is presented with a volume distribution and the half right with a surface distribution on a slice.

According to Figures 4.3 and 4.7, for a bubbly flow regime with 10% inlet void fraction, based on equivalent inlet mass flow rates, the observations made for equivalent volume flow rates are still true. For the void distribution, the gas does not remain between two rows of cylinders in steam/water, consequently the profiles are lower in this area. This is due to the smaller bubbles in steam/water. Transverse velocities are also less disturbed in steam/water due to the smaller bubble size. The axial liquid velocities are similar. Therefore the gas properties and surface tension are responsible of the discrepancies in the flow distribution between these two mixtures.

For the bubbly flow regime, whether in equivalent mass or volume flow rates, the overall conclusions are the same. Bubbles, being smaller in steam/water, do not disturb the liquid flow like in freon/water. Hence, a steam/water mixture should yield a wall fluid-force similar to the single-phase case. However, with freon/water, given that there are high peaks of void fraction between cylinders, the pressure profile at the cylinder wall is probably different, as well as the force spectrum.

4.1.2 Churn flow

Equivalent volume flow rates

According to Figure 4.4 and 4.8, for a churn flow regime with 50% inlet void fraction, based on equivalent inlet volume flow rates, the observations from the previous regime are different. In fact, the

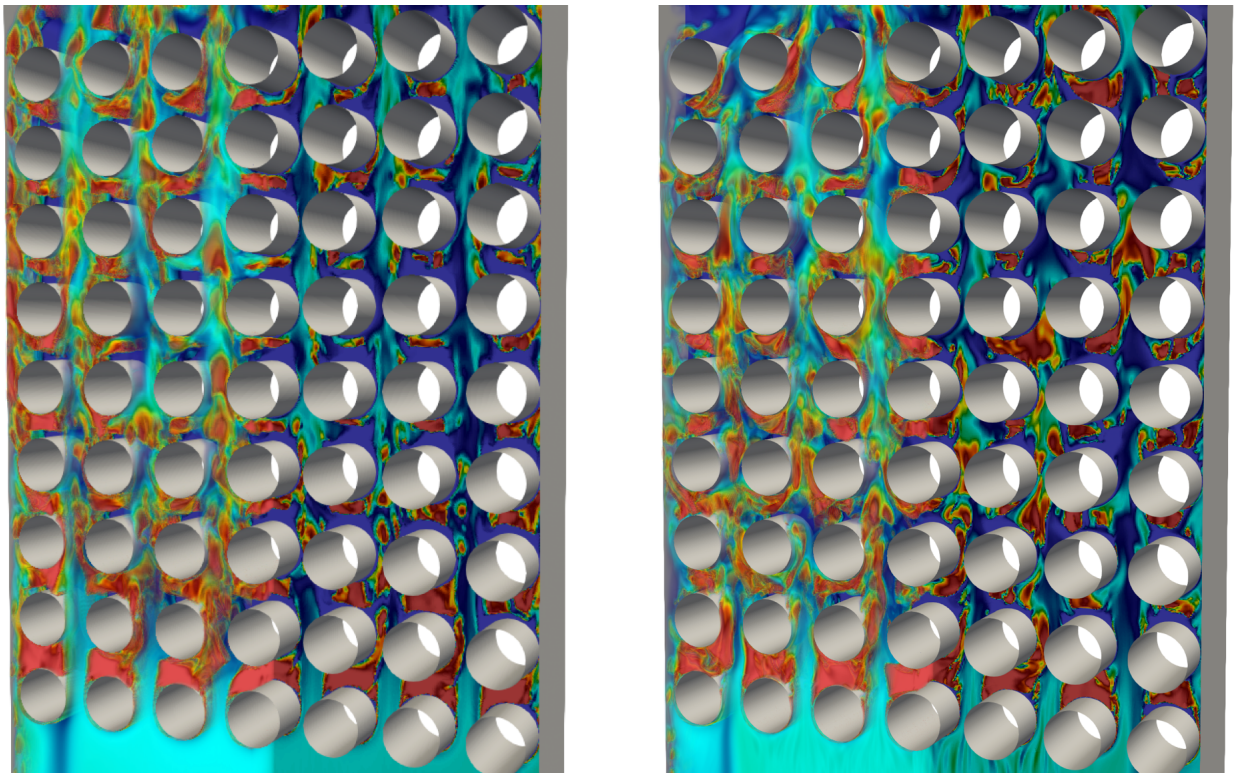

Figure 4.4 Void fraction distribution across the tube bundle for water/freon (left) and water/steam (right) for equivalent inlet volume flow rates with a 50% inlet void fraction. The half left of each tube bundle is presented with a volume distribution and the half right with a surface distribution on a slice.

instantaneous snapshots of the void fraction distributions are very similar. Even if the amplitudes are slightly different, void fraction profiles are similar in terms of variations with both mixtures. Then, the axial liquid velocity is exactly the same. Consequently, the reduction of axial liquid velocity due to the presence of the gas is the same whether we are in steam/water or in freon/water. Then, for the transverse velocity profiles, they are different for the first rows but similar for the following ones. The size of bubbles from the dispersed field are different but more homogeneous than before. From the present profiles, it appears that for higher void fractions, the size of large gas structures are probably limited by the tube bundle geometry. Consequently, after a given void fraction, it is possible to have very similar flows with different gas properties and surface tensions since the gap between tubes controls the size of large gas structures (responsible of the void distribution and of the liquid velocity change). This is one of the major conclusions of the present work. However, even if the freon/water flow pattern appears to be reproduced with steam/water for the churn flow, it does not necessarily lead to the same fluid force spectrum.

Equivalent mass flow rates

According to Figure 4.5 and 4.9, for a churn flow regime with 50% inlet void fraction, based on equivalent inlet mass flow rates, the void distribution is different. Previously, we had similar profiles with amplitude discrepancies only. Here, in steam/water the gas is concentrated in-between the rows of cylinders. In contrast, the amplitude of the freon gas distribution is larger with a peak between rows and smaller peaks (not present with steam/water) in-between two columns of cylinders. This observation is

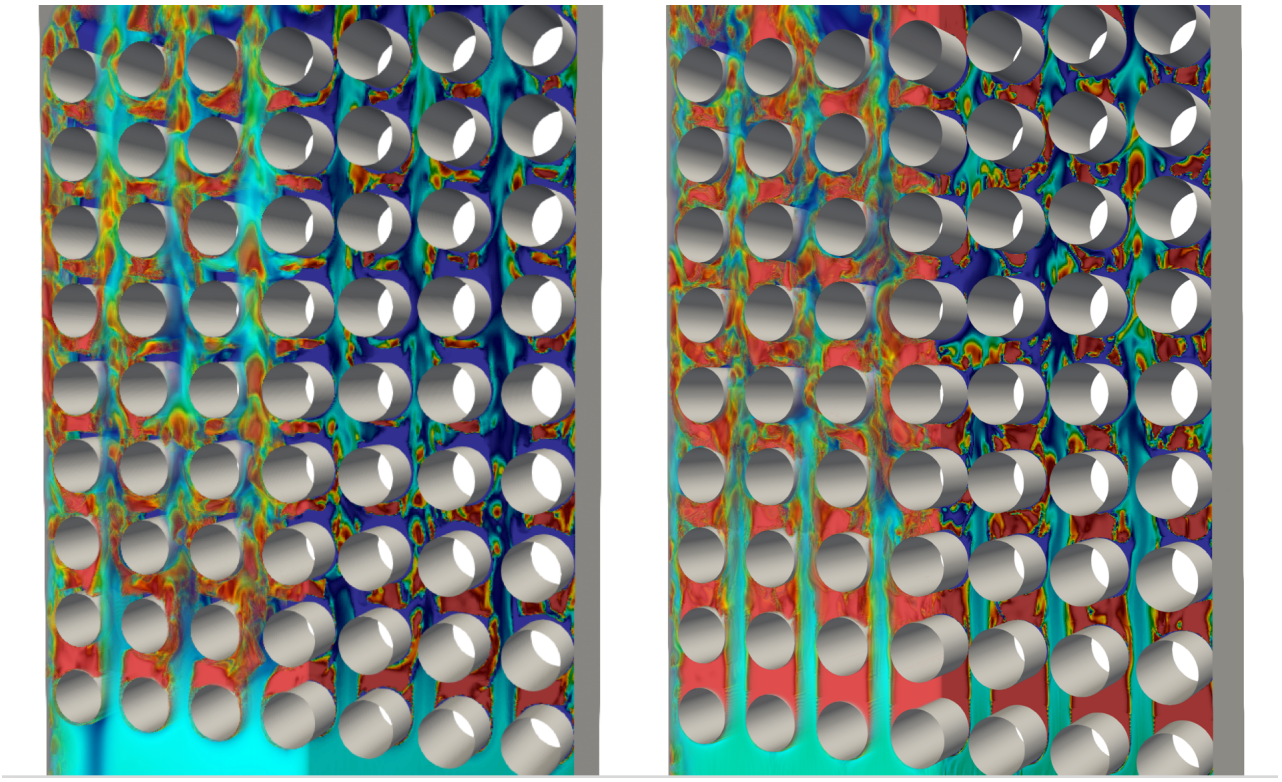

Figure 4.5 Void fraction distribution across the tube bundle for water/freon (left) and water/steam (right) for equivalent inlet mass flow rates with a 50% inlet void fraction. The half left of each tube bundle is presented with a volume distribution and the half right with a surface distribution on a slice.

probably due to the larger gas structures in water/freon which might break up easier and could explain the discrepancy in terms of distribution with a real change of flow pattern. In fact, the profile of void in steam/water is similar to the one in bubbly flow with higher peaks. Steam/water stream-wise liquid velocity has a larger amplitude with higher peaks in the gaps and lower in between cylinders. There are two ways to explain this discrepancy. First, the inlet assumptions made of equivalent mass flow rate might explain the higher peaks. Secondly, the change of flow pattern in water/freon tends to disturb the liquid stream due to the larger gas structures and their break-ups. In the transverse profiles, we have similar features even if, the amplitude in water freon is reduced with the altitude due to the reduction of gas structure size. Finally, it appears that the dispersed part of the GLIM gives smaller bubbles in water/steam (due to surface tension effect). It would be interesting to measure the size of the continuous gas structures to enrich this study.

In the present comparison, it appears that the flows are more similar based on equivalent volume flow rates. These studies does not allow to conclude on vibration mechanism, only on two-phase flow behaviors. A major remark is that for higher void fraction, it is possible to reproduce a very similar flow with another mixture using an equivalent volume flow rate since the gas structure characteristic sizes are no longer dependent on the surface tension only but by the tube bundle gap. A very interesting case would therefore be to continue this work for higher void fractions and to compare force spectra to see the impact of the mass and viscosity ratios.

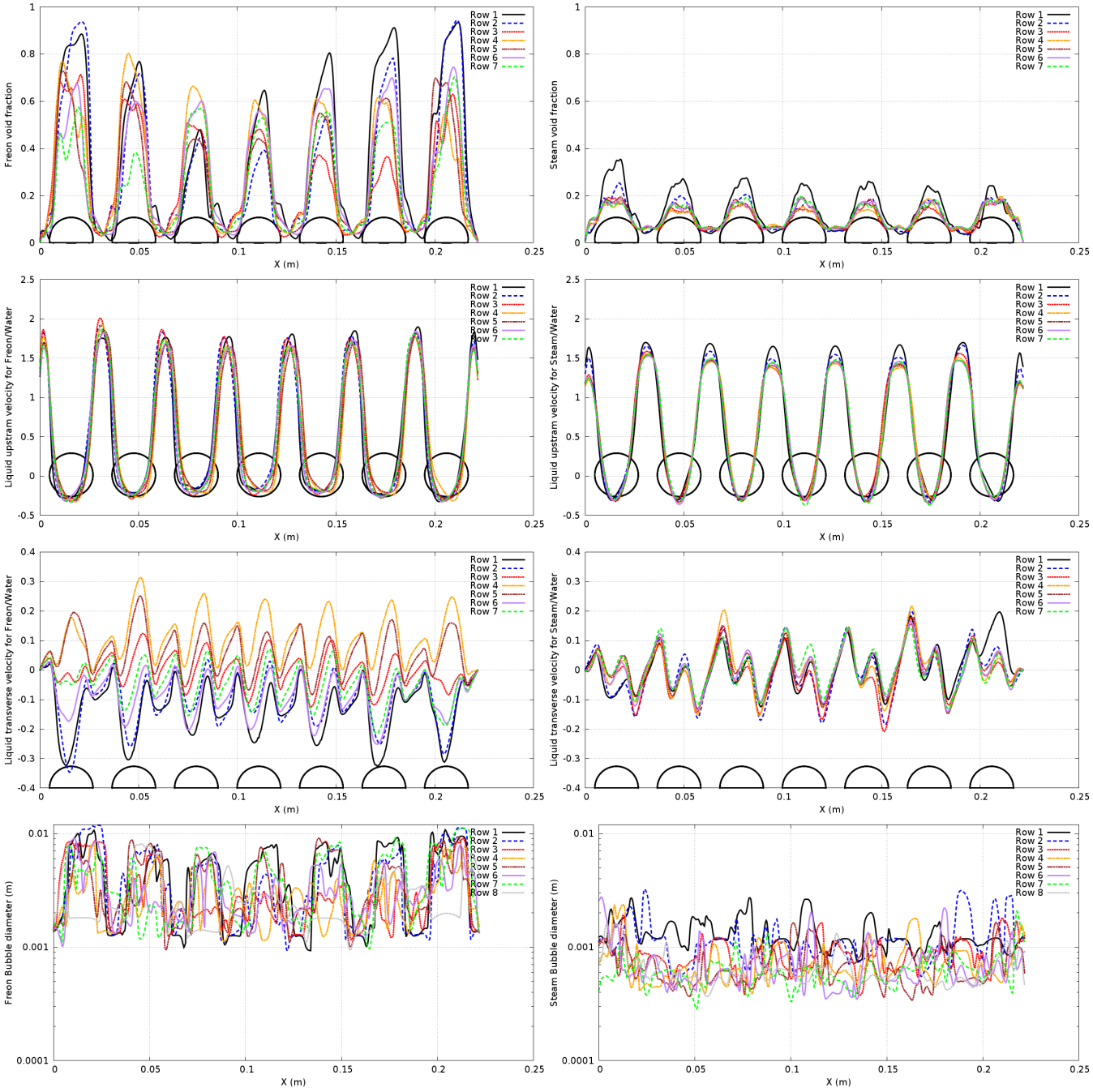

Figure 4.6 Comparison of (from top to bottom) time-averaged void fraction, time-averaged streamwise liquid velocity, time-averaged transverse liquid velocity and instantaneous bubble diameter along the different rows of the tube bundle. Results are respectively on the left and right for water/freon and water/steam for a 10% inlet void fraction with equivalent volume flow rates.

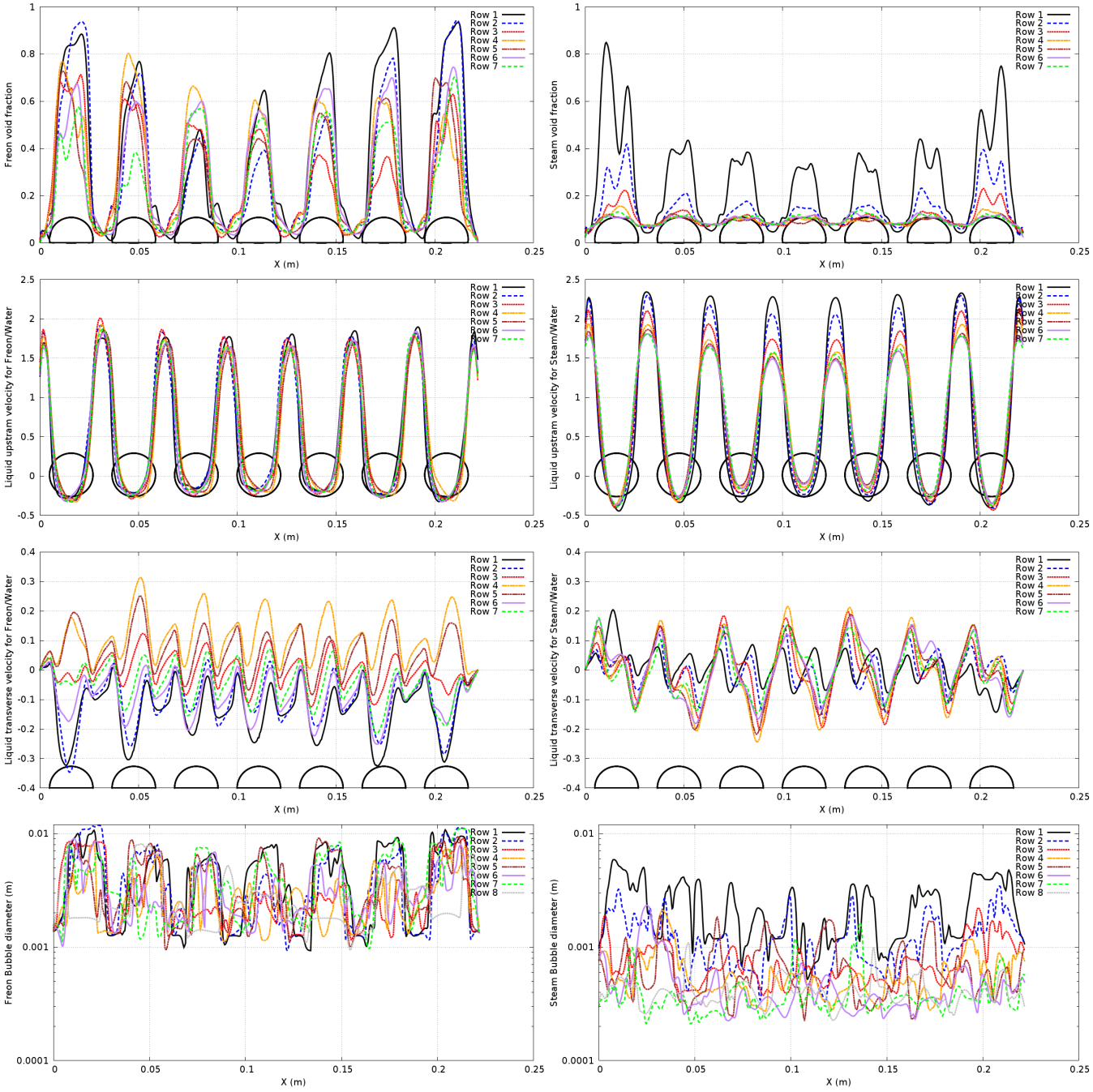

Figure 4.7 Comparison of (from top to bottom) time-averaged void fraction, time-averaged streamwise liquid velocity, time-averaged transverse liquid velocity and instantaneous bubble diameter along the different rows of the tube bundle. Results are respectively on the left and right for water/freon and water/steam for a 10% inlet void fraction with equivalent mass flow rates.

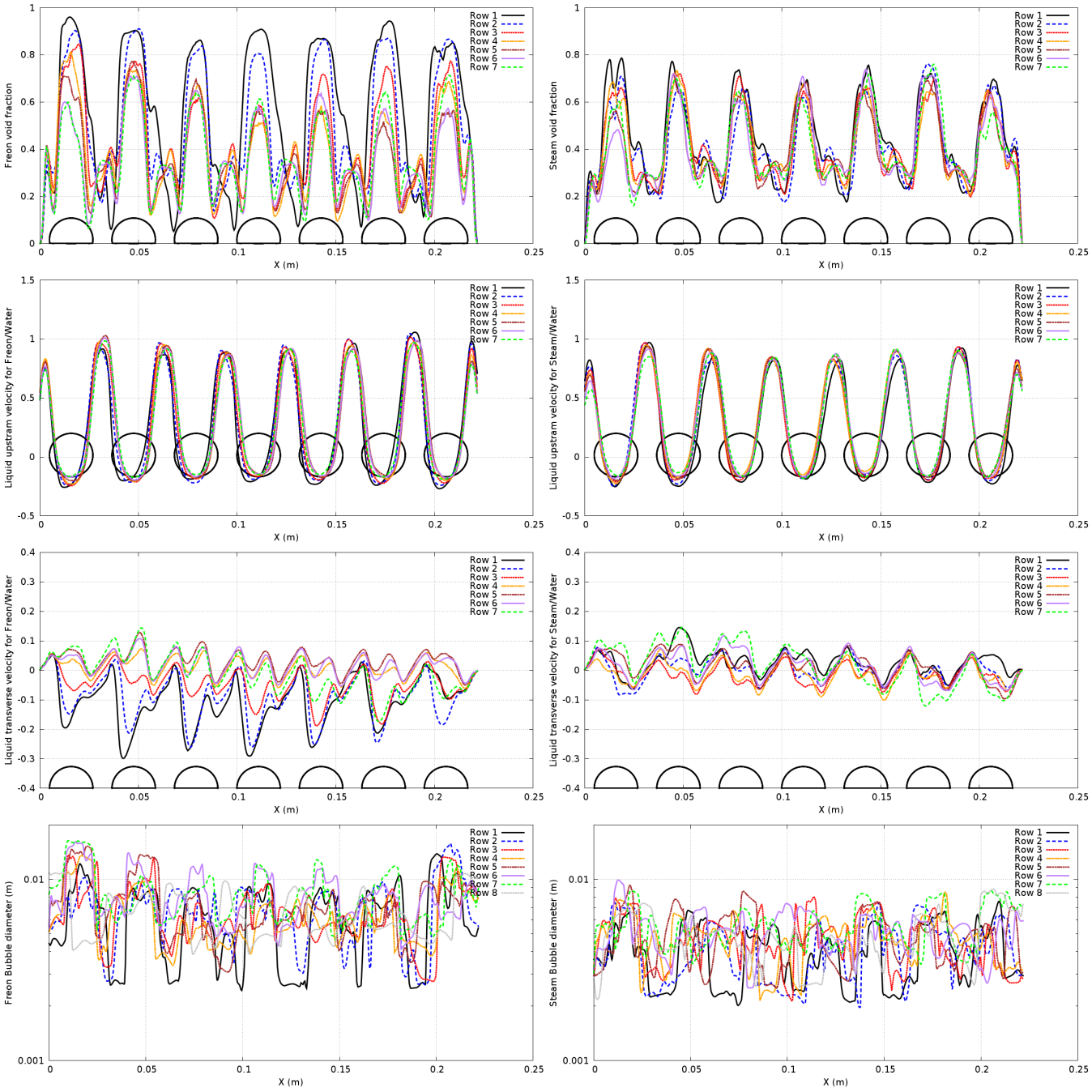

Figure 4.8 Comparison of (from top to bottom) time-averaged void fraction, time-averaged stream-wise liquid velocity, time-averaged transverse liquid velocity and instantaneous bubble diameter along the different rows of the tube bundle. Results are respectively on the left and right for water/freon and water/steam for a 50% inlet void fraction with equivalent volume flow rates.

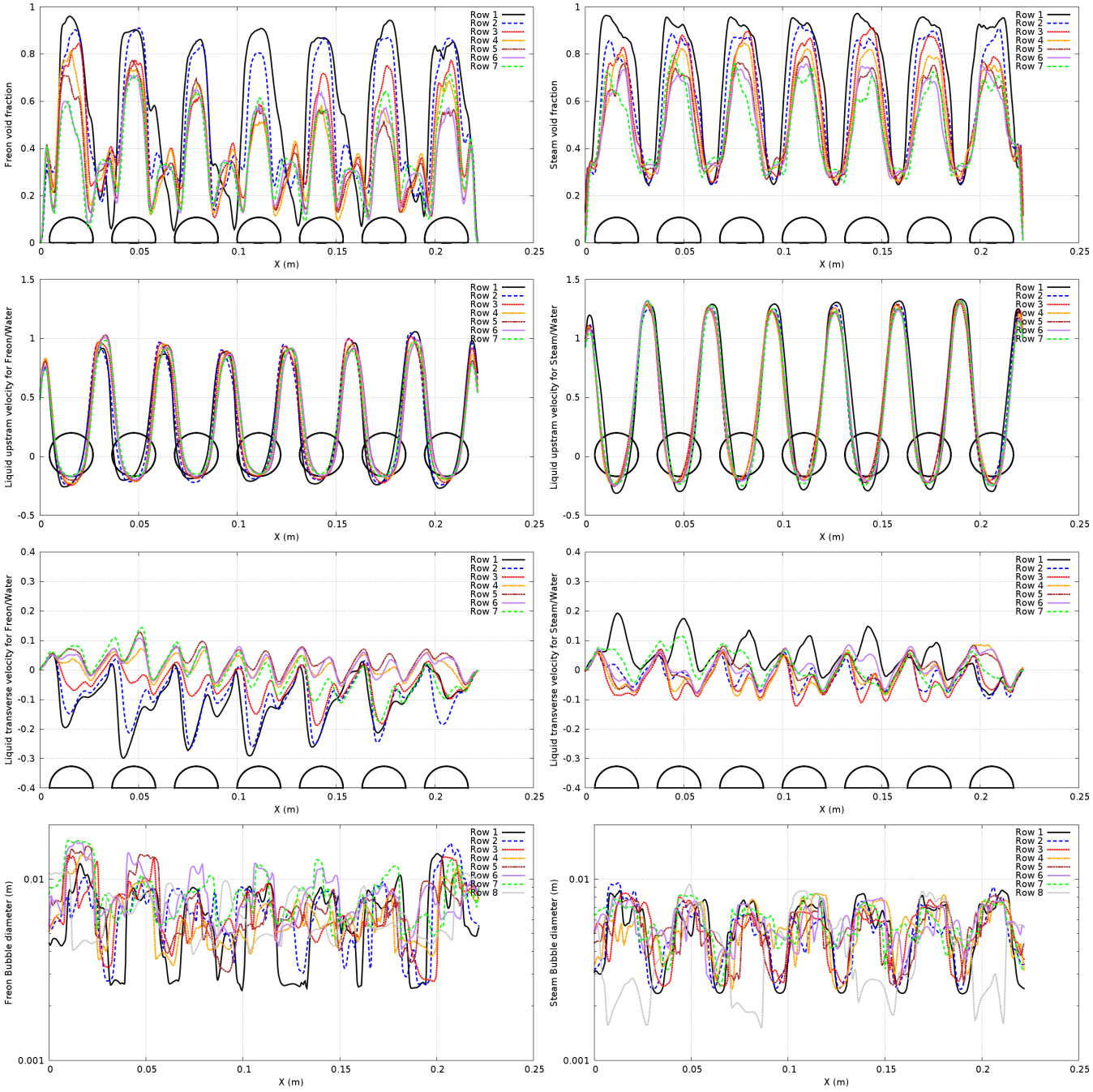

Figure 4.9 Comparison of (from top to bottom) time-averaged void fraction, time-averaged streamwise liquid velocity, time-averaged transverse liquid velocity and instantaneous bubble diameter along the different rows of the tube bundle. Results are respectively on the left and right for water/freon and water/steam for a 50% inlet void fraction with equivalent mass flow rates.

4.2 Fluid-structure interaction in an in-line tube bundle

The objective of the present section is to show the ability of the Time and Space Dependent Porosity method, developed and validated (for imposed and free motion) in previous chapters, to predict flow induced vibration on feasibility test cases; even if there is still development required to optimize these kinds of computation that will be discussed in the general conclusions. The computation of the porosity field is optimized in order to reduce the computational cost: instead of re-computing each cylinder, only the mobile one is updated.

For these feasibility test cases and in order to reduce the time of computation, we made strong assumptions for the present study listed below:

- use of the R_{ij} EBRSM turbulent model in order to have a low Reynolds model (no wall laws) at the walls (even if, sometimes, the mesh is probably too coarse). In fact, different way to model turbulence are possible, the use of URANS models are often questioned when it comes to investigate the transient nature of flow turbulence like here. However for high Reynolds number, the use of Direct Numerical Simulation or Large Eddy Simulation appears to be difficult due to the required computational power and time. In single-phase flow, Berland et al. (2014, 2016) obtained impressive results in the prediction of vibration of a single or 9-tubes with Large Eddy Simulation. For two-phase flow across tube-bundle simulated using a two-fluid approach, we chose to work with URANS models since the time of computation has to be affordable. Dehoux et al. (2017); Benhamadouche and Manceau (2018) show the relevance of R_{ij} EBRSM turbulence model for tube bundle geometry. The prediction of force is as correct as the Large Eddy Simulation. The only difference, and the not least, is the reduced computational time and its ability to reach higher Reynolds numbers. Investigation of turbulence models in single and two-phase flows are consequently of primary interests. The development of models like the R_{ij} EBRSM are required to allow the numerical prediction of vibration induced by single and two-phase flow in a reasonable computational-time.

- work with a 2D-domain on a regular cartesian mesh for the tube bundle. This is a real strong assumption since we know that the turbulence is 3D. This choice has been made due to the lack of time. However, a few 3D runs have been performed in order to confirm the results of the feasibility test cases. Despite this choice, the overall phenomenon at the coupling frequency is known to be 2D since the coherence length is very high.

Upstream and downstream the tube bundle, a channel of 8 cylinder diameter long is meshed in order to initialize the flow and to avoid any outlet effect on the flow inside the arrays. The mesh inside the tube bundle is cartesian and regular with 50 cells within one tube diameter. Consequently, we have respectively for the single and two-phase flow a mesh of 410 000 cells and 485 000 cells (since there are more tubes in two-phase flow configurations).

The ismulated physical-time is 5s, using an unsteady algorithm and a maximum Courant number of 1.

4.2.1 Vibration of a single-tube induced by a single-phase flow across a 7x7 tube-bundle

First, to validate the method, we choose to work in single-phase flow and to compare our results to experiment (Granger et al., 1993) and a proper 3D-numerical simulation using Large Eddy Simulation Berland et al. (2014).

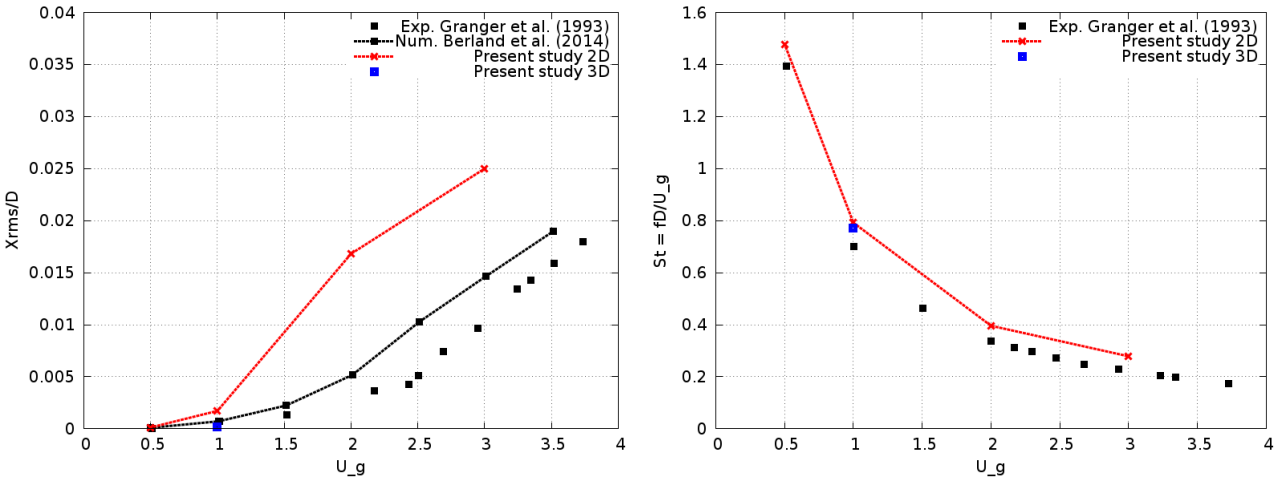

Figure 4.10 Root-mean-square amplitude of cylinder motion (left) and dominant Strouhal number $St = fd/U_g$ (right) as functions of the gap velocity U_g for lift direction only. Comparison of the results from the present study, Granger et al. (1993) and Berland et al. (2014)

In Figure 4.10, the root-mean-square amplitude of cylinder motion and the dominant Strouhal number $St = fd/U_g$ (right) are presented versus the gap velocity U_g for lift direction. The frequency of vibration is correctly reproduced by the simulation using the method developed in the present work. However, even if the RMS evolution is correct, the amplitude of displacement is over-estimated.

For industrial application, the interest is to know the critical velocity before going in fluid-elastic instability. The couple of coefficients C_d and C_k are extracted from experiments and used to predict the stability of steam generator tubes. These coefficients are function of the frequency and the fluid damping only. Given that the amplitude evolution is in agreement with the experiment it can be assumed that the fluid damping is also correctly computed. In fact, the amplitude depends on many non-linear effects that can be considerably disturbed by the choice of the turbulence model and the 2D-domain for examples. Its value is consequently not of great interest, it is consequently not a problem to over-estimate it. The use of the same mesh for the different inlet velocities might also explain the error for higher ones. In fact, the mesh should be more refined for higher velocities. In order to complete this analysis, we performed a 3D run. The results highlights a reduction of the error in both the prediction of the frequency and the displacement. Consequently, it is possible using a R_{ij} EBRSM turbulence model with the Time and Space Dependent Porosity method and the fluid-structure coupling algorithm developed in the present work to reproduce correctly the behavior of the vibration induced by the flow. In future calculations, it could be relevant interest to perform 3D-calculations with more complex post-treatments to complete this work.

4.2.2 Vibration of a single-tube induced by a two-phase flow across a 7x9 tube-bundle

Since the previous feasibility test cases are positive, the vibrations of a single-tube induced by a two-phase flow across a 7x9 tube-bundle (Delenne et al., 1997) are computed with our numerical model for two different inlet void fractions: 10% corresponding to a bubbly flow and 50% corresponding to a churn flow.

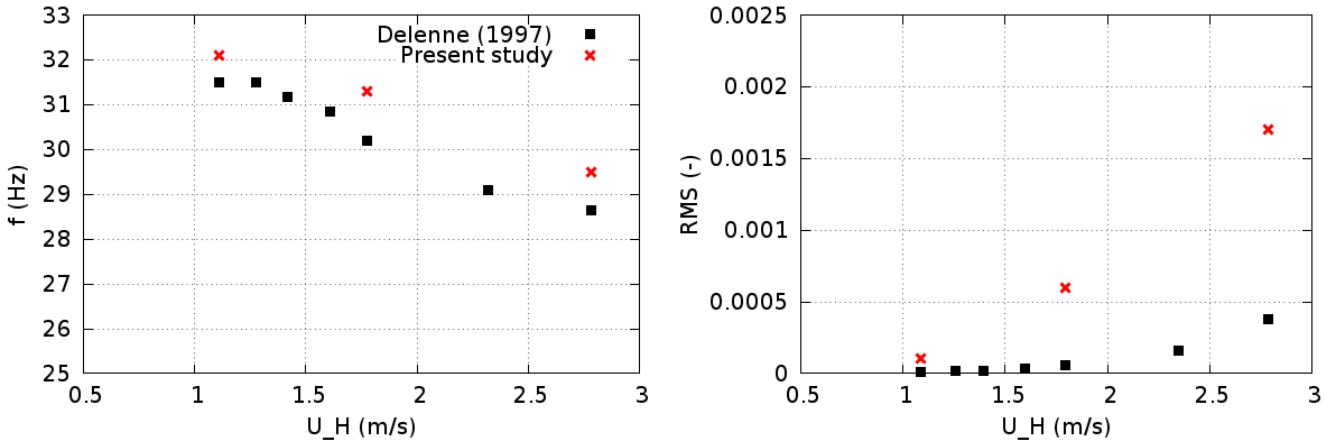

Figure 4.11 Tube frequency (left) and root-mean-square amplitude of cylinder motion (right) as functions of the homogeneous velocity U_g for a **bubbly flow**. Comparison for lift direction only of the results from the present study, and Delenne et al. (1997).

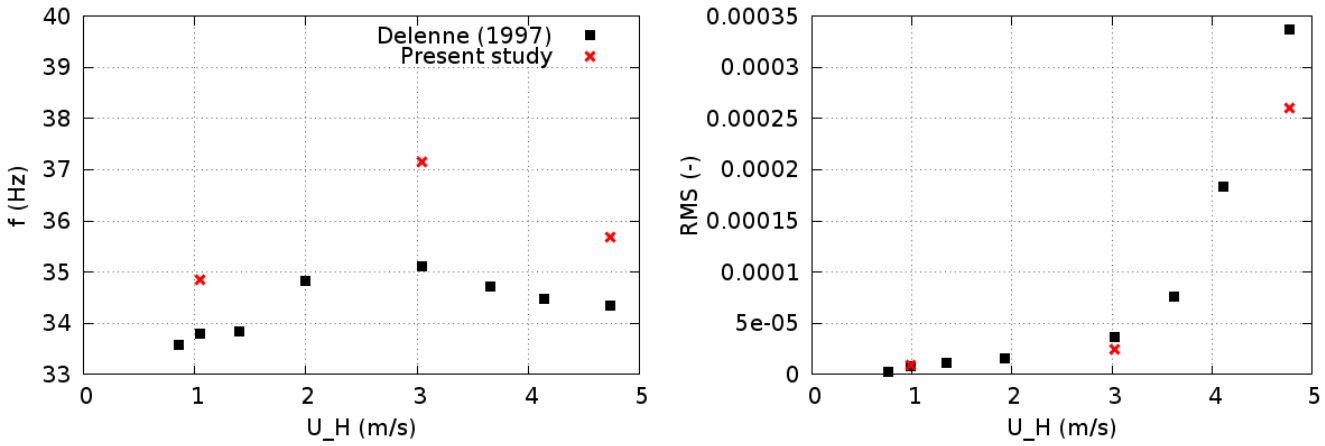

Figure 4.12 Tube frequency (left) and root-mean-square amplitude of cylinder motion (right) as functions of the homogeneous velocity U_g for a **churn flow**. Comparison for lift direction only of the results from the present study, and Delenne et al. (1997).

Like in single-phase flow, the feasibility test cases presented in Figures 4.11 and 4.12 for two different inlet void fractions are in correct agreement for frequency prediction. The two-phase effect seen in the evolution of the frequency is consequently correctly captured by the numerical model despite the assumptions. The amplitude is over-estimated for bubbly flow and luckily correctly estimated for churn flow. Once again, this is due to the different non-linear effects that could be modified by the use of a 3D domain or a finer turbulence model. Concerning the fluid damping (which is for now not extracted),

given the evolution of amplitude between the bubbly and the churn flow, it is reasonable to say that its evolution is correct since it is higher for 50% of void fraction (lower amplitude).

Summary and Remarks

First, we tried to compare for equivalent inlet mass or volume flow rates a freon/water flow and a steam/water flow. If for a bubbly flow, results are very different, it is not the same conclusion for a churn flow. The geometry seems to be the crucial parameter for higher void fractions. However, if the flow patterns appear to be similar for both mixtures for higher void fraction, it does not mean that the force would be equivalent (so the vibration). This study has to be continued for higher void fraction in order to see if these conclusions are confirmed. Moreover, a force record on different cylinders would allow to see the eventual discrepancy between the force spectrums from both mixtures.

Then, based on the method developed in previous chapters to perform two-phase flow induced vibration, feasibility test cases were performed. In single and two-phase flows, results were encouraging given the assumptions made. The general properties of the phenomenon are captured. Additional post-treatments are now required to get the overall damping. Its evolution appears to be correct regarding the amplitude of displacement. A numerical simulation is running with 9 free cylinders (see Figure

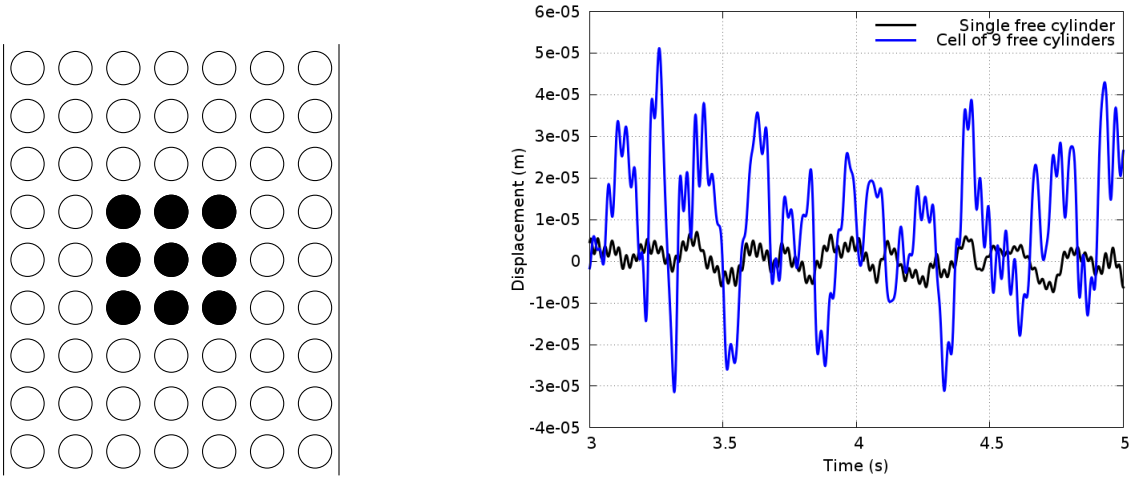

Figure 4.13 a) VISCACHE tube bundle geometry for single-phase flow (left). Rigid tubes are filled in white and flexible tubes in black. b) Displacement of the center tube for a unique mobile tube and mobile flexible cell of 9 tubes.

4.13). In order to get correct force spectra, a longer physical time is required. However, given the first results, the rms of the displacement seems in agreement with the experimental data and tubes are coupled between each other. In Figure 4.13, it is possible to see that the center tube motion is strongly impacted by the motions of the other tubes around. Different optimizations are now required to go further with a reasonable computational time for industrial use:

- The mesh is here homogeneously cartesian. Based on different blocks of mesh, it would be possible to refine close to the wall of each cylinder and to have coarser cells between them. This would allow to increase the accuracy of the simulation and to optimize its computation.

- For the iterative coupling algorithm, we remark that the convergence of the different iterations were very similar during the simulations. By interpolation, it could be possible to reduce this number of sub-cycles and consequently to decrease the time of computation of the whole simulation.

Finally, the numerical simulation of steam/water flow induced vibration being possible, a comparison (based on equivalent inlet mass or volume flow rates) of the regime of vibrations would be a major step toward the characterization of the mixture effect on vibration.

Conclusion and Perspectives

This PhD work aimed at two goals:

- To develop a numerical model able to simulate fluid-structure interaction in two-phase flows.
- To characterize the mixture effect on the vibration induced by two-phase flow.

The targeted industrial application was the prediction of two-phase flow-induced vibration in steam-generator-like tube bundle experiments. This work has been performed by using a multi-phase flow CFD code based on a single pressure (two-fluid approach). The thesis was divided in three distinct parts according to the two objectives and the industrial application.

The Time and Space Dependent Porosity method, developed to allow solid motion, is now part of the official version of NEPTUNE_CFD and is published in a journal (Benguigui et al., 2018). Different studies are using the method whether to reduce the complexity of the mesh like for the emptying of a bottle, or to have imposed solid motion like for opening/closing valves in pipes (for hydraulic power plant).

Based on an existing algorithm, the method has been used to perform fluid-structure coupling. The accuracy of the wall reconstruction was a key point in the reproduction of the motion induced by the flow. These developments are now also part of NEPTUNE_CFD sources. They are now used to simulate hydraulic dashpots since it requires a method able to perform large displacements with a correct refinement at the wall. Previously, the study of this kind of case was not or hardly performed by CFD. The main perspective is now to add the rotational motion in order to be able to perform free-fall of solid objects for example.

Since it is expensive to perform two-phase flow across tube bundle experiments with realistic operating conditions, other mixtures with different physical properties are used to simulate the real configuration. The choice of the mixture appears to be of primary interest when it comes to correctly reproduce the flow pattern and the subsequent flow-induced vibrations. Unfortunately, only few studies have been looking at two-phase cross flow on fixed geometries despite it is probably an interesting way to understand two-phase flow induced vibration. The work was mainly interested in simple cases without any motion in order to come back to the essence of this kind of flow. In order to understand the role of the surface tension, of flow patterns, or of the gas structure on vibration, some additional experiments are required. For example, with a reasonable cost, by adding soap in the liquid, it is possible to reduce the surface tension of a given mixture and to study its influence. A concrete numerical validation would be then possible on the same geometry for different surface tensions. Numerical models need experiments to be validated and to be trusted in. Consequently, experimental efforts are still required in the characterization of the two-phase flows (and not only of the vibration) to fully address the phenomenon.

With only feasibility test cases, based on the strong assumption of a 2D domain, it has been possible to reproduce the tube vibration behavior in single and two-phase flows. Moreover, with some optimizations in terms of mesh and fluid-structure coupling, it would be possible to perform 3D simulations with reasonable computational times. Thanks to the ability of the method to have several objects without additional cost, an example has shown the possibility to perform simulation with multiple mobile cylinders.

Finally, this thesis proposes a numerical way to understand two-phase flow across tube bundle and demonstrates the possibility to predict tube vibration despite strong assumptions. In order to answer the remaining questions, a devoted experimental project and numerical simulations would probably allow to fully understand vibration induced by two-phase flow in tube arrays.

Bibliography

Aristoff, J., Truscott, T., and Bush, A. T. J. (2010). The water entry of decelerating spheres. *Physics of fluids*, 22.

Arquis, E. and Caltagirone, J. (1984). Sur les conditions hydraulique au voisinage d'une interface milieu fluide milieu poreux: application à la convection naturelle. *C.R Math. Acad. Sci. Paris II*, pages 1–4.

Axisa, F., Villard, B., Gibert, R., and Boheas, M. (1985). Vibration of tube bundles subjected to steam-water cross flow: a comparative study of square and triangular pitch arrays. *Internation Conference on Structural Mechanics in Reactor Technolofy*, Vol. B.

Azuma, S., Morita, H., Hirota, K., Kondo, Y., Utsumi, S., Komuro, Y., Kawakamo, R., Nariai, T., and Nishikawa, Y. (2018). Investigation of critical flow velocity of a triangular u-tube bundle subjected to two-phase flow. *Flow-Induced Vibration Toronto*.

Bai, W., Mingham, M., Causon, D., and Qian, L. (2010). Finite volume simulation of viscous free surface waves using the cartesian cut cell approach. *International Journal of Numerical Methods in Fluids*, 63(1):69–95.

Baj, F. (1998). Amortissement et instabilité fluide-elastique d'un faisceau de tubes sous écoulement diphasique. *Thèse de doctorat, Université Paris VI*.

Bartosiewicz, Y., Lavieville, J., and Seynhaeve, J.-M. (2008). A first assessment of the neptune_cfd code: Instabilities in a stratified flow comparison between the vof method and a two-field approach. *International Journal of Heat and Fluid Flow*.

Benek, J. A., Steger, J. L., and Dougherty., F. (1983). A flexible grid embedding equations. *AIAA Paper*.

Benguigui, W., Deri, E., Lavieville, J., Mimouni, S., and Longatte, E. (2017). Numerical experiment on two-phase flow behaviors in tube-bundle geometry for different mixtures. *Pressure Vessel and Piping, Hawai, USA*.

Benguigui, W., Doradoux, A., Lavieville, J., Mimouni, S., and Longatte, E. (2018). A discrete forcing method dedicated to moving bodies in two-phase flows. *International Journal of Numerical Methods in Fluids*.

Benhamadouche, S. and Manceau, R. (2018). Numerical simulations of flow and heat transfer in wall bounded pin matrix. *International Journal of Heat and Fluid Flow (in press)*.

Benito, I. and Mureithi, N. (2017). Identification of two-phase flow patterns using support vector classification. *Pressure Vessel and Piping, Hawai, USA*.

Bergmann, M., Hovnanian, J., and Iollo, A. (2012). An accurate cartesian method for incompressible flows with moving boundaries. *Communications in Computationnal Physics*, 15:1266–1290.

Berland, J., Deri, E., and Adobes, A. (2014). Large-eddy simulation of cross-flow induced vibrations of a single flexible tube in a normal square array. *ASME PVP Conference, Anaheim*.

Berland, J., Deri, E., and Adobes, A. (2016). Investigation of cross flow induced vibrations in a normal square tube array by means of large eddy simulations for tube damage risk assesment. *CFD4NRS-6, Boston*.

Bhaga, D. and Weber, M. (1981). Bubbles in viscous liquids: shape, wakes and velocities. *Journal of Fluid Mechanics*, 105:61–85.

Bnà, S., Manservisi, S., Scardovelli, R., Yecko, P., and Zaleski, S. (2015a). Numerical integration of implicit functions for the initialization of the vof function. *Journal of Computers & Fluids*, 113:42–52.

Bnà, S., Manservisi, S., Scardovelli, R., Yecko, P., and Zaleski, S. (2015b). Vofi - library to initialize the volume fraction scalar field. *Computer Physics Communications*, 200:291–299.

Bottin, M., Berlandis, J., Hervieu, E., Lance, M., ?Özt?ürk, M. M. O., and Serre, G. (2014). Experimental investigation of a developing two-phase bubbly flow in horizontal pipe. *International Journal of Multiphase Flow*.

Bouillet, C., Grandotto, M., and Pascal-Ribot, S. (2007). Comparison between a simulation and local measurements of a two-phase flow across a 60 inclined tube bundle. *International Congress on Multiphase-Flows*.

Bouzidi, S. E., Hassan, M., Fernandes, L., and Mohani, A. (2014). Numerical characterization of the area perturbation and timelag for a vibrating tube subjected to cross-flow. *Fluid-Structure Interaction ASME 4*.

Brackbill, J., Kothe, D., and Zemach, C. (1992). A continuum method for modeling surface tension. *Journal of Computational Physics*, 100.

Caltagirone, J. and Arquis, E. (1986). Recirculating flow in porous media. *C.R Math. Acad. Sci. Paris IIb*, 302:843–846.

Carbou, G. and Fabrie, P. (2003). Boundary layer for a penalization method for viscous incompressible flow. *Advances in Differential Equations*, 8:1453–1480.

Chen, S. (1983). Instability mechanisms and stability criteria of a group of circular cylinders subjet to cross-flow. part i : Theory. *Journal of Vibration, Acoustics, Stress and Reliability in Design*, 105:51–58.

Chen, S. (1987). Flow induced vibration of circular cylindrical structures. *Hemisphe, New York*.

Clarke, D., Salas, M., and Hassan, H. (1986). Euler calculations of multi-element airfoils using cartesian grids. *AIAA Journal*, 24:1128–1135.

Clift, R., Grace, J., and Weber, M. (1978). Bubbles, drops, and particles. *Academic Press New York*.

Coste, P. (2013). A large interface model for two-phase cfd. *Nuclear Engineering and Design*, 255:38–50.

Coste, P. and Laviéville, J. (2009). A wall function-like approach for-two-phase cfd condensation modeling of the pressurized thermal shock. *NURETH-13*.

Coste, P., Pouvreau, J., Laviéville, J., and Boucker, M. (2008). A two-phase cfd approach to the pts problem evaluated on cosi experiment. *ICONE*.

Coste, P., Pouvreau, J., Morel, C., Laviéville, J., Boucker, M., and Martin, A. (2007). Modeling turbulence and friction around a large interface in a three-dimension two-velocity eulerian code. *NURETH-12*.

Coutanceau, M. and Brouard, R. (1977). Experimental determination of the main features of the viscous flow in the wake of a circular cylinder in uniform translation. part 1 : Steady flow. *Journal Fluid Mechanics*, 79:231–256.

Dehoux, F., Benhamadouche, S., and Manceau, R. (2017). An elliptic blending differential flux model for natural, mixed, and forced convection. *International Journal of Heat and Fluid Flow*, 63:15.

Delenne, B., Gay, N., Campistron, R., and Banner, D. (1997). Experimental determination of motion dependent fluid forces in two-phase water freon cross-flow. *AD- American Society of Mechanical Engineers. Aerospace Division Newsletter* .

Denèfle, R., Mimouni, S., Caltagirone, J., and Vincent, S. (2014). Multifield hybrid approach for two-phase flow modeling - part 1: Adiabatic flows. *Journal of Computers & Fluids*.

Deri, E. (2018). Operational modal analysis of a triangular-pitch tube bundle subjected to two-phase cross-flow. *Journal of Pressure Vessel Technology*, 140:1–8.

Donea, J., Huerta, A., Ponthot, J., and Rodriguez-Ferran, A. (2004). Arbitrary lagrangian-eulerian methods. *Encyclopedia of Computational Mechanics*.

English, E., Qiu, L., Yu, Y., and Fedkiw, R. (2013). Chimera grids for water simulation. *Harvard report*.

Étienne, S. and Pelletier, D. (2005). A general approach to sensitivity analysis of fluid–structure interactions. *Journal of Fluids and Structures*, 21(2):169 – 186.

Feenstra, P. and Weaver, D. (2000). An improved void fraction model for two-phase cross-flow in horizontal tube bundles. *International Journal of Multiphase Flow*, 26:1851–1873.

Fleau, S. (2017). Multifield approach and interface locating method for two-phase flows in nuclear power plants. *Université Paris-Est Marne La Vallée*.

Fleau, S., Mimouni, S., Mérigoux, N., and Vincent, S. (2015). Validation of multifield approach for the simulations of two-phase flows. *Computational Thermal Sciences*.

Gao, F. (2003). An efficient finite element technique for free surface flow. *Ph.D thesis, Brighton University UK*.

Gay, N., Decembre, P., and Launay, J. (1988). Comparison of air/water to water/freon two-phase cross-flow effects to the vibratory behaviour of a tube bundle. *Winter Annual Meeting of the ASME, SYmposium on Flow-Induced Vibrations*.

Granger, S. (1991). A global model for flow-induced vibration of tube bundles in cross)flow. *ASME Journal of Pressure Vessel Technology*, 113:446–458.

Granger, S., Campistron, R., and Lebret, J. (1993). "motiondependent excitation mechanisms in a square in-line tube-bundle subject to water cross-flow: an experimental modal analysis. *Journal of Fluids and Structures*, 7:521–550.

Grant, I. and Chisholm, D. (1977). Two-phase on shell-side of a segmentally baffled shell-and-tube heat exchanger. *ASME Winter Annual Meeting, Atlanta*.

Green, S. and Hestroni, G. (1995). Pwr steam generators. *International Journal of Multiphase Flow*, 21:1–97.

Hara, F. (1982). Vibration of circular cylinder in cross two-phase flow (2nd report; karmann vortex shedding and pressure fluctuations. *Japanese Society of Mechanical Engineering*, 48:1371–1379.

Hara, F. and Ohtani, I. (1982). Vibration of circular cylinder in cross two-phase flow (1st report; karmann vortex shedding and pressure fluctuations. *Japanese Society of Mechanical Engineering*, 48:962–971.

Hassan, M., Gerber, A., and Omar, H. (2010). Numerical characterization of the area perturbation and timelag for a vibrating tube subjected to cross-flow. *Journal of Pressure Vessel Technology*, 432.

Hou, G., Wang, J., and Layton, A. (2012). Numerical methods for fluid-structure interaction — a review. *Communications in Computational Physics*, 12(2):337–377.

Hu, Z., Yang, Y., Liu, L., and Zhou, F. (2006). Local flow regime transition criteria of gas-liquid two phase flow in vertical upward tube with a horizontal rod. *Chinese Journal of Chemical Engineering*, 14:442–449.

Hübner, B., Walhorn, E., and Dinkler, D. (2004). A monolithic approach to fluid–structure interaction using space–time finite elements. *Computer Methods in Applied Mechanics and Engineering*, 193(23):2087 – 2104.

Huvelin, F., Longatte, E., Verreman, V., and Soulie, Y. (2006). Numerical simulation of dynamic instability for a pipe conveying fluid. *Pressure Vessel and Piping*.

Inoue, A., Kozawa, Y., Yokosawa, M., and Aoki, S. (1985). Studies on two-phase cross-flow. part i:flow characteristics around a cylinder. *International Journal of Multiphase Flow*, 12:149–167.

Ishii, M. (1975). *Thermo-fluid dynamic, theory of two-phase*. Eyrolles.

Ishii, M. and Zuber, N. (1979). Drag coefficient and relative velocity in bubbly, droplet or *American Institute Chemical Engineers Journal*.

Janosi, I., Jan, D., Szabo, K., and Tel, T. (2004). Turbulent drag reduction in dam-break flows. *Experiments in Fluids*.

Johansen, H. and Colella, P. (1998). A cartesian grid embedded boundary method for poison's equation on irregular domains. *Journal of Computational Physics*, 147(1):60–85.

Kanizawa, F. and Ribatski, G. (2016). Two-phase flow patters across triangular tube bundle for air-water upward flow. *International Journal of Multiphase Flow*, 80:43–56.

Koumoutsakos, P. and Leonard, A. (1995). High resolution simulations of the flow around an implusively started cylinder using vortex methods. *Journal of Fluid Mechanics*.

Küttler, U. and Wall, W. (2008). Fixed-point fluid-structure interaction solvers with dynamic relaxation. *Computational Mechanics*, 43:61–72.

Labourasse, E., Lacanette, D., Toutant, A., Vincent, S., Lubin, S., Lebaigue, O., Caltagirone, J., and Sagaut, P. (2007). Towards large eddy simulation of isothermal two phase flows: governing equations and apriori test. *International Journal of Multiphase Flow*, 33:1–39.

Langre, E. D. (2002). *Fluides et Solides*. Ecole Polytechnique.

Lavieville, J., Merigoux, N., Guingo, M., Baudry, C., and Mimouni, S. (2017). A generalize turbulent dispersion model for bubbly flow numerical simulation in neptune_cfd. *Nuclear Engineering and Design*, 312:284–293.

Lighthill, M. (1958). On displacement thickness. *Journal Fluid Mechanics*, 4:382–392.

Mao, K. and Hibiki, T. (2017). Flow regime transition criteria for upward two-phase cross-flow in horizontal tube bundles. *Journal of Applied Thermal Engineering*, 112:1533–1546.

Marcel, T. (2010). Simulation numérique et modélisation de la turbulence statistique et hybride dans un écoulement de faisceau de tubes à nombre de reynolds élevé dans le contexte de l'interaction fluide-structure. *Thèse de doctorat, Université de Toulouse*.

Matthies, H. G., Niekamp, R., and Steindorf, J. (2006). Algorithms for strong coupling procedures. *Computer Methods in Applied Mechanics and Engineering*, 195(17):2028 – 2049. Fluid-Structure Interaction.

Matthies, H. G. and Steindorf, J. (2002). Partitioned but strongly coupled iteration schemes for nonlinear fluid–structure interaction. *Computers & Structures*, 80(27):1991 – 1999.

Matthies, H. G. and Steindorf, J. (2003). Partitioned strong coupling algorithms for fluid–structure interaction. *Computers & Structures*, 81(8):805 – 812. K.J Bathe 60th Anniversary Issue.

Meng, H. (1993). On dispersed two-phase flows past obstacles. *Technische Universiteit Eindhoven*.

Mer, S., Praud, O., Neau, H., Merigoux, N., Magnaudet, J., and Roig, V. (2018). The emptying of a bottle as a test case for assessing interfacial momentum exchange models for euler-euler simulations of multi-scale gas-liquid flows. *International Journal of Multiphase Flow*, 106.

Merigoux, N., Lavieville, J., Mimouni, S., Guingo, M., and Baudry, C. (2016). A generalized large interface to dispersed bubbly flow approach to model two-phase flows in nuclear power plant. *CFD4NRS-6, Boston*.

Mimouni, S., Archambeau, F., Boucker, M., Lavieville, J., and Morel, C. (2010). A second order turbulence model based on a reynolds stress approach for two-phase boiling flow and application to fuel assembly analysis. *Nuclear Engineering and Design*.

Mitra, D., Dihr, V., and Catton, I. (2009). Fluid-elastic instability in tube arrays subjected to air-water and steam-water cross-flow. *Journal of Fluids and Structures*, 25:1213–1235.

Mittal, R. and Iaccarino, G. (2005). Immersed boundary methods. *Annual review of fluid mecanics*.

Mohany, A., Janzen, V., Feenstra, P., and King, S. (2012). Experimental and numerical characterization of flow-induced vibration of multispan u-tubes. *Journal of Pressure Vessel Technology*, 134:113.

Murakawa, H., Baba, M., Sugimoto, K., Takenaka, N., and Saito, D. I. Y. (2016). Evaluation of void fraction around a tube in two-phase flow across horizontaltube bundle. *International Conference on Multiphase Flow*.

Mureithi, N. W., Nakamura, T., Hirota, K., Murata, M., and Utsumi, S. (2002). Dynamics of an in-line tube array subjected to steam-water cross-flow. part ii: unsteady fluid forces. *Journal of Fluids and Structures*, 16:137–152.

Murzyn, F. and Chanson, H. (2009). Free surface fluctuations in hydraulic jumps: experimental observations. *Experimental Thermal and Fluid Science*.

Nakamura, T., Fujita, K., Kawanishi, K., Yamaguchi, N., and Tsuge, A. (1995a). Study on the vibrational characteristics of a tube array caused by two-phase flow. part i: Random vibration. *Journal of Fluids and Structures*, 9.

Nakamura, T., Fujita, K., Kawanishi, K., Yamaguchi, N., and Tsuge, A. (1995b). Study on the vibrational characteristics of a tube array caused by two-phase flow. part ii: Fluidelastic vibration. *Journal of Fluids and Structures*, 9:539–562.

Newmark, N. (1959). A method of computation for structural dynamics. *Journal of Engineering Mechanics*, pages 67–94.

Noghrehkar, G., Kawaji, M., and Chan, A. (1999). Investigation of two-phase flow regimes in tube bundles under cross-flow conditions. *International Journal of Multiphase Flow*, 25:857–874.

Noh (1964). A time dependant two-space-dimensional coupled eulerian-lagrangian code. *W.F.alderb edn. Academic Press*.

Olsson, E. and Kreiss, G. (2005). A conservative level set method for two-phase flow. *Journal of Computational Physics*.

Païdoussis, M. (2006). Real-life experiences with flow-induced vibration. *Journal of Fluids and Structures*, 22:741–755.

Pascal-Ribot, S. and Blanchet, Y. (2007). Buffeting lift forces and local air-water flow aspects around a rigid cylinder. *International Journal of Multiphase Flow*, 33:1237–1254.

Pedro, B. D., Parrondo, L., Meskell, C., and oro, J. (2016). Cfd modelling of the cross-flow through normal triangular tube arrays with one tube undergoind forced vibrations or fluidelastic instability. *Journal of Fluids and Structures*, 64:67–86.

Peskin, C. (1972). Flow patterns around heart valves: A numerical method. *Journal of Computational Physics*.

Pettigrew, M. (1989). Vibration of tube bundles in two-phase cross-flow: Part 2—fluid-elastic instability. *Journal of Pressure Vessel Technology*, 111:478.

Pettigrew, M. (1995). Vibration of a tube bundle in two-phase freon cross flow. *Journal of Pressure Vessel Technology*, 117:321–329.

Pettigrew, M. and Knowles, G. (1997). Some aspects of heat exchanger tube damping in two-phase mixtures. *Journal of Fluids and Structures*.

Pettigrew, M. and Taylor, C. (1991). Fluidelastic instability of heat exchanger tube bundles : Review and design recommendations. *Proceedings, Internatinal Conference On Flow Induced Vibrations*.

Pettigrew, M. and Taylor, C. (1994). Two-phase flow induced vibration: An overview. *Journal of Pressure Vessel Technology*, 116:233–253.

Pettigrew, M. and Taylor, C. (2003). Vibration analysis of shell-and-tube heat exchangers : an overview – part 1 : vibration response, fretting wear, guidelines. *Journal of Fluids and Structures*, 18:485–500.

Pierson, J. and Magnaudet, J. (2018a). Inertial settling of a sphere through an interface. part 1. from sphere flotation to wake fragmentation. *Journal of Fluid Mechanics*, 835:762–807.

Pierson, J. and Magnaudet, J. (2018b). Inertial settling of a sphere through an interface. part 2. sphere and tail dynamics. *Journal of Fluid Mechanics*, 835:808–851.

Pomarede, M., Longatte, E., and Sigrist, J. (2010). Numerical simulation of an elementary vortex-induced-vibration problem by using a fully coupled fluid solid system computation. *International Journal of Multiphysics*, 4(3):273–291.

Price, S. (1995). A review of theoritical models for fluidelastic instability of cylinder arrays in cross-flow. *Journal of Fluids and Structures*.

Remy, F. (1982). Flow induced vibration of tube bundles in two phase cross flow in vibration in nuclearplant. *3rd International Conference British Nuclear energy society, London*.

Rogers, R., Taylor, C., and Pettigrew, M. (1984). Fluid effects on multispan heat exchanger tube vibration. *Pressure Vessels and Piping, San Antonio*.

Ruyer, P., Seiler, N., Beyer, M., and Weiss, F. (2007). A bubble size distribution model for the numerical simulation of bubbly flows. *International Conference on Multiphase Flow*.

Sadek, O., Mohany, A., and Hassan, M. (2018). Numerical investigation of the cross flow fluidelastic forces of two-phase flow in tube bundle. *Journal of Fluids and Structures*, 79:171–186.

Sagaut, P. (2004). *Large Eddy Simulaiton for Incompressible flows*. Springer-Verlag.

Sarthou, A. (2009). Méthode de domaines fictifs d'ordre élevé pour les équations elliptiques et de navier-stokes: application au couplage fluide-structure. *PhD thesis, Université de Bordeaux*.

Shiels, D., Leonard, A., and Roshko, A. (2001). Flow-induced vibration of a circular cylinder at limiting structural parameters. *Journal of Fluids and Structures*, 15:3–21.

Shinde, V., Marcel, T., Horau, Y., Deloze, T., Harran, G., Baj, F., Cardolaccia, J., Magnaud, J., Longatte, E., and Braza, M. (2014). Numerical simulation of the fluid-structure interaction in a tube array under cross flow at moderate and high reynolds number. *Journal of Fluids and Structures*, 47:99–113.

Song, M., Lefrançois, E., and Rachik, M. (2013). A partitioned coupling scheme extended to structures interacting with high-density fluid flows. *Journal of Computers & Fluids*, 84:190–202.

Soussan, D., Gontier, A., and Saldo, V. (2001). Local two-phase flow measurement in an oblique tube bundle geometry - the maxi program. *International Conference on Multiphase Flow*.

Sun, D., Xu, J., and Chen, Q. (2014). Modeling of the evaporation and condensation phase-change problems with fluent. *Journal of Numerical Heat Transfer*.

Taira, K. and Colonius, T. (2007). The immersed boundary method: a projection approch. *Journal of Computational Physics*, 225:2118–2137.

Tomiyama, A., Tamai, H., Zun, I., and Hosokawa, S. (2002). Transverse migration of single bubbles in simple shear flows. *Chemical Engineering Science*.

Tritton, D. (1959). Experiments on the flow past a circular cylinder at low reynolds number. *Journal Fluid Mechanics*, 22:673–688.

Tseng, Y. and Ferziger, J. (2003). A ghost-cell immersed boudary method for flow in complex geometry. *Journal of Computational Physics*, 192(2):593–623.

Ulbrich, R. and Mewes, D. (1994). Vertical, upward gas-liquid two-phase flow across a tube bundle. *International Journal of Multiphase Flow*, 20:249.

Vincent, S., Tavares, M., Fleau, S., Mimouni, S., Ould-Rouis, M., and Estivalezes, J.-L. (2016). A priori filtering and les modeling of turbulent two-phase flows. application to phase separation. *Journal of Computers & Fluids*.

Wang, S. and Zhang, X. (2011). An immersed boundary method based on discrete stream function formulation for two and three dimensional incompressible flows. *Journal of Computational Physics*, 230:3479–3499.

Weaver, D. and Fitzpatrick, J. (1987). A review of flow induced vibrations in heat exchangers. *Proceedings, International Conference on Flow Induced Vibrations,*.

Weaver, D., Lian, H., and Huang, X. (1993). Vortex shedding in rotated square arrays. *Journal of Fluids and Structures*, 7:107–121.

Ye, T., Mittal, R., Udaykumar, H., and Shyy, W. (1999). T. ye, r. mittal, h. udaykumar, w. shyy. *Journal of Computational Physics*, 156:209–240.

Zuber, N. (1964). On the dispersed two-phases flow in the laminar flow regime. *Chemical Engineering Science*.

Appendix A

Two-phase flow modeling with NEPTUNE_CFD

A.1 Toward two-phase flow numerical modeling

For an incompressible single phase flow, to follow the fluid motion, three conservation equations are solved : mass balance, momentum, and energy. Energy equation is neglected since the thermodynamic of the system is not a major concern in the present study.

Mass balance equation:

$$\frac{\partial \rho}{\partial t} + \underline{\nabla} \cdot (\rho \mathbf{U}) = 0 \tag{A.1}$$

with ρ the density, and $\mathbf{U}$ the velocity field.

Momentum balance equation:

$$\frac{\partial (\rho \mathbf{U})}{\partial t} + (\rho \mathbf{U} \cdot \underline{\nabla})\mathbf{U} = -\underline{\nabla} P + \rho \mathbf{g} + \underline{\nabla} \cdot \overline{\overline{\tau}} \tag{A.2}$$

with $\overline{\overline{\tau}} = \mu \left(\overline{\overline{\nabla}} \mathbf{U} + \overline{\overline{\nabla}} \mathbf{U}^T \right)$ the viscous stress tensor, $\mathbf{g}$ the gravity acceleration, P the pressure.

To deal with two-phase flow, a k-phase indicator function is defined equal to 1 in phase k, and to 0 everywhere else. The main property of this function is the following :

$$\sum_k \chi_k(\mathbf{x}) = 1 \tag{A.3}$$

with $\chi_k(\mathbf{x}) = \begin{cases} 1 & \text{if } \mathbf{x} \in \Omega_k \\ 0 & \text{otherwise} \end{cases}$, and Ω_k the volume occupied by phase k. Three other properties link the k-phase indicator functions:

$$\begin{aligned} \chi_m \chi_n &= \delta_{nm} \chi_m \\ \nabla \chi_k &= -\mathbf{n}_k^{Int} \delta_{Int} \\ \tfrac{\partial \chi_k}{\partial t} &= \mathbf{u}^{Int} \mathbf{n}_k^{Int} \delta_{Int} \end{aligned} \tag{A.4}$$

with $\mathbf{n}_k^{Int}$ the unit normal vector at the interface separating both phases, δ_{Int} the Dirac function centered at the interface, and $\mathbf{u}^{Int}$ the interface velocity.

Consequently, each local quantity is defined with a two-phase formulation taking into account the k-phase indicator functions : $\chi_k\Phi_k$. The discontinuity of the k-phase indicator functions induces the apparition of interfacial source terms in the two (three) balance equations and interface jump conditions. More details can be found in Labourasse et al. (2007).

Different approach are possible to solve this balance equations, as the one fluid-approach where the assumption is that the mechanical balance is reached by both phase and that they have the same local averaged velocity. Quantities are therefore expressed as followed:

$$\Phi = \sum_k \chi_k \Phi_k \tag{A.5}$$

Consequently, in one-fluid approach, equation solved are the same as in single phase flows. However, specific models are dedicated to solve two-phase flow characteristics such as the interface in order to compute the χ_k in each cell.

An other approach, called "two-fluid model“, is possible solving balance equations for each phase and assuming a single pressure for both phases.

A.2 Two-fluid approach

This description is used in NEPTUNE_CFD for bubbly flows and more generally liquid-vapor flows in nuclear power plant. It is an eulerian-eulerian model based one the two-fluid model of Ishii extended to n-phase. The main assumption is that both phases have the same pressure. The CFD code NEPTUNE_CFD is a three-dimensional, two-fluid code developed for multiphase flows and more especially for nuclear reactor applications. The NEPTUNE_CFD solver, is based on a pressure correction approach Ishii (1975), on a finite-volume discretization with a collocated arrangement for all variables. A volume averaging method (like in many other code) is used for phase volumetric fractions, and for the different quantities :

$$\begin{array}{c} \alpha_k = \langle\chi\rangle_k = \frac{1}{\Omega}\int_\Omega \chi_k d\Omega = \frac{\Omega_k}{\Omega} \\ \langle\chi_k\Phi_k\rangle_k = \alpha_k\langle\Phi_k\rangle_k \end{array} \tag{A.6}$$

Consequently, for each phase k, the two (three) balance equations solved are written :

$$\begin{array}{c} \frac{\partial(\alpha_k\rho_k)}{\partial t} + \underline{\nabla}\cdot(\alpha_k\rho_k\mathbf{U}_k) = \sum_{p\neq k}\Gamma_{p\to k} \\ \frac{\partial(\alpha_k\rho_k\mathbf{U}_k)}{\partial t} + \underline{\nabla}\cdot(\alpha_k\rho_k\mathbf{U}_k\mathbf{U}_k) = -\underline{\nabla}(\alpha_k P) + \alpha_k\rho_k\mathbf{g} + \underline{\nabla}\cdot\overline{\overline{\tau}}_k \\ + \sum_{p\neq k}\mathbf{M}_{p\to k} \end{array} \tag{A.7}$$

In the present work, the study is restricted to adiabatic cases, simplifying the system to the mass and momentum equations for each phase k :

$$\Gamma_{p\to k} + \Gamma_{k\to p} = 0 \tag{A.8}$$

$$\sum_k \alpha_k = 1 \tag{A.9}$$

where α, ρ, $\mathbf{U}$, Γ, P, τ, $\underline{g}$ and $\mathbf{M}$ are respectively the volume fraction, the density, the velocity, the mass transfer, the pressure, the Reynolds tensor, the gravity and the momentum transfer of the phase k. Because of the coupling between both phases, mass transfers occur, and the interfacial momentum transfer $\mathbf{M}$ can be written as :

$$\mathbf{M}_{p\to k} = \mathbf{M}^{hydro}_{p\to k} + \Gamma_{p\to k}\mathbf{U}^{Int}_{kp} \tag{A.10}$$

where U^{Int}_{kp} is the interfacial velocity between phases k and p. The difference between models are detailed below. For a dispersed bubbly flow or a two-continuous-field approach the closure laws are different. Depending on the forms of the same physical components, e.g.: a continuous or dispersed field, the interfacial momentum transfers of each phase are defined. Different approaches are consequently possible depending on the two-phase flow regime. For a bubbly flow, a dispersed approach for the gas field is more appropriate Mimouni et al. (2010). However, for stratified or slug flow, a Large Interface approach seems to be more suitable Coste et al. (2007, 2008); Coste and Laviéville (2009); Coste (2013).

A.3 Dispersed approach - Spherical bubbles

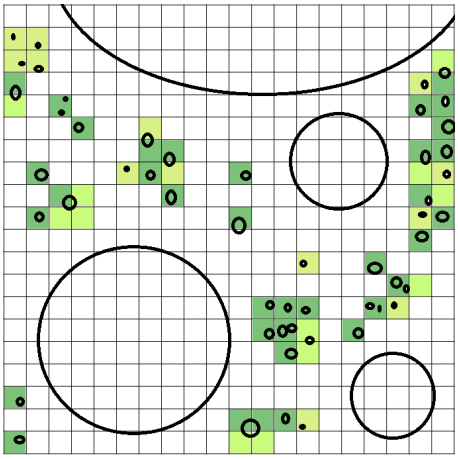

Figure A.1 Sketch of a dispersed approach.

Various numerical experiment tried to solve the distortion of one bubble in a liquid flow or it breaking. This kind of study requires a huge amount of time. Consequently, because of the time of computation, it is not possible to solve each bubble interface in a bubbly flow, an other method had to be condisered. The following approach is dedicated to spherical or near-spherical bubbles (or dropplets). It consists in modeling hydrodynamic forces due to bubbles in each cell. The bubble size is in this method smaller than the cell size as indicated in Figure. A.1. For a gas dispersed field k, drag, lift, added-mass (being

the force induced by the fluid displaced by bubbles) and turbulent dispersion (expressing the interaction between bubbles and turbulence) hydrodynamic forces are modeled.

$$\mathbf{M}_{p\to k}^{hydro} = \mathbf{M}_{p\to k}^{D} + \mathbf{M}_{p\to k}^{L} + \mathbf{M}_{p\to k}^{AM} + \mathbf{M}_{p\to k}^{TD} \tag{A.11}$$

In NEPTUNE_CFD, the classical drag of Ishii and Zuber (1979) developed for spherical and slightly deformed bubbles, the lift ofTomiyama et al. (2002) postulated for the different bubble shapes, the virtual-mass of Zuber (1964) being the force induced by the fluid displaced by bubbles; and turbulent dispersion from Lavieville et al. (2017) are used. Further details can be found in Mimouni et al. (2010) where the dispersed approach is validated for industrial complex geometries.

A.3.1 Drag force

The force exerted bu the fluid on an obstacle in the flow direction is called *drag force*. For bubbles with small deformartions, Ishii proposed the following expression Ishii and Zuber (1979):

$$\mathbf{M}_{L\to G}^{D} = -\mathbf{M}_{G\to L}^{D} = -\frac{1}{8} C_D \rho_l A_i \,||\, \mathbf{U}_g - \mathbf{U}_l \,||\, (\mathbf{U}_g - \mathbf{U}_l) \tag{A.12}$$

with A_i interfacial area, and C_d the drag coefficient modeled empirically as it follows for slightly deformed bubbles:

$$C_D = \frac{2}{3} d \sqrt{\frac{g \mid \rho_g - \rho_l \mid}{\sigma}} \frac{1 + 17.67(1-\alpha)^{9/7}}{18.75(1-\alpha)^{3/2}} \tag{A.13}$$

with σ the surface tension, α the void fraction and d the bubble diameter.

A.3.2 Lift force

The force exerted by the fluid on an obstacle in the flow normal direction is called *lift force*.

$$\mathbf{M}_{L\to G}^{L} = -\mathbf{M}_{L\to G}^{L} = -\rho_l \alpha C_L (\mathbf{U}_g - \mathbf{U}_l) \wedge (\nabla \wedge \mathbf{U}_l) \tag{A.14}$$

with C_L the lift coefficient. For spherical bubble, $C_L = 0.5$. However, for slightly deformed bubbles, Tomiyama Tomiyama et al. (2002) takes into account the Eotvos number:

$$Eo_H = \frac{g \mid \rho_g - \rho_l \mid d_H^2}{\sigma} \tag{A.15}$$

with $d_H = D_b \sqrt[3]{1 + 0.163 Eo^{0.757}}$ with D_b the spherical equivalent diameter. Then, depending on the Eotvos number C_L is defined:

- if $Eo_H < 4$:

$$C_L = \min(0.288 \tanh(0.121 Re), 0.00105 Eo_H^3 - 0.0159 Eo_H^2 - 0.0204 Eo_H + 0.474) \tag{A.16}$$

- if $4 < Eo_H < 10$:

$$C_L = 0.00105Eo_H^3 - 0.0159Eo_H^2 - 0.0204Eo_H + 0.474 \tag{A.17}$$

- if $Eo_H > 10$:

$$C_L = -0.27 \tag{A.18}$$

A.3.3 Added mass force

Acceleration of the bubbles introduces a force on the fluid motion called *added mass force*. According to Zuber Zuber (1964), the expression is given by:

$$\mathbf{M}_{L\to G}^{AM} = -\mathbf{M}_{L\to G}^{AM} = C_A \frac{1+2\alpha}{1-\alpha}\rho_l \alpha \left[\left(\frac{\partial \mathbf{U}_g}{\partial t} + \mathbf{U}_g \underline{\nabla} \cdot \mathbf{U}_g\right) - \left(\frac{\partial \mathbf{U}_l}{\partial t} + \mathbf{U}_l \underline{\nabla} \cdot \mathbf{U}_l\right)\right] \tag{A.19}$$

with $C_A = \frac{1}{2}$ for spherical bubbles.

A.3.4 Turbulent dispersion

The interaction between turbulence and bubbles is computed by a force called *turbulent dispersion*. Turbulent dispersion is proposed by Lavieville et al. (2017):

$$\mathbf{M}_{L\to G}^{DT} = -GTD\ \rho_l\ k_l\ \nabla \alpha_g \tag{A.20}$$

with $GTD = (< \mathbf{M}_{L\to G}^{D} > \tau_{12}^t - 1)\ \frac{\eta_r + b}{\eta_r + 1} + C_{VM} b^2 + \frac{\eta_r}{1+\eta_r}$. Details are found in the publication.

A.4 Continuous approach - Large interfaces

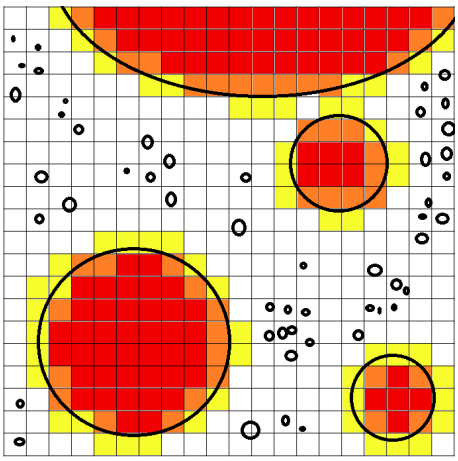

Figure A.2 Large interface approach.

Various scenarios involve interfaces between liquid and vapor or gas which are generally much larger than the computational cells size: separated flow or *large interface*. Specific models to deal with them

were developed such as in NEPTUNE_CFD: the Large Interface Model (LIM) Coste (2013), and the Large Bubble Model Denèfle et al. (2014); Fleau et al. (2015) (LBM). Large interface flow are located thanks to interface tracking method. Then, based on local quantities, interfacial transfer terms between liquid and gas in the momentum balance are modeled by forces such as drag, surface tension or friction. Other models are present in the literature based on the same kind of equations using an interface location and closure laws. Their discrepancies depends on interfacial transfer terms models and the choice of an interface tracking method which can be Immersed Boundary Method or Volume of Fluid for example.

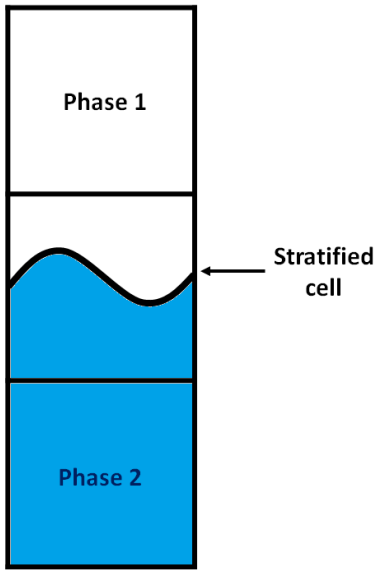

Figure A.3 Three cell stencil.

A.4.1 Large Interface Model

To locate interface tracking method at each time step on the computational domain, an interface tracking method is required. In the LIM (Large Interface Model) Coste et al. (2007, 2008); Coste and Laviéville (2009); Coste (2013), the first step is the interface recognition step as illustrated in Figure A.3. The *Large Interface represented with 3 cells thick layers* method (LI3C) consists in defining three cells to describe the liquid gas interface: one cell with only gas, one cell with only liquid, and one stratified cell containing the interface. Based on the liquid volume fraction gradient, the stratified cell is detected. This three-cell stencil around the large interface is used to compute on both sides (liquid and gas) the distance from the first computational cell to the large interface. Both distance are then used in models written in a wall law-like format. To locate accurately interfaces within the two-fluid model, an interface sharpening equation adapted from Olsson and Kreiss (2005) can be solved in order to avoid numerical diffusion of the interface Denèfle et al. (2014):

$$\frac{\partial \alpha_k}{\partial \tau} + \beta \nabla.(\alpha_k(1-\alpha_k)\mathbf{n}) = \varepsilon\beta\Delta\alpha_k \tag{A.21}$$

with $\beta = \begin{cases} \beta_{min} & \text{for } \alpha_k \leq 0 \\ \frac{1-\beta_{min}}{\alpha_k} + \beta_{min} & \text{for } 0 < \alpha_k < \alpha_{sat} \\ 1 & \text{for } \alpha_k \geq \alpha_{sat} \end{cases}$. Denèfle et al. (2014) assessed the consistency of the present interface sharpening method by different validation test cases. The drag force model is written Coste (2013):

$$\mathbf{M}^D_{L\to G} = \alpha_g \alpha_L C_D (\mathbf{U}_l - \mathbf{U}_g) \tag{A.22}$$

with C_D the two-phase flow standard coefficient described previously in the dispersed approach. Within the three cell stencil, the drag force is only applied in the interface normal direction and the friction model is applied in the tangent direction to take into account the friction along the interface. Since large interface have a finite thickness due to the cell size and can not be considered as resolved, a velocity sliding is allowed. The gas friction force is written:

$$\mathbf{M}^F_{L\to G} = \rho_g (\mathbf{U}^*_\mathbf{g})^2 \frac{\mathbf{U}_l - \mathbf{U}_g}{|| \mathbf{U}_l - \mathbf{U}_g ||} A^{Int} \tag{A.23}$$

with $\mathbf{U}^*_\mathbf{g}$ the gas friction velocity and A^{Int} the interface area. However this model does not take into account the effect from surface tension.

Turbulent velocities, phase change, heat&mass transfer and further details can be found in Coste et al. (2007, 2008); Coste and Laviéville (2009); Coste (2013) for dedicated to large interfaces.

A.4.2 Large Bubble Model

Large Bubble Model developed in Denèfle et al. (2014); Fleau et al. (2015) is similar to the Large Interface Model in term of concept but different in closures laws. The interface recognition method is exactly the same as for the LIM. First Denèfle et al. (2014), the drag force was expressed like:

$$\mathbf{M}^D_{L\to G} = \frac{1}{\tau} \alpha_g \alpha_L (\mathbf{U}_l - \mathbf{U}_g)(\alpha_l \rho_l + \alpha_g \rho_g) \tag{A.24}$$

with τ a characteristic time depending on the time step. Unfortunately, the drag force depends on the time step and for small liquid viscosities the shape prediction is not in agreement with experimental data. Consequently a new drag force Fleau (2017) is postulated and implemented:

$$\begin{aligned} \alpha_g < 0.3 \qquad & \mathbf{M}^D_{L\to G} = \alpha_g \alpha_l \frac{18\mu_l}{\alpha_l d^2} (\mathbf{U}_l - \mathbf{U}_g) \\ \alpha_g > 0.7 \qquad & \mathbf{M}^D_{L\to G} = \alpha_g \alpha_l \frac{18\mu_g}{\alpha_g d^2} (\mathbf{U}_l - \mathbf{U}_g) \\ 0.3 \geq \alpha_g \geq 0.7 \quad & \mathbf{M}^D_{L\to G} = \frac{0.7 - \alpha_g}{0.7 - 0.3} \mathbf{F}_{\mathbf{bubble}} + \frac{\alpha_{g-0.3}}{0.7 - 0.3} \mathbf{F}_{\mathbf{droplet}} \end{aligned} \tag{A.25}$$

The major discrepancy with the LIM is the fact that surface tension effect is modeled in the LBM. Given that the interface has a finite thickness, the *Continuum Surface Force* model proposed by Brackbill et al. (1992), and adapted for the two-fluid approach Bartosiewicz et al. (2008) is used:

$$\mathbf{M}^{ST}_k = \sigma \beta_k \kappa \nabla \alpha_k \tag{A.26}$$

with $\beta_k = \frac{\alpha_k \rho_k}{\sum \alpha_i \rho_i}$, σ the surface tension and $\kappa = -\nabla.(\frac{\nabla \alpha_k}{||\nabla \alpha_k||})$. Moreover, the interface sharpening previously defined in LIM is used in order to avoid numerical diffusion of the gas-liquid interface.

LIM and LBM are compared and validated in different publication highlighting their own advantages and disadvantages. Both of them are used in order to postulate a multi-regime model using dispersed and Large Interface approaches.

A.5 Multi-regime approches

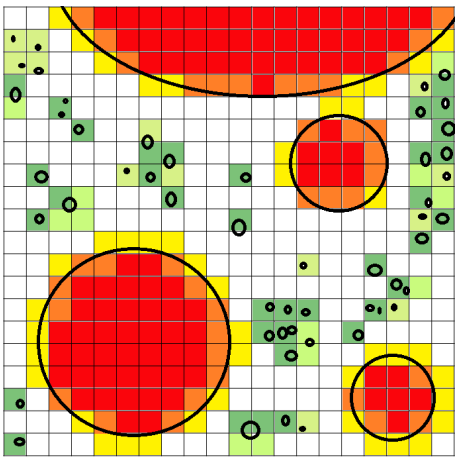

Figure A.4 Sketch of the multi-regime approach.

Initially, two approaches were distinguished: dispersed and large interface; however these two methods are too restrictive for steam generator kind of flow where different regimes are present. As shown in Figure.A.1, each approach does not capture a mixed regime (large interface for dispersed, and bubbles for large interface). Consequently, a multi-regime model (represented in Figure.A.4) is necessary to go through this problem: multi-regime flow, where small and large bubbles are present. Two models using respectively two and three fields are implemented in NEPTUNE_CFD: the Generalized Large Interface To Dispersed approach and the multi-field approach. These models are benchmarked on an original case in Mer et al. (2018).

A.5.1 Generalized Large Interface To Dispersed approach

In order to manage different kinds of vapor shapes, a generalized two-field approach unifying Large Interface Model (LIM originally developed for pressure thermal chocks applications or free surface flows) and dispersed bubbly flow models has been created (Merigoux et al., 2016). This approach only requires two fields (for gas and liquid) to model both separated phases and dispersed bubbly flows at the same time. It takes advantage from both models by adjusting automatically the closure terms of the momentum conservation equation $\mathbf{M}_{p \to k}$. This adjustment is based on the interface recognition capability of the LIM and the local void fraction. In each cell of the domain, the interfacial transfer of momentum (friction) from LIM is applied everywhere a large interface is recognized by the model. Afterwards, the drag, added mass, turbulent dispersion, lift and wall lubrication coefficients are computed according to the standard

dispersed bubbly flow model defined in previous paragraph. Then a weighting is done to only account for these dispersed bubbly flow momentum interfacial transfer closure terms in the dispersed bubble areas:

$$C_\omega = \omega C \tag{A.27}$$

where C is the drag, added-mass, turbulent dispersion, lift or wall lubrication coefficient and ω a weighting coefficient defined according to the void fraction:

$$\begin{array}{ll} \omega = 0 & \text{for } \alpha > 0.5 \\ \omega = \dfrac{0.5-\alpha}{0.5-0.3} & \text{for } 0.3 < \alpha \leq 0.5 \\ \omega = 1 & \text{for } \alpha \leq 0.3 \end{array} \tag{A.28}$$

A final coefficient correction is applied to take into account the eventual presence of a large interface where only the liquid-gas friction issued from the LIM should be applied:

$$C_{fscorr} = C_\omega(1 - \min(6.fscorr, 1)) \tag{A.29}$$

where $fscorr$ is a correction coefficient taking into account the presence of a large interface and depending on the liquid fraction(α_l), the cell's volume (V) and surface vector (S_i):

$$fscorr = || \nabla \alpha_l || \tag{A.30}$$

with $\nabla \alpha_l = \dfrac{\partial \alpha_l}{\partial x_i} \dfrac{V}{| S_i |}$. Applying this approach, the model tends towards the dispersed bubbly flow model in area with low void fractions and behaves as the LIM when the mesh is fine enough to capture the large interfaces.

A.5.2 Multi-field approach

An other method consists in using 2 gas fields to deal with the different vapor shapes. In NEPTUNE_CFD, the multi-regime method having 3-fields (Fleau, 2017) is based on the Large Bubble Model (LBM) and the dispersed approach.

The key point of the method is the transfer between the dispersed and the continuous field. Two kind of transfers are modeled: break-up and coalescence. In the first case, dispersed bubbles are created from the continuous field. The corresponding mass transfer has the following expression:

$$\Gamma_{LBM \to Disp} = \alpha_{LBM} \frac{\rho_g}{\Delta t} C_{LBM \to Disp} H(\kappa \, || \nabla \alpha_g || \, \Omega - \frac{\Delta x}{20}) \tag{A.31}$$

with H the Heaviside function and $C_{LBM \to Disp}$ a relaxation time modeling the fragmentation time scale.

In case of coalescence, a part of the dispersed field is added to the continuous field. The criterion to consider this phenomenon is based on the volume fraction and its gradient. The critical volume fraction is fixed at 0.3 since it is the limit usually used in the literature for bubbly flows Murzyn and Chanson (2009); Sun et al. (2014). The critical gradient is fixed at $\frac{1}{10\Delta x}$ corresponding to half the gradient for the

badly resolved structures.The mass transfer is then defined:

$$\Gamma_{Disp\rightarrow LBM} = \alpha_{Disp}\frac{\rho_g}{\Delta t}C_{Disp\rightarrow LBM}H(\alpha_{Disp}-0.3) \tag{A.32}$$

with $C_{Disp\rightarrow LBM}$ a relaxation time modeling the coalescence time scale. To take into account the possibility of having three fields (continuous liquid, continuous gas and dispersed gas) at the same time, the total mass transfer appearing in the mass balance equation is defined:

$$\Gamma^{TOT}_{Disp\rightarrow LBM} = \Gamma_{Disp\rightarrow LBM} - \Gamma_{LBM\rightarrow Disp} \tag{A.33}$$

with $\Gamma^{TOT}_{Disp\rightarrow LBM} + \Gamma^{TOT}_{LBM\rightarrow Disp} = 0$. The model proposed here is a first approach to consider mass transfer between two fields coming from the same phase.

A.6 Turbulence models

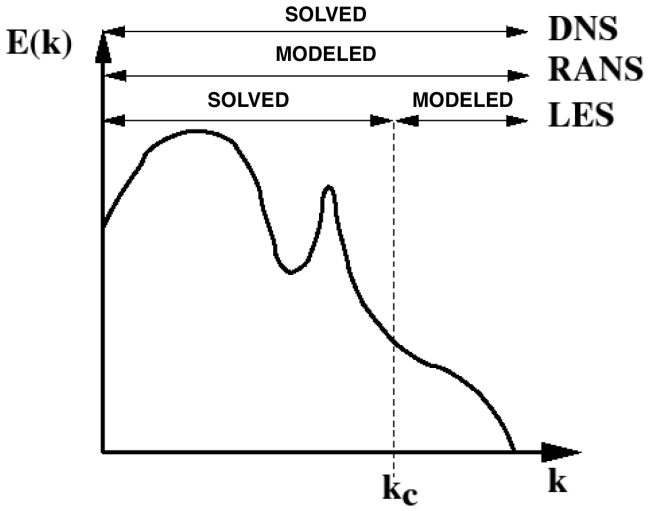

Figure A.5 Turbulent scale, different methods.

Running a fluid mechanic numerical simulation may be time-consuming depending on the required accuracy. In fact, a Reynolds number quantifies how turbulent is a flow. Higher it is, more turbulent is the flow, more time-consuming is the simulation. That is why different choices more or less expensive in terms of time of calculation are possible:

1. Direct numerical simulation (DNS) where each structure is solved. DNS is the most accurate and the most time-consuming turbulence model.

2. Large Eddy simulation (LES) where large structures are solved, others are modeled.

3. Reynolds Averaged Navier-Stokes or Unsteady Reynolds Averaged Navier-Stokes (RANS or URANS) where each structure is modeled.

Turbulence is three dimensional, unsteady, and diffusive. Thanks to turbulence, mixtures are more efficient what may be a great advantage for different industrial applications such as chemistry. Turbulence is characterized by an energy spectrum shown in Figure A.5. Depending on the required accuracy, it can be entirely solved thanks to a DNS or modeled with URANS.

In two-phase flow, especially in gas-liquid flow, bubbles generates agitation called pseudo-turbulence. The presence of bubbles in a flow modify the energy production, transfer and dissipation. Extra turbulent fluctuations are created by bubbles especially in rising cases. In their wake, an other mechanism is shear-induced turbulence. A reverse coupling may deform bubble and other gas structure, turbulence might consequently be absorbed by a slug distortion for example. These three mechanisms induce non-linear effects arguing why the two-phase flow turbulence is today still a main concern for two-phase flow modeling.

Turbulence modeling in two-phase flow might be computed with each way. However, for industrial cases with a two-fluid approach, a $R_{ij} - \varepsilon$ (Reynolds Stress Transport Model) model is used (Mimouni et al., 2010; Sagaut, 2004). Some recent works tried to improve the turbulence modeling using a two-fluid approach with LES (Vincent et al., 2016).

Titre : Modélisation de la réponse dynamique d'une paroi solide mise en vibration par un écoulement fluide diphasique

Mots clés : interaction fluide-structure, écoulement diphasique, frontières immergées, simulation numérique, faisceau de tubes

Résumé : Les tubes des générateurs de vapeur des centrales nucléaires vibrent sous l'effet d'écoulement eau/vapeur. Pour appréhender ce phénomène et le comprendre, des expériences à échelles réduites sont réalisées. La simulation numérique a montré son habilité à reproduire l'interaction fluide-structure sur ce type de géométrie pour des écoulements monophasiques. L'objectif est désormais de faire de même en écoulement diphasique et de caractériser les propriétés physiques du mélange liquide/gaz influant sur la vibration.
Pour se faire, un code CFD avec une approche bi-fluide est utilisé. Une méthode dite de "Discret Forcing" est implémentée pour permettre le mouvement imposé de corps solides au sein d'un écoulement à plusieurs phases. Celle-ci est alors validée sur des cas simples et intégraux avec une comparaison systématique à des résultats expérimentaux ou théoriques.
En se basant sur un algorithme implicite existant dans la littérature, un couplage fluide-structure utilisant cette méthode de suivi d'interface est implémenté. Validé sur des cas monophasiques et diphasiques, ce couplage offre désormais la possibilité de déplacer un solide en fonction des forces fluides diphasiques qui lui sont appliquées.
Les différentes méthodes numériques présentes dans NEPTUNE_CFD sont ensuite évaluées pour un écoulement fréon/fréon au travers d'un faisceau de tubes inclinés. La nécessité d'utiliser un modèle dit "multi-régime" est mis en avant. Afin de déterminer l'influence sur l'écoulement des différentes propriétés physiques d'un mélange diphasique, plusieurs cas d'études simples sont réalisés.
Finalement, l'application industrielle cible, un écoulement eau/fréon dans un faisceau de tubes à pas carré, est simulée et comparée à un écoulement en conditions réelles (eau/vapeur à 70 bar). Les vibrations induites par écoulement monophasique puis diphasique sont correctement reproduites sur des cas dit de "faisabilité".

Title : Numerical simulation of two-phase flow induced vibration

Keywords : fluid-structure interaction, two-phase flow, immersed boundary, CFD, tube bundle

Abstract : In nuclear power plants, steam generator tubes vibrate because of the steam/water cross flows. In order to understand this phenomenon, reduced-scale experiments are performed. Numerical simulations have shown their ability to accurately reproduce the vibration induced by a single-phase flow in a tube bundle. The aim of the present work is to do the same with two-phase flow and to characterize the effect of the physical mixture properties on vibration.
To do so, a CFD code based on a two-fluid approach is used. A "discrete forcing" method is implemented in order to allow solid body motion in a two-phase flow. The validation is performed with simple and industrial cases using experimental data and theoretical results. Using an existing implicit algorithm, a fluid-structure coupling based on the developed interface tracking method is implemented. Validated for single and two-phase flows, it is now possible to have a solid motion induced by fluid forces.
The different numerical models dedicated to two-phase flows are then evaluated on a freon/freon flow across an inclined tube bundle. The use of a multi-regime model is required. In order to investigate the role of the different physical properties on the vibration, three simple studies are performed.
Finally, the industrial application, a freon/water flow across a square pitch tube bundle, is performed. First, it is compared to a steam water flow in order to characterize the discrepancies when we are using a modeling mixture. Then, the vibration induced by single and two-phase flow is reproduced by the developed method on feasibility test cases.

Université Paris-Saclay
Espace Technologique / Immeuble Discovery
Route de l'Orme aux Merisiers RD 128 / 91190 Saint-Aubin, France